The Henryk Niewodniczanski
Institute of Nuclear Physics
Polish Academy of Sciences

and

University of Lorraine

Anna Nykiel

THE MORPHOLOGY, STRUCTURE, AND MAGNETIC PROPERTIES OF METALLIC NANOWIRES SYNTHESIZED BY ELECTRODEPOSITION

Doctoral dissertation
Field of Study: Physics

Thesis written under the supervision of
dr hab. inż. Małgorzata Kąc, prof. IFJ PAN
and
dr hab. Alain Walcarius, CNRS Research Director

Kraków, 2024

ACKNOWLEDGMENTS

I would like to express my gratitude to all people who accompanied and supported me during my PhD studies.

In the first place, I would like to thank my Polish supervisor dr hab. inż. Małgorzata Kąc, for being the most wonderful supervisor a PhD student could ever dream of. Thanks for giving me the opportunity to work under her guidance and sharing her immense knowledge with me. I am grateful for the inspiration, helping me solve countless problems over the last four years and being understanding during multiple turmoils I encountered.

I would also like to extend my deepest appreciation to my French supervisor dr hab. Alain Walcarius, for his valuable advices and important support, especially during my stays in France.

I wish to express my warm and sincere thanks to my Head of the Department dr hab. Łukasz Laskowski, dr hab. inż. Wojciech Maziarz, prof. dr hab. inż. Magdalena Parlińska-Wojtan, dr hab. Magdalena Fitta, dr hab. inż. Michał Krupiński, dr Jaafar Ghanbaja and my colleagues from NO3 who helped me reach the moment of submitting this thesis and and made the journey much more enjoyable: dr Dominika Kuźma, dr Agnieszka Karczmarska, dr Arkadiusz Zarzycki, dr Mateusz Schabikowski, dr Oleksandr Pastukh, dr Svitlana Pastukh, mgr Aleksandra Pacanowska.

Last but not least, words fail to express my appreciation to my parents, who have always believed in me.
And a huge thanks to my husband, Mateusz, for all his moral support and faith in me, especially when I didn't. For listening to my ideas, reflections and complaints. For being so patient with my night work and my annual trips to France.

Thank You!

Preface

Nanotechnology is currently one of the most dynamically developing fields of science, mainly due to its potential applications and interesting properties from the point of view of fundamental studies. Materials in this field, called nanomaterials, are characterized by at least one dimension on the nanometer scale (1-100 nm). These small sizes are responsible for specific properties that make nanomaterials unique compared to their macroscopic counterparts. Their distinctive feature is a large surface-to-volume ratio, which enhances the system response in the case of chemical reactions or other applications where the sensitivity of the device depends on the surface development. Nanostructures alone or incorporated into bulk materials significantly improve their mechanical, thermal, electrical and magnetic properties. Moreover, thanks to their small size, nanostructures are essential in the dynamically progressing miniaturization process in various field of nanotechnology such as nanoengineering, nanomedicine or nanobiotechnology. The wide range of the potential applications of nanostructures along with their specific properties make them extremely attractive materials for studying new correlations between their morphology, structure and physicochemical properties.

An interesting example of nanostructures are one-dimensional nanostructures called nanowires. Such objects most often take form of cylindrical wires with a length of micrometers and a diameter of the order of nanometers. Due to their highly elongated shape, nanowires exhibit anisotropy of physical properties, significantly expanding the scope of their applications compared to other nanostructures. Particularly important electrical, optical, and magnetic properties of nanowires determine their use in biomedicine, spintronics, environmental protection, and broadly understood consumer electronics.

The subject of interest in this work are magnetic nanowires consisting of an alloy based on iron, cobalt and nickel. Specially built nanowires in the form of magnetic segments with various chemical compositions along nanowires can create non-volatile three-dimensional magnetic memory units in racetrack memory applications. The aim of this work is to prepare such nanostructures with well-characterized structural and magnetic properties by applying different potentials during one electrodeposition process.

The thesis consists of two main parts: a theoretical part and a description of the results. The first part contains six chapters presenting the aim of the work together with a description of the possible application of nanowires (3D racetrack memory), methods of nanowire production, and the main parameters that affect the nanowire properties. This part also includes a description of magnetism in nanowires and a short description of applied research techniques. The second part of the work contains my own research, in which I present electrochemical studies of Fe, Co, and Ni nanowires and their mixture, as well as the investigations of morphology, structure, and magnetic properties of nanowires in the form of single elements, and binary and ternary alloys. Finally, I show results concerning multi-segmented nanowires and conclusions from my work. Short, last chapter is devoted to my scientific plans for the near future, where I present preliminary results of FeCoNi nanowires deposited in alumina membranes and doped with Cu. The work also contains supplementary materials, in which I briefly characterize nanowire applications.

List of Scientific Achievements

I Publications

1) **Anna Nykiel**, Piotr Ledwig, Piotr Pawlik, Jaafar Ghanbaja, Grzegorz Cempura, Adam Kruk, Alain Walcarius, Małgorzata Kąc, *The influence of electrodeposition potential on the chemical composition, structure and magnetic properties of FeCoNi nanowires*, Journal of Alloys and Compounds, 982 (2024) 173709

2) Michal Silarski, Katarzyna Dziedzic-Kocurek, Franciszek Sobczuk, **Anna Nykiel**, Pawel Moskal, Szymon Niedzwiecki, Ewelina Stepien, Marcin Szczepanek, *A new detector concept based on the prompt gamma radiation analysis for in vivo boron monitoring in BNCT*, Oxford University Press, Radiation Protection Dosimetry, 15-16 (2023) 1932

3) Aleksandra Manecka-Padaz, Piotr Jenczyk, Ryszard B. Pecherski, **Anna Nykiel**, *Experimental investigation of Euler's elastica: in-situ SEM nanowire post-buckling*, Bulletin of the Polish Academy of Sciences Technical Sciences, 70 (2022) e143648

4) Małgorzata Kąc, **Anna Nykiel**, Oleksandr Pastukh, Marek Kopec, Arkadiusz Zarzycki, Alexey Maximenko, Magdalena Parlinska-Wojtan, Erazm M. Dutkiewicz, Agnieszka Kopia, *The role of the addition of Cu in alloyed and multilayered Fe-based nanowires*, Materials Science and Engineering B, 281 (2022) 115732

5) Małgorzata Kąc, **Anna Miś**, Beata Dubiel, Kazimierz Kowalski, Arkadiusz Zarzycki, Iwona Dobosz, *Template-assisted iron nanowire formation at different electrolyte temperatures*, Materials, 14 (2021) 4080

II Conferences and seminars

1) **MULTIS - Multiscale Phenomena in Condensed Matter**, 16-19 September 2024, Magnetization reversal mechanism observed in FeCoNi nanowires - poster

2) **Inauguration of the academic year 2023/2024** at KISD, 2 October 2023, The morphology, structure and magnetic properties of metallic nanowires - oral presentation

3) **74th Annual Meeting of the International Society of Electrochemistry**, 3-8 September 2023, Influence of template-assisted electrodeposition parameters on the properties of FeCoNi nanowires - oral presentation

4) **YOUNG MULTIS - Multiscale Phenomena in Condensed Matter**, 3-7 July 2023, Influence of the electrodeposition parameters on the properties of FeCoNiCu nanowires - oral presentation (online)

5) **NO3 department seminar**, 27 June 2023, Morphology, structure and magnetic properties of metallic nanowires synthesized by electrodeposition - oral presentation

6) **LCPME Scientific Meeting** *(Science Day)* at the Laboratory of Physical Chemistry and Microbiology of Materials and the Environment (LCPME) in Nancy, 23 May 2023, Structure and magnetic properties of electrodeposited metallic nanowires - oral presentation

7) **6th Conference Of Doctoral Students Of The Polish Academy Of Science**, 21-23 October 2022, Application of nanowires in today's world - oral presentation

8) **MULTIS 2022 - Multiscale Phenomena in Condensed Matter - Multis**, 27-30 June 2022, Structure and magnetic properties of FeCo nanowires - poster presentation (online)

9) **2nd International Multidyscyplinary Doctoral Conference at the University of Szczecin MKDUS 2.0**, 22-24 June 2022, Effect of the template-assisted electrodeposition parameters on the structure and magnetic properties of FeNi nanowires - oral presentation (online)

10) **1st International Multidyscyplinary Doctoral Conference at the University of Szczecin MKDUS 2.0**, 23-25 June 2021, Morphology of metallic nanowires prepared by template-assisted electrodeposition - oral presentation (online)

11) **Young Researchers' Innovative Ideas**, 27-28 May 2021, Magnetic nanowires - innovation in nanotechnology - poster presentation (online)

12) **Krakowski Salon Naukowy (Cracow Science Salon)**, 19 May 2021, Fascynujacy swiat nanotechnologii - nanodruty magnetyczne (The fascinating world of nanotechnology - magnetic nanowires) - oral presentation (online),
Award for the best presentation

13) **The 4th Conference of the PhD Students of the Polish Academy of Sciences - KonDokPAN**, 23 November 2020, Nanodruty - przyszłość nanotechnologii (Nanowires - future of nanotechnology) - poster presentation (online)

III Other activities

1) Member of the Doctoral Council of the Institute of Nuclear Physics Polish Academy of Sciences, November 2020 - September 2024

2) Conducting workshops for children as part of the summer school ' Water Secrets ', Zator, Poland, 10-14 June 2024

3) Participation in the jury of the *'Oczarowani Fizyka 2'* competition as part of the project *Physics as the key to understanding the world*, February 2024

4) Presenter during the Tricks of Physics shows organized as part of the *Malopolska Noc Naukowcow*, IFJ PAN, Krakow, 29 September 2023

5) Student helper in 74th Annual Meeting of the International Society of Electrochemistry, Lyon, 3-8 September 2023

6) Participation in the jury of the *'Oczarowani Fizyka'* competition as part of the project *Physics as the key to understanding the world*, February 2023

7) Assistance in organizing the 6th Conference of Doctoral Students of The Polish Academy Of Science, Krakow, 21-23 October 2022

8) Presenter during the Tricks of Physics shows organized as part of the *Malopolska Noc Naukowcow*, IFJ PAN, Krakow, 30 September 2022

9) Presenter during the popularization lectures for kids *Kids day in Institute of Nuclear Physics*, 1 June 2022

10) Co-organizing popularizing event as part of the project *Physics as the key to understanding the world (Fizyka kluczem do zrozumienia swiata)*: presenter during the popularization lectures *'Zaskakujaca fizyka'*, 10-15 January 2022

11) Co-organizing popularizing event as part of the project *Physics as the key to understanding the world (Fizyka kluczem do zrozumienia swiata)*: presenter during the popularization lectures *'Fascynujaca fizyka'*, 25-28 October 2021

12) Presenter during the Tricks of Physics shows organized as part of the *Malopolska Noc Naukowcow*, IFJ PAN, Krakow, 24 September 2021

13) Help with the organizing popularizing event 'Credo i promieniowanie kosmiczne' (CREDO and cosmic radiation), 12-13 May 2021

Contents

Abstract

The subject of these studies are nanowires, *i.e.* one-dimensional nanostructures with lengths of several micrometers and diameters of the order of nanometers. Especially interesting magnetic nanowires with strong effective magnetic anisotropy are promising materials for possible applications as 3D magnetic memory carriers due to the observed ability of the domain wall to spread smoothly at a very high speed along the nanowires *(3D racetrack memory)*. Nanowires with the desired geometry, composition, and structure were obtained by template-assisted electrodeposition process.

The presented thesis is interdisciplinary, and its main goal was to modify the magnetic properties along the nanowires in order to obtain segmented nanowires with individual segments exhibiting changes in chemical composition and associated changes in magnetic properties.

The work presents the results of the studies of the morphology, chemical composition, structure, and magnetic properties of nanowires based on iron, cobalt, and nickel, as well as their alloys. Single-element Fe, Co, and Ni nanowires prepared in polycarbonate membranes were characterized by different types of structure and magnetic parameters, such as coercivity and squareness. Binary FeCo and FeNi alloys were studied in terms of the effect of changing the cathodic potential on their chemical composition and, consequently, their properties. FeCo nanowires were characterized by poor sensitivity of chemical composition to the applied potential, in contrast to FeNi nanowires, which showed an increase in Ni content with increasing voltage and an associated increase in coercivity and squareness.

The main part of the thesis concerned FeCoNi nanowires with different diameters and lengths, whose chemical composition was also modified by changing the applied potential. It was observed that the increase in the cathodic potential caused an increase in nickel content with simultaneous depletion of the systems in iron and cobalt. Morphology observations confirmed the continuity of the nanowires and their smooth surfaces, and constant diameters measured along the axes, while X-ray diffraction measurements revealed a polycrystalline fcc FeCoNi structure with a preferred growth direction changing from [111] to [220] with increasing voltage. All nanowires showed magnetic anisotropy with an easy axis along the nanowire axis. Depending on the nanowire geometry, we observed a different dependence of the saturation magnetization, coercivity, and squareness on the applied potential, which was explained based on magnetostatic interactions. Measurements of the coercive field as a function of the angle changing from the easy axis to the hard direction showed an increase in coercivity up to an angle of 70 degrees, followed by a decrease for an angle of 90 degrees. This dependence was interpreted as a change in the magnetization reversal mechanism, which for angles close to the easy direction was typical for the movement of the vortex domain wall and changed into the mode characteristic for the transverse domain wall motion or coherent rotation for angles close to the hard direction. Moreover, magnetic measurements rather indicated a single-domain structure of FeCoNi nanowires. The last stage of the work was the study of segmented FeCoNi nanowires, which were obtained by applying a specific sequence of voltages during electrodeposition. The boundaries of segments in these nanowires were identified as the domain wall pinning sites, which made such materials promising candidates for applications in the creation of three-dimensional racetrack memory units.

Streszczenie*

Przedmiotem badań niniejszej pracy są nanodruty, czyli jednowymiarowe nanostruktury o długości kilku mikrometrów i średnicach rzędu nanometrów. Szczególnie interesujące magnetyczne nanodruty o silnej efektywnej anizotropii magnetycznej są obiecującymi materiałami do zastosowań jako nośniki pamięci magnetycznych 3D ze względu na obserwowaną w nich zdolność do płynnego rozprzestrzeniania się ściany domenowej z bardzo dużą prędkością wzdłuż nanodrutów *(3D racetrack memory)*.

Prezentowana praca jest pracą interdyscyplinarną, a jej głównym celem była modyfikacja właściwości magnetycznych wzdłuż nanodrutów w celu uzyskania segmentowanych nanodrutów, których poszczególne segmenty wykazują zmiany składu chemicznego i związane z tym różne właściwości magnetyczne.

W pracy przedstawiono wyniki badań morfologii, składu chemicznego, struktury i właściwości magnetycznych nanodrutów na bazie żelaza, kobaltu i niklu, a także ich stopów. Jednoelementowe nanodruty Fe, Co i Ni przygotowane w membranach poliwęglanowych charakteryzowały się różnymi typami struktury oraz parametrami magnetycznymi, takimi jak koercja i kwadratowość. Stopy binarne FeCo i FeNi były badane pod kątem wpływu zmiany potencjału katodowego na ich skład chemiczny, a co za tym idzie, właściwości. Nanodruty FeCo charakteryzowały się słabą wrażliwością składu chemicznego na przyłożony potencjał w przeciwieństwie do nanodrutów FeNi, które wykazywały wzrost zawartości Ni wraz ze wzrostem napięcia i związany z tym wzrost koercji i prostopadłości.

Główna część pracy dotyczyła nanodrutów FeCoNi o różnych średnicach i długościach, których skład chemiczny był także modyfikowany poprzez zmiany przyłożonego potencjału. Zaobserwowano, że wzrost potencjału katodowego powodował wzrost zawartości niklu z jednoczesnym ubożeniem układów w żelazo i kobalt. Obserwacje morfologii potwierdziły ciągłość nanodrutów i gładkość ich powierzchni oraz stałe średnice mierzone wzdłuż osi, natomiast pomiary dyfrakcji rentgenowskiej ujawniły polikrystaliczną strukturę fcc FeCoNi z preferowanym kierunkiem wzrostu zmieniającym się ze wzrostem napięcia z [111] do [220]. Wszystkie nanodruty wykazywały anizotropię magnetyczną z łatwą osią wzdłuż osi nanodrutu. W zależności od geometrii nanodrutu, obserwowano różną zależnośc namagnesowania nasycenia, koercji i kwadratowości od przyłożonego potencjału, wyjaśnioną na podstawie oddziaływań magnetostatycznych. Pomiary pola koercji w funkcji kąta zmieniającego się od osi łatwej do kierunku trudnego, pokazały wzrost koercji do kąta o wartości 70 stopni, a następnie spadek dla kąta 90 stopni. Zależność tę zinterpretowano jako zmianę trybu przemagnesowania, który dla kątów bliskich łatwemu kierunkowi był typowy dla przemieszczania się wirowej ściany domenowej, a dla kątów bliskich kierunku trudnego przechodził w tryb charakterystyczny dla ruchu poprzecznej ściany domenowej lub koherentnej rotacji. Ponadto pomiary magnetyczne wskazywały raczej na jednodomenową strukturę nanodrutów FeCoNi. Ostatnim etapem pracy były badania segmentowych nanodrutów FeCoNi, które zostały uzyskane poprzez zastosowanie określonej sekwencji napięć podczas elektrodepozycji. Granice segmentów w tych nanodrutach zidentyfikowano jako miejsca przypinania ścian domenowych, co sprawiło, że takie materiały są obiecującymi kandydatami do zastosowań w tworzeniu trójwymiarowych jednostek pamięci 3D racetrack memory.

*Rozszerzone streszczenie w j. polskim wymagane w związku z umową Cotutelle zostało zamieszczone na końcu rozprawy.

Résumé*

Le sujet de cette étude concerne les nanofils, c'est- a-dire des nanostructures unidimensionnelles d'une longueur de plusieurs micromètres et d'un diamètre nanométrique. Les nanofils magnétiques à forte anisotropie magnétique effective sont des matériaux prometteurs étudiés pour leurs applications en tant que supports de mémoire magnétique 3D en raison de la capacité observée de la paroi de domaine à se propager en douceur à une vitesse très élevée le long des nanofils (mémoire de piste de course 3D).

Des nanofils présentant la géométrie, la composition et la structure souhaitées ont été obtenus grâce au processus d'électrodépôt assisté par gabarit.

La thèse présentée est interdisciplinaire et son objectif principal était de modifier les propriétés magnétiques le long des nanofils en formant des nanostructures segmentées dont les segments individuels présentent des variations de composition chimique et donc des propriétés magnétiques différentes qui y sont associées.

Ce document présente les résultats de recherches sur la morphologie, la composition chimique, la structure et les propriétés magnétiques de nanofils à base de fer, de cobalt et de nickel, ainsi que de leurs alliages. Les nanofils mono-élémentaires Fe, Co et Ni préparés dans des membranes de polycarbonate sont caractérisés par différents types de structure et de paramètres magnétiques, tels que la coercivité et la perpendicularité. Les alliages binaires FeCo et FeNi ont été étudiés en termes d'effet du potentiel cathodique appliqué pour leur synthèse sur leur composition chimique et, par conséquent, leurs propriétés associées. Les nanofils FeCo se caractérisent par un faible effet du potentiel sur leur composition chimique, contrairement aux nanofils FeNi qui présentent une augmentation de la teneur en Ni à de plus grandes surtensions et une augmentation associée de la coercivité et de la perpendicularité.

La partie principale de la thèse concerne les nanofils FeCoNi de différents diamètres et longueurs, et dont la composition chimique varie selon le potentiel appliqué. Il a été observé que des potentiels plus cathodiques induisent une augmentation de la teneur en nickel avec un appauvrissement simultané du fer et du cobalt. Les observations morphologiques ont confirmé l'uniformité des nanofils, des surfaces lisses, ainsi que des diamètres constants sur toute leur longueur, tandis que les mesures de diffraction des rayons X ont révélé une structure FeCoNi fcc polycristalline avec une direction de croissance préférée changeant de [111] à [220] avec l'augmentation de la tension. Tous les nanofils se caractérisent par une anisotropie magnétique le long de l'axe du nanofil. En fonction de la géométrie du nanofil, nous avons observé une dépendance différente de la magnétisation de saturation, de la coercivité et de la perpendicularité au potentiel appliqué, s'expliquant par des interactions magnétostatiques. Les mesures du champ coercitif en fonction de l'angle passant de l'axe facile à la direction difficile ont montré une augmentation de la coercivité jusqu'à un angle de 70 degrés, suivie d'une diminution pour un angle de 90 degrés. Cette dépendance a été interprétée comme un changement dans le mécanisme d'inversion de la magnétisation, qui pour les angles proches de la direction facile sont typiques du mouvement de la paroi du domaine vortex et se transforment en mode caractéristique du mouvement transversal de la paroi du domaine ou de la rotation cohérente pour les angles proches de la direction dure. De plus, les mesures magnétiques ont plutôt indiqué une structure à domaine unique des nanofils de FeCoNi. La dernière étape du travail a été l'étude de nanofils de FeCoNi segmentés, qui ont été obtenus en appliquant une séquence spécifique de tensions lors de l'électrodépôt. Les limites des segments de ces nanofils ont été identifiées comme les sites d'ancrage des parois de domaine, ce qui a fait de ces matériaux des candidats prometteurs pour des applications dans le domaine des mémoires tridimensionnelles.

*Le résumé détaillé en français requis dans le cadre de l'accord de Cotutelle a été inclus à la fin de these de dectorat.

List of acronyms

AAO	anodic alumina oxide
AC	alternating current
AFORC	angular first order reversal curves
bcc	body centered cubic
BF	bright field
CV	cyclic voltammetry
CVD	chemical vapor deposition
DC	direct current
DF	dark field
DW	domain wall
EA	easy axis
EDS	energy disperssive spectroscopy
EDX	X-ray spectroscopy
EELS	electron energy loss spectroscopy
ICDD	International Center of Diffraction Data
IS	isomer shift
fcc	face centered cubic
FORC	first order reversal curves
FWHM	full width at half maximum
hcp	hexagonal close-packed
HAADF	high-angle annular dark field
HER	hydrogen evolution reaction

HR-TEM	high-resolution transmission electron microscopy
LA	laser ablation
L-TEM	Lorentz microscopy
MBE	molecular beam epitaxy
MD	multi-domain
NWs	nanowires
PC	polycarbonate
PSD	pseudo-single-domain
PVD	physical vapor deposition
QS	quadrupole splitting
RKKY	Ruderman-Kittel-Kasuya-Yosida interaction
SAD	selected area diffraction
sc	simple cubic
SD	single-domain
SEM	scanning electron microscope
SR	selectivity ratio
STEM	scanning transmission electron microscopy
SQUID	superconductive quantum interference device
TEM	transmition electron microscopy
TDW	transverse domain wall
VDW	vortex domain wall
XPS	X-ray photoelectron spectroscopy
XRD	X-ray diffraction

Chapter 1

Nanostructures - nanowires

Nanotechnology is a science dealing with the production, design and modification of nanoscale structures, which has opened up unprecedented opportunities to revolutionize various industries, from electronics and energy to medicine and materials science. Nanostructures exhibit properties different from their bulk counterparts, including electrical, optical and magnetic properties or increased mechanical strength. These materials include nanoparticles, nanotubes, nanowires, and other objects with various morphology, size, and geometric parameter ratios maintaining one dimension on the nanometer scale.

The exceptionally interesting are nanowires - cylindrical, one-dimensional structures with a length of micrometers (L) and a diameter (ϕ) of the order of nanometers. Their geometry results in a high aspect ratio (length to width ratio L/ϕ), which provides many interesting properties different from their analogs in two- and three-dimensions. One of the most important aspects is the increased surface-to-volume ratio compared to bulk structures, which significantly improves the surface sensitivity of nanowire-coated devices.

Nanowires can be made of various materials, such as metals, composite materials or oxides. Their structure and properties depend not only on the type of material, but also on the method of their synthesis. By controlling the production process and using different templates, it is possible to modify the concentration and geometry of the nanowires and, consequently, obtain nanowires with the desired properties. A huge diversity of nanowire properties and the possibility of manipulating them made such structures attractive for both industrial applications and fundamental studies.

Especially interesting magnetic nanowires, which are the subject of the presented work, due to their magnetic anisotropy, have found many applications in spintronics, microwave electronics, permanent magnets, medical treatments, drug delivery, consumer electronics, high-density magnetic recording media, and many others. More detailed descriptions of the potential applications of nanowires are provided in Appendix 1.

In my study, I will focus on the use of nanowires in high-density magnetic recording media, which became the motivation for my studies. Magnetic nanowires are promising candidates for next-generation data storage devices in a 3D approach. It is expected that such magnetic memory units can achieve a density of tens of terabits per square inch [1, 2, 3, 4]. This application will be described in detail in the next section.

1.1. 3D magnetic memory media - motivation

Current magnetic data storage devices are based on a two-dimensional design. Due to the superparamagnetic behavior observed when the size of the magnetic bits is reduced, the density of such storage media cannot be improved. In this case, an alternative approach is to construct 3D devices in which vertically arranged magnetic domains are used to store information in parallel arrays of tall columns – a nanowire matrix. For the first time, the concept of such 3D memories was proposed by Parkin in Science in 2008 [5]. To build them, multi-domain structures are needed, in which each magnetic domain should correspond to the magnetic bit. The data could be written in such a device using a small magnetic field generated by ferromagnetic nanowires and reading could be done by a magnetic tunnel junction element, which would detect the changes in the magnetization. The application of 3D magnetic memory media devices could increase the density of magnetic bits per area unit while lowering energy consumption, increasing the reading speeds, and improving reliability due to eliminating mechanical motion as in the case of rotating hard disks [6, 7, 8, 9].

In such magnetic structure, called racetrack memory, the individual bits are associated with domain walls (DW) formed at the boundaries between magnetic domains magnetized in opposite directions (up or down) along the nanowires. The domain wall, which alternates between north-to-north or south-to-south poles is used to store information, while the space between them is the bit length. The nanowire matrix acting as such racetrack memory is embedded in a non-magnetic template, which causes most of the domains to be located deep in the membrane. To obtain information encoded in bits away from the surface, the domain wall motion must be considered. This can be achieved by applying nanosecond current pulses [8]. The current passing through the magnetic wire becomes spin-polarized due to the spin-dependent scattering. The spin angular momentum is transferred by the current to the wall causing the DW motion. A properly selected pulse length, adjusted to the distance between subsequent domain walls, allows the entire sequence of domain walls to be shifted. They can move towards the surface or backward depending on the direction of electron flow, which is opposite to the current direction. The velocity of the domain wall, which can reach even 1000 m/s [8, 10] is reduced to a value of about 100 m/s (enough for racetrack memory applications) because of the limitations associated with the applied current densities (with a threshold connected with the temperature increase caused by Joule heating and perturbation in spin momentum transfer), local pinning at defects, the domain wall structure (transverse or vortex) and other problems related to *e.g.* changes in the DW propagation mode at too high velocity [5].

Another important challenge that needs to be solved is an undesired domain wall drift out of its position caused by thermal fluctuation, stray currents or magnetic fields, and imprecise estimation of the magnitude and duration of the current pulses. To control the domain wall positions and ensure their stability, the pinning sites must be fabricated at the intended places along the nanowires. The chosen pinning sites should be strong enough to protect DW against external perturbations, while maintaining the ability of the DW to move from one position to another under the influence of the applied current pulses. Such anchoring can be reached by forming blockages along nanowires (notches, anti-notches, or constrictions), diameter modulations, or modifications of the material properties.

1.2. The goal of the thesis

The last of the mentioned possibilities of the domain wall pinning *i.e.* modification of the magnetic properties of materials along nanowires, is the aim of this work. This will be achieved by the electrodeposition of alloy and segmented nanowires composed of Fe, Co, and Ni. By choosing an appropriate electrolyte composition and applying various cathodic potentials, I obtained, in one electrodeposition process, nanowires built of magnetic segments with different element content, which caused changes in their magnetic properties. Such a chemical modification combined with different magnetic parameters, should lead to the creation of pinning sides at the subsequent segment boundaries, making these structures good candidates for 3D racetrack memory applications.

1.3. Methods of nanowire production

In the case of nanomaterials, their production techniques can be divided into two groups: top-down and bottom-up methods (Fig. 1.1). In the first approach, the material size is reduced to the nanoscale size. In this group, one can highlight techniques like lithography, mechanical abrasion, high temperature oxidation, sputtering or chemical etching [11, 12]. On the other hand, in the bottom-up methods, the nanostructures are produce from atoms and molecules. This group include molecular beam epitaxy (MBE), chemical vapor deposition (CVD), laser ablation (photoablation), lithography, sol-gel and electrodeposition [12].

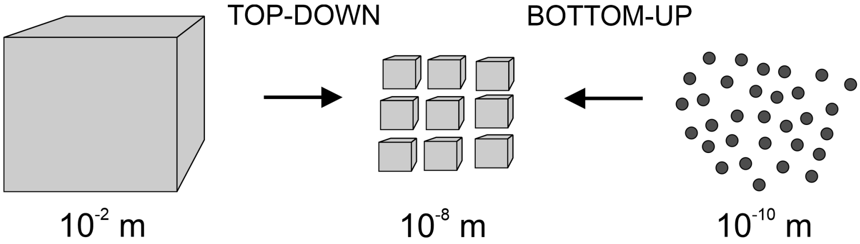

Figure 1.1: Schematic representation of two nanomaterial fabrication strategies: top-down and bottom-up.

Among the preparation techniques mentioned, there are many different methods for producing metallic nanowires that allow for more or less precise control of dimensions, shape, crystal structure and chemical composition. One of them is chemical vapor deposition (CVD), which enables the production of nanowires with a specific chemical composition, but the high temperatures required limit the range of materials that can be obtained by this technique. Another method is physical vapor deposition (PVD), which in turn allows to obtain nanowires with a favorable crystallographic orientation along the nanowire axis. Other methods such as laser ablation (LA), MBE or lithography are also used, but in general, all these techniques are very expensive and require advanced equipment, usually operating in high or ultra-high vacuum conditions [11, 12, 13, 14].

A simple, high yield and low-cost method of producing nanowires is **electrochemical deposition**. This technique was used to prepare the nanowires studied in my work and will be described in more detail in the next chapter.

Chapter 2

Electrodeposition process

Electrodeposition of metals and alloys is a well-known method of the preparation of solid deposits on the surface as well as nanomaterials. Metal electrodeposition is a process in which, the metal ions from an electrolyte (like an aqueous solution of a simple or a complex salt type, known as an electrolyte bath) are reduced to a metallic form on the conducting surface – the cathode. During the electrodeposition process, the oxidation and the reduction occur at the anode (the positive electrode) and cathode (the negative electrode), respectively. The overall reactions occurring during the process can be represented as:

$$Cathode : M^{n+} + ne^- \rightarrow M \tag{2.1}$$

$$Anode : M \rightarrow M^{n+} + ne^- \tag{2.2}$$

And additional:

$$2H_2O + 2e^- \rightarrow H_2 \uparrow + 2OH^- \quad (cathode) \tag{2.3}$$

$$2H_2O \rightarrow 4H^+ + O_2 \uparrow + 4e^- \quad (anode) \tag{2.4}$$

The electrodeposition process is usually performed using a three-electrode system with a working electrode (cathode) – 1, reference electrode – 4 and counter electrode (anode) – 5 (Fig. 2.1)

In the case of studied materials, for non-dissoluble anodes, the following reactions take place on electrodes:

$$Cathode : \quad M^{2+} + 2e^- \leftrightarrow M \tag{2.5}$$

$$2H^+ + 2e^- \leftrightarrow H_2 \tag{2.6}$$

$$Anode : \qquad 2H_2O \leftrightarrow 4H^+ + O_2 + 4e^- \quad for\ pH \leq 7 \tag{2.7}$$

$$4OH^- \leftrightarrow 2H_2O + O_2 + 4e^- \quad for\ pH \geq 7 \tag{2.8}$$

where M^{2+} are metallic ions of Fe, Co, Ni or Cu dissolved in the electrolyte, while M are metals of the corresponding ions reduced at the cathode.

The potential applied between these two electrodes causes ion transport, which can occur by migration, diffusion, and convection.

The principle mechanism of ion transport is migration, defined as the ordered movement of positive ions – cations towards the negative electrode (cathode) and negative ions

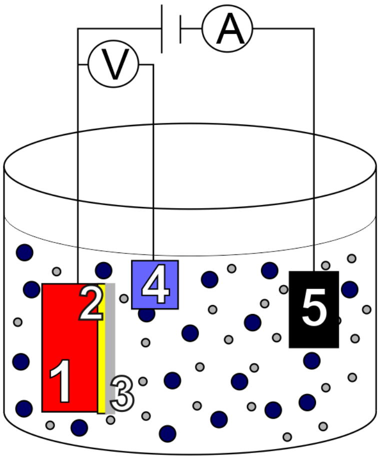

Figure 2.1: Scheme of a three-electrode setup: with working electrode (cathode) − 1, reference electrode − 4 and counter electrode (anode) − 5. Additionally marked contact layer − 2 and membrane − 3 are used in the template-assisted electrodeposition process described in the later chapter.

− anions towards the positive electrode (anode). This can be readily determined by measuring the electrical conductivity or resistivity. All ions in electrolyte take part in the migration transport and the amount of charge transferred by a particular type of ions is proportional to their concentrations. However, the number of ions in an electrolyte does not have to be identical to the concentration of the electrolyte due to the interactions of the ions with the solvent and with each other [15].

The diffusion current results from the difference in ion concentration near the electrode and in the bulk electrolyte. To eliminate the migration current from the analysis of the determined ions, a basic electrolyte should be used with a concentration at least 1000 times higher than the concentration of determined ions. Then, the basic electrolyte takes over the entire migration current. A well-chosen basic electrolyte enables the separation of peak potentials or half-wave potentials (see chapter devoted to measurement techniques). The convection current is induced by, for example, mixing.

The electrode potential at which the current density is zero is of particular importance. If this potential corresponds to the thermodynamic equilibrium of the electrode process, it is defined as the equilibrium potential. For metal electrodeposition, it is necessary to shift the electrode potential in the cathodic (negative) direction from the equilibrium value. A negative potential shift accelerates reduction processes, while a positive shift accelerates anodic reactions (oxidation). This potential is called overpotential.

To calculate the reversal potential of a metal immersed in an electrolyte solution containing metal ions, the Nernst equation is used. It relates the potential of the electrochemical cell to the standard potential of the half-cell (E^o) and the molar concentrations of oxidized (Ox) and reduced (Red) substances taking part in electrode reactions at equilibrium. It takes the general form:

$$E = E^0 + \frac{RT}{nF} ln(\frac{|Ox|}{|Red|}) \tag{2.9}$$

where:
E − equilibrium half-cell potential [V]

E^0 – standard half-cell potential [V]
R – gas constant [8.314 J/(mol · K)]
T – temperature [K]
n – number of electrons taking part in the reaction taking place at the electrode
F – Faraday's constant [96500 C/mol]
|Ox| – molar concentration of the oxidized form
|Red| – molar concentration of the reduced form.

The standard potential (E^0), *i.e.* the numerical value for the tendency of elements to form ions in an aqueous solution. It is determined relative to the standard hydrogen electrode (SHE), whose normal potential value is assumed to be equal to zero. This electrode is used to define potentials, but in most applications, a calomel electrode (Hg_2Cl_2) or silver/silver chloride electrode (Ag/AgCl) are found as reference electrodes. I used an Ag/AgCl (3 M KCl) reference electrode, which is based on the reduction of AgCl to Ag. It is an unsaturated electrode that is less sensitive to temperature changes than an electrode filled with saturated KCl (4.69 M KCl) because at higher temperatures the solubility of KCl increases and the potential of the electrode decreases. The relationship between the standard hydrogen electrode and silver chloride electrodes filled with saturated (4.69 M) and 3 M KCl is shown in Fig. 2.2. All potential values given in this work refer to the Ag/AgCl (3 M KCl) electrode.

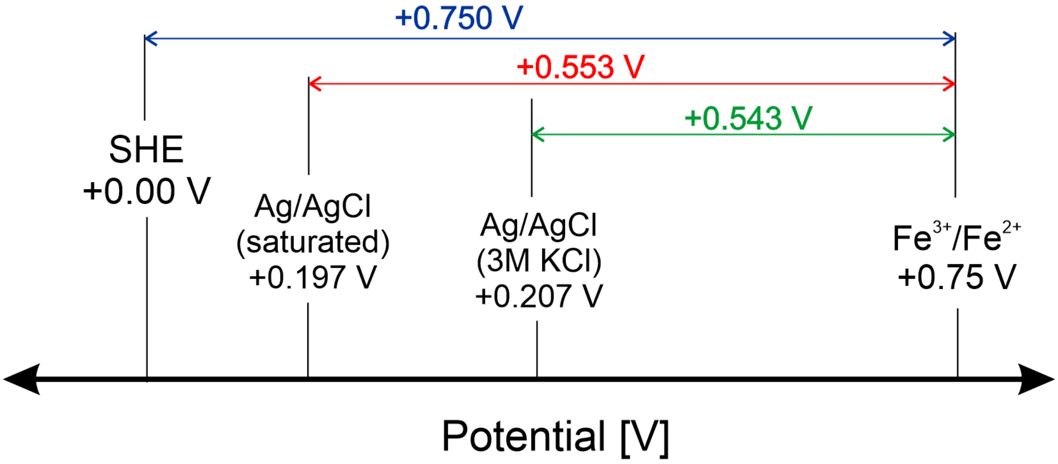

Figure 2.2: Relationship between the potential of an Fe^{3+}/Fe^{2+} half-cell to the different reference electrodes: standard hydrogen electrode (SHE), Ag/AgCl (KCl saturated), Ag/AgCl (3 M KCl).

A list of chemical elements with metallic properties ordered according to their values of normal potentials, known as the electropotential series or activity series, shows the tendency of metals to be oxidized (the metals at the top of the table with more negative potential are less noble, more active) or to be reduced (the metals at the bottom of the table with more positive potentials are more noble, less active).

The standard potentials of selected metals shown relative to standard hydrogen electrode (SHE) and silver/silver chloride electrode (Ag/AgCl) filled with saturated and 3 M KCl are presented in Table 2.1.

Quantitatively, the electrolysis process is described by Faraday's laws. Faraday's first

Table 2.1: Standard reduction potential (E_0) relative to a standard hydrogen electrode (SHE) and silver/silver chloride electrode Ag/AgCl filled with saturated KCl and 3 M KCl.

Reaction	Potential E_0 [V]		
	vs. SHE	vs. Ag/AgCl (saturat. KCl)	vs. Ag/AgCl (3 M KCl)
$Fe^{2+} + 2e^- \leftrightarrow Fe$	-0.44	-0.64	-0.65
$Co^{2+} + 2e^- \leftrightarrow Co$	-0.28	-0.47	-0.49
$Ni^{2+} + 2e^- \leftrightarrow Ni$	-0.25	-0.45	-0.46
$2H^+ + 2e^- \leftrightarrow H_2$	0.00	-0.20	-0.21
$Cu^{2+} + 2e^- \leftrightarrow Cu$	+ 0.34	0.14	0.13

law states that the mass of a substance released on the electrode during electrolysis is proportional to the amount of electric charge that flowed through the electrolyte:

$$m = k \cdot q = k \cdot I \cdot t \tag{2.10}$$

where:
m – mass of the substance released on the electrode during electrolysis
k = $\frac{M}{nF}$ – electrochemical equivalent
F – Faraday constant is an electrical charge of one mole of elementary carries ($F = e \cdot N_A$)
q – electrical charge
I – current flowing during electrolysis
t – duration of electrolysis
M – molar mass of the released ion
n – number of electrons transferred in the electrode reaction (valance).

Faraday's second law states that the ratio of the masses of substances released at the electrode to the product of electrochemical equivalent (k) and the number of electrons transferred in the electrode reaction (n) per 1 mole of a substance with molar mass (M) is a constant quantity called Faraday constant:

$$\frac{M}{k \cdot n} = F \tag{2.11}$$

The relationship connecting both Faraday′s laws is called the electrolysis equation:

$$m = \frac{M \cdot I \cdot t}{n \cdot F} = \frac{M \cdot q}{n \cdot F} \tag{2.12}$$

and expresses the charge needed to deposit or release the mass of substance at the electrodes:

$$q = \frac{F \cdot m \cdot n}{M} \tag{2.13}$$

The electrodeposition process includes faradaic and non-faradaic reactions, which are associated with faradaic and non-faradaic currents. The currents described by Faraday′s laws involving charge transfer are called faradaic currents and connect the amount of the substances transferred with the amount of electrical charge delivered to the electrode. The faradaic current is proportional to the electrode reaction rate, which in extreme cases depends on the mass transport and charge transfer rate. If the process is controlled by mass transport limitation (charge transfer is much faster than mass transport), the value of polarizing voltage is described by the Ox/Red concentration ratio using the Nernst equation and these processes are reversible. The current in this case depends only on the ion diffusion rate, which is proportional to the ion concentration gradient between the electrode surface and the bulk electrolyte. The maximum concentration gradient is reached when the surface concentration of ions on the electrode surface is zero, then the mass transport rate and current value are proportional to the bulk concentration. The limit value of faradaic current corresponding to the current value at the peak or plateau of the wave on the current versus voltage measurements (CV – cyclic voltammetry, described in the chapter on measurement techniques) is proportional to the concentration of the analyzed ingredient and carries quantitative information about the composition of the analyzed sample while its identification qualitative is based on the value of peak potential or half-wave potential.

Usually, more than one faradaic reaction occurs at the cathode electrode during the electrodeposition process, but only one of them is related to the deposition of materials. Thus the fraction of the current consumed for the desired deposit to the total current passing through the cell is the current efficiency (χ). It is defined as the ratio of the actual mass (m_a) of a substance separated from the electrolyte as a result of current flow to the theoretical mass (m_{th}) of this substance (m_a/m_{th}). The theoretical mass of sediment calculated from Faraday's law multiplied by current efficiency gives the actual mass of the deposit:

$$m_a = \chi \cdot (\frac{M}{n} \cdot \frac{q}{F}) \tag{2.14}$$

The current efficiency can range from 0 to 100%. Most electrodeposition processes are characterized by a current efficiency of less than 100% due to simultaneously occurring side reactions, such as hydrogen evolution described in the later chapter [15].

As mentioned, the current flowing through the cell is limited by the current corresponding to the slowest reaction step. Generally, one can distinguish: 1) activation controlled or charge transfer process, 2) mixed controlled process, or 3) mass transport or diffusion controlled process [15]. If there are many electrochemically active substances near the phase boundary, the reaction rate depends on the electrode potential and is called activation controlled. In this type of electrodeposition process, the current changes exponentially as a function of the overpotential and even a small swap of overpotential results in a huge change in the current density [15]. If the migration of ions to and from electrodes is slow, the ion depletion at the cathode vicinity occurs (there is no homogeneity of the electrolyte near the electrode) and a further increase in overpotential is not accompanied by any changes in current density. In this case, the reaction rate is limited by mass transport and the process is diffusion controlled. This kind of process is observed in most metal electrodepositions [15].

The diffusion process is described by two Fick's laws.

Fick's first law gives the relationship between the flow of a diffusing substance (*i.e.* the amount of substance flowing per unit of time through a unit surface perpendicular to the flow) and its concentration gradient:

$$J = -D\frac{\partial c}{\partial x} \tag{2.15}$$

where:
J – the flux of the diffusing component in the x direction
c – concentration of the component in the flow plane
$\partial c/\partial x$ – concentration gradient of the diffusing component perpendicular to the plane
D – diffusion coefficient $[m^2/s]$, is proportional to the speed of diffusing molecules, it also depends on temperature.

Fick's second law gives the relationship between the local rate of change in the concentration of a diffusing substance and its concentration gradient:

$$\frac{\partial c}{\partial t} = D\frac{\partial^2 c}{\partial x^2} \tag{2.16}$$

The diffusion coefficient is related to the temperature dependence, via **Arrhenius law**:

$$D = D_0 \cdot e^{-\frac{E_A}{RT}} \tag{2.17}$$

where:
D_0 – diffusion coefficient at an infinite temperature
E_A – activation energy [J/mol]
T – temperature [K]
R – gas constant (8.31 J/(mol · K))
The Arrhenius equation enables the determination of the activation energy and preexponential factor.

After applying potential, the metal electrodes immersed in the solutions become polarized. As a consequence, the density of electrons in the metal surface changes, which results in the formation of a double electrical layer in the form of a compensating space charge in the electrolyte adjacent to the electrode, called a double layer. A diagram of an electrical double layer in an aqueous solution at the interface with a negatively charged electrode surface is shown in Figure 2.3. The first layer, positive or negative surface charge, consists of ions that are adsorbed on the electrode. The second layer consists of free ions that move in the fluid and are attracted to the surface charge by the Coulomb force. This second layer with the opposite charge to the first layer is loosely bonded to the electrode material and is called the diffuse layer. Double layers are most visible in systems with a high surface-to-volume ratio, such as porous surfaces [17]. The typical thickness of double layer is in the order of nanometers and decreases with increasing ion valence and their concentration and depends on the electrolyte temperature. The process of double layer formation belongs to non-faradic reactions, and the current associated with the charging and discharging of the double layer is also called non-faradaic current or capacity current. The value of this current does not depend on the ion concentration

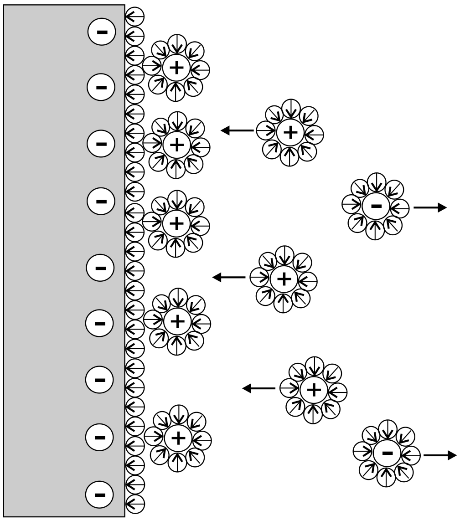

Figure 2.3: Scheme of an electrical double layer in an aqueous solution at the interface with a negatively charged cathode (Graheme model) [15].

and is the additive background of the faradaic current. The ratio of the faradaic current to the capacity current is treated as the signal-to-noise ratio and determines the detection limit of the measurement techniques used.

The electrodeposition process is influenced by factors such as the value of the cathodic potential (or current density), temperature, pH and composition of the electrolyte as well as by electrodeposition type, which will be described in the next section [18].

2.1. Electrodeposition types

The electrodeposition can be performed in either potentiostatic or galvanostatic mode. In the first one, a constant potential is applied between the cathode and the anode, and the electrodeposition process is monitored by measuring current changes. In turn, in the galvanostatic mode, a constant current density is maintained between the anode and the cathode, and the potential response is recorded during the process. The potentiostatic mode allows the study of the mechanism of deposit growth. Furthermore, providing the necessary critical energy needed for nucleation (supplied by applied potential) ensures a uniform and desired morphology of the deposits, which is difficult to achieve in galvanostatic mode due to the lack of direct control of the potential occurring at the cathode. Additionally, by applying various potentials, it is possible to modify the chemical composition of alloyed deposits [19, 20, 21]. Both these modes offer the simplicity of controlling reduced charge, which enables the deposition of segmented nanowires with high accuracy [22].

These two electrodeposition modes can be used in the form of a constant value of applied potential or current (DC), as described above, or in the form of alternating signals (AC) or pulses. In Fig. 2.4 the different types of current transient applied are shown. As mentioned, direct current (DC) electrodeposition includes the previously described galvanostatic and potentiostatic modes (Fig. 2.4 a).

Alternating current (Fig. 2.4 b) or potential (AC) introduces dynamic changes to the deposition process and can be used to obtain certain benefits, such as improving the uniformity of layer deposition. AC electrodeposition with a modified frequency and waveform (sine, square, triangular) can also influence the surface properties of the deposited material, its crystal structure and consequently, physical properties. This also allows the templates to be homogeneously filled with various metals in nanowire production but makes it impossible to precisely control the morphology of the obtained structures [23]. This mode is necessary during the deposition of nanowires in alumina membranes with a barrier oxide layer, but a high alternating potential in the range of 10 V and above is needed [15]. Deposition at high voltage or current is associated with high hydrogen evolution, which impairs the efficiency of the electrodeposition process. In general, nanowires grown at low current density are very short, while those grown under high current density are not compact and contain many defects [23]. On the other hand, application of high current frequency significantly reduces the hydrogen evolution, but ions do not have sufficient time to relax and the deposition will not follow diffusion-controlled mechanism that is more common in the electrodeposition of metal ions [15].

Pulse electrodeposition (Fig. 2.4 c) is characterized by the alternating appearance of a conduction pulse (time on) and an off pulse (time off). Electrical pulses can be unipolar (all pulses are in one direction) or bipolar (positive and negative directions). During the conduction pulse (time on), when the suitable voltage or current is applied, the material is deposited but, at the same time, ions are depleted in the immediate vicinity of the reduction site. The subsequent short time off pulse allows the ion concentration to be recovered and the double layer formed at the deposit/electrolyte interface to be discharged. Unfortunately, during the pulse time off (when very low or zero voltage or current is applied), the dissolution of reduced atoms can be observed [24, 25, 26], especially visible in the case of deposition of layered nanowires composed of metals with significantly different standard potentials. Using the pulse deposition technique, segmented nanowires consisting of layers with different chemical compositions can be produced by applying pulses with various potential values.

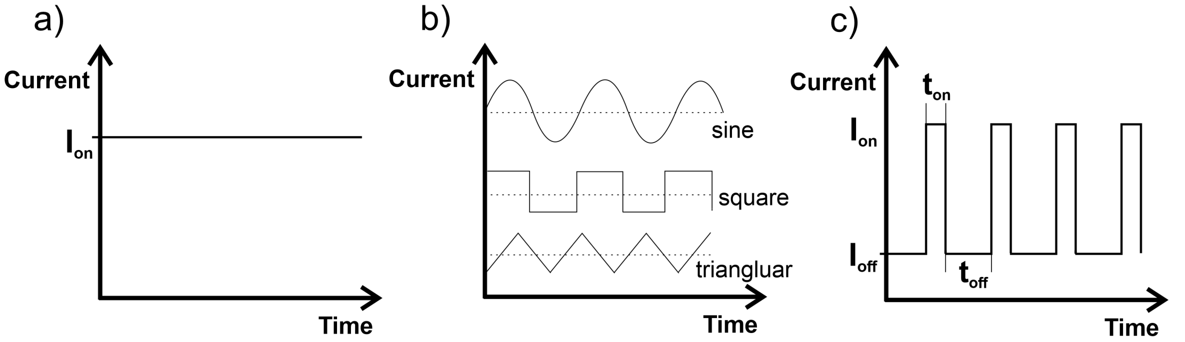

Figure 2.4: Schematic plot of current vs. time for (a) direct current (DC), (b) alternating current (AC) and (c) pulse current electrodeposition [15].

Described methods, along with their advantages and disadvantages, are suitable for the deposition of various nanowires. In practice, the choice between DC and AC electrodeposition depends on the specific goals of the process and the required characteristics of the produced material. Appropriate selection of electrodeposition mode allows for controlling the morphology and physical properties of the deposit to obtain materials with parameters suitable for desired applications [19, 27, 28].

Considering the above, I used a DC technique with a potentiostatic mode, which allowed me to control the particular electrodeposition stages and precisely determine the reduced charge to obtain nanowires with desired length, morphology, chemical composition, structure and, consequently, required physical properties. Thanks to the acquired knowledge, I was able to produce homogenous alloyed nanowires and segmented nanowires with controlled chemical composition and well-defined lengths of individual segments.

2.2. Types of templates

Porous membranes enable the production of nanowires with a monodisperse diameter and easily controlled length during unidirectional growth. There are several types of templates, but the most popular are polycarbonate (PC) membranes and anodic alumina oxide (AAO) membranes.

The PC membranes are produced in two steps. In the first step, a thin polycarbonate layer is irradiated with heavy ions, which results in the creation of the ion tracks (damage zone) with a density depending on the applied ion fluence. In the next step, the ion-irradiated PC layer is etched in NaOH. The etching time affects the pore diameter and may reduce the membrane thickness [29]. The pore distribution determined by ion irradiation is irregular as seen in SEM images (Fig. 2.5 a, b). These membranes have relatively low pore density, which allows the creation of nanowires with low or negligible interactions between them [30, 31, 32, 33]. Moreover, a significant advantage of PC membranes is the ability to produce pores with uniform diameters and easy-to-control density. Additionally, they are flexible, relatively resistant to damage, and stable in use.

The AAO templates are produced by anodization, during which pure aluminum foil (necessary to obtain an ordered porous structure) is oxidized using oxalic, phosphoric or sulfuric acid. The electrolyte applied influences the pore diameter, while the oxidation conditions (temperature, pH, electrolyte concentration) determine the rate of oxide formation [34]. Such porous membrane has an irregular pore arrangement. To obtain a well-ordered structure with a hexagonal pore distribution, the alumina layer is removed and the resulting u-shape surface covering the Al foil should be anodized for a second time. As a consequence, AAO membranes are created with high-density hexagonally arranged porous structures, with a pore distance close to the pore diameter (Fig. 2.5 c).

During the alumina membrane production, a thick insulating barrier oxide layer is formed (200 nm), as seen in Fig. 2.6 b [35]. It is too thick to enable electron transfer by tunneling, thus the barrier must be thinned by chemical etching, but in any case, a high potential must be applied in electrodeposition process. This is associated with a large hydrogen evolution, which results in instability of the electrodeposition process and makes uniform pore filling impossible. An alternative approach is to detach alumina from the Al substrate (using NaOH) to obtain a membrane with open pores from both sides, but this is only applicable for free-standing thick alumina membranes (>20 µm). Membranes with smaller thicknesses are not stable enough to be handled due to their brittleness.

The parameters, which define the membranes are pore diameter (ϕ), membrane thickness, which is a maximum nanowire length (L), inter-pore distance (d), pore density (number of pores per square centimeter) (ρ), and porosity (open area) (P). Schemes illustrating these parameters are shown in Fig. 2.6. As can be seen, there is a very clear difference in the pore distribution between PC (Fig. 2.5 a, b, and Fig. 2.6 a) and AAO (Fig.

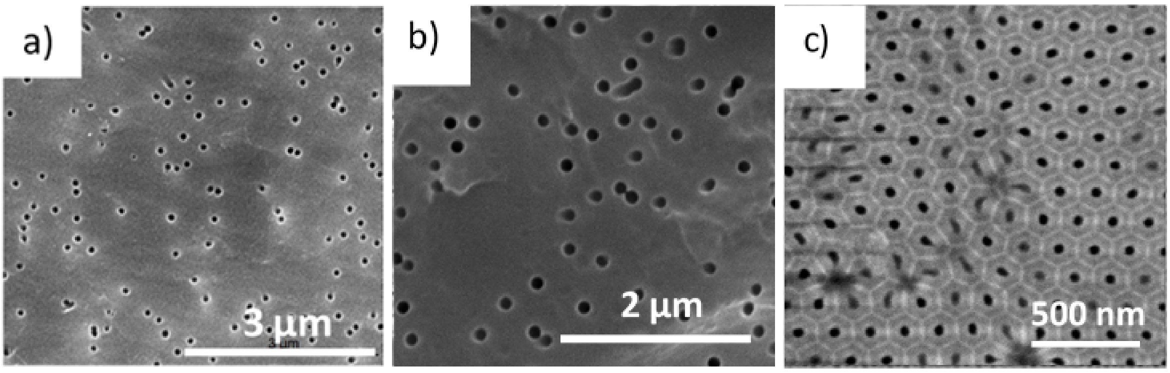

Figure 2.5: SEM pictures of two types of templates: polycarbonate (PC) membranes with a pore diameter of (a) 40 nm, (b) 100 nm; and (c) anodic alumina oxide (AAO) membranes with pores diameter of 40 nm.

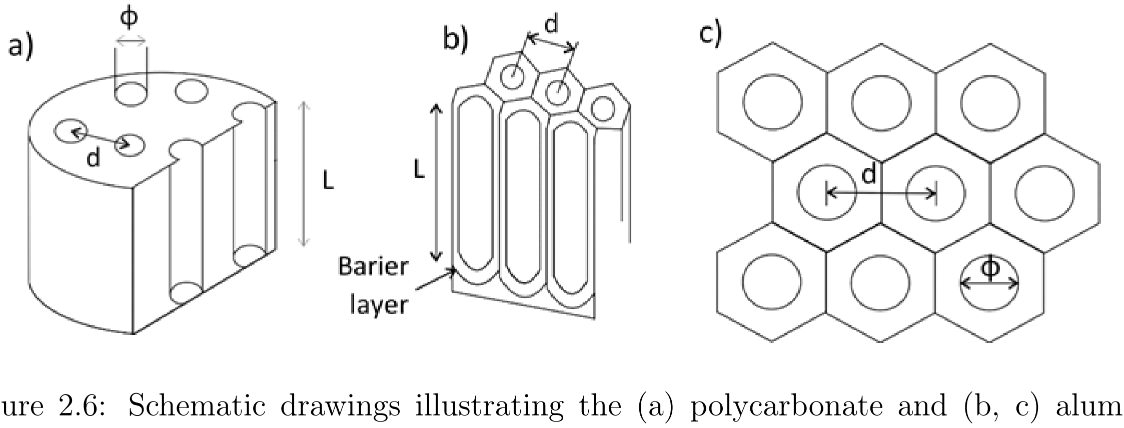

Figure 2.6: Schematic drawings illustrating the (a) polycarbonate and (b, c) alumina membranes with marked pore diameters (ϕ), membrane thickness (L) and inter-pore distance (d).

Table 2.2: Parameters of polycarbonate and anodic alumina oxide membranes.

Pore diameter [nm]	Pore density [pores/cm^2]	Open area [%] (Porosity)	Nominal thickness [µm]
Polycarbonate membranes (PC)			
120	4 x 10^8	4.5	6
100	4 x 10^8	3.1	6
40	6 x 10^8	0.7	6
Anodic alumina oxide membranes (AAO)			
40	10^9	15	50

2.5 c and Fig. 2.6 b) membranes. This results in various inter-pore distances, different pore densities, and porosities. The porosity (P) and pore density (ρ) in the case of ideal hexagonal pore arrangement (AAO membranes) can be expressed by equations (2.18) and (2.19), respectively [34, 36]:

$$P = \frac{\pi}{2\sqrt{3}}(\frac{\phi}{d})^2 \tag{2.18}$$

$$\rho = \frac{10^{14}}{\sqrt{3} \cdot d^2} \tag{2.19}$$

In the case of PC membrane, the pore density, and therefore the porosity and the inter-pore distance are determined by the ion fluence.

The parameters of the membranes used in this work are listed in Table 2.22.

As mentioned above, the main difference between the PC and AAO membranes is the pore distribution and the average distance between pores, which, as in the case of alumina membranes, can result in a strong interaction between the nanowires [37, 38, 39, 40, 41]. Thus, the main advantage of polycarbonate membranes is the relatively large distance between the pores, which reduces interaction between nanowires, while the main advantage of alumina membranes is a very regular pore distribution, which is crucial for use as magnetic memory units. Finally, considering the above, greater handling stability, and the not-mentioned low price of polycarbonate membranes, I chose the PC membrane as the main template for nanowire production, although some nanowires in alumina membranes (open from both sides) were also prepared.

The pores in PC membranes and in AAO membranes (after removing the substrate and barrier layer) are open on both sides. To perform the electrodeposition, the membranes must be covered with a thin conductive layer of gold or copper, which closes the pores on one side and ensures electrical contact during the electrodeposition process. The gold layers were deposited by sputtering, while the copper layers were evaporated using an e-gun. The thicknesses of the layers depend on the pore diameters and are listed in Table 2.3. They must be thick enough to prevent material leakage. Additionally, such a layer forms a substrate for nanowires after they are dissolved (PC membranes).

PC and AAO membranes covered with conductive layers serve as working electrodes (cathodes) in a three-electrode setup. The working areas determined by the diameter of the Teflon seal (0.8 − 1 cm) and the pore density were calculated from the formula:

$$P_{working\ area} = Open\ area\ [\%] \cdot P_{seal} \tag{2.20}$$

Table 2.3: Thicknesses of gold and copper conductive layers.

Pore diameter [nm]	Gold layer [nm]	Copper layer [nm]
Polycarbonate membranes (PC)		
120	320	-
100	250	400
40	180	-
Anodic alumina oxide membranes (AAO)		
40	300	-

and are listed in Table 2.4 for PC and AAO membranes for various diameters used in the work.

Table 2.4: Working areas determined for polycarbonate and alumina membranes used in the electrodeposition process.

Pore diameter [nm]	Working area [cm^2]
PC membranes	
120	$2.2 \cdot 10^{-2}$
100	$1.6 \cdot 10^{-2}$
40	$3.8 \cdot 10^{-3}$
AAO membranes	
40	$7.5 \cdot 10^{-2}$

2.3. Electrodeposition inside porous membranes

The template-assisted method combined with electrochemical technique is the most common way to obtain a system of nanowires with well-defined geometry, chemical composition and structure.

In a diffusion controlled process, the rate of electrodeposition is determined by the movement of ions from regions of high to low concentration. Ions approaching from the bulk region towards the active membrane surface (pores) create a spherical diffusion zone (Fig. 2.7) that extends at the mouth of each pore, leading to the overlapping of neighboring diffusion volumes. The ions move rapidly towards the electrode surface and reduce at the bottom of the pores forming a depleted region on and near the electrode surface. A concentration gradient is created along the nanochannels and in the electrolyte between the mouth of the nanopore and the bulk region. Continuous linear diffusion prevails along nanochannels, normal to the spherical diffusion zones formed on the electrode surface [15, 42]. Therefore, the diffusion layer in the case of template-assisted electrodeposition includes the area of the channels (with linear diffusion) and near the membrane surface area (with a spherical diffusion), called the outer diffusion layer. The spherical diffusion areas of adjacent pores can overlap depending on the distance between the pores, which creates a continuous outer diffusion layer increasing its effective thickness [43].

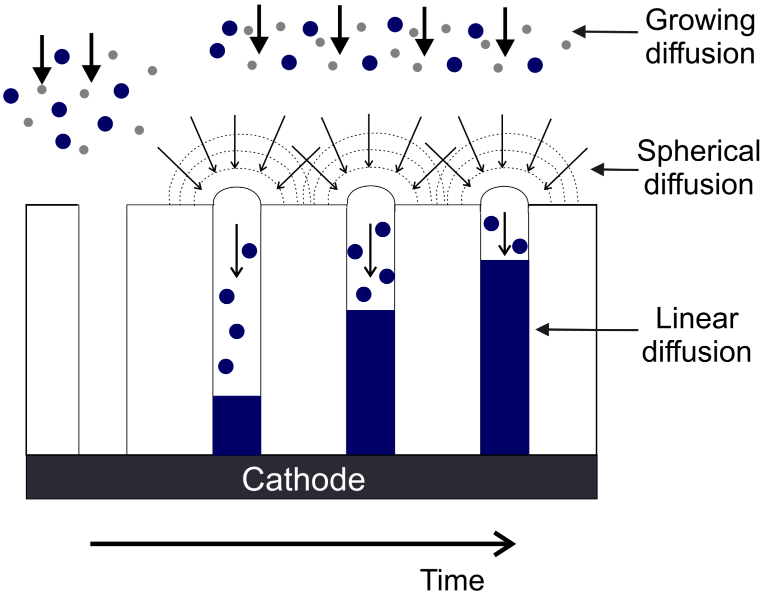

Figure 2.7: Scheme of deposition of nanowires in porous membrane with a distinct linear diffusion zone inside the pores and a spherical diffusion zone outside the membrane [42].

The electrodeposition process performed in the potentiostatic mode is monitored by measurements of the cathodic current as a function of time. Figure 2.8 a illustrates an example of a current versus time graph recorded during the deposition of Ni nanowires in a polycarbonate membrane with a pore diameter of 100 nm from a sulfate electrolyte (details of the electrodeposition process and electrolyte parameters can be found in the figure captions). Five different regions can be distinguished in the current transient. The initial current increase associated with the double layer charging is followed by a sudden drop in the current (stage 1) related to the mass transport limitation. At this stage of the electrodeposition process, the nucleation occurs at the pore bottoms. Then there is a little increase in current, which indicates the growth of nanowires inside the pores (stage 2). The current rises gently as the diffusion length decreases until the nanowires reach the membrane surface. SEM image recorded on the membrane surface shows only empty pores (Fig. 2.8 stage 1-2). Then there is a sharp increase in current (stage 3), which is a signal that the pores are completely filled. This is confirmed by the appearance of nanowires in the membrane pores, visible in the SEM image (Fig. 2.8 stage 3). Usually, the process is stopped at this stage, to avoid overdeposition caps on the membrane surface. If the process continues, the caps will grow (stage 4) and then connect, resulting in a layer being formed on the membrane surface. The current measured at this stage is stable and has a high value (stage 5) [31, 44]. SEM images depicting these two stages reveal an irregular distribution of ovedeposited hemispherical structures at stage 4, which expands into the continuous layer seen on the SEM image recorded in stage 5 (Fig. 2.8). The shape of the overdeposited structure carries information about the crystallographic structure of nanowires and their preferred growth direction [15, 25, 26].

The process of nanowire production is shown schematically in Fig. 2.9. Depending on further research, the nanowires were kept in the membranes (Fig. 2.9 b) or released from them (Fig. 2.9 c). The PC membranes were dissolved using dichloromethane (CH_2Cl_2).

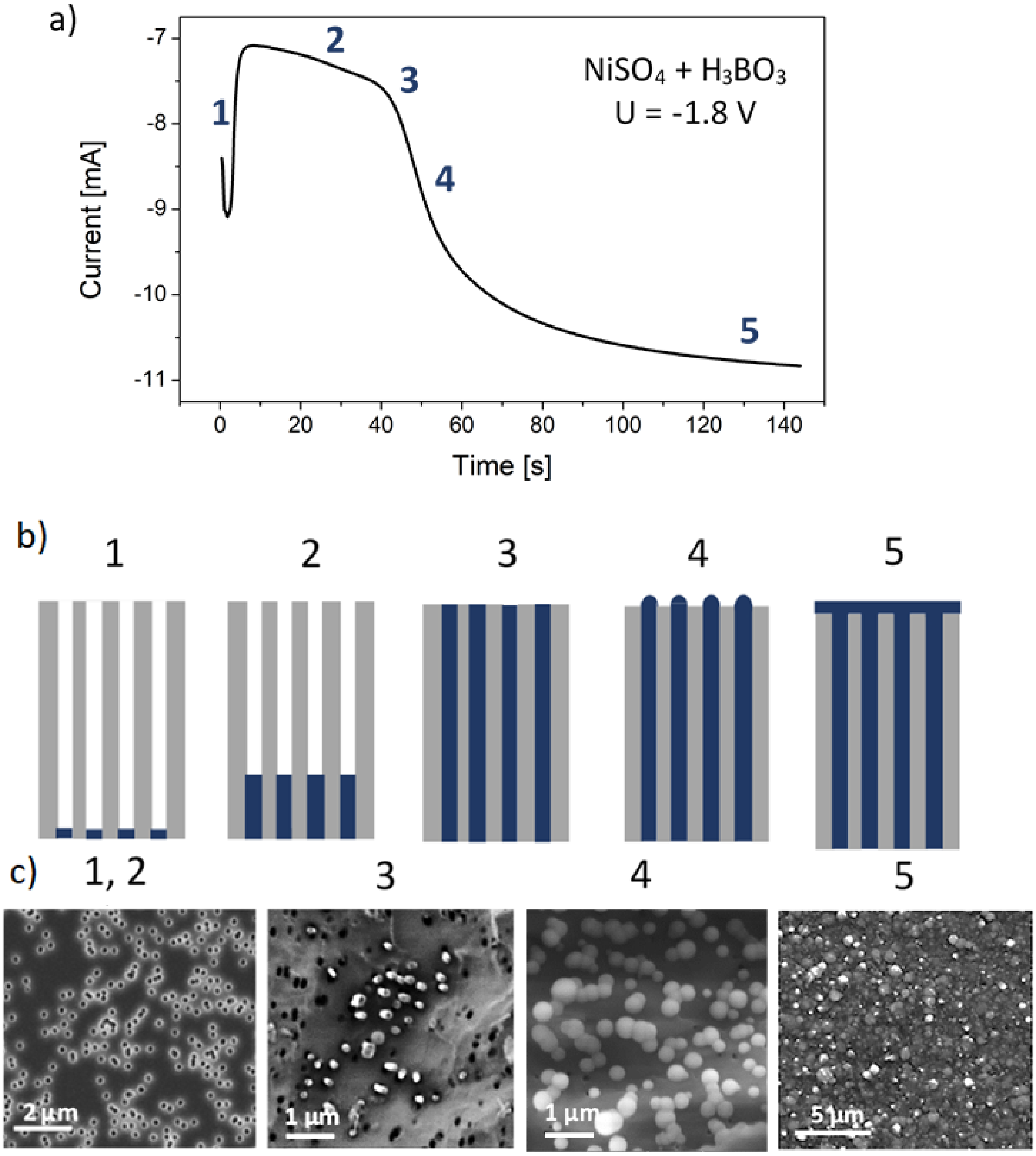

Figure 2.8: Template-assisted electrodeposition process: (a) current versus time dependence with numbers indicating subsequent stages, (b) schematic representation of these stages together with (c) appropriate SEM images.

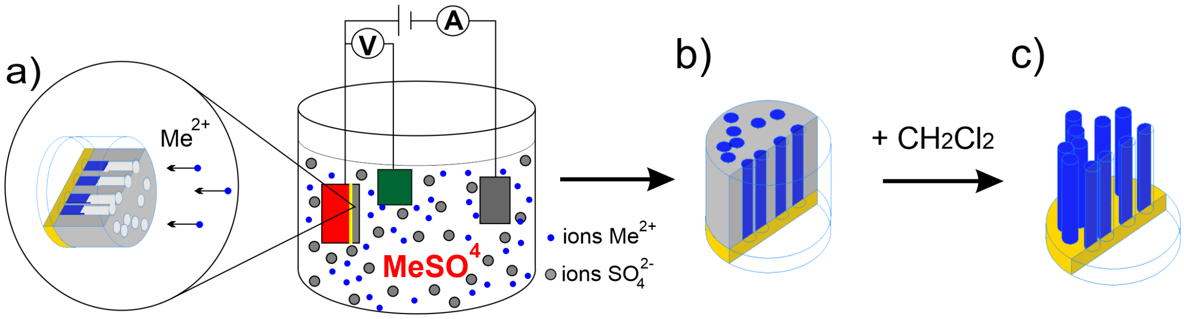

Figure 2.9: Schematic diagram of nanowires preparation: (a) electrochemical cell with a three-electrode system (as presented in Fig. 2.1), (b) membrane with filled pores, (c) free-standing nanowires after membrane dissolution.

For this purpose, a piece (approx. 0.5 cm^2) of the membrane with filled pores was glued with the contact layer side to a copper tape and placed on a Petri dish, and then directly poured with 2 ml of dichloromethane. After 10 min, the nanowires were obtained released from polycarbonate and standing on the contact layer.
To reveal the nanowires from the AAO membranes, the membranes were broken. Unlike polycarbonate membranes (which are flexible), AAO membranes break easily due to their brittleness, and the cross-sections created in this way enable the observation of nanowires in SEM images. SEM pictures of free-standing nanowires after PC membrane dissolution with an inset showing nanowires with caps (confirming complete filling of pores) as well as an SEM image of the cross-section of nanowires embedded in alumina membranes are presented in Figure 2.10.

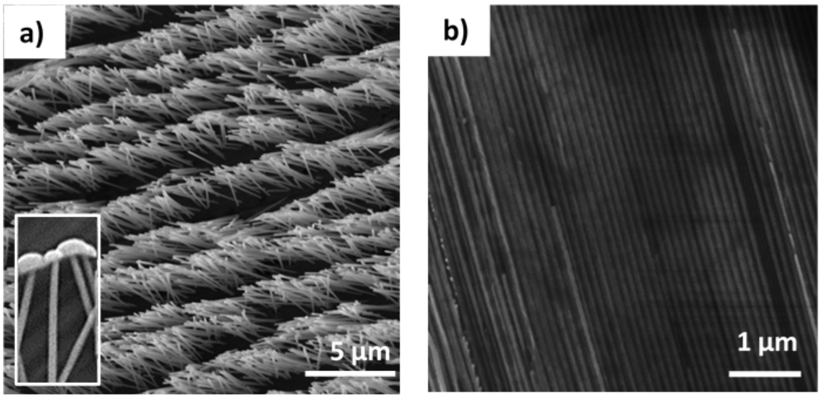

Figure 2.10: SEM images of (a) free-standing nanowires after PC membrane dissolution with an inset showing nanowires with caps and (b) cross-section of nanowires embedded in alumina membranes.

2.4. Nucleation and growth

The electrodeposition process takes place in two stages: the formation of the nuclei and their growth. Their mutual relationships determine the morphology and structure of deposits. A fine crystalline structure can be obtained at a relatively higher nucleation rate than the crystallite growth rate. The main parameters influencing nucleation and growth, and therefore, the morphology and structure of deposits include the applied potential (or current) ion concentration, mixing intensity, and electrolyte temperature.

As written above, nucleation followed by growth occurs at the bottom of the pores at the beginning of the template-assisted electrodeposition process. Assuming that the electrodeposition process is under diffusion control, two types of nucleation can be distinguished: instantaneous, when all nuclei are formed immediately in a small number of sites (which are quickly exhausted) and then grow with the electrodeposition time (Fig. 2.11 a), and progressive, when the nuclei are formed continuously during crystallite growth in a large number of sites and overlap (Fig. 2.11 b) [45, 46, 47]. In the case of instantaneous nucleation, the obtained materials are characterized by better quality and oriented growth, in contrast to the progressive one (Fig. 2.11 b) [48].

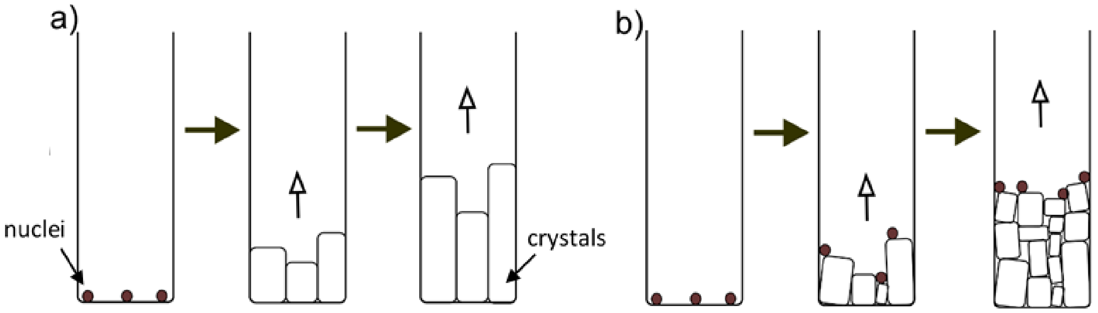

Figure 2.11: Scheme of the nucleation and growth of nanowires grown by electrodeposition inside pores: (a) instantaneous nucleation, (b) progressive nucleation [48].

The instantaneous and progressive nucleation models are given by the equations:

$$\frac{i^2}{i_{max}^2} = \frac{1.9542}{t/t_{max}}\{1 - exp[-1.2564(\frac{t}{t_{max}})]\}^2 \tag{2.21}$$

$$\frac{i^2}{i_{max}^2} = \frac{1.2254}{t/t_{max}}\{1 - exp[-2.3367(\frac{t}{t_{max}})^2]\}^2 \tag{2.22}$$

where i_{max} is the current and t_{max} is the time from a chronoamperometric peak [45, 46, 47]. The above equations will be used to analyze the growth mechanism of nanowires with different diameters deposited under various conditions.

2.5. Alloy deposition

Deposition of various ions from one bath requires different overpotentials, which in turn results in various current densities, being a measure of the deposition rate of the growing metals. In the simple case of two metals, two situations can be considered: the current-potential curves do not intersect (Fig. 2.12 a) and the opposite situation (Fig.

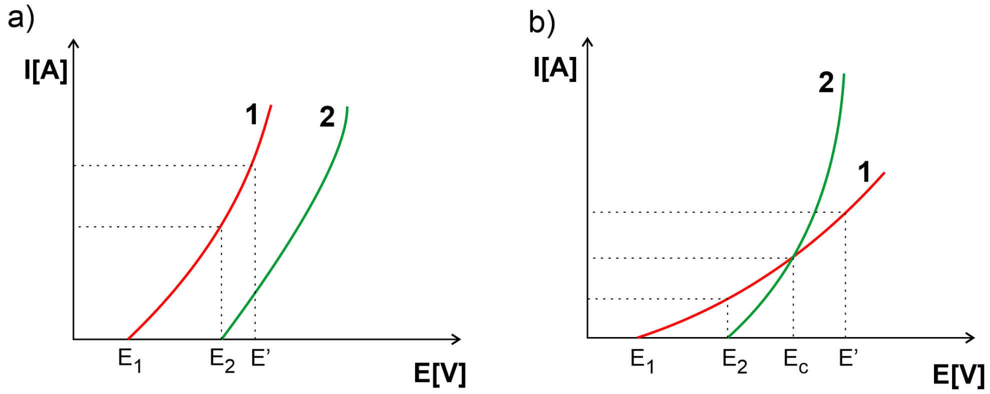

Figure 2.12: Current-potential curves of the co-deposition of two metals with the situation (a) non-intersecting and (b) intersecting curves [15].

2.12 b) [15].

In the first case, the reduction process starts with the discharge of ions with a lower standard potential, thus the deposit contains only this one kind of atoms. Then, at a more cathodic potential, the reduction of a second kind of ions with less noble standard potential occurs, and the deposit contains two kinds of atoms (E'). The greater the overpotential applied, the higher will be the content of atoms with a less noble standard potential in the deposit, but the content of the elements with a lower standard potential always exceeds the content of atoms of the second kind.

Another situation, presented in Fig. 2.12 b, shows the two intersecting current-potential curves. Initially, only more noble metal is deposited, then both metals are reduced (with a higher amount of lower standard potential element) and their content equalizes at the intersection point (E_c). A further potential increase causes the inverse composition due to the steeper slope of the curve measured for a metal with a more cathodic standard potential. This results in a higher content of less noble atoms compared to low-standard potential atoms.

This simple consideration can be applied to the electrodeposition of alloys. One can distinguish homogenous alloys consisting of one phase in the form of a solid solution or an intermetallic compound and heterogeneous alloys, in which the deposit can be composed of various phases such as alloys or pure elements, depending on the phase diagram. To obtain an alloy by electrodeposition, the overpotentials of deposited metals should be close to each other with a difference of less than one volt. If this condition is not met, there are two methods to approach electrodeposition potentials. The first one is based on the relationship between the electrode potential and ion concentration resulting from the Nernst equation. As a rule of thumb, a 10 mV shift in the electrode potential can be achieved by changing the ion concentration in the case of doubly charged ions by 100 [15]. Taking into account the limited possibilities of modifying the electrolyte composition, this method allows only a slight potential shift. The other method uses a complexing agent that brings the electrode potentials much closer, creating favorable conditions for the deposition of alloys composed of metals with initially very different electrode potentials.

The deposition of the alloy composed of Fe, Co, and Ni elements that are the subject of this work is more complicated because of the anomalous co-deposition described in the next chapter.

2.6. Anomalous co-deposition

During the electrodeposition of an alloy from an electrolyte containing various metallic ions belonging to the iron group, anomalous co-deposition can be observed. This type of deposition means that less noble metals are deposited preferentially compared to metals with higher standard potentials. As a result, the atomic concentration ratio in the deposit does not reflect the ratio of ion concentration in the electrolyte [49, 50].

Among others, the deposition of Fe, Co, and Ni is described as anomalous co-deposition [50, 51, 53]. Electrodeposition of those elements occurs not only from metal ions (Me^+) but also from the hydroxide ions ($MeOH^+$), which show higher deposition rate constants compared to free ions [54]. A possible explanation for the principal features of the anomalous co-deposition is based on the assumption that the metal hydroxide ions are the primary precursors competing with each other for surface sites on the electrode [50, 54]. It is assumed that the inhibition of the electrodeposition of more noble elements results from preferential coverage according to $FeOH^+ > CoOH^+ > NiOH^+$, which is related to differences in kinetics [55]. Anomalous co-deposition depends on the electrodeposition parameters such as the applied potential (or current), electrolyte temperature, and pH [20, 21, 50, 51, 53, 54, 56, 63]. High current density promotes the anomalous co-deposition, similarly, an increase in surface pH leads to the formation of iron hydroxide, which adsorbs on the electrode surface inhibiting Ni reduction, causing anomalous behavior [57]. However, anomalous co-deposition was also observed at low hydrogen evolution, low current density, and low surface pH [49, 58]. The above observations show that the mechanism of anomalous co-deposition is still an open issue and requires in-depth understanding.

As was mentioned above, anomalous co-deposition depends on the applied potential [20]. This means that by changing the cathodic potential it should be possible to control the type of deposition and, consequently, the chemical composition of the obtained materials.

The type of electrodeposition can be determined using the selectivity ratio (SR) parameter, which is defined as the atomic ratio in the deposited material to the molar ratio in the initial electrolyte. It ranges from 1 to 15, where 1 indicates standard deposition and 15 informs about anomalous co-deposition, but in general, the higher the SR coefficient, the more anomalous co-deposition is [41, 53].

2.7. Hydrogen evolution

As written earlier, a hydrogen evolution reaction may occur during the electrodeposition of metals from an aqueous solution. The hydrogen evolution reaction (HER) is a two-electron transfer process that yields H_2. Finally, H_2 leaves the electrode surface in the form of hydrogen bubbles.

Hydrogen evolution is pH dependent and in acid pH follows the general formula:

$$2H^+ + 2e^- \rightarrow H_2 \tag{2.23}$$

while in alkaline or neutral pH follows the formula:

$$H_2O + 2e^- \rightarrow H_2 + 2OH^- \tag{2.24}$$

The mechanism of hydrogen evolution can proceed in three principal steps with different proton donors in acid and alkaline pH media, which are hydronium cations H_3O^+ and water molecules (H_2O), respectively.

In the first step, known as the Volmer reaction, a proton reacts with an electron and generates an adsorbed hydrogen atom (H_{ad}) on the electrode surface. In the next step, the production of H_2 occurs via either the Heyrovsky or Tafel pathway or both. In the Heyrovsky pathway, another proton diffuses to the adsorbed hydrogen atom (Had) and reacts with a second electron to form H_2. In the Tafel reaction, two nearby Had combine on the electrode surface generating H_2 [59].

The above steps, in the case of acid medium, follow the formulas (2.25) and (2.26) or (2.25) and (2.27):

$$\textit{Volmer pathway:} \quad H_3O + e^- \rightarrow H_{ad} + H_2O \tag{2.25}$$

$$\textit{Heyrovsky pathway:} \quad H^+ + e^- + H_{ad} \rightarrow H_2 \tag{2.26}$$

$$\textit{Tafel pathway:} \quad 2H_{ad} \rightarrow H_2 \tag{2.27}$$

While in the alkaline medium they follow the formulas (28) and (29) or (28) and (30):

$$\textit{Volmer pathway:} \quad H_3O + e^- \rightarrow H_{ad} + OH^- \tag{2.28}$$

$$\textit{Heyrovsky pathway:} \quad H_3O + e^- + H_{ad} \rightarrow H_2 + OH^- \tag{2.29}$$

$$\textit{Tafel pathway:} \quad 2H_{ad} \rightarrow H_2 \tag{2.30}$$

The hydrogen evolution reaction is an unwelcome side reaction during the electrodeposition process. It acts as a barrier and can hinder the deposition by creating gas bubbles that, when adsorbed on the surface, block the nucleation sites of the deposition process. Larger bubbles may even block pores preventing their uniform filling [45]. High hydrogen evolution significantly modifies the deposit morphology increasing its porosity (voids) and roughness. Additionally, cavities, micro-holes, and gaps are created, which become the corrosion sites. Hydrogen evolution also contributes to the low current efficiency, prolonging the electrodeposition process and making it unstable [15, 42].

Parameters such as pH and applied potential strongly influence hydrogen evolution. Low pH values favor the hydrogen evolution, therefore, to minimize this adverse effect, the electrolyte pH should be appropriately selected. Hydrogen evolution also increases at high cathodic potential (or high current density). Besides the potential lowering (which is not always possible), the use of pulse deposition with time off or AC deposition with high frequency can significantly limit hydrogen evolution. This occurs by lowering the hydrogen ad-atom adsorption, which results in a more stable electrodeposition process and better material homogeneity without the porosity typical of deposits obtained at high current densities. [15].

The consequences of hydrogen evolution can be diminished by surfactant addition to the electrolyte. Such additives reduce the surface energy and facilitate the detachment of hydrogen bubbles from the surface [60, 61].

The reduction of base metal ions takes place in an area where the evolution of hydrogen gas cannot be avoided [61], however, in the case of the reduction of noble metal ions, electrodeposition conditions allow deposition without the accompanying hydrogen evolution, both as result of proton reduction and from the water-splitting reaction.

Positive aspects of hydrogen evolution can also be found [61]. Li and Podlaha exploited HER to produce porous nanostructures [61]. They used electrolytes with very low pH values (<1), which caused high hydrogen evolution. Furthermore, they modified electrolytes to limit the size of the hydrogen bubbles to a nanosize diameter, which enabled them to produce porous nanowires with a random distribution of nanopores along nanowires. An important aspect to take into account is the risk of dissolution of the alumina templates, which increases at low pH.

Another interesting and ecologically useful aspect of HER application is the efficient hydrogen production for hydrogen-based alternative energy technologies. This can provide a stable and cost-effective method for hydrogen production, which appears to be the most promising way to meet the continuously growing demand for renewable energy storage. [62].

Chapter 3

Influence of electrodeposition parameters on the nanowire properties

3.1. Electrolyte pH

An important parameter that indicates the concentration of hydrogen ions (H^+) in a given solution is the pH of the electrolyte. The electrolyte pH affects the kinetics and equilibrium of chemical reactions and the ability to ionize.

The electrolyte pH directly influences the electrodeposition process itself. First of all, as the pH of the electrolyte increases, the deposition rate rises: when the pH changes from 2.3 to 3.2, a rapid increase in the deposition rate is observed, while in the case of pH above 3.2, the deposition rate increases slowly [63]. This behavior is caused by hydrogen evolution, which, as shown in the previous section, decreases with increasing pH [63]. While the pH is less than 2.3, hydrogen evolution is rapid, which results in low current efficiency and strongly defected structure. If the pH value is between 2.3 and 3.2, hydrogen evolution slows down and the morphology of deposited material improves. As soon as the pH exceeds 4.0, hydroxides are easily released, which hinders the deposition process and deteriorates the quality of the material. Based on this, it can be concluded that the best pH value of the electrolyte for the nanowire deposition is between 2.3 and 3.2. Yang et al. also revealed that pH changes do not affect the anomalous deposition behavior [63].

The pH value, apart from influencing the electrodeposition process, also has an impact on the structure of the deposited materials. Hu et al. observed that a decrease in pH from 3.7 to 2.6 caused changes in the preferred growth direction from (111) to (200) in Fe nanowires [64]. In the case of Co nanowires, changes in pH induce structural modification [31, 65, 67, 68]. Low pH values (2.4 - 2.7) stabilized the fcc structure (or their mixture [65]), at medium pH (3.5) a mixture of hcp and fcc was observed, while at higher pH (5.0 - 6.4), the hcp phase dominated. Cortes et al. investigated the influence of the pH value of the electrolyte on the structure of Ni nanowires [69]. They did not note any effect of pH value on the preferred crystallographic orientation but they did notice changes in crystallite size. As the pH increased (2.0 - 4.0), the size of the crystallites decreased from 113 nm to 102 nm.

The pH also influences the magnetic properties of the material. This is especially visible in the case of Co nanowires, due to the strong correlation between the structure and magnetic properties of nanowires [16, 65, 66, 67, 70, 71, 72]. This subject will be described in more detail in the magnetic section of the work.

3.2. Temperature

The temperature of the electrolyte has a significant impact on the electrodeposition parameters and, consequently, on the properties of nanowires [31, 32, 63, 73, 77, 78]. In the literature, one can find many works talking about the influence of temperature during the deposition of both single elements and alloys.

It is known that temperature swap induce changes in the growth rate of nanowires. As the temperature increases, the electrodeposition process is faster and the current achieved is higher, which shortens the electrodeposition time. The temperature growth is also accompanied by a diffusion coefficient increase according to the Arrhenius plot. At the same time, the diffusion layer is elongated as the temperature decreases, thus the concentration gradient decreases, indicating diffusion-controlled transport behavior in nanopore channels. Therefore, according to Fick's law, a decrease in the diffusion coefficient and concentration gradient leads to the mentioned growth rate decrease with temperature lowering [73]. Additionally, temperature affects the morphology of nanowires. At low temperatures, when the process is slower, more precise packing is possible, and as a result, the obtained nanowires are characterized by high uniformity. Such a temperature dependence was observed during the deposition of nanowires made of Cu, Co, Fe, and Ni [73, 31, 32, 78]. The electrolyte temperature also influences the properties of the obtained nanomaterials. Kafil et. al. showed that a drop in temperature increases the grain size in Ni nanowires, which directly translates into a change in magnetic properties [78]. A similar relationship was also observed in other works concerning Fe nanowires [32, 75]. This condition can be explained by a local increase in current density. However, one can find works in which the opposite relationship was observed – at higher temperatures the size of crystallites was larger [38, 76]. The authors elucidated such behavior based on the rise in surface diffusion that favors the growth of already existing nuclei. As mentioned, the electrolyte temperature also affects the magnetic properties of nanowires. It has been observed, for example, that as the temperature grows, the coercivity increases [31, 32], which is assigned with the greater release of hydrogen, increasing the number of defects in the material.

If there is more than one type of ions in the electrolyte, a temperature change additionally affects the ratio of elements in the material [77]. Wang et. al. in their studies of FeNi nanowires observed that an increase in temperature causes an increases in Ni content and decrease in the iron concentration due to the oxidation of Fe^{2+} ions. Changes in the chemical composition of the deposit were also observed in the case of FeCoNi films, in which a temperature drop results in a decrease in the Fe content and an increase in the Co and Ni contents [63]. As mentioned above, with increasing temperature, the diffusion rate increases leading to the growth of the deposition rate. It was noticed that the nanowire surfaces are smooth when the deposition temperature does not exceed 40^0C.

Temperature changes can also influence anomalous co-deposition behavior, as temperature increases the co-deposition becomes less anomalous [54, 63].

Based on the above considerations, it can be concluded that to obtain smooth, non-porous nanowires, they must be deposited at an optimal temperature below 30^0C [63].

3.3. Nanowire geometry

In addition to the above-mentioned electrolyte parameters, the membrane parameters that determine the nanowire geometry are very significant factors tailoring the nanowire properties. The entire electrodeposition process begins with the selection of an appropriate membrane, which primarily decides on the nanowire diameter, maximal length, and the distance between them. Another very important parameter describing nanowire geometry is the aspect ratio, which is defined as the ratio of the nanowire length to its diameter (L/ϕ).

Differences in the pore diameters and membrane thickness can be noticed already in the electrodeposition process, specifically in the differences in growth rates. Zach et al. found that the smaller the diameter of the nanowires, the higher the growth rate [79]. A similar relationship was observed by Jensen et al. [80]. Besides affecting the growth rate, the nanowire geometry influences their properties, in particular the magnetic ones [32, 81, 82]. As the diameter of the nanowires increases, the magnetic structure of nanowires changes from a single-domain structure for small-diameter nanowires to a multi-domain structure for diameters above 50 nm [21]. The diameter and length of nanowires together with the distance between them, strongly influence the inter-wire interactions, which also result in changes in their magnetic properties [21, 81, 83, 84]. Furthermore, the nanowire geometry, especially their diameters and lengths is responsible for changes in crystalline structure. The small pore diameter favors a single crystalline structure. On the other hand, the nanowires with a diameter above 50 show a polycrystalline structure, in which additionally the preferred growth direction may change with the nanowire diameter resulting also in a modification of the magnetic properties [81, 83]. The nanowire length can also affect the nanowire composition. Saedi et al. found that in longer nanowires, the concentration of diluted electrolyte components decreases with a simultaneous increase in the component dominating in the electrolyte. Such a modification of the chemical composition in nanowires was explained by hindering the mass transport of low-concentration ions over a long diffusion distance [50].

Based on these considerations, it can be concluded that the geometry of the nanowires is a significant parameter, therefore the membranes must be well-selected to obtain the nanowires with the desired properties. A more detailed description of the influence of the nanowire geometry on the magnetic properties will be presented in the magnetic part of the work.

3.4. Applied potential

The applied potential is a parameter that has a very significant impact on the electrodeposition process and can be used to produce materials with various physical properties [41, 53, 63]. The value of the applied potential influences the rate of both migration of metal ions and charge transfer. As the value of the applied potential grows, the current increases causing an increase in the growth rate. The faster the deposition, the shorter the pore filling time, but the degree of the pore filling and the uniformity of the nanowires are worse.

At low applied potential, the ion reduction occurs slowly and the growth rate exceeds the rate of formation of new nuclei. Such conditions favor the growth of coarse crystalline structures. As the potential increases, the rate of formation of nuclei increases, and the deposit shows fine crystalline structure. At very high overpotential, the ion concentration near the cathode decreases, which results in the growth towards the bulk region with higher ion concentration, causing dendrite formation.

As shown earlier, a high value of cathodic potential affects the hydrogen evolution, which causes changes in the morphology of the nanowires, making them more porous and less uniformly filled. These changes also result in a modification of the magnetic properties, which will be presented in the magnetic part of the work.

In the case of alloyed nanowires, the applied potential affects the element content in the deposit. Already in two-element FeNi nanowires, a more cathodic potential results in an increase in the Ni content while a decrease in Fe content [41, 85]. Such changes are not observed in FeCo systems, which are found to be less sensitive to the applied potential [41]. Modification of the chemical composition of deposits was also observed in FeCoNi alloys. A more cathodic potential leads to a higher Ni content with simultaneous lower concentrations of Co and Fe. Such a relationship between the element ratio and the applied potential has been observed in coatings [51, 52, 21, 20], but to our knowledge, there are no studies concerning nanowire deposition.

To observe the modification of the chemical composition under the applied potential, the electrolyte composition must be carefully selected. This is confirmed by the research of Xiao et al., who, despite the change in deposition potential, did not observe any changes in the chemical composition of nanowires [86].

As mentioned earlier, the applied potential can influence the co-deposition character. Dragos et al. calculated the selectivity ratio for nanowires deposited at different potentials and showed that this parameter has a maximum value at a potential of approximately $-$ 1.0 V, indicating the anomalous nature of the deposition, and gradually loses this anomalous character when applied potential shifts from 1 to the cathodic or anodic directions [53]. Similar behavior with a maximum at low cathodic current was observed in Co/Ni and Fe/Ni nanowires [54].

Changes in chemical composition affect the properties of the deposited materials, including their structure and magnetic parameters [53, 63, 85]. The use of various cathodic potentials during electrodeposition allowed me to obtain FeCoNi nanowires with distinct chemical compositions and, consequently, different structural and magnetic properties.

Chapter 4

Magnetism in nanostructures

In the general approach, magnetism can be defined as a set of physical phenomena related to a magnetic field, which can be generated by both electric current and magnetic materials. All materials exhibit magnetic properties, although only some types of them, consisting of atoms with a non-zero magnetic moment, are commonly called magnetic materials. The magnetic moment is the resultant of the spin, orbital magnetic moments of electrons and the magnetic moment of the nucleus. The non-zero net magnetic moment only occurs in atoms that have unpaired electrons, *i.e.* in transition metals such as Fe, Co, Ni, and lanthanides [87].

The magnetic properties of materials depend on their electronic structure, which in systems with reduced dimensionality is significantly modified by breaking their translational symmetry. The changes in the electronic structure in materials with a large contribution of surface or interface atoms to bulk atoms cause its evolution to the structure typical for free atoms leading to the increase in the spin magnetic moment. This symmetry breaking is the main reason for the differences between the magnetic properties of bulk materials and their nanomaterial counterparts. Moreover, the reduction of the number of neighbors around the surface atoms leads to the narrowing of bands, which results in an increase in the density of electronic states at the Fermi level and can lead to ferromagnetic ordering in non-magnetic materials with reduced dimensionality.

One of the basic magnetic parameters is magnetization (M), which measures the material response to the applied field H and is a quantity of permanent or induced magnetic moments in material per unit volume (V).

$$M = \frac{1}{V}\sum_{i=1}^{n} m_i \tag{4.1}$$

The unit of magnetization is ampere per meter [A/m] or [emu/cm3] in CGS system. Knowing the above units, one could define the volume magnetic susceptibility χ, which is a dimensionless proportionality constant indicating the degree of material magnetization under the influence of an external magnetic field (H) expressed in [A/m] or [Oe] in CGS system (1 Oe = $10^3/4\pi$ = 79.6 A/m and 1A/m = $4\pi\cdot$ $10^{-}3$Oe = 0.0126 Oe):

$$M = \chi \cdot H \tag{4.2}$$

The magnetic susceptibility assumes different values depending on the material behavior in an external magnetic field and allows the material to be assigned to the appropriate

magnetic type (Fig. 4.1):
- $\chi < 0$ - diamagnetic material
- $\chi > 0$ - paramagnetic material
- $\chi >> 0$ - ferromagnetic material
- χ = -1 - ideal diamagnetic material - superconductor (B=0).

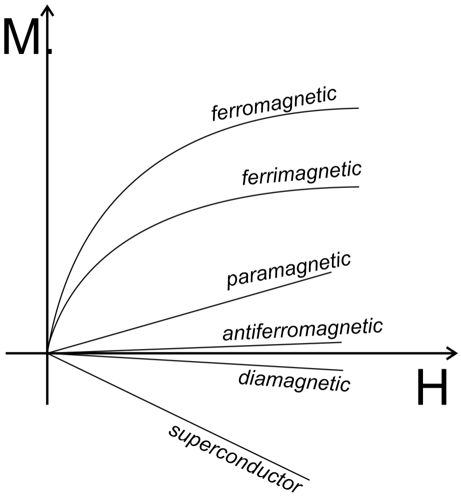

Figure 4.1: Schematic dependence of magnetization on an applied external magnetic field.

In a vacuum, the magnetic field strength (H) is related to the magnetic induction vector (B) through the vacuum permeability (μ_0):

$$B = \mu_0 \cdot H \tag{4.3}$$

Magnetic induction depends on the properties of the material and is expressed in [T = N/(A · m)]. It is defined through the force (Lorentz force) (F) acting on electrical charge (q) moving with the velocity (v):

$$F = q(vxB) \tag{4.4}$$

The relationship between magnetic induction, magnetization and magnetic field strength is following:

$$B = \mu_0(H + M) \tag{4.5}$$

As already mentioned, the substances belonging to the distinguished types of magnetic materials behave differently in the presence and absence of an external magnetic field. Diamagnetics respond to an external magnetic field by inducing an opposite field, thereby diminishing the impact of the external magnetic field (Fig. 4.2 a). Perfect diamagnetism is observed in superconductors whose interior is completely isolated from the external magnetic field (Meissner effect). In turn, paramagnetic materials, magnetize toward an external magnetic field (Fig. 4.2 b). Paramagnetic atoms maintain a constant, non-zero net magnetic moment, but weak interactions between them result in zero magnetization in the absence of an external magnetic field. In antiferromagnetic substances, adjacent magnetic moments tend to align antiparallel, mutually compensating and preventing spontaneous magnetization (Fig. 4.2 c). Similar behavior can be observed in ferrimagnets, but in these materials, opposite magnetic moments, because of different magnetization values of magnetic sublattices, exhibit spontaneous magnetization (Fig. 4.2 d) [87]. The last group of magnetic materials is ferromagnets, in which the magnetic moment occurs even in the absence of an external magnetic field. These substances are described in more detail in the next section. In addition to the mentioned class of magnetic materials, one can also distinguish superparamagnetic materials. This state is observed in the case of low-dimensional objects with a size of 10-20 nm or in other nanostructures of limited size. In these materials, small, magnetically ordered areas are oriented randomly. Such a system is similar to a paramagnetic sample, in which instead of disorder magnetic atoms there are small magnetic areas – particles. The thermal vibrations do not destroy the ferromagnetic orientation in particles but cause the fluctuation of magnetization vectors of particular ferromagnetic objects, giving zero resultant magnetization.

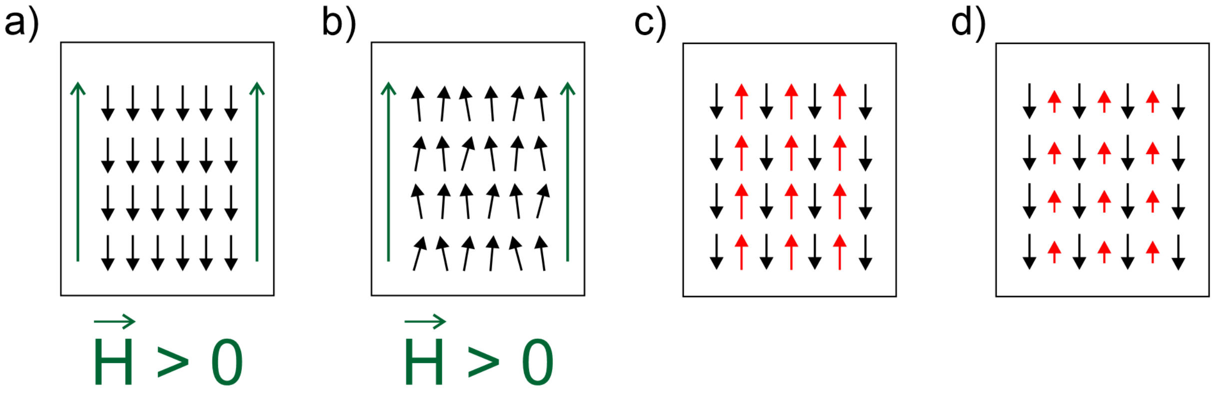

Figure 4.2: Schematic drawing of the magnetic moment alignment in the: (a) diamagnetic, (b) paramagnetic, (c) antiferromagnetic, (d) ferrimagnetic material.

4.1. Ferromagnetic materials

Ferromagnets are materials, in which strong exchange interactions, below a certain temperature (T_c, called the Curie temperature), lead to a parallel ordering of magnetic moments even in the absence of an external magnetic field (Fig. 4.3 a). At the absolute zero temperature, spontaneous magnetization reaches its maximum value (Fig. 4.3 b). As the temperature increases, the orientation of individual magnetic moments is rearranged and, as a result, spontaneous magnetization decreases until the temperature reaches the critical value T_c (Fig. 4.3 b) [87].

Above this temperature, at which the second-order phase transition occurs, spontaneous magnetization disappears and the system exhibits paramagnetic behavior. The temperature dependence of the magnetic susceptibility for ferromagnets above the Curie temperature is determined by the Curie-Weiss law:

$$\chi = \frac{Const}{T - T_c} \tag{4.6}$$

The model of ferromagnetism proposed by Weiss postulated the presence of magnetic domains – macroscopic areas magnetized homogeneously along different directions with the resultant zero magnetization in the absence of an external magnetic field. Weiss also assumed that this spontaneous magnetization of magnetic moments in ferromagnets

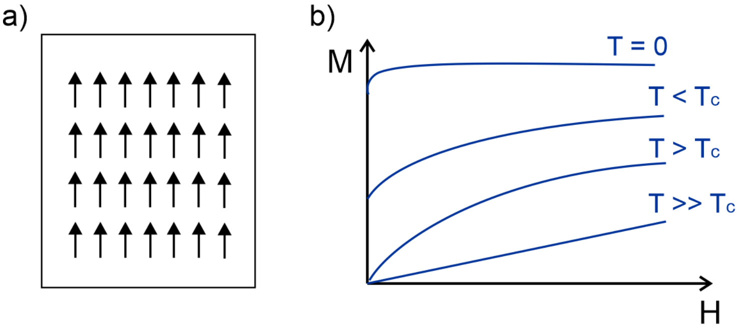

Figure 4.3: Behavior of ferromagnetic materials: (a) schematic drawing of the magnetic moment alignment in a ferromagnetic material, (b) macroscopic magnetization as a function of field at various temperatures.

is caused by the existence of a strong internal magnetic field called a molecular field (B_M), proportional to the magnetization vector (M). However, to maintain such a parallel orientation of the spins at a temperature close but below the T_c of Fe, a field of order of 1000 T is needed (estimated based on a relationship $mB_M = k_B T$, where m is the magnetic moment of the atom).

In the quantum mechanics approach the molecular field describes the electrostatic exchange interactions between the pairs of spins. The exchange interactions are quantum mechanical interactions of wave functions associated with neighboring atoms, which are responsible for spontaneous ferromagnetic ordering in the domain area. The exchange interaction can also assume an indirect nature, when the distance between the interacting magnetic moments is larger than the lattice constant. In this case, the exchange interactions occur by delocalized conduction electrons, which are polarized by magnetic ions (spins of the electrons are homogenously oriented). The polarized conduction electrons transverse their spin into the next magnetic ions via an indirect exchange interaction orienting them. This exchange type called RKKY (Ruderman, Kittel, Kasuya, Yosida), describes the interactions of magnetic ions distributed in a non-magnetic matrix. There are also other types of indirect exchange interactions, such as superexchange (interactions via two electrons with opposite spins) or double exchange (in the ions with different valences whose electrons hop from the ion of lower to higher oxidation states through non-magnetic ions between them) observed in magnetic ions separated by non-magnetic anions.

In the case of transition metals (Fe, Co, Ni), which can be considered as a lattice of ions and delocalized conduction electrons, the ferromagnetism can be described by a band model. The exchange interactions split the energy states, which results in a shift between the bands with the spin-up and spin-down electrons. To keep the same Fermi level for these bands, electrons move between them, giving the resultant magnetic moment. This net magnetic moment can be reached for the strong molecular field and the large density of states on the Fermi level (narrow band). This condition, called the Stoner criterion, is fulfilled for Fe, Co, and Ni, which show ferromagnetic ordering.

4.1.1 Interactions in ferromagnetic materials

The total energy of the ferromagnetic material in an external magnetic field can be expressed as a sum of the contributions originating from exchange energy (E_{EX}), Zeeman energy (E_H), magnetostatic energy (E_D), magnetoelastic energy (E_{ME}), and crystalline anisotropy energy (E_{CA}):

$$E = E_{EX} + E_H + E_D + E_{ME} + E_{CA} \tag{4.7}$$

The exchange energy is connected with the interactions between the spins (S_i and S_j) and depends on their mutual orientation:

$$E_{EX} = \sum_{i,j} J(S_i \cdot S_j) \tag{4.8}$$

where J_i is the exchange integral, which takes a positive value (J $>$ 0) for ferromagnetic materials and a negative value (J $<$ 0) for antiferromagnets. Exchange interactions can be described by the exchange stiffness constant (A), which is a measure of the force that holds the spins in order [88]:

$$A = JS^2\frac{c}{a} \tag{4.9}$$

where S is the magnitude of the individual spins, c is the geometric factor, which assumes 1, 2, 4 or $2\sqrt{2}$, respectively for simple cubic (sc), bcc, fcc, hcp structures and a is the lattice parameter. For most ferromagnetic materials, A is between 1 x 10^{-6} and 2 x 10^{-6} erg/cm^2 (1 x 10^{-11} and 2 x 10^{-11} J/m). Exchange interactions are a kind of quantum interaction of wave functions identified with electrostatic interactions between electrons described by Coulomb's law. These are short-range interactions (of the order of lattice constant), which decrease exponentially with distance. They belong to strong interactions of an order of $0.1 - 50$ meV. The exchange energy reaches its minimum value with a parallel spin orientation.

The next term, also called external field energy is related to the interactions of the magnetization vector with the external magnetic field and is minimized when magnetic moments in the sample are oriented in the direction of the external field.

$$E_H = -\mu_0 \int M \cdot H dV \tag{4.10}$$

Magnetostatic energy is connected with the magnetic field generated by the sample itself. A magnetic sample with non-zero magnetization has north and south poles, which creates a stray field outside the sample and a demagnetization field (H$_d$) inside the sample. The demagnetization field has a direction opposite to the magnetization vector, therefore the magnetic induction generated by ferromagnet is diminished by H$_d$:

$$B = \mu_0(M - H_d) \tag{4.11}$$

The demagnetization field depends on the shape of the sample and for a homogenously magnetized sample H$_d$ = - N$_d$·M, where N is a demagnetizing factor depending on the sample shape and direction of the magnetization (Nd is the demagnetization factor along M). In the case of an elongated sample with the magnetization vector aligned along the major axis (c), N takes the smallest value (N$_c$ decreases with increasing sample length (L)), and when M lies along the short axis – the largest one. The demagnetization factor along the axis of an ellipsoid (a, b, c) fulfills the condition N$_a$ + N$_b$ + N$_c$ = 1 (and 4π in CGS). This factor ranges between 0 and 1 (SI) or 0-4π (CGS) and for spheres it is N$_a$ = N$_b$ = N$_c$ = $\frac{1}{3}$ and for nanowires N$_a$ = N$_b$ = $\frac{1}{2}(2\pi)$, N$_c$ = 0 (0) (SI/CGS) [89, 90, 92].

The demagnetization field can be generated by itself, by the neighboring domains, or by an external magnetic field. Magnetostatic energy is minimized when the magnetic field lines follow a closed path and is expressed by:

$$E_D = -\frac{1}{2}\int H_d \cdot M dV \tag{4.12}$$

which for elongated, homogeneously magnetized samples assumes form $E_D = \frac{1}{2}N_d M_s^2$.

Magnetostatic interactions also concern dipole interactions between magnetic moments but they are three orders of magnitude smaller than exchange interactions. They are long-range interactions and decrease with the cube of the distance. Such dipole interactions also act in the matrix of nanowires and will be discussed in the next part of the thesis. Similarly, shape anisotropy, which has its origins in magnetostatic interactions will also be discussed in the next section.

Magnetoelastic energy shows the effect of strain on magnetization. This energy is directly related to the magnetostriction effect, in which the magnetic materials change their dimensions under the influence of a magnetic field or to an inverse effect called the Villari effect, where the mechanical stresses cause a modification of the magnetization vector. This kind of interaction and the associated magnetoelastic anisotropy will be briefly described in the next section.

The latter term, called magnetocrystalline anisotropy, combines the crystallographic directions with the magnetization vector and will be also described in the chapter on anisotropy.

4.2. Magnetic anisotropy

Typically, magnetic materials are non-isotropic but anisotropic. Magnetic anisotropy is the directional dependence of the magnetization vector. Thus, the magnetic moments prefer to be aligned in a fixed direction, called the easy axis. The easy axis is the energetically favorable direction of spontaneous magnetization. The energy needed to rotate the magnetization vector from the easy to hard direction is the magnetic anisotropy energy.

Magnetic anisotropy may originate from magnetocrystalline anisotropy, shape anisotropy, magnetoelastic anisotropy, surface anisotropy, and as well as from dipolar interaction [4, 70, 95, 96, 97, 98]. Among the anisotropies mentioned, only magnetocrystalline and magnetoelastic anisotropies are material-dependent.

4.2.1 Magnetocrystalline anisotropy

Magnetocrystaline anisotropy is connected with the arrangement of magnetic moments along the preferred crystalline axis due to the interaction of spin-orbit coupling with the crystal electric field. In the absence of an external magnetic field, the magnetic moments are ordered along the easy axis (EA), in which the absolute minimum free energy is achieved.

In the case of uniaxial anisotropy (single axis of high symmetry), the magnetocrystalline anisotropy energy density is:

$$E_{CA} = K_u sin^2\theta \tag{4.13}$$

where K_u is the anisotropy constant and θ is the angle between the magnetization and the easy axis.

Magnetic anisotropy can be determined by the anisotropy constants K or by the anisotropy field H_K, which represents a hypothetical field that can align the magnetization perpendicular to the easy direction [99]and is defined by:

$$H_K = \frac{2K_u}{M_s} \tag{4.14}$$

In the case of a cubic system, the magnetocrystalline anisotropy energy density is:

$$E_{CA} = K_1(\alpha_1^2\alpha_2^2 + \alpha_2^2\alpha_3^2 + \alpha_3^2\alpha_1^2) + (K_2\alpha_1^2\alpha_2^2\alpha_3^2) + ... \tag{4.15}$$

Usually, the contribution of the second term is small and can be neglected.

Thus for $K_2 = 0$ and $K_1 > 0 \rightarrow$ EA || <100>
for $K_2 = 0$ and $K_1 < 0 \rightarrow$ EA || <111>.

If $K_2 \neq 0$ easy axes depend on K_1 and K_2 [100].

In the hexagonal system, the energy density takes the form:

$$E_{CA} = K_1 sin^2\theta + K_2 sin^4\theta + ... \tag{4.16}$$

where θ is the angle between the magnetization vector and the c-axis. In this system, when $K_1 > 0$ and K_2 is small and can be neglected, the energy is smallest if $\theta = 0$, *i.e.* the easy axis lies along the c-axis.

The table below shows the values of the anisotropy constant for Fe Co and Ni crystalizing in bcc, hcp, and fcc structures.

Table 4.1: Room-temperature anisotropy constants for different crystallographic structures [101].

Crystallographic structure	Element	$K_1[J/m^3]$	$K_2[J/m^3]$	Easy axis
bcc	Fe	$4.8 \cdot 10^4$	$-1.0 \cdot 10^4$	<100>
hcp	Co	$4.5 \cdot 10^5$	$1.5 \cdot 10^5$	{0001}
fcc	Ni	$-4.5 \cdot 10^3$	$-2.3 \cdot 10^3$	<111>

Magnetocrystalline anisotropy may contribute to effective anisotropy only in single-crystalline or textured samples. It does not occur in polycrystalline samples without a preferred grain orientation [95].

The easy axis in FeCoNi fcc alloys lies in the [111] direction [102], which is typical for a Ni-based fcc phase.

The magnetocrystalline anisotropy depends strongly on temperature and decreases as temperature approaches the Curie temperature, so the crystal becomes isotropic.

4.2.2 Shape anisotropy

An object with a non-spherical shape, in which a long and short axis can be distinguished, is easier to magnetize along its long axis. This is related to the magnetic poles described above and the induced demagnetization field, which increases as the distance between poles decreases. Therefore, the demagnetization field is minimized when the magnetization vector lies along the long axis. The origin of such an anisotropy called the shape anisotropy, is the long-range dipole interactions. The shape anisotropy contribution to the effective anisotropy increases as the object elongates and reaches saturation for an aspect ratio above 10. Shape anisotropy favors the orientation of the magnetization direction along the main axis of elongated objects.

The shape anisotropy constant can be written as:

$$K_d = \mu_0(N_a - N_c)/2 \tag{4.17}$$

where Na and Nc are demagnetization factors along a and c axis. If $N_a < N_c$ then the shape anisotropy is minimal with M_s along the c-axis.

In the case of the 3d metals, the shape anisotropy constant (Table 4.2), which is proportional to M_s^2 is usually larger than the magnetocrystalline constant.

Table 4.2: Shape anisotropy constant Kd for Fe, Co and Ni [95].

Element	$K_d[J/m^3]$
bcc-Fe	$1.92 \cdot 10^6$
hcp-Co	$1.34 \cdot 10^6$
fcc-Ni	$1.73 \cdot 10^5$

4.2.3 Surface anisotropy

The dimensionality reduction responsible for translation symmetry breaking modifies the magnetic anisotropy and leads to an increase in effective anisotropy. This is due to the edge atoms, whose energy is several dozen larger than the energy of bulk atoms and reaches the value of meV/atom (compared µeV/atom in bulk). These atoms contribute to surface anisotropy, also called Néel anisotropy. Surface anisotropy is sensitive to defects and can be modified by small changes in chemical composition and surface roughness. This anisotropy is inversely proportional to the layer thickness and may therefore be important in ultrathin magnetic layers (« 10nm).

4.2.4 Magnetoelastic anisotropy

Magnetoelastic or stress anisotropy is related to the mechanical stresses that act on the samples and influence the magnetization. Such mechanical stresses cause lattice deformation, which affects the spin-orbit coupling and results in the appearance of a preferred magnetization direction. Magnetoelastic anisotropy often comes from stresses arising during the deposition or annealing processes due to the difference in the thermal expansion coefficient between the substrate or templates and the deposit. The magnetoelastic energy produced by a stress σ is proportional to this stress and the resulting deformation (magnetostriction), λ. In a uniaxial system the magnetoelastic energy is defined by:

$$E_{ML} = -3\sigma\lambda_s cos^2\theta/2 \tag{4.18}$$

where λ_s is an isotropic magnetostriction coefficient and θ is the angle between the magnetization M_s and σ. Stress-induced anisotropy constant is given by:

$$K_{ML} = 3\sigma\lambda_s/2 \tag{4.19}$$

The stress axis is an easy direction of magnetization if $\sigma\lambda_s > 0$ [103]. This kind of anisotropy is usually neglected compared to other anisotropies in nanowires studied at room temperature [70].

4.2.5 Dipolar interactions in the nanowire matrix

The effective magnetic anisotropy in nanowires is strongly affected by dipole interactions between nanowires. The dipole interactions are magnetostatic interactions that depend on the distance between the nanowires and decrease with the cube of the distance as mentioned above. The direct parameter determining the inter-wire distance is porosity (P), the greater the porosity, the shorter the inter-wire distance and the larger the dipole interactions. Low porosity membranes enable the production of nanowires with strong anisotropy along the main nanowire axis, which is typical for quasi-non-interacting nanowires. On the other hand, in a high porosity nanowire matrix, strong dipolar interactions contribute to the perpendicular alignment of the magnetization vector, which reduces the effective anisotropy and, at very high porosity, can lead to the isotropic behavior or even a 90-degree reorientation of the easy axis.

Dipolar interactions are proportional to the saturation magnetization, thus an increase in the nanowire volume also results in large dipole interactions [33, 104, 105, 106]. This means that dipolar interaction will increase with increasing nanowire length [105].

Therefore, to minimize dipolar interactions, relatively short nanowires separated by d » ϕ [104] should be used. In the case of a nanowire matrix with an inter-wire distance comparable to the nanowire diameter, the dipole interactions play a key role.

4.2.6 Magnetic anisotropy in nanowires

In general, magnetic anisotropy in nanowires is determined by magnetocrystalline anisotropy, shape anisotropy, dipolar interactions, and magnetoelastic anisotropy [4, 96, 98]. As mentioned above, the contribution of magnetoelastic anisotropy can be neglected at room temperature compared to other anisotropies.

The effective anisotropic field of the nanowire matrix can be expressed as the sum of shape anisotropy field ($2\pi M_s$), inter-wire magnetostatic dipole interaction field ($6.3\pi M_s r^2 L d^{-3}$), and magnetocrystalline anisotropy field (H_{MC}):

$$H_K = 2\pi M_s - 6.3\pi M_s r^2 L d^{-3} + H_{MC} \tag{4.20}$$

where r is the radius of the nanowire, L is its length, and d is the distance between the nanowires. Magnetocrystalline anisotropy is usually smaller than shape anisotropy and additionally may contribute to effective anisotropy only in single-crystalline or highly textured samples. Polycrystalline samples without a preferred orientation of grains do not possess magnetocrystalline anisotropy [95]. Moreover, if the aspect ratio of the nanowires is greater than 10, the shape anisotropy contribution is constant [33]. Therefore, the main parameter determining effective anisotropy in nanowires with high aspect ratios are dipole interactions. As can be seen from the above formula (53), these interactions are largely influenced by the dimensions of the nanowires: their length, diameter, and the distances between them [105, 107].

4.3. Domain structure

Despite the presence of spontaneous magnetization, ferromagnetic samples often have zero net magnetic moment at zero field. This is due to the formation of magnetic domains - macroscopic areas magnetized homogeneously along different directions.

Two competing interactions are involved in the process of magnetic domain formation. The first is the exchange interaction, which tends to ferromagnetic ordering of magnetic moments and the second is the dipole interaction, which is weaker than the exchange interaction, but a large number of ferromagnetically ordered magnetic moments have large enough dipole energy to overcome exchange energy. Therefore, the magnetic moments are arranged ferromagnetically to minimize the exchange energy, which maximizes their dipole energy. The spontaneous domain formation oriented in different directions significantly reduces the dipole energy but increases exchange energy, which is, however, relatively small because it is only related to a small area at the domain boundary called the domain wall (DW).

An abrupt change in the magnetization direction between adjacent domains would be energetically unfavorable, which is why the domain walls are characterized by a certain width (δ_{DW}). The width of the domain wall is usually several orders of magnitude smaller than the domain size and spans across around 100-150 atoms. For example, when the size of domains in bulk materials is in the order of micrometers ($10^{-4} - 10^{-6}$m), the domain wall width can be about 100 nm. The structure of the domain wall is determined by a competition between exchange, anisotropy and dipolar energies [108]. Especially, the thickness of the domain wall depends on the magnetocrystalline anisotropy, which shows how easily the magnetic moment can rotate in crystalline structure, and although an anisotropy energy is smaller than an exchange energy, it affects the rate of spatial reorientation of the magnetic moments. The large anisotropy energy, keeping the magnetic moment strongly oriented along the easy axis, favors a narrow domain wall to minimize the area with spins deviated from the easy axis. On the other hand, the large exchange interactions expressed by exchange stiffness constant (A) promoting the ferromagnetic ordering of magnetic moments, hinder their rotation and the domain wall thickness becomes large. Thus, the anisotropy energy collapses δ_{DW}, while exchange energy expands it [109].

A domain wall is an area, in which the direction of magnetic moments gradually changes from the magnetization direction of one domain to the direction of a neighboring domain. These magnetic moments can rotate around the normal of the domain wall (rotation occurs in the plane of the domain wall) - Bloch wall or around a line that is orthogonal to the normal of the domain wall (in the plane of the magnetization vector of adjacent domains) - Néel wall.

The domain wall width for hard magnetic materials with a Bloch-type domain wall shows the following relationship with the exchange stiffness constant (A) and uniaxial anisotropy energy constant (K_u) [109]:

$$\delta_{DW} = 3\sqrt{\frac{A}{K_d}} = \sqrt{\frac{2A}{\mu_0 M_s^2}} \tag{4.21}$$

The domain structure is directly related to the hysteresis loop (Fig. 4.4). When a small external magnetic field is applied to a ferromagnetic material, the magnetization vector of individual domains begins to align along this field, which leads to the formation of non-zero magnetization. An increasing magnetic field causes a rise in the volume of these domains, whose directions of the magnetization are close to the direction of the magnetic field. At the same time, the volume of the domains, whose magnetization directions differ significantly from the direction of the magnetic field decreases, until they completely disappear. As the magnetic field increases, the magnetization increases and reaches a saturation state (M_s).

The magnetic field corresponding to the saturation of the magnetization (M_s) is a saturation field (H_s). When reducing the magnetic field after reaching M_s, the magnetic curve follows a different curve than the original one. As a result of this cyclical change of the magnetic field, a hysteresis loop is created (Fig. 4.4). The hysteresis loop is characterized by remnant magnetization M_r defined as the value of M at $H = 0$ and the coercive force H_c, being a field needed to demagnetize the sample, defined as the value of the field H at the point $M = 0$. There is also another useful parameter - squareness, *i.e.* the ratio of M_r to M_s (M_r/M_s). A perfect square hysteresis loop with $M_r/M_s = 1$ can be obtained for a single-domain structure perfectly aligned along the external magnetic field. For samples showing magnetic anisotropy, measurements along easy and hard directions give different shapes of magnetic curves. In this case, the anisotropy field (H_K), which is a field needed to saturate the sample along its hard direction, can be determined. The saturation field (H_s) taken from the loop measured along the hard axis is equal to the anisotropy field (H_K).

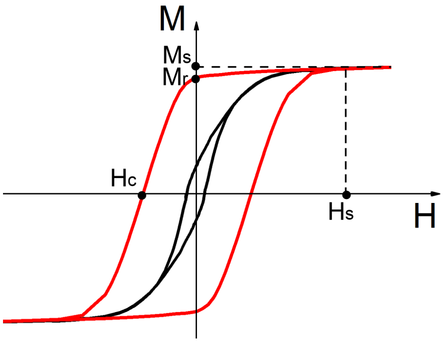

Figure 4.4: An example of a hysteresis loop of a ferromagnetic material measured along easy and hard direction.

Due to the nature of the magnetization processes, ferromagnetic materials are divided into hard, semi-hard, and soft magnetic materials.

HARD MAGNETIC MATERIALS are a group of materials that maintain the remnant magnetization after removing the external magnetic field. Their coercivity value is above 100 kA/m ($\sim$ 1260 Oe). Hard magnets are characterized by a wide hysteresis loop due to high H_c.

SEMI-HARD MAGNETIC MATERIALS are a group of materials with a coercivity value within the range of 1-100 kA/m ($\sim 12.5 - 1260$ Oe). Similar to hard magnetics, semi-hard materials retain their magnetized state when the magnetic field is removed. However, not too high values of the coercive field allow for relatively easy removal of the magnetization or its polarity reversal. This property is used in magnetic memory applications to store information.

SOFT MAGNETIC MATERIALS are a group of materials that lose magnetization when the magnetic field is removed. Their remagnetization takes place in a weak magnetic field with a value below 1kA/m ($\sim$ 12.5 Oe). They have a narrow hysteresis loop and are easily magnetized and demagnetized.

The shape of the hysteresis loops and magnetic parameters such as coercivity or squareness strongly depend on magnetic anisotropy; the stronger the anisotropy, the harder the material. In the case of nanowires, hysteresis loops measured with a magnetic field applied along nanowires and perpendicular to them show a clear difference, resulting from strong anisotropy (Fig. 4.4). However, the effective anisotropy can be significantly reduced due to the dipolar interactions, which in the extreme case (high membrane porosity = short inter-wire distances) can cause isotropic behavior because, as was mentioned, the dipole interactions contribute to the alignment of the magnetization vector perpendicular to the main axis of the nanowires. Consequently, strong dipolar interactions decrease the coercivity and remnant value (as well as squareness) [105] and are responsible for the appearance of steps on the magnetic curve called the Barkhausen effect [110, 111], which for a large number of closely spaced nanowires is manifested by the slope of the hysteresis loop.

4.3.1 Domain structure in nanowires

The domain structure is created in all ferromagnetic objects whose size is larger than the critical volume of a single domain, regardless of whether they are single crystals, polycrystals, or alloys. The process of domain formation depends on the shape and size of the magnetic object. If the size of domain walls constitutes a significant contribution in the sample volume, the energy cost to create a domain wall overcomes the advantages of domain formation and a single-domain structure (SD) is energetically more favorable.

The theoretically predicted critical size of nanostructures, below which the material forms a single domain is 100 nm. In the case of elongated nanostructures such as nanowires, a single-domain structure is expected in objects up to 50 nm in diameter, but this critical value may vary depending on the lengths and other nanowire parameters [105, 112, 113, 114, 115]. Samanifar et al. observed an SD structure in nanowires with a diameter of 175 nm and a transition from SD through a pseudo-single-domain structure (PSD) state (L = 22 to 31 µm) to a multi-domain (MD) structure for longer nanowires. A pseudo-single-domain structure is a state of gradual transition between SD and MD structures, characterized by intermediate values of magnetic parameters between the SD and MD states showing a gradual variation of squareness and coercivity instead of sharp changes [116]. The critical diameter decreases with an increase in the demagnetization factor, which occurs when the magnetic poles approach each other *i.e.* the length of nanowires decreases.

The critical radius (r_{sd}), below which each nanoobject in the form of a prolate ellipsoid has a single-domain structure is expressed by the function:

$$r_{sd} = \sqrt{\frac{6A}{N_c M_s^2}[ln(\frac{2r_{sd}}{\alpha_1}) - 1]} \tag{4.22}$$

where N$_c$ is the demagnetization factor along the major axis, and α_1 is the near-neighbor spacing [cm] [88, 117]. Calculations of Sun et al., performed based on the above equation show that, assuming L/ϕ = 10, the critical diameter for a single-domain structure would be 600 nm and 140 nm for Ni and Fe (or Co) nanowires.

Geometric confinement that occurs in nanowires results in the formation of other kinds of domain walls: transverse (TDW) and vortex (VDW), which belong to a new category of magnetic boundaries [108, 118]. In the case of TDW, magnetic moments rotate transverse to the nanowire length (a significant component of magnetization is along a direction transverse to the wire), while the vortex is a configuration of magnetic moments with cylindrical symmetry (curling of magnetization vector around the axis). The vortex domain wall is called according to other reference as a Bloch point DW [5, 91, 92, 93, 119]. The type of domain wall in nanowires is mainly determined by geometric parameters.

In nanowires with small diameters (10 - 50 nm), which reach the minimum internal energy in the domain structure, a transverse DW is created, while in nanowires with larger diameters (above 100 nm) the vortex domain wall is favored. In some interval diameter (between transverse and vortex DW), both types of DW can coexist although their energies are substantially different (with the minimum energy state of TDW) [5, 91]. According to Moreno et al., the critical diameters that separate the mentioned domain wall regimes are characteristic of each material [34], however, Bruno maintains that domain wall structure is almost independent of material parameters [108]. Besides the domain type, the nanowire diameter also influences domain wall width (δ_{DW}), which as shown by Parkin et al. scales approximately with the nanowire diameter [5, 8] and is always larger than the diameter of the nanowire for both types of DW [91]. Moreover, Moreno et al. also showed in their simulation that, in the case of TDW, the width of the domain wall increases linearly with the nanowire diameter (with deviation only for very narrow NWs) and decreases with increasing M$_s$ (in the absence of a strong magnetocrystalline anisotropy). In the case of infinitely long and narrow nanowires, the domain wall width (δ_{DW}) can be described by:

$$\delta_{DW} = \pi\sqrt{\frac{2A}{\mu_0 M_s^2 N_a}} = \pi\sqrt{\frac{4A}{\mu_0 M_s^2}} \tag{4.23}$$

where N$_a$=1/2. However, for larger diameter (VDW regime), contradictory relationships between M$_s$ and δ_{DW} are observed [93, 118].

The domain wall is also determined by the nanowire length. Samanifar et al. found VDW in nanowires with a length of up to 22 µm and noticed a transition from VDW to TDW for longer nanowires [105].

The wall type influences the nanowire properties, for example, the nanowires with TDW are characterized by higher coercivity [120] than the materials with VDW, while nanowires with VDW show higher mobility, than TDW, which makes them useful for high frequency applications [121].

4.3.2 Pinning and dynamics of domain wall

Domain walls are usually formed in the so-called pinning sites, which not only determine the domain length but also ensure the stability of the domain walls and their resistance to external disturbances such as magnetic field, thermal fluctuation, or stray currents [5]. The presence and type of the pinning sites decide on the magnetic response of the system, which is reflected in the coercivity value. The pining strength depends on the type of DWs and their chirality [5]. Besides the natural pinning sites (point and line defects, grain boundaries, surface roughness, strains) [122] there are also artificial methods of forming pinning sites such as the creation of notches and anti-notches, controlled diameter change or material composition modification along the nanowires [5, 7, 123, 124, 125, 126]. The pinning sites where the magnetic domain boundaries are created protect them against undesired drift, but should also enable the domain walls to move. The applying of a uniform external magnetic field could cause domain walls to move, but it cannot be used to shift the series of domain walls in the same direction and as a consequence would lead to domain annihilation [5]. The applying non-uniform local magnetic field cannot be used in the 3D matrix of nanowires. In this case, a unique solution to achieve a controlled domain wall movement is applying a pulsed current with an accurate magnitude and duration of pulses. This allows the domain walls to be moved with the velocity from 100 m/s [8] to even 1000 m/s [7] However, the Walker breakdown effect, also known as the Walker limit, appears above some velocity threshold [127]. This effect is related to the introduction of a periodic contribution (connected with the precession motion of the magnetic moment) to a steady domain propagation, which leads to oscillatory DW propagation. Thus, the DW dynamics alters and at a velocity of several hundred meters per second it is almost impossible to displace the domain walls in a simple way to a well-defined position [7]. This grave problem is suppressed in nanowires with cylindrical geometry [7, 91], in which VDW turned out to be stable even at a velocity of 1000 m/s. However, such a high velocity requires a high current density, which results in a temperature increase because of Joule heating, hence the critical value of current density indicates a maximum velocity of the domain wall rather close to 100 m/s, which is large enough for race track memory applications [5, 128]. Other surface-induced effects such as Dzyaloshinskii-Moriya (associated with curvature-induced interactions, favoring perpendicular orientation of neighboring moments across DW with rotation of the magnetization along a local vector-spiral spin structure [129] and Cherenkov effect (connected with spontaneous emission of a spin density wave from a spin wall moving with the velocity equal to the minimum spin wave phase velocity [7]) can be omitted for considered nanowire diameter larger than few nanometers [92].

The production of nanowires with segments showing various chemical compositions creates the boundaries, which can become domain wall pinning sites, meeting the criteria required by race trace memories in the 3D approach.

4.3.3 Magnetization reversal mechanisms

In the absence of an external field, the magnetization vector in a single-domain structure orients along the easy axis direction, whereas in the multi-domain structure with zero or remnant net magnetization value, the domain magnetization vectors assume the directions minimizing their internal energy. Applying an external magnetic field causes, the magnetic moments to rotate toward its direction. The mechanism of the switching process (reversal mechanism) depends on the magnetic structure of the sample (single/multi-domain), its geometry, the kind of materials (soft/hard), the domain wall type (transverse/vortex) and, of course, the mutual orientation of the external field and the magnetic easy axis and many others factors such as structure, sample volume, chemical composition, presence of the pinning sites (grain boundaries and other defects), etc.

There are two basic reversal modes: coherent rotation (CR) of magnetic moments (the Stoner-Wohlfarth model) and domain nucleation and domain wall motion (the Kondorsky model) [130, 131].

The shape of the hysteresis loop is a primary indicator of the reversal mode. Experimentally, the reversal mechanism is determined based on the angular dependence of the coercivity field, since different switching modes give various coercivities.

The coherent rotation mode is the fast uniform rotation of magnetic moments observed in single-domain objects with uniaxial anisotropy that are smaller than the critical diameter (function 4.22). In such a case, the angular dependence of the coercivity field is described by the Stoner-Wohlfarth model, in which H$_c$ decreases monotonically as a function of θ, where θ is an angle between the easy axis and the external field direction (Fig. 4.5, 4.7). Depending on the θ, two regions can be distinguished.

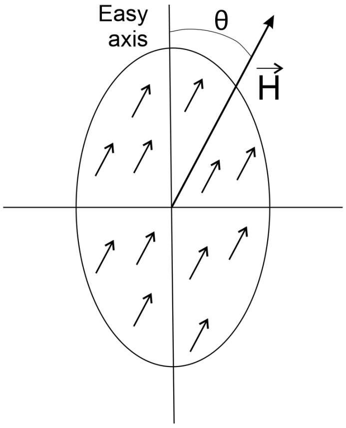

Figure 4.5: Relationship between magnetization vector and external magnetic field in a single-domain particle with an elongated shape.

In the first range, when $0^o < \theta < 45^o$, the coercive field (H$_c$) coincidences with the switching field (H$_{SW}$) [133] and is expressed by:

$$H_c^{CR}(\theta) = H_{sw}(\theta) = H_K(cos^{2/3}\theta + sin^{2/3}\theta)^{-32} \tag{4.24}$$

where H$_K$ is an anisotropy field (H$_K$ = 2K$_u$/(μ_0M$_s$)). In this range, the magnetization curve is infinitely steep at the coercive field. In the second range, when $45^o < \theta < 90^o$:

$$H_c^{CR}(\theta) = (H_K/2)sin2\theta \tag{4.25}$$

and switching occurs only when the magnetization changes sign [131].

Besides coherent rotation, uniaxial magnetic systems with a single-domain structure can switch magnetically by domain nucleation and domain wall motion. This process is illustrated in Fig. 4.6. If a magnetic field is applied to the system in the direction opposite

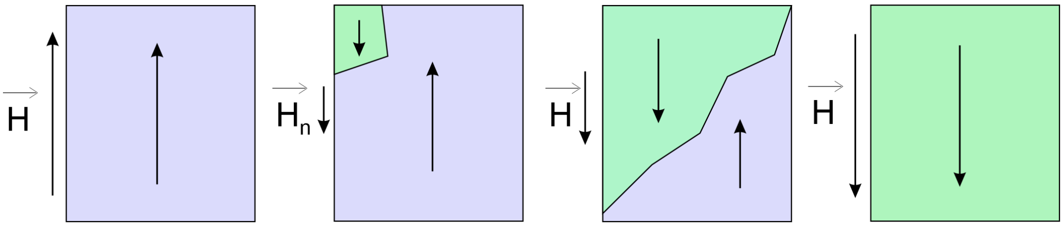

Figure 4.6: Model of the magnetization reversal by nucleation and domain wall motion in a uniaxial single-domain structure. The subsequent schemes show the structures of SD, PSD, MD, and SD.

to its magnetization, a small domain will be created with the magnetization oriented along the external field. The value of the magnetic field at which this small domain appears is called the nucleation field (H_n). As the external magnetic field increases, the domain wall moves, increasing the area of the domain oriented along the applied field.

In the case of multi-domain structures, the magnetization reversal process occurs through the domain wall movement. Applying an external magnetic field causes the domains with magnetization vector close or parallel to the field direction to expand, which results in the diminishing of the adjacent domains that are not oriented along the external field. Magnetic reversal modes involving domain wall movements are strongly dominated by DW pinning, described in the previous section.

The processes of domain nucleation and domain wall motion are slower than coherent rotation. They are described by the Kondorsky model, in which the coercivity H_c^{Kon} (θ) increases monotonically as a function of the angle (Fig. 4.7) and is expressed as follows:

$$H_c^{Kon}(\theta) = \frac{H_c^{Kon}(0)}{cos\theta} \tag{4.26}$$

where $H_c^{Kon}(0)$ is a coercivity along the easy axis. However, this expression diverges at angles close to $\theta = 90^o$, which is a consequence of the assumption that the magnetization vector does not rotate away from the anisotropy axis, regardless of the field angle and field strength [131]. Moreover, in real samples, structural defects generate pinning sites that hinder the domain wall movements and affect the angular dependence of the coercive field. This is responsible for the observed discrepancies between model and experimental results. Additionally, in certain conditions, domain wall motion and domain rotation can occur simultaneously in the same part of the sample [132]. Thus, attempts to create the model describing magnetization reversal in real multi-domain structures led to a new modified Kondorski model, which takes into account the reversible rotation of magnetization vectors in neighboring domains [134, 135, 136]. The angular dependence of coercivity in this model shows a strong increase in H_c with increasing angle, followed by a sharp coercivity decrease at angles close to the hard axis direction. Thus, the modified Kondorsky model begins with the depinning of the domain wall, analogous to the Kondorsky model, and then with increasing field, domain switching is not abrupt but determined by the gradual displacement of DWs [131]. This model combines the mechanism of domain wall motion with a coherent rotation of magnetic moments (Fig. 4.5). The angular dependence of the coercive field in the modified Kondorski model is described as:

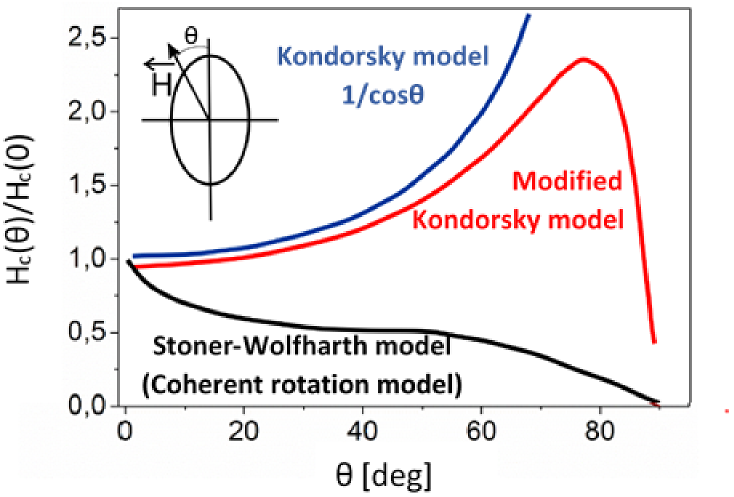

Figure 4.7: Angular dependences of coercivity H$_c(\theta)$ corresponding to the magnetization reversal mechanisms described by the Stoner-Wohlfarth, the Kondorsky, and the modified Kondorsky model.

$$H_c^{MKon}(\theta) = H_c(0)\frac{(N_a + N_N)cos\theta}{N_c sin^2\theta + (N_a + N_N)cos^2\theta} \tag{4.27}$$

where N$_c$ and N$_a$ are the demagnetizing factors of the prolate ellipsoid (along the c and a axis), and N$_N$ is a parameter interpreted as an effective demagnetizing factor due to the effect of magnetocrystalline anisotropy [131]. The modified Kondorsky model accurately describes different systems, such as ferromagnetic alloys, films of magnetic alloys, and multilayer thin films exhibiting perpendicular magnetic anisotropy [131].

Using the models described above, based on the angular dependencies of the coercive field (H$_c$), it is possible to determine the reversal magnetization mechanism of the sample (Fig. 4.7).

In such case of a single domain structure, the magnetization switching is modeled by coherent rotation (Fig. 4.8 a) or curling mode (Fig. 4.8 c) depending on the nanowire diameter [88, 117]. The curling mode is observed in single-domain structures, in which the magnetization reversal is non-uniform. One can also distinguish buckling mode, appearing in samples with a high aspect ratio. This mode is expected at the transition between coherent and curling mode and, because of its minor significance, is usually omitted from discussion (Fig. 4.8 b).

The curling mode appears when the nanowire diameter is larger than the critical value ϕ_c (still in the single-domain regime), which for a prolate ellipsoid with an external field parallel to the long axis is expressed by [88, 137]:

$$\phi_c = q\sqrt{\frac{8A}{N_a M_s^2}} = 2.08\sqrt{\frac{A}{M_s^2}} \tag{4.28}$$

where q is a geometrical parameter equal to q = 1.8412 for nanowires. The critical diameter calculated for Fe, Co, and Ni are equal to 12 nm, 15 nm, and 27 nm, respectively

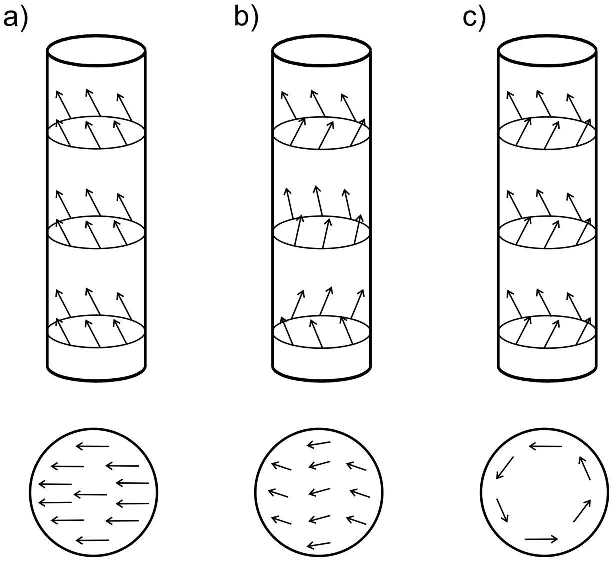

Figure 4.8: The reversal magnetization mechanism observed in nanowires: (a) coherent rotation, (b) buckling, and (c) curling mode.

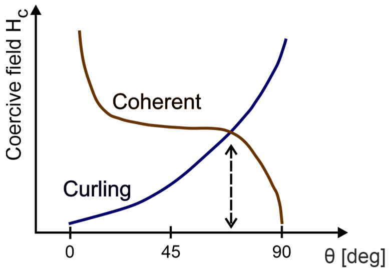

Figure 4.9: Angular dependence of coercivity in nanowires coherent and curling modes [88, 137].

[138].

In the curling mode, the rotation of the magnetic moments is abrupt, thus, $H_c = H_{sw}$, and both quantities depend on L/ϕ and the size of the ellipsoid. The angular dependence of coercivity for a prolate ellipsoid in the curling mode is expressed by [88]:

$$H_c = 2\pi M_s \frac{(2N_c - \frac{3.39A}{\pi r^2 M_s^2})(2N_a - \frac{3.39A}{\pi r^2 M_s^2})}{\sqrt{(2N_c - \frac{3.39A}{\pi r^2 M_s^2})^2 sin^2\theta + (2N_a - \frac{3.39A}{\pi r^2 M_s^2})^2 cos^2\theta}} \tag{4.29}$$

where r is the nanowire radius, and θ is the angle between the external magnetic field and the magnetic easy axis. According to the curling model, based on calculations performed for $\theta = 0$ with the expression 4.29, one predicts a significant increase in coercivity with decreasing nanowire radius ($H_C \sim 1/r^2$).

In the coherent model, coercivity (H_c) increases with increasing angle (θ), while in the curling mode the opposite behavior with increasing H_c as a function of θ is observed. The angular dependence of the coercive field for coherent rotation and curling mode is shown in Fig. 4.9.

The models described can only be used as a first approach to study the reversal mechanism in nanowires, which usually are not single domain structures, which complicates their switching mode.

In multi-domain structures, a vortex or transverse domain wall propagation may occur. The shape of the transverse reversal mode is similar to the coherent rotation transient but has a much lower coercivity value, which makes this reversal mode energetically more favorable. In the vortex domain wall mode, the coercivity continuously increases with increasing angle. The most frequently observed behavior of the coercivity as a function of angle in nanowire arrays is an initial coercivity increase and then a decrease with increasing angle. This non-monotonic variation of the angular dependence of coercivity may indicate the transition between vortex and transverse domain wall propagation modes [165]. Another possible combination is the transition between vortex domain wall propagation to the coherent rotation, which switches the magnetic moments in the final stage of the reversal process when the angle of the magnetic moments is close to the hard direction [168].

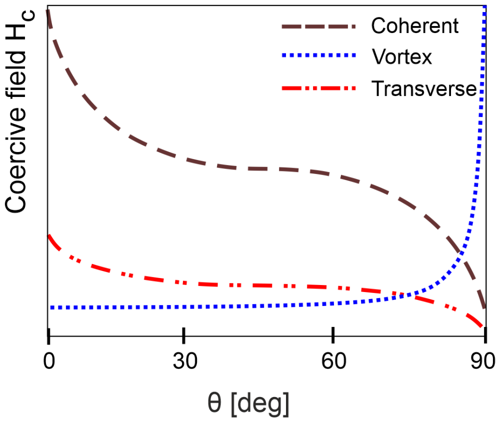

Figure 4.10: Calculated angular dependence of coercivity for nanowires [165]

To examine the magnetization reversal modes, the equations of the angular dependence of the nucleation field for coherent [$\mathrm{H}_n^{Coherent}(\theta)$], transverse [$\mathrm{H}_n^{T}(\theta)$], and vortex [$\mathrm{H}_n^{V}(\theta)$], modes are needed:

$$\frac{H_n^{Coherent}(\theta)}{M_s} = -\frac{1-3N_c}{2}\frac{\sqrt{1-t^2+t^4}}{1+t^2} \tag{4.30}$$

$$\frac{H_n^{T}(\theta)}{M_s} = -\frac{1-3N_a}{2}\frac{\sqrt{1-t^2+t^4}}{1+t^2} \tag{4.31}$$

$$\frac{H_n^{V}(\theta)}{M_s} = \frac{(N_c - \frac{q^2L_x^2}{R^2})(N_a - \frac{q^2L_x^2}{R^2})}{\sqrt{(N_c - \frac{q^2L_x^2}{R^2})sin^2\theta_0 + (N_a - \frac{q^2L_x^2}{R^2})^2cos^2\theta_0}} \tag{4.32}$$

where t = $\tan^{1/3}(\theta)$ [105, 165, 168, 169].

Chapter 5

Structural and magnetic properties of the Fe, Co, Ni elements and their alloys - literature review

5.1. Magnetic and structural properties of Fe, Co, Ni

Fe, Co, and Ni belong to the group of transition metals (d block) with an incompletely filled d subshell, which is responsible for their ferromagnetic character. Table 7 compares the structural and magnetic properties of bulk Fe, Co, and Ni (or nanowires). As can be seen, these three ferromagnetic elements are significantly different from each other, despite their adjacent positions in the periodic table. They crystalize in different structures with various lattice parameters and atomic radii. In the case of nanowires, Fe and Ni grow in bcc and fcc structure, respectively, while Co depending on pH, may grow in bcc or hcp structure as was mentioned in chapter 3.1.

These elements also show different magnetic parameters. The magnetic moment is greatest for Fe and smallest for Ni. The same relationship is observed for the coercivity measured for nanowires with a diameter from 10 to 20 nm and length from 400 nm to 1 µm [180]. The maximum coercivity achieved at room temperature for Fe, Co, and Ni nanowires is 3000, 2600, and 950 Oe, respectively [180].

The difference in the crystal structure of Fe, Co, and Ni affects the magnetocrystalline anisotropy, which is reflected in changes in the easy and hard axis directions (Fig. 5.1). The easy axis in iron and nickel cubic structures are [100] and [111], respectively, while in the case of cobalt crystallizing in a hexagonal structure, the easy axis lies along the c-axis.

The combination of the above elements in the form of binary or ternary alloys with various concentrations enables the design of materials with desired magnetic properties suitable for applications.

Table 5.1: Selected physical parameters of Fe, Co, and Ni.

Parameter	**Iron**	**Cobalt**	**Nickel**
Atomic number	26	27	28
Electron configuration	$3d^64s^2$	$3d^74s^2$	$3d^84s^2$
Atomic radius [A]	1.72	1.67	1.62
Allotropic form	body centered cubic (bcc)	hexagonal lattice (hcp)	face centered cubic (fcc)
Lattice parameter [nm]	a = 0.286	a = 0.251 c = 0.407	a = 0.352
Easy axis	[100]	<0001>	[111]
Difficult axis	[111]	<1010>	[100]
Melting temperature [°C]	1535	1495	1455
Density [g/cm^3]	7.9	8.9	8.9
Curie temperature [°C]	770	1115	354
Magnetic moment [µB/atom]	2.22	1.72	0.61
Saturation magnetization M_s [emu/cm^3]	1707	1400	485
Coercivity H_c [Oe]	1100	1000	350
Maximum coercivity for nanowires H_c [Oe]	3000	2600	950

5.2. Binary systems Fe-Co, Fe-Ni

Iron-Cobalt (Fe-Co)

The phase diagram of the Fe-Co system is presented in Figure 5.2 [139]. Below the liquidus line (app.1500°C), there are five FeCo phases depending on the alloy composition and temperature. At lower temperatures (closest to room temperature) bcc (α (A2), α' (B2)), and hcp (ϵ(A3)) structures appear as the Co content increases. The fcc (γ (A1)) structure is stable only at higher temperatures (above app. 150°C in the case of Co-rich alloys. An Fe-rich alloy (not less than 90%) crystallizes in a disordered solid solution of Co in Fe bcc (α). At Fe concentration ranging from 20 to 90 at.% ordered FeCo alloy with a bcc structure (B2 - CsCl type) appears in the mixture with adjacent phases. In contrast, in Co-rich alloys a solid solution of Fe in Co hcp with limited Fe solubility to 3% can be observed. At higher Fe concentration (3-20 at.%), a mixture of B2 and A3 phases occurs.

Chemical composition modification and the resulting changes in the FeCo nanowire structure can, obviously, be achieved by the appropriate selection of the electrolyte

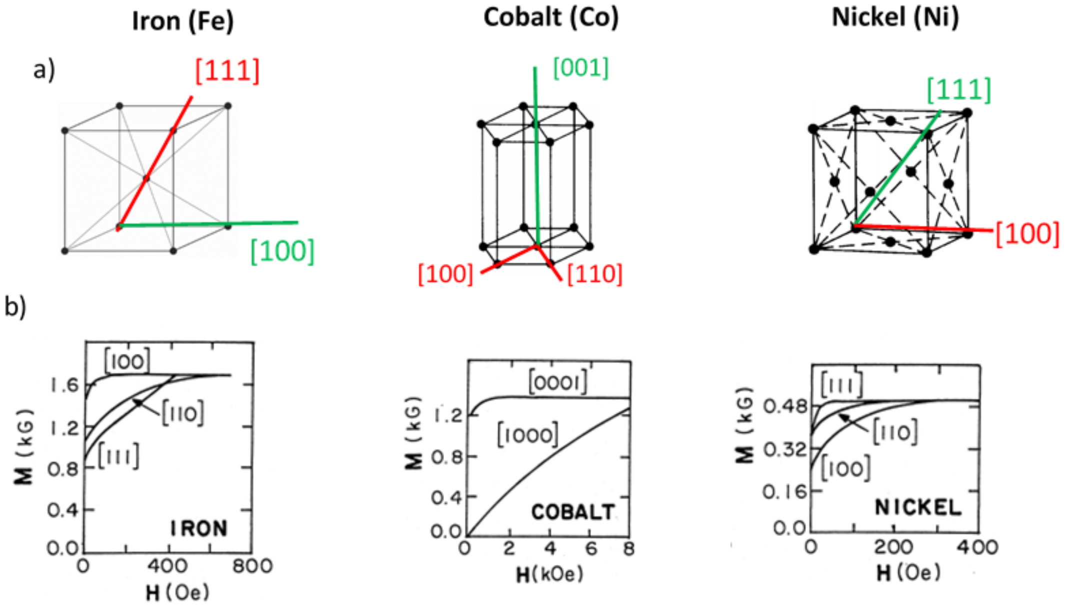

Figure 5.1: (a) Orientation of the easy (green) and hard (red) axes of magnetization in Fe bcc, Co hcp, and Ni fcc structures, (b) magnetic curves measured with a magnetic field applied along different crystal axes [87].

composition, as well as the manipulation of electrodeposition parameters such as temperature, pH, and applied potential and also by electrodeposition type [81, 158]. At low temperatures, the growth of the (110) FeCo planes is energetically more favorable than the growth along the [100] and [111] directions [149]. Additionally, an increase in electrodeposition temperature leads to the polycrystalline structure formation [149]. No less important is the pH, which, based on the results obtained on studies of Co nanowires, should promote the fcc or hcp structure at low (2.4 - 2.7) or high pH (5.0 - 6.4), respectively [31, 65, 67, 68]. The other important parameter is the applied potential, which may lead to an increase in the Fe content with increasing potential or, depending on the electrolyte composition, may not affect the chemical composition of the nanowires [158]. In general, FeCo nanowires show a rather weak dependence on the applied potential [41]. Moreover, in the FeCo alloys, anomalous co-deposition is observed, in which less noble Fe metal is preferentially deposited. However, this anomalous behavior is weak and exhibits a selectivity ratio in the range of 1.4 - 1.5, which values are close to normal deposition [41].

The magnetic character of FeCo alloy is determined by the Tc line that varies with the Fe content. As can be seen, changes in the chemical composition lead to the structural modification of FeCo alloy. These structural modifications induce changes in the magnetic properties. Literature studies show that an increase in Co content results in greater coercivity and squareness [81, 82, 149, 157], but these changes are strongly dependent on the nanowire diameter [140]. However, H_c and M_r/M_s decrease with the appearance of the Co hcp phase (especially in the single-crystalline sample), which exhibits strong magnetocrystalline anisotropy along the c-axis, which aligns perpendicular to the NW axis. The magnetocrystalline anisotropy constant (K_1) of hcp Co is approximately 10 times higher than that of cubic CoFe alloys [82]. Therefore, in the case of hcp structure with high Co-content and pure Co nanowires, the coercivity and squareness decrease

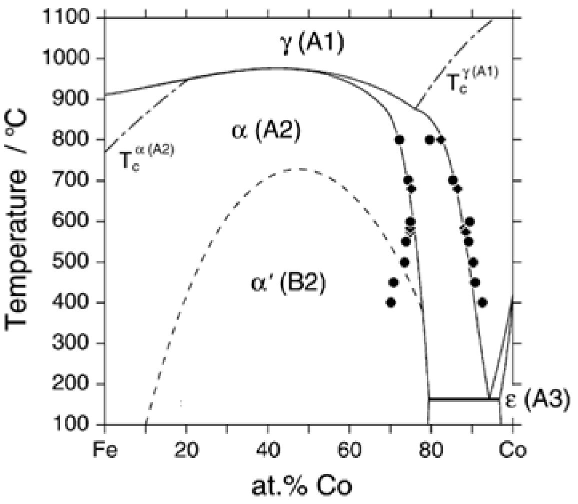

Figure 5.2: The phase equilibrium diagram of FeCo system [139].

compared to Fe-rich nanowires [81, 140]. These magnetic parameters are obviously affected by nanowire geometry. The decrease in the nanowire diameter results in an increase in the coercivity and squareness of nanowires taken from the loops measured with a magnetic field applied along nanowire axis [82, 140, 158], however, the observed changes depend on the nanowire composition. An increase in the nanowire length above an aspect ratio of 10 no longer increases the shape anisotropy contribution, but causes an increase in dipole interactions, which are responsible for the decrease in the coercivity and squareness with increasing nanowire length [33, 41, 110, 141, 142, 158]. The chemical composition and geometry of nanowires influence the reversal mechanism, which can switch from coherent rotation to curling mode at different nanowire diameters (such as 10 nm or 40 nm), depending on the FeCo nanowire composition [140, 158].

Iron-Nickel (Fe-Ni)

Figure 5.3 shows the phase equilibrium diagram of the Fe-Ni system. At higher temperatures, the fcc structure of the Îł-FeNi phase with unlimited solubility is stable. Additionally, directly below the liquidus line at high Fe concertation, the $\delta-$Fe phase occurs (a high-temperature solid solution of Ni in the Fe bcc structure). The most interesting part of the diagram at low temperatures shows the various phases that appear as the alloy composition changes. At high Fe concentrations, $\alpha-$Fe (a solid solution of Ni in Fe bcc structure) disordered phase is observed, while at higher Ni concentrations, the fcc-based structure dominates. The disordered structure A1 transforms into ordered L12 and L10 structures with atom arrangement shown in the unit cells (Fig. 5.3). In the indicated limited concentration ranges, substitutional structures Fe_3Ni, FeNi, and $FeNi_3$ appear. In the concentration regions between these specified areas, the mixture of neighboring phases is stable. The Fe_3Ni (L12-type) structure called the Invar alloy is characterized by a low or even negative value of the thermal expansion coefficient. FeNi (L10-type) called Elinvar alloys are known for their unique elastic properties with negligible thermal expansion and constant elasticity modulus over a wide temperature range. The most known ordered L12-FeNi$_3$ alloy called permalloy (20 at.% Fe) is a soft magnetic material (low coercivity) characterized by high magnetic permeability, low value of magnetic anisotropy, significant remnant magnetization, and near zero magnetostriction. In the Ni$_3$Fe phase, each Ni atom has 4 Fe neighbors and 8 Ni neighbors. Fe atoms are located at the corners, while Ni atoms are on the walls of the unit cell.

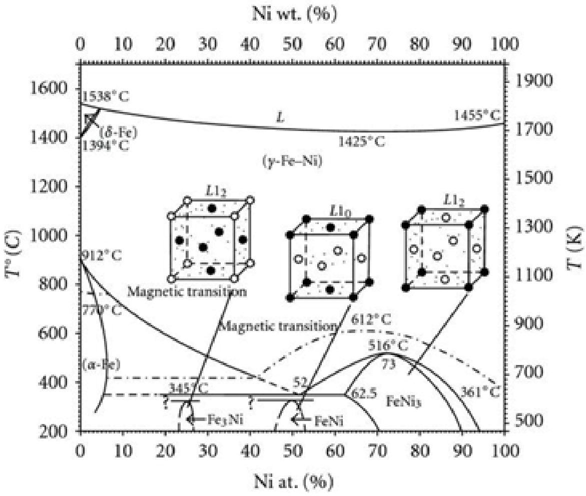

Figure 5.3: Fe-Ni phase equilibrium diagram [143]. L is the FeNi liquid solution. The presented crystal structures of the three stoichiometric ordered phases (at T = 0): L12 − Ni$_3$Fe (Permalloy), L10 − NiFe (Elinvar), and L12 − NiFe$_3$ (Invar), where ○ - Ni, ● - Fe.

The ferromagnetic character of FeNi alloys is determined by the Curie temperature, which increases significantly in the permalloy concentration range. Compared to Fe/Co, FeNi alloys exhibit different behavior in many respects. As in the case of FeCo NWs, the same dependence of coercivity and squareness is observed as a function of nanowire geometry [144], but an increase in both parameters with increasing nanowire length was also observed [41]. This unexpected behavior was explained by the inhomogeneity of FeNi nanowires along the growth direction with the formation of Fe-rich FeNi alloy on the top of the nanowires. Inhomogeneity was also observed by other groups [148, 159], but depending on the applied potential and other parameters, the elemental composition shows a different distribution [148], or does not reveal significant changes [144]. The increase in diameter favored multi-domain structure and impacted the reversal mechanism that switches from coherent to curling mode [144].

Unlike the FeCo nanowires, the chemical composition of FeNi nanowires can be easily modified by applied potential [41, 85]. The increasing cathodic voltage causes an increase in the Ni content with a simultaneous decrease in the Fe concentration [41, 85, 148, 159], except for a small potential range (-0.9 V − -0.1 V), in which opposite relationship occurs [148]. Moreover, this alloy shows strong anomalous behavior, even more visible in nanowires compared to thin films [148], with a high selectivity ratio [41]. The applied potential usually affects the grain size resulting in their reduction at more cathodic potentials [85, 159]. In the all concentration range the fcc structure dominates [85, 159], however depending on the Ni content, the ordered alloys such as permalloy or other solid solutions can appear. Besides the fcc structure, the bcc crystals can also be found [41, 144].

The changes in the chemical composition affect the magnetic properties of nanowires, in which an increasing potential (increase in Ni content), depending on the diameters of nanowires, causes the increase [159] or decrease in the coercivity and squareness, however non-monotonous behavior, related probably to the ordered phase formation, can also be observed [85].

5.3. Ternary system Fe-Co-Ni

The phase equilibrium diagram of the FeCoNi system presented at a temperature of 293 K is shown in Fig. 5.4. Depending on the composition, four different phases can be distinguished. The $\alpha-$Fe phase appears in Fe-rich alloys with an Fe content above 97%. On the contrary, the γ-Ni phase is observed in almost the entire Ni content range. Co-based alloys in the form ϵ-Co phase occupy the smallest area in a narrow concentration range. Apart from the mentioned disordered solid solutions, in all other concentration areas the ordered Ni_3Fe phase occurs as a single phase or in a mixture with the above solid solutions. At the higher temperature of 600^{o}C (not shown), the system exhibits only three phases, without permalloy [154].

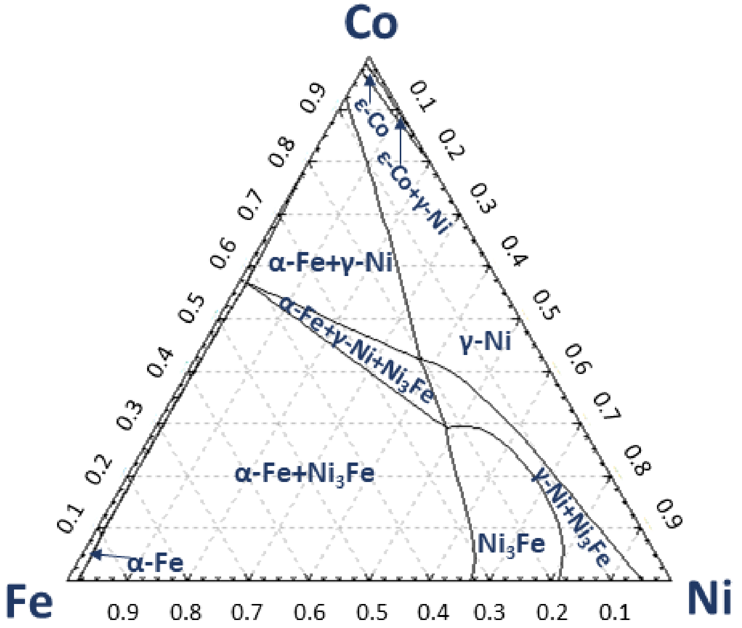

Figure 5.4: Ternary phase diagram of the FeCoNi system – isothermal cross-section at 293 K generated using the FactStage package and the SGTE database.

The content of individual elements in the material significantly affects its magnetic properties, as observed in FeCoNi thin layers [20, 21, 81, 105, 145, 146]. The desired chemical composition can be achieved by appropriate electrolyte selection and adjustment of the electrodeposition parameters. Changes in the applied potential can modify the chemical composition of the nanowires, leading to the variation of the magnetic parameters. Sarac et. al. studied the effect of the applied potential on the properties of FeCoNi thin films and noticed that as the potential became more cathodic, the Co content decreased and the Ni content increased (non-monotonous changes in Fe concentration) leading to a decrease in the coercivity value, which made the materials softer magnetically [147]. A similar relationship between the applied potentials and the chemical composition was observed by Hanafi et. al., with a difference that increasing the potential caused a decrease in the Fe content. However, the increase in potential resulted in greater coercivity, contrary to Sarac's results [52]. The impact of a potential change was also studied by Budi et. al., who found the same correlation as Hanafi et al. both in terms of chemical composition and magnetic parameter changes [20]. Changes in the magnetic properties induced by modification of the chemical composition of alloys due to cathodic potential variation result from differences in the values of magnetic moments for these elements ($m_{Fe}>m_{Co}>m_{Ni}$) [20].

Despite many studies on FeCoNi thin layers, only a few works regarding the properties of FeCoNi nanowires deposited into the porous matrix can be found in the literature. Except for one, all the others report the studies of nanowires prepared in alumina membranes and show the changes in the magnetic properties of FeCoNi wires as a function of annealing, nanowire geometry [105, 107, 152, 153] or describe the possibility of the modification their geometry or morphology [50, 61, 156]. In general, an increase in the diameter and length of the nanowire matrix results in a decrease in the coercivity and squareness and causes the magnetic structure to change from SD through PSD to MD as well as transition from VDW to TDW, modifying the reversal mode [105, 107]. Other works show the influence of the electrodeposition parameters (cathodic potential, AC frequency) on the chemical composition of nanowires [86, 153]. In the case of nanowires deposited at various cathodic potentials, the selected electrolyte did not reveal any visible differences in the composition of the nanowires, therefore their magnetic parameters, such as coercivity or squareness, also did not change significantly [86]. On the other hand, Sharma et al. in their studies of AC frequency influence on the chemical composition, indicated that significant changes in the chemical composition and the resulting modification of the magnetic properties can only be achieved for a well-selected electrolyte. So far, no work has been performed examining the structural and magnetic properties of FeCoNi nanowires as a function of the chemical composition varied by the cathodic potential.

FeCoNi ternary alloys are the main subject of this work. This system is gaining increasing interest among scientists, especially due to its unique magnetic properties, which allow for applications of FeCoNi films as anti-corrosion, or anti-reflective coatings, MEM systems or memory units [20, 145, 146, 151, 154, 155]. As shown, intensive studies have mainly focused on coating and thin films, and only a few works regarding FeCoNi nanowires were found [50, 61, 81, 86, 105, 152, 156].

Chapter 6

Materials and methods

6.1. Electrodeposition parameters

Before the nanowire deposition, the thin contact layer (copper or gold) was sputtered on one side of the templates to close the pores and act as a cathode. The electrodeposition processes were performed in an electrochemical cell in a three-electrode system as presented in Fig. 2.1 (Chapter 2). PC and AAO membranes were used as templates (as described in Table 2.2) (Chapter 2.2).

The deposition processes were controlled using an AUTOLAB PGSTAT302N potentiostat operating in potentiostatic mode with different values of cathodic potential. The deposition was carried out in an electrolyte bath containing $FeSO_4$, $CoSO_4$, $NiSO_4$ ions and their mixture (Table 6.1) with the addition of boric acid (to stabilize pH extending the region of proton reduction to more negative potentials and avoiding metal hydroxide precipitations) [160] and ascorbic acid (to prevent against iron oxidation by residual oxygen). The deposition temperature was 20^{o}C (except for iron samples studied as a function of the electrolyte temperature), and the applied voltage varied as shown in Table 6.1. Additionally, the FeCoNi flat samples with a thickness of approximately 10 µm were prepared on the thin copper foil to compare the properties.

Table 6.1: Concentrations of electrolytes used to produce nanowires.

Nanowire	Concentration [g/dm^3]						pH	Applied potential [V]*
	$FeSO_4$	$CoSO_4$	$NiSO_4$	$CuSO_4$	$C_6H_8O_6$	H_3BO_3		
Fe	55.6	-	-	-	1	24.72	2.9	-1.1
Co	-	33.73	-	-	-	24.72	2.8	-1.0
Ni	-	-	44.71	-	-	24.72	3.2	-2.0
FeCo	2.78	5.62	-	-	1	24.72	2.8	-1.0, -2.0
	16.68	33.73						
FeNi	2.78	-	44.71	-	1	24.72	3.2	-1.0 ÷ -2.0
FeCoNi	2.78	5.62	44.71	-	1	40.0	3.0	-1.0 ÷ -1.8
FeCoNiCu	2.78	5.62	44.71	0.26	1	40.0	3.6	
				0.53				

* All potential values given in this work refer to the Ag/AgCl (3 M KCl) electrode.

6.2. Cyclic voltammetry

Cyclic voltammetry (CV) is a popular and often-used electrochemical technique to examine electrochemical reactions, such as reduction and oxidation processes of molecular species. It quickly provides information on the thermodynamics of redox processes, as well as on the kinetics of heterogeneous electron transfer reactions. Cyclic voltammetry is usually the first experiment performed in electroanalytical research. In this experiment, an applied, cyclically varying voltage causes a current response creating a cyclic voltammogram. Typically, the measurement starts at potential 0 and then moves towards negative values, followed by the reverse scan. Figure 6.1 shows a current transient as a function of cyclic voltage changes. Two important parts can be distinguished in this curve. The first is measured when the voltage changes towards negative values (1-2-3), which results in a negative current in response. This is the cathodic part of the curve informing about the reduction process. The second part, measured when the potential moves towards positive values (3-4-1), gives a positive current and is called the anodic scan. This anodic part carries information about the oxidation process, which in the case of electrodeposition is directly connected with the dissolution of the deposit. This cycle can be repeated many times.

When a potential, changing towards negative values, is applied to electrodes immersed in the solution containing Me^+ ions, the Me^+ at the electrode is reduced to Me, resulting in a cathodic current signal. This is associated with a steady depletion of Me^+ near the electrode surface, which creates a diffusion layer, growing with the scan. This slows down mass transport. As a consequence, the lower M^+ ion diffusion rate causes a current decrease and the appearance of a maximum called the cathodic peak. During a reverse scan, an anodic current is generated as a result of the oxidation process, which in turn leads to the anodic peak formation and the mentioned dissolution of the previously reduced deposit [161]. The voltammogram allows for determining the potentials (E_p^c, Ep_p^a) and currents (i_p^c, i_p^a) at the cathodic and anodic peak positions as well as the peak-to-peak separation voltage ($\Delta E = E_p^a$- E_p^c), which is a distance between potentials at the peaks, and half potential parameter ($E_{1/2}$) defined as an average potential between maxima ($E_{1/2} = \Delta E/2$) (Figure 29). The half potential parameter is the point at which the concentrations of oxidized and reduced substances are equal and provides a simple way to estimate the standard potential (in the case of reversible reaction).

An essential quantity, related to CV measurements is the scanning speed of the applied potential (v), which determines the slope of the CV signal. As the scanning speed increases, the entire process will run faster and, consequently, the diffusion layer will form closer to the electrode. As a result, the flux onto the electrode surface will be greater, and since the current is proportional to the flux, the current peak will be higher at high scanning speeds (Fig. 6.1 b). In this case, the increasing scan rate value does not affect the position of the maximum that appears at a specific voltage value and does not change the shape of the curve but increases the total current value. This is a characteristic feature of electrode reactions showing fast electron transfer kinetics, *i.e.* reversible reactions.

There are four conditions for the reversibility of a reaction:

- the amplitudes of the anodic and cathodic peaks are equal ($i_p^c/i_p^a = 1$)
- peak-to-peak separation parameter assumes a constant value (ΔE = 58 mV) and does not depend on the scan rate

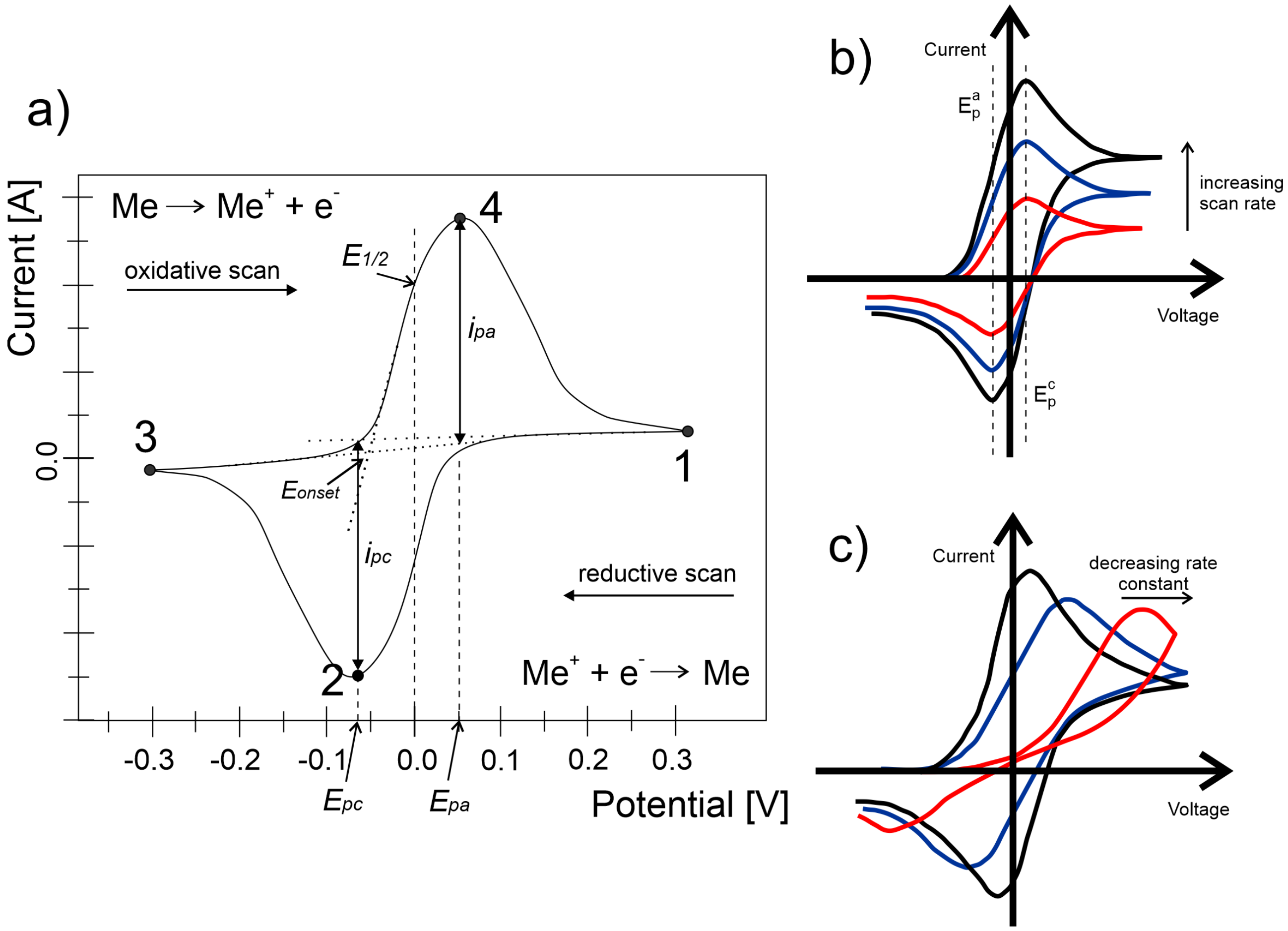

Figure 6.1: (a) Cyclic voltammogram diagram of reversible reduction, (b) series of voltammograms recorded when total current increases with increasing scan rate, (c) series of voltammograms recorded at a single voltage sweep rate for different values of the reduction rate constant [161].

- the peak position of half potential $E_{1/2}$ does not change with a scan rate
- the peak currents are proportional to the square root of the scan rate (i_p^c and $i_p^a \sim \sqrt{v}$).

Chemical reversibility informs that the reduced substance is stable and can be subsequently reoxidized, while electrochemical reversibility refers to the fast electron transfer, in which a low electron transfer barrier allows for equilibrium to be established immediately after a change in the applied potential [161].

If the current increases with the square root of the scanning rate, this indicates that the electrode response is controlled by mass transport (fast electron transfer). The concentration of a substance in the solution near the electrode changes with time according to the Nernst equation. The concentration of Me^+ ions as a function of distance from the electrode surface depends on the applied potential.

In irreversible systems (with slow exchange of electrons compared to mass transport), the individual peaks are reduced in size and far apart. Completely irreversible systems are characterized by a shift in the peak potential with the scanning rate. In quasi-reversible systems, the current is controlled by charge transfer and mass transfer. The voltammogram of quasi-reversible systems is very stretched and shows greater separation of peak potentials compared to reversible systems.

In the case of quasi-reversible or irreversible reactions, the slow electron transfer is about the voltage scanning speed. The electron transfer barrier is high and a more negative (positive) potential is required to observe the reduction (oxidation) reaction, which results in higher ΔE values. In a slow reaction kinetics, the equilibrium is established slower compared to the scanning rate. For this reason, the position of the peak maximum varies depending on the reduction rate constant because it takes longer for the current to respond to the applied voltage than in the reversible process [161]. As the rate constant decreases the peaks shift and the peak-to-peak separation parameter increases (Fig. 6.1 c).

Analysis of the shape and peak positions on the CV curve as a function of the scan rate allows us to determine the reaction mechanism with an indication of the process limiting the reaction rate. If the cathodic and anodic peaks are equal and close to each other, the process is limited by mass transport, which means that the electron transfer is fast and the reaction is reversible. In the opposite case, a slow electron exchange points out that the reaction is irreversible and is controlled by electron transfer. However, the process can also be more complicated, in such a case both charge transfer and mass transfer determine the reaction mechanism.

Cyclic voltammetry measurements, as well as nanowire deposition, were performed using the AUTOLAB PGSTAT302N potentiostat (Metrohm Autolab B.V., Utrecht, The Netherlands). CV was performed for electrolytes containing separate $FeSO_4$, $CoSO_4$, and $NiSO_4$ and also all of them in mixture (50 mM each) with boric acid and ascorbic acid in the potential window between -1.2 V and 0.0 V (or 0.2 V). The scan rate for single elements was 10 mV/s and differ from 10 to 160 mV/s for ternary system.

6.3. Electron microscopy (SEM, EDS, TEM)

Electron microscopy methods are the most often used to observe the material surface. In electron microscopy, electrons of primary beam are accelerated by applying voltage of the order of a few kV in the case of scanning electron microscope (SEM) or a few hundred or even thousand kV in transmission electron microscope (TEM). The basis of those methods is irradiation of the sample with an electron beam, which may results in electron scattering, absorption, and passage through the material. The signal emitted on the top of the sample is used in SEM while electron transmitted through the sample are measured in TEM.

The most relevant phenomenon in electron microscopy is scattering - interaction between the electron beam and atoms or electrons of a sample, whereby there is a change in the trajectory or energy of the beam. Scattering could be divided into elastic (change of beam trajectory and insignificant change of electron energy) and inelastic (substantial loss of electron energy and a slight change of beam trajectory).

Elastic scattering is the result of collisions of high-energy beam electrons with atom nuclei and consequently, there is a change in the trajectory of the electron. There are two mechanisms: low-angle elastic scattering which is the result of the Coulomb interaction with the electron cloud and high-angle elastic scattering is the effect of Coulomb interactions with the nucleus.

Scanning electron microscopy (SEM) is one of the electron scattering-based methods. It uses an electron beam to scan the surface of the material and detects the scattered signal.

The effect of elastic scattering is backscatter electrons (BSE). The ratio of the number of backscattered electrons to the total number of primary electrons increases with increasing atomic number of target elements and with increasing tilt and is marginally affected by the primary beam energy. The dependence of the BSE production on the atomic number enables the analysis of the chemical composition of the sample. As a consequence, the higher atomic number elements, the brighter the materials appears in the SEM image. In inelastic scattering, there is an energy transfer from the primary beam electrons to the target sample electrons or atoms resulting in an X-ray emission, electron emission and cathodolumienscence.

For different sample depths, a different effect from electron interactions prevails (Fig. 6.2).

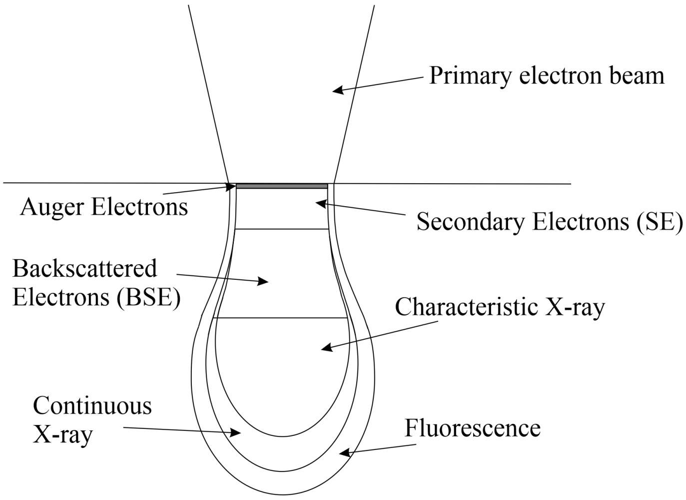

Figure 6.2: Scheme showing the interaction of an electron beam with a sample.

Near the surface, about 10 Å, the Auger process prevails. In this effect the electron from the incident beam ejects electron out of the inner shell, leaving a hole. The electron from the higher shell fills the gap and excess energy is transmitted to external shell electron which leaves atom. This electron is called the Auger electron.

At the depth from 50 to 500 Å, inelastic scattering dominates causing the electrons to be ejected from the shell. These electrons are called secondary electrons (SE) and have energy below 50 eV. Secondary electron yield increases with increasing tilt of the sample with respect to the electron beam direction and increase with decreasing energy. The low energy of secondary electrons limits their application to the topography examination ($<$ 10 nm).

As seen in Fig. 6.2, secondary electrons come from surface area while back scattered electrons originate from deeper regions of the sample. The other phenomena such as characteristic X-ray, continuous X-ray and secondary fluorescence can get out from even greater depth.

The main signal in the SEM originates from backscatter electrons but the secondary electrons and signal coming from the background are also recorded. Fig. 6.3 shows the intensity of the scattered beam of electrons as a function of their energy, with a high-intensity peak at low energy coming from secondary electrons and a lower-intensity maximum at higher energy, indicating backscattered electrons.

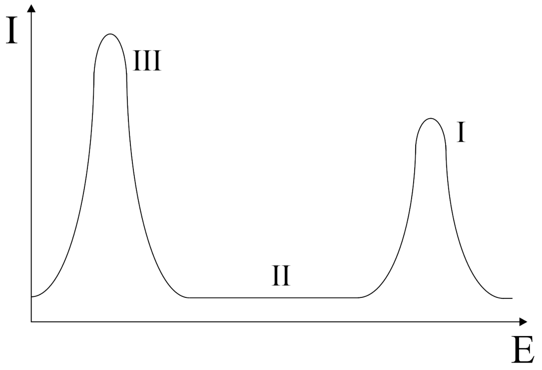

Figure 6.3: Intensity of the scattered beam as a function of electron energy: I - range of the electronic spectrum for SE electrons (to 50 eV), II - range of the electronic spectrum for BSE electrons.

The important parameter in SEM is the resolution (r), which determines the distinguishability of the two image details. From the visible light diffraction theory the formula for resolution follows:

$$r = \frac{0.61\lambda}{\mu sin\alpha} \tag{6.1}$$

where: λ − wavelength, μ − refractive index, α − half the angle of the cone of light from specimen plane accepted by the objective (halve aperture angle).

For the refractive index equal to 1 for the vacuum and small halve aperture angle the resolution in electron microscope is:

$$r = \frac{0.61\lambda}{\alpha} \tag{6.2}$$

Application of an electron beam in the electron microscopes instead of the light beam used in optical ones significantly increased the resolution from micrometers to nanometers and magnification from 1000x to 500,000x.

To observe the morphology of the nanowires, it was necessary to dissolve the membrane. For this purpose, the sample was glued to a copper tape, flooded with 2 ml of dichloromethane and left for 10 min. After this time, the sample was gently removed and left to dry.

The pore-filling and morphology of the nanowires presented in this work were studied using a scanning electron microscope: Tescan Vega 3 (in IFJ PAN) and also JEOL JSM-IT500HR (in LCPME UL). SEM was used for observing the nanowires before and after membrane dissolution in dichloromethane, by applying low (1-5 keV) and high (20-30) voltages respectively. The morphology of nanowires was analyzed using Image-J software.

Energy-dispersive spectrometry (EDS) is a technique for the chemical characterization of a sample. Electrons from the primary beam irradiating the sample may create an electron hole (by electron ejection), which will be filled with an electron from the outer shell. The energy resulting from the electron transition between these two energy levels can be emitted in the form of X-ray radiation, characteristic of each element. The number of X-rays recorded as the function of their energy creates a spectrum measured by an energy-dispersive spectrometer. Due to the fundamental principle that each element shows a unique atomic structure, the detected emission spectrum can be used for the elemental characterization of the sample. The intensity of the spectrum lines provides quantitative information about individual elements. The spectrum may contain artifacts mainly related to the summary peak (two X-ray photons are registered in the detector simultaneously as one quantum of double energy) and escaped peak (the additional peak that is created when an X-ray photon excites the fluorescence of the material from which the detector is made, resulting in a visible peak with the energy minus fluorescence energy of that material).

The chemical composition of the prepared nanowires was studied by energy-dispersive spectroscopy measurements performed in SEM (both Tescan Vega 3 and JEOL JSM-IT500HR). The research included point and linear measurements, and maps of the elements in selected areas.

Another technique based on the interactions of an electron beam with a sample is **Transmission Electron Microscopy (TEM)**, in which a beam of electrons is transmitted through the material and crates the image detected behind the sample. The accelerating voltage determines the maximum thickness of the sample, which varies from 100 nm for 500 kV to 10 µm for 3 MV.

The incident electron beam may pass through the sample without being scattered (central beam of diffraction pattern) or may be scattered (diffracted). Unscattered electrons create a bright field image (BF) that shows mass-thickness contrast resulting in a dark image in areas of greater mass or thickness. Diffracted electrons scattered at a particular Bragg angle (corresponding to a given lattice constant) form dark field (DF) images and slight changes in crystalline orientation (*i.e.* Bragg conditions) influence the image contrast. These two mechanisms (mass-thickness contrast and diffraction contrast), which affect the amplitude of wave associated with transmitted electrons belong to an amplitude-contrast image formation and are obtained by selecting an unscattered or diffracted electron beam before the image plane.

In addition to changing the amplitude, the scattering of the incident electron beam can also alter the phase of the electron wave. Phase-contrast images, also known as high-resolution transmission microscopy, occur when the unscattered and diffracted Bragg beams, which are phase-shifted, interfere with each other in a constructive or destructive way. As a result, one can observe lattice fringes in HR-TEM images, Fresnel fringes at the sample edge, or Moir*é* pattern. Phase contrast significantly increases spatial resolution due to multiple beams, including those scattered at higher angles (smaller lattice constant).

Besides conventional imaging, transmission electron microscopy offers a wide range of operating modes such as diffraction, scanning TEM imaging (STEM), and spectroscopy techniques as well as combinations of them.

Measuring electrons scattered at characteristic Bragg angles allows the generation of diffraction patterns. For single-crystalline samples, these patterns have the form of dots, while for polycrystalline samples, they create diffuse rings with the radii corresponding to the lattice constant. The smaller the crystallite size, the more diffuse the rings, which expand in the case of amorphous samples. Diffraction pattern acquisition can be performed on a precisely selected area of the sample, resulting in high-quality selected area diffraction (SAD) patterns.

High-angle-scattered electrons excluded from BF images are used for scanning transmission electron microscopy (STEM) imaging. In this case, the primary beam scanning the sample surface is convergent (unlike the parallel beam in TEM measurements). The scattered electrons are collected by a high-angle annular dark field (HAADF) detector and the atomically resolved mass-thickness contrast images reveal maps of atomic column position.

The imaging modes briefly described above use elastically scattered electron beams. Inelastically scattered electrons with a measurable energy loss (from meV to several hundred eV) generate X-ray emission, secondary electrons, and even visible light (cathodoluminescence). The most popular techniques using inelastic signals are electron energy loss spectroscopy (EELS) and X-ray spectroscopy (EDX). EELS measures excitation and ionization events providing information on core-shell transitions and phonon emission. The widely used EDS spectroscopy detects de-excitation events. Inelastically scattered electrons emit characteristic X-rays coming from the interaction of the electron beam with the inner electron shell of target atoms or continuous X-rays resulting from the interaction of the electron beam with atomic nuclei. Characteristic X-rays carry information about local elemental composition while continuous spectrum, used in biological studies to analyze the average atomic number of samples, in the case of material studies is treated as a background obscuring the characteristic X-rays.

Electron microscopy allows for the observation of the structure of crystals and their defects such as grain and phase boundaries, and dislocations. TEM provides information about atom positions and crystal orientation, as well as the elemental composition of the samples and chemical bonds.

The combination of inelastic scattering methods with high-resolution imaging provides an advanced tool for observing atomic-scale structure and analyzing the chemical composition of nanoareas. This makes electron microscopy an irreplaceable technique in nanotechnology and material science applications.

TEM results presented in this work were obtained at the AGH University using Transmission Electron Microscope FEI Tecnai G2 20 X-TWIN electron microscope equipped with a LaB6 emission source, and FEI Titan Cubed G2 60-300 microscope (FEI) equipped with the ChemiSTEM system, and also in Institute Jean Lamour at UL using a JEM - ARM 200 F Cold FEG TEM/STEM operating at 200 kV and equipped with a spherical aberration (Cs) probe and image correctors. Scanning transmission electron microscopy (STEM) images were acquired using a high-angle annular dark-field (HAADF) detector. The STEM-EDS data was analyzed by Esprit software (Bruker) in which the standardless Cliff-Lorimer quantification method was used. Indexing of electron diffraction patterns was performed with the use of JEMS software.

TEM microscopy can also be used to image the micromagnetic structure of a nanomaterial using **Lorentz microscopy (L-TEM)**. Especially, it is possible to investigate the domain wall distribution of ferromagnetic samples and magnetization reversal mechanisms.

The objective lens used in TEM produces a strong magnetic field along the axis of the microscope (up to 2 T). This field magnetizes the sample, which loses its domain

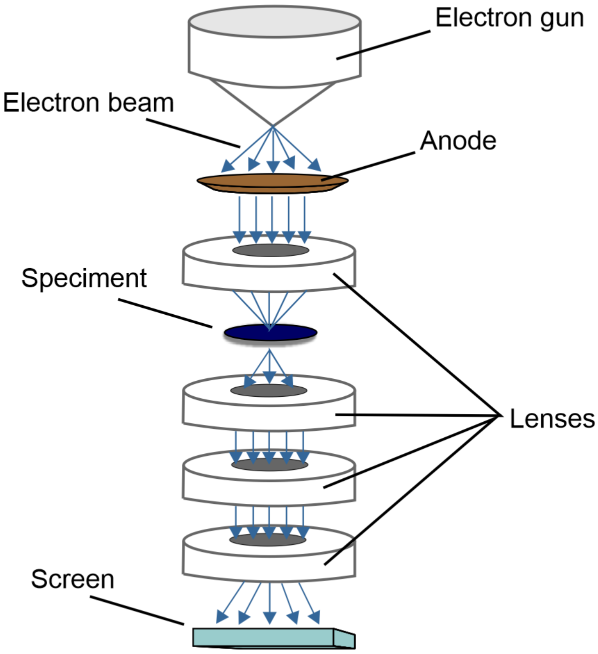

Figure 6.4: Scheme of the transmission electron microscope (TEM).

structure, becoming a single-domain object. In the Lorentz microscope, to avoid such a modification of the magnetic structure, the objective lens is replaced by a special Lorentz lens, which is an objective mini lens generating a negligible small magnetic field. This lens is installed below the objective lens, away from the sample, and focuses the image after the electrons pass through the sample. Thus, Lorentz's lens takes over the function of the objective lens that can be turned off.

The electron beam passing through the ferromagnetic sample experiences the Lorentz force acting, which deflects it from its normal direction. According to Lorentz's rule, this deflection will vary depending on the magnetization vector direction. Therefore, the areas of two magnetic domains (with magnetization vectors rotated by 180^o) will deflect the electron beam in opposite directions. This phenomenon allows the study of domain structures. Electron microscopy using a Lorentz lens has two modes: Fresnel mode and Foucault mode. The difference between these two modes will be discussed on the example of a sample in which the magnetization directions in adjacent magnetic domains differ by 180^o.

In the Fresnel mode, in adjacent magnetic domains, incident electron beams are deflected in opposite directions, as shown in Fig. 6.5. In one DW region, electrons passing through adjacent domains are deflected closer to each other (overlapping) and increase the intensity of the electron beams, while in the other DW area, electrons are deflected away relative to each other and reduce the intensity of the electron beams. The magnetic domain wall is difficult to observe when the lens is focused on the bottom surface of the sample because the overlapping electron region is narrow. When the focus is moved (defocused), the overlapping area is enlarged and the DW appears as light (or dark) lines. Typically, the image is over-focused or under-focused by about 1 µm [162], which results in a slightly different magnification. The two images are also shifted laterally with respect to each other [163]. Fresnel mode is also called the defocused method.

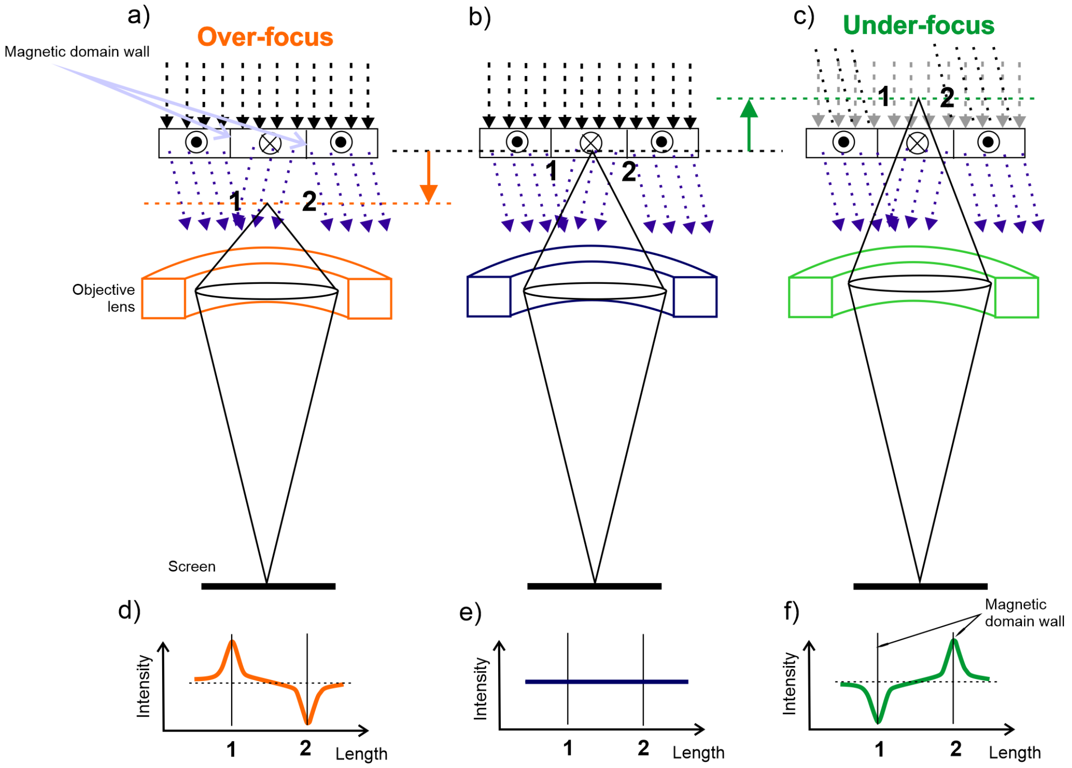

Figure 6.5: Scheme of image acquisition in Fresnel mode with intensity distribution for over-focus and under-focus conditions.

In the Foucault mode, diffraction spots from adjacent magnetic domains arise at slightly different locations on the back focal plane, and one of these spots is selected for imaging. The domain corresponding to the selected diffraction point appears bright, while the domain corresponding to the unselected diffraction point appears dark. This technique is called the focus method.

In Fresnel imaging mode, magnetic domain walls appear as bright or dark lines, while in Foucault mode, magnetic domains are bright or dark depending on the magnetization vector direction.

We used a JEOL JEM-2010 TEM operated at 200 kV for L-TEM. Fresnel images were taken under-focus in low magnification mode, using the objective mini-lens as the imaging lens, with the objective lens slightly excited (at 10% of the value used for eucentric focus), in order to impart a specimen- tilt-angle-dependent magnetic field to the sample.

6.4. X-ray photoelectron spectroscopy (XPS)

X-ray photoelectron spectroscopy (XPS) is a very effective technique for quantitative analysis of the elemental composition (all elements except hydrogen and helium), chemical state, and electronic structure of elements occupying the surface area of the sample (1-10 nm of detected depth). It is a type of photoelectron spectroscopy, in which a sample irradiated by a focused, monochromatic X-ray beam (Kα Mg or Kα Al) emits core electrons. The ejected electron enters the free state with kinetic energy E_K. The kinetic energy of the emitted photoelectron depends on its binding energy on the appropriate electron shell of the atom (characteristic of their elements) and is described by the relationship based on Einstein's equation:

$$E_K = hv - E_B - \Phi \tag{6.3}$$

where: E_B - electron binding energy in the atomic core measured relative to the vacuum level (eV), hv - the energy of the photon falling on the sample, while Φ is a work function resulting from the energy loss when an electron leaves the atom and when is absorbed by the detector (quantity of the order several eV, estimated from calibration).

The XPS spectra show the intensity corresponding to the number of ejected electrons as a function of the binding energy. Elastically scattered electrons in the first few atomic layers, which release the sample without energy loss, create sharp peaks in the spectrum, while the electrons that have undergone collisions and lowered their energy contribute to the inelastic background of the spectrum. In the spectrum, one can also distinguish multiplet splitting, which occurs when unfilled shells contain unpaired electrons (the unpaired electron remaining after ionization couples with an unpaired electron in the originally incompletely filled shell and generates splitting of the orbital). Moreover, satellites can appear due to a sudden change in effective charge caused by the loss of shielding electrons when a core electron is removed by photoionization. Two types of satellite can be detected: shake-up and shake-off. The shake-up satellite arises when the outgoing electron interacts with a valance electron and excites it (shakes it up) to a higher energy level. This causes a slight energy loss of core electron and appears in the spectrum as an additional low-intensity peak shifted from the main peak by a few eV (below the main line). In the case of a shake-off satellite, the valence electron is ejected from the ion and contributes to a noise signal or causes the broadening of the main peak. The photoelectron emission process is accompanied by the emission of Auger electrons and photons.

XPS is a very sensitive technique. The detection limit for elements ranges from 1% of the surface layer for light elements to less than 0.1% of the surface layer for heavy elements. Quantitative analysis in XPS is possible with an accuracy of 90-95 at.%. Due to the low lateral resolution (millimeter range), XPS is not a very suitable technique for mapping. Using XPS in combination with ion sputtering can obtain a depth profile, but this technique is not very effective.

The presented XPS research was performed in a Vacuum System Workshop at AGH to analyze the oxidation state of the Fe nanowires. The measurements were carried out with a residual pressure below 5 x 10^{-8} mbar during analyses, operating at Kα Mg radiation of energy 1253.6 eV. A concentric hemispherical electron analyzer worked in a fixed-analyze transmission mode with a constant pass energy of electrons set at 22.5 eV. The binding energy scale was calibrated by fixing the position of the dominant C1s peak of the adventitious carbon to 284.6 eV.

6.5. X-ray diffraction (XRD)

The X-ray Diffraction (XRD) technique is an analytical method that provides information about the crystal structure, preferred crystal orientation (texture), crystallite size, lattice strain, and phase composition of the tested materials. This method uses the phenomenon of diffraction of monochromatic X-ray beam on periodic structures. Since the wavelength of an X-ray is similar to the distance between atoms in the crystal, the diffraction of X-ray on the periodic lattice of atoms can be used to measure the distance between atoms.

In this effect, the incident beam is elastically scattered by electrons around atoms forming the planes of the crystal lattice (the strength with which an atom scatters X-rays is proportional to the number of electrons around the atom). Crystallographic planes are marked as a set of parallel lines on which the atoms are arranged, and each pair of adjacent planes is separated by a constant distance from each other (d_{hkl}). (Fig. 6.6). The angle between the incident beam and the plane defined by the sample surface is θ and is equal to the angle between the diffracted beams and the sample plane, the angle between the incident beam and the diffracted beam is 2 θ. The diffraction vector bisects the angle between the incident and the diffracted beam.

The X-ray beams reflected from two adjacent planes can interfere constructively causing the signal to be amplified or destructively resulting in the signal extinction. For a diffraction pattern to occur, the Bragg's condition must be fulfilled. This means that to observe a constructive interference, the difference in the optical path length of the incident and diffracted beams (x) must be equal to an integer (n) of the wavelength (λ), that is nλ.

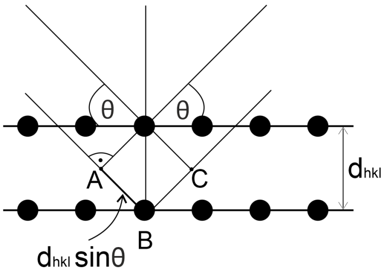

Figure 6.6: Diffraction of X-ray beams on atomic planes in a crystal.

Optical path difference is:

$$\Delta S = AB + BC \tag{6.4}$$

$$AB = d_{hkl} sin\theta \tag{6.5}$$

$$BC = d_{hkl} sin\theta \tag{6.6}$$

Hence:

$$\Delta S = 2d_{hkl} sin\theta \tag{6.7}$$

The condition for the constructive interference expressed by Bragg's law is as follows:

$$2d_{hkl} sin\theta = n\lambda \tag{6.8}$$

where: d_{hkl} - distance between planes [Å], θ - reflex angle [^{o}], n - integer, λ - wavelength [Å]. The constrictive interference forms an interference pattern with the peaks, whose positions are determined by the space between diffracting planes (d_{hkl}).

An X-ray instrument contains an X-ray source, a sample stage, and an X-ray diffracted beam detector. In the Bragg-Brentano geometry used in this work, the sample is placed on a fixed support and the radiation source and detector are moved on a circle that is centered on the sample (Fig. 6.7).

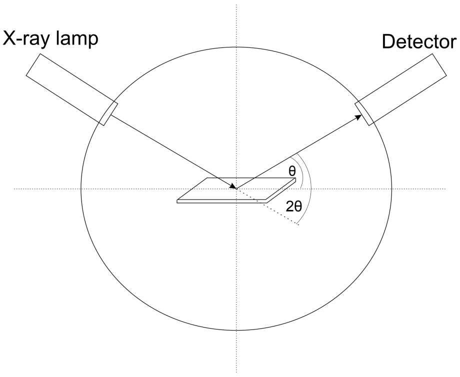

Figure 6.7: Scheme of a diffractometer in Bragg-Brentano geometry.

X-ray tubes that are the source of monochromatic X-rays, depending on the anode material, can emit electromagnetic waves with different wavelengths. The most typical, Cu X-ray tube (in our instrument), emits an X-ray with three distinct lengths related to the $K_{\alpha 1}$, $K_{\alpha 2}$, K_{β}, transition. The use of the Ni-filter allows the K_{β} line to be removed, but the $K_{\alpha 1}$ $K_{\alpha 2}$ doublet will almost always be present (these two lines overlap strongly at low angles but are more separated at higher angles near 100 deg). Therefore, the average value of the wavelength $K_{\alpha} = 1.5418$ Å is usually assumed.

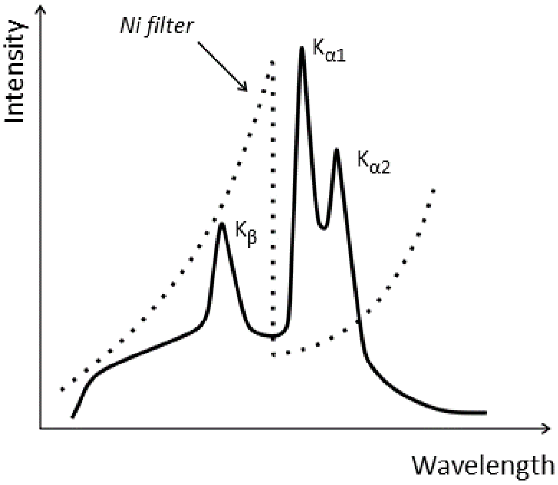

Figure 6.8: The radiation spectrum emitted by Cu anode tube $K_{\beta} = 1.3922$ Å, $K_{\alpha 1} = 1.5406$ Å, $K_{\alpha 1} = 1.5444$ Å with the marked absorption edge of the nickel filter.

In Bragg-Brentano geometry, the diffraction vector is always normal to the surface of the sample. The observed diffraction peaks correspond to the planes of atoms and are described by Miller indices (hkl). Only atomic planes, whose normal vector [hkl] is parallel to the diffraction vector contribute to the diffraction pattern. Amorphous materials such as glass do not have a periodic long-range ordering of atoms and only produce a broad scattering peak or contribute to the background.

Depending on the atomic structure, some reflexes cannot be observed because of the extinction rule, which indicates forbidden reflections. This systematic lack of reflections in some reflection orders is related to the centering of unit cells.

Table 6.2: The rules determining which reflexes can be observed in particular crystal structures.

Crystal structure	Condition for reflection to be present
bcc	h+k+l = 2n (even)
fcc	all h,k,l odd or all even
hcp	-h+k+l = 3n

In a single crystal sample, only one family of peaks can be observed in the diffraction pattern, provided that the normal vector of the crystallographic planes is parallel to the diffraction vector. In a polycrystalline sample, there is a set of crystallites that are properly oriented *i.e.* their normal vector is parallel to the diffraction vector.

Irradiating a large volume of material ensures a statistically significant number of grains contributing to the diffraction pattern. A small sample quantity limits the number of crystallites that can produce a diffraction pattern. This situation is observed in the case of analysis of nanowires, which show low peak intensities in diffractograms.

Diffraction patterns are collected as 2θ vs. absolute intensity (*i.e.* the number of X-rays observed in a given peak, which can vary due to the instrumental (wavelength of X-ray) and experimental parameters). Using Brag's law, 2θ can be converted to d_{hkl}, which is an instrument-independent, material property, while the absolute intensity can be replaced by an instrument-independent relative intensity, obtained by dividing the absolute intensity of each peak by the absolute intensity of the most intense peak and showing it as a percentage.

To identify the phase composition, the measured X-ray diffraction pattern is compared to standards found in reference databases such as the ICDD database (International Center of Diffraction Data) or to own measurements of pure-phase diffraction patterns.

The diffractograms, and in particular the position of the peaks, their intensity, and shape (the width of the peak at half its height) provide qualitative and quantitative information about the structure and phase composition of the tested sample. As mentioned, the peak positions are determined by the space between diffracting planes (d_{hkl}). The intensity of reflections depends on the incident beam intensity, the positions of atoms in the unit cell, the number of hkl planes, and other factors such as the type of atoms, etc. The ability of an atom to scatter X-ray depends on the number of electrons (Z), their spatial distribution, the diffraction angle θ, and the wavelength λ. If the grains in the sample are not randomly oriented *i.e.* the sample has a preferred crystallographic direction (texture), the pattern will contain the peaks with enhanced intensity indicating the preferred growth direction. In analysis, peak areas are a much more reliable measure of intensity than peak heights. The peak broadening may result from limited crystalline size (crystallites smaller than app. 120 nm cause the broadening of the diffraction peaks) and the strain in the lattice. Table 6.3 shows the relationship between individual diffractogram parameters and selected properties of the crystal structure.

Table 6.3: Relationship between individual diffractogram parameters and selected properties of the crystal structure.

Diffractogram parameter	Crystal structure
Position	Unit cell parameters
	Crystal structure
	Atom positions
Intensity	Preffered orientation
	Amount of materials in multiphase samples
	Crystallite size
Shape	Lattice defects
	Strain

The crystallite size can be estimated using the equation proposed by Scherrer:

$$D_{cryst} = \frac{K\lambda}{Bcos\theta} \tag{6.9}$$

where B = B$_{obs}$ - B$_{std}$ (B$_{obs}$ is FWHM - the width of the peak at half its height, B$_{std}$ is the instrumental width taken from a standard sample that does not exhibit any structural broadening, K is shape factor (ranging between 0.83 and 0.91 for a cubic shape of crystals), and D_{cryst} is the crystallite size. This method determines the crystal size along the direction of the scattering vector. The above equation shows that with smaller crystallite sizes, the peaks become broader. As mentioned above, peak broadening can also indicate lattice strain (η). The Hall-Williamson method can be used to separate the macrostrain and crystallite size. In this approach, the peak width should be analyzed over a long range of 2θ and η is equal to the slope coefficient in the equation, where x = sinθ, y = Bcosθ, and the y-intercept is $\frac{K\lambda}{D_{cryst}}$:

$$Bcos\theta = \frac{K\lambda}{D_{cryst}} + \eta sin\theta \tag{6.10}$$

As shown, the X-ray Diffraction technique is a versatile, non-destructive method, very useful in the analysis of the structure and phase composition of the samples and can be successfully used in the studies of nanowires.

The structure of the nanowires embedded in the polycarbonate membrane presented in this work was investigated through X-ray diffraction using a X'Pert MRD Pro diffractometer with Cu Kα radiation operating at 40 kV and 30 mA in $\theta-2\theta$ geometry. The measurements were performed at the IFJ PAN.

6.6. Mössbauer Spectroscopy

Mössbauer spectroscopy provides precise information about the local atomic environment of nuclei, which determines the physicochemical and crystallographic properties of the solid. It is based on the Mössbauer effect, involving the almost recoilless emission and absorption of gamma radiation by the nucleus.

In the case of the free nucleus during the emission and absorption of a γ ray, the nucleus suffers the recoil effect. The recoil energy of an atom with mass m is equal to $E_R = \frac{p^2}{2m}$, and the recoil momentum is $p = \frac{E}{c}$, thus:

$$E_R = \frac{E_\gamma^2}{2mc^2} \tag{6.11}$$

where c is the speed of light and E_γ is the energy of γ-ray.

This reduces the emitted γ ray energy and creates a requirement for more energy (then the transition energy) in the case of the absorbing nucleus. The recoil energy is 5-6 orders of magnitude greater than the natural linewidth (Γ), therefore the recoilless absorption and emission are impossible between free atoms or molecules (in gas or liquids) (Fig. 6.9).

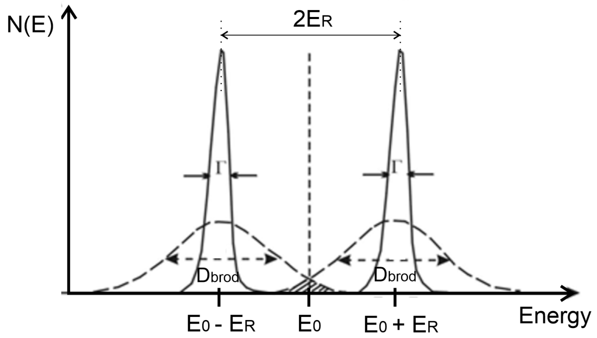

Figure 6.9: Emission and absorption lines in the case of free nuclei with slight overlap due to the Doppler effect [164].

The thermal motion of the atoms increases the line width (Doppler effect) and an extremely small overlap, can be observed but this is not sufficient for resonant absorption and emission of γ ray (Fig. 6.10, dashed line). Thus, there is an energetic mismatch between the emitted and absorbed photons with the value of 2E$_R$, which for nuclear processes is much larger than the natural width of the spectral line (Fig. 6.10).

Mössbauer discovered that when the atoms are bonded in a crystal lattice, the recoil during the emission or absorption of the photon is taken over the whole crystal. Consequently, in formula 6.11, the mass of the atom m, will be replaced by the mass of the whole crystal, so the recoil energy will be minimal. Thanks to this, the recoil energy can be reduced almost to zero, which enables the observation of resonant absorption and emission (Fig. 6.10). If emitting and absorbing nuclei are in identical, cubic environments, the energy absorbed by the sample will produce the spectrum with a single absorption line.

The probability for such recoil-free emission/absorption is described by the Debye-Waller factor. The smaller the recoil-free factor (f), the smaller the resonance effect. The factor f becomes larger with increasing wavelength of γ-ray (λ) (or decreasing $E_\lambda = hv = hc/\lambda$) and with decreasing recoil energy (E$_R$). Moreover, the weaker the bond in the crystal, the greater the mean square vibrational amplitude of the nucleus $<$x^2$>$, and the smaller the resonance effect (smaller f). The recoil-free fraction is temperature-dependent and increases as temperature decreases:

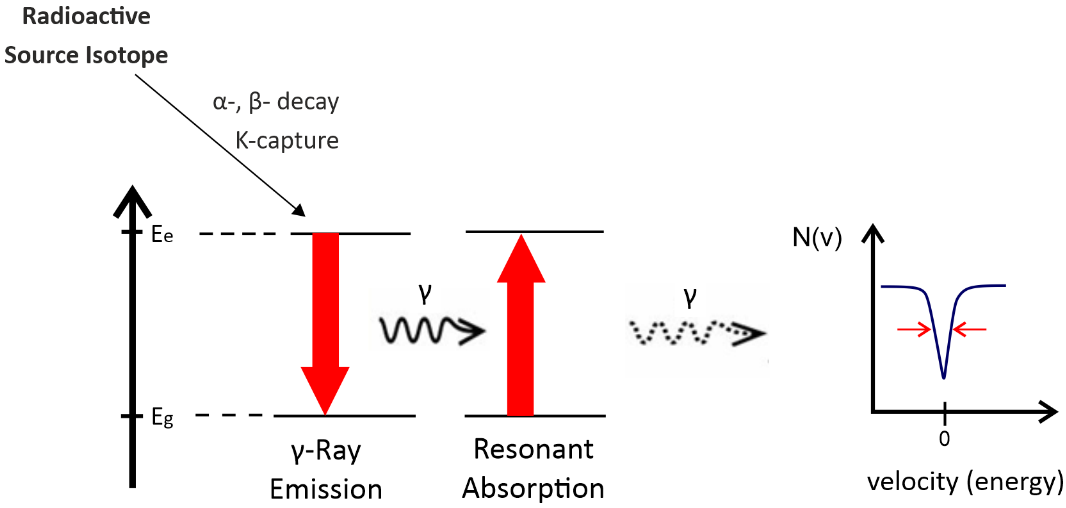

Figure 6.10: Recoil-free resonant absorption and emission of γ-ray with a recorded spectral line.

$$f = exp - [(< x^2 > /\lambda^2)(2\pi)^2] = exp - [(2\pi)^2 E_\lambda^2 < x^2 > /(hc)^2] \qquad (6.12)$$

The absorption and emission lines will not overlap sufficiently if the lines are too narrow or too broad. The suitable lifetime (line width) for Mössbauer spectroscopy is 10^{-6} s $\geq \tau \geq 10^{-11}$ s. As the resonance only occurs when the transition energy of the emitting and absorbing nucleus are exactly matched, this effect is isotopic specific and is only detected in isotopes with very low transition energy (E_γ). The most common Mössbauer isotope ^{57}Fe is characterized by E_γ = 14.4 keV, E_R = 1.95 x 10-3 eV, Γ = 4.7 x 10-9 eV, τ = 1.4 x 10-7s, and $D_{brod} \sim$ 10-2 eV (300K). The small line width compared to the energy of γ-ray gives an extremely high resolution of the Mössbauer spectroscopy, of the order of 10-12eV.

As mentioned above, when the absorbing and emitting nuclei are in identical surroundings, a single absorbing line is detected in the Mössbauer spectrum. However, the surroundings of the source and studied nuclei are usually different, which induces changes in the energy of the nuclear transition. Energy changes caused by the interaction between the nuclear moments and extranuclear electric and magnetic fields are called nuclear hyperfine interactions. These interactions result in the shift and splitting of the ground and excited state of nuclei by app. 10-7 eV. Such energy changes, make it impossible to observe resonance gamma absorption.

This energetic mismatch can be eliminated by the Doppler effect (types I and II), which causes both a shift and a broadening of the spectral line. In the first-order Doppler effect, the energy mismatch is compensated by the movement of the γ-source towards and away from the absorber with a velocity of a few mm/s according to $V \approx \frac{E_R}{E_0} \cdot c$. This movement gives the energy shift of $\Delta E = E_\gamma \cdot \frac{v}{c}$. Due to the connection between the energy changes and the velocity, the energy scale in the Mössbauer spectrum is replaced by the source velocity given in mm/s. The second-order Doppler effect is related to the thermal motion of atoms and causes an increase in the mean square vibrational amplitude.

The Doppler line width can be estimated from the formula:

$$D = \sqrt{2E_R kT} = \frac{E}{c}\sqrt{\frac{kT}{M}} \tag{6.13}$$

where T is the absolute temperature and k is the Boltzmann constant. At a sufficiently high temperature, a partial overlap of the emission and absorption lines can be achieved.

In the Mössbauer spectroscopy, three types of hyperfine interaction can be distinguished: the isomer shift (IS), quadrupole splitting (QS), and magnetic hyperfine splitting (B_{hf}). Fig. 6.11 shows the modification in the Mössbauer spectra caused by appropriate hyperfine interactions.

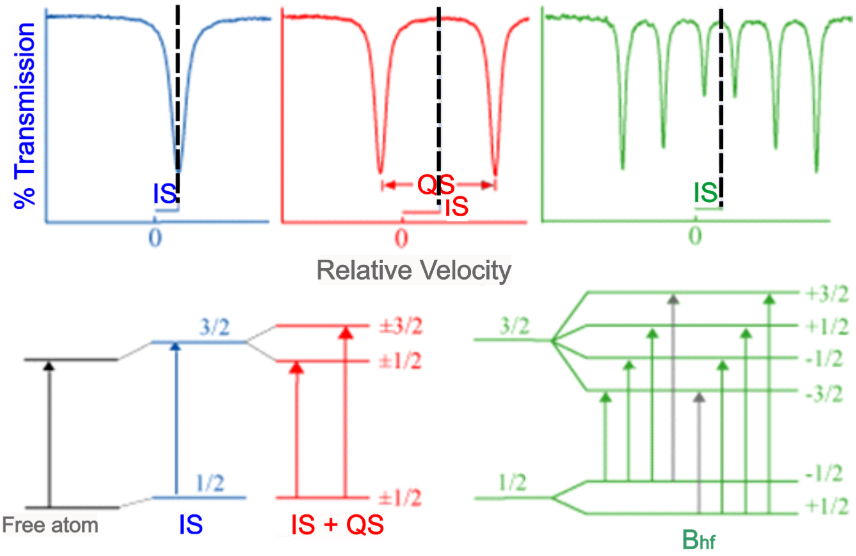

Figure 6.11: Shift and splitting of the energy levels caused by the hyperfine interactions and the corresponding Mössbauer spectra shown on the example of the ^{57}Fe isotope [164].

The isomeric shift (IS) is related to the shift of nuclear levels due to the electrostatic interaction of the nuclear charge with the s electrons, which have a finite probability of being found in the nucleus region. This shift occurs when the radiating and absorbing nuclei are in different chemical environments and results from different radii in the excited and ground states affecting s-electron density. In the case of ^{57}Fe, the radius of the excited state is larger than in the ground state, hence the decreasing electron density causes a decrease in the isomer shift. The energy shift is as small as 10^{-10}eV and is measured relative to a standard (for example the isomer shift in the ^{57}Fe Mössbauer spectra is shown relative or α-Fe at RT). The isomeric shift allows determining the oxidation state and chemical surroundings of the nucleus. It provides information about electron density in the nuclear region and the valence states of iron (Fe^{2+} or Fe^{3+}). For example, the ferrous ions (Fe^{2+}) have less s-electrons at the nucleus due to the greater screening of the d-electrons, thus the ferrous ions have larger positive isomer shifts than ferric ions (Fe^{3+}).

The quadrupole splitting (QS) arises from the interactions of the quadrupole moment of the excited state of the nucleus (with a spin of $I > 1/2$ showing a non-spherical charge distribution) with the electric field gradient. This gradient may come not only from the valence electrons of a given atom but also from the charges of its neighboring ligands.

The interaction of the electric field gradient with the quadrupole moment of the nucleus leads to the splitting of nuclear energy levels. The electric quadrupole interaction, in the case of the Mössbauer transition of ^{57}Fe, has no effect on the ground state with I = 1/2, but abolishes the degeneracy of the excited state (I = 3/2), leading to its splitting into two sublevels with $m_I = \pm 1/2$ and $m_I = \pm 3/2$. The distance between these sublevels is determined by the quadrupole splitting parameter. QS of a cubic structure is close to zero and takes non-0 values if the symmetry of its own electrons and distribution of surrounding ions deviates from cubic symmetry. This parameter provides information about the valence state and the degree of crystallographic site distortion.

(B_{hf}) The hyperfine magnetic splitting is related to the dipolar interactions of nuclear magnetic moment and the effective magnetic field acting on the nucleus. This field combines contributions from (i) the partially filled electron shell, whose electrons polarize the spin density at the nucleus, (ii) the orbital moment of these electrons, (iii) the dipolar field due to the spin of those electrons and (iiii) the applied external field. In the case of ^{57}Fe, magnetic splitting results in a sextet in the Mössbauer spectrum (Fig. 6.11 (3)). This parameter provides information about the magnetic surrounding of the nucleus and is evidence of the existence of magnetic ordering in the sample.

The relative line intensities in the sextet 3:x:1:1:x:3 allow the identification of the magnetization vector direction (M) relative to the γ-ray direction, where $x = \frac{4sin^2\theta}{2-sin^2\theta}$, and θ is the angle between magnetization vector and γ-ray direction. The relative line intensity 3:4:1 informs about the magnetization vector perpendicular to the γ-ray propagation direction, 3:0:1 indicates M II γ and 3:2:1 points out the random orientation of magnetic moments.

The Mössbauer spectrum is a superposition of the spectra corresponding to all ^{57}Fe surroundings that occur in the sample. The abundance of the ^{57}Fe in natural iron is app. 2% and only this isotope contributes to the Mössbauer spectrum. This extends the scope of the Mössbauer technique by the use of a ^{57}Fe isotope as a probe of the selected area to study the interfaces or other regions of the samples deeply buried under the sample surface. Hyperfine parameters provide the chemical, physical, and crystallographic information about the studied sample, and enable the identification of iron-containing phases.

The experimental setup in the Mössbauer spectroscope consists of three main parts:

- a source of gamma radiation (moving in oscillatory motion) - the ^{57}Co isotope (which decays by electron capture with a half-life of 270 days and produces, among others, γ-rays with an energy of 14.4 eV) is used to excite the ^{57}Fe isotope

- absorbent (tested sample contains natural iron or is enriched in the ^{57}Fe- isotope),

- a detector recording the radiation intensity after passing through the sample.

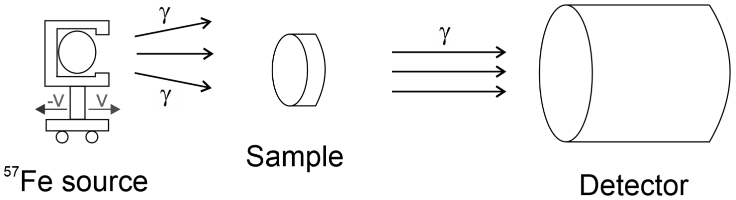

Figure 6.12: Scheme of a Mössbauer spectroscope operating in transmission geometry.

The presented Mössbauer studies for Fe nanowires were conducted in transmission geometry using 100 mCi ^{57}Co(Rh) source and He-10%CH4 gas flow counter. The measurements were taken at room temperature, the direction of the γ-ray propagation was perpendicular to the sample surface. The Mössbauer spectra were fitted as the sum of the Lorentzian sites using Recoil software (D. G. Rancourt).

6.7. Superconductive Quantum Device SQUID

SQUID (Superconducting Quantum Interference Device) is a very sensitive magnetometer designed for magnetic measurements that use the quantization effect of the magnetic induction flux in a superconducting ring with the Josephson junctions. A Josephson junction is formed when two superconducting regions are separated by an insulator (or non-superconducting metal). Superconductivity in such a junction occurs by electron pairs (so-called Cooper pairs of two electrons with opposite spins, interacting through vibrations of the crystal lattice) bounded together at low temperature (thermal energy can easily break the pair whose energy of the pairing interaction (long range - even hundreds of nanometers) is of the order of 10-3 eV). The Cooper pairs, unlike electrons, are allowed to be at the same quantum state and are described by in-phase wave functions. Tunneling the superconducting current through the Josephson junction causes the phase of the wave function to change. In the absence of an external magnetic field, the current is divided equally into the two branches of the ring, and the phase shifts at both Josephson junctions are the same. If a small external magnetic field is applied to the superconducting coil, the magnetic flux passing through the coil can lead to constructive or destructive interference, depending on whether the magnetic flux is an integral multiple of the flux quantum or not. The interference of the wave functions results in the field-dependent current oscillation. Using such a SQUID sensor, it is possible to measure magnetic field as low as 10-15 T (1 femtotesla).

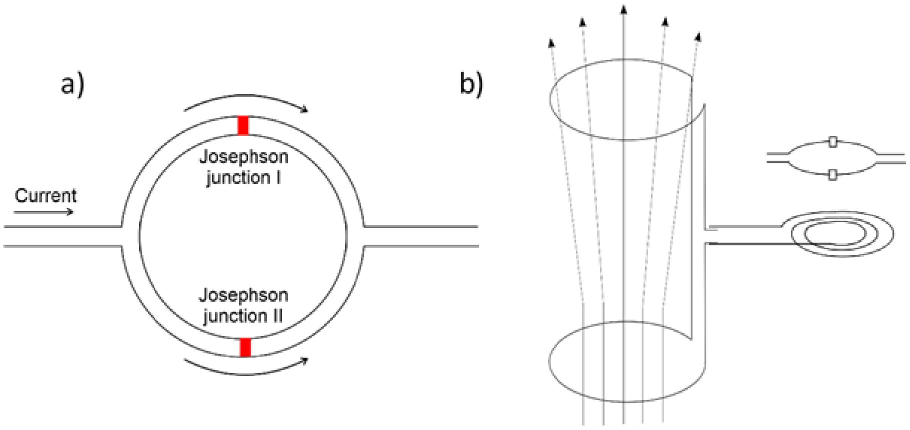

Figure 6.13: Scheme of the: (a) DC SQUID build of two Josephson junctions, (b) SQUID magnetometer.

The SQUID device consists of a cryostat with a variable field superconducting magnet, superconducting pickup coils, and a SQUID sensor. There are two types of magnetometers: dc-SQUID and ac-SQUID. The former consists of two Josephson junctions located on opposite sides of the superconducting ring, while the second contains only one Josephson junction. The scheme of the SQUID device is shown in Fig. 6.13.

To perform the measurement, the sample is placed in a polymer straw and introduced into a superconducting coil. During measurement, the sample is periodically moved vertically inside the coils with a frequency of 1 Hz and with an amplitude of 4 cm. This causes changes in the magnetic flux through the coils, which induce a current proportional to the magnetic moment of the sample. The signal is then detected by the SQUID sensor and amplified. The sensitivity of the Quantum Design SQUID magnetometer operating at the Institute of Nuclear Physics reaches the value of 10-8 emu, wherein the magnetic moment of 1 g of Fe is 200 emu.

As described in the previous chapters there are many factors that determine the magnetic behavior of nanowires. In order to more precisely characterize magnetic samples and indicate the dominant interactions in the nanostructures (its magnetization resulting from exchange interactions and dipolar interactions between nanowires) a **First Order Reversal Curves (FORC)** method was developed. This is an advanced characterization method based on SQUID measurements, which is mainly a qualitative tool for identifying the magnetic state in single-domain, pseudo-single-domain, and multi-domain systems of nanostructures that interact or do not interact with each other. FORC measurements allow determining the coercive field distribution (ΔH_c - arising from non-uniform length distribution in an array of nanowires), the interaction field distribution (ΔH_u - describes magnetostatic interaction between nanowires), magnetic phases (soft/hard), magnetization reversal mode (coherent, TDW, VDW).

Using FORC measurements, it is possible to extract reversible M_{rev} and irreversible magnetization M_{irr} [165]. However, the FORC diagram shows only irreversible switching events and reversible magnetization does not contribute to a FORC diagram [170], but can be identified from angular FORC measurements [AFORC]. Irreversible magnetization can result from nucleation of new domain walls, unpinning domain boundary walls, and coherent or incoherent domain reversal modes [174] (dissipation of energy through domain wall motion or moment switching in single-domain particles [173]). Reversible magnetization can be connected with domain wall bowing with reversible rotation of domain magnetization vector [Crew1999] (moment rotation or domain wall displacement in a single potential well [173]). These two processes can also be differentiated by heat generation, which occurs only in the irreversible process (without heat generation in the reversible process) [173]. The reversible and irreversible rotations are marked in Fig. 6.14.

Irreversible magnetization is defined as a value of magnetization remaining when the magnetization changes along the recoil curve and the field is reduced to zero [174]. The maximal value of M_{irr} is achieved for a major loop and equals to the remanence value (Fig. 6.14 b). Reversible magnetization is a difference between the magnetization and the irreversible component (this definition is valid only for closed and reversible recoil curves, with a constant M_{irr}). The character of M_{rev} versus M_{irr} dependence can identify the magnetization reversal mechanism [114, 174].

The irreversible magnetization is the difference between the major hysteresis curve and FORC magnetization, given by the equation:

$$dM_{irr} = lim_H M(H) - M(H_r, H) \tag{6.14}$$

The reversible magnetization is given by:

$$dM_{rev} = lim_H M(H_r, H) - M(H_r) \tag{6.15}$$

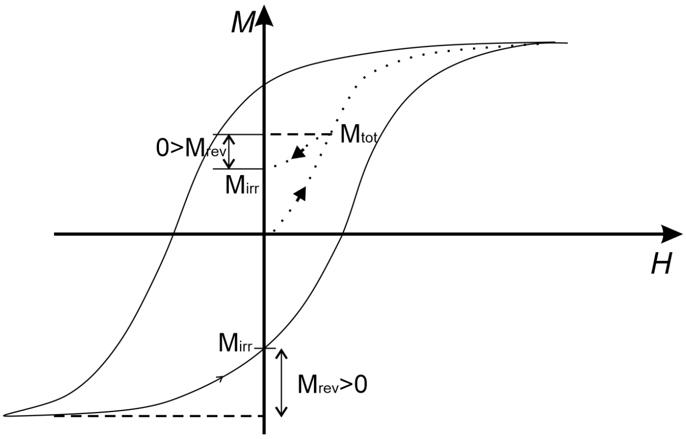

Figure 6.14: The reversible and irreversible rotations [105, 171, 172, 173, 174].

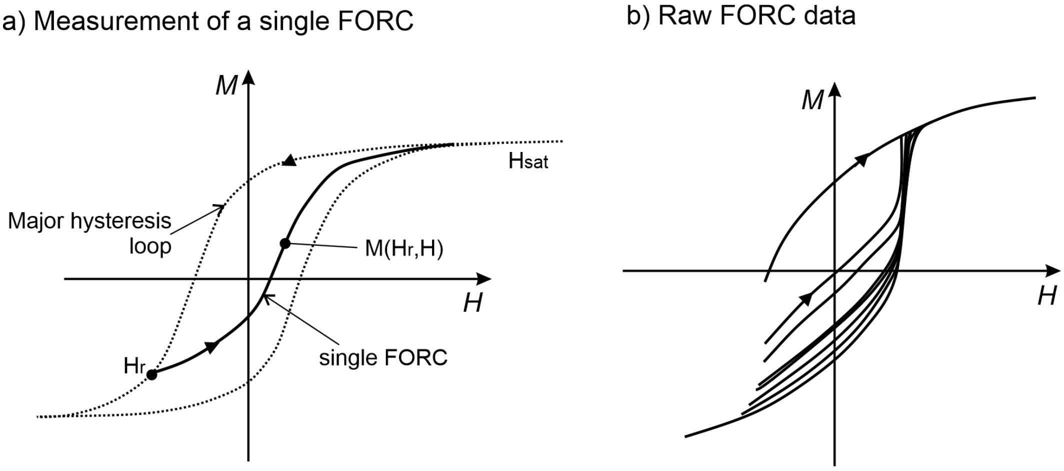
a) Measurement of a single FORC

b) Raw FORC data

Figure 6.15: The subsequent steps of the FORC measurements acquisition: (a) single FORC, (b) series of FORCs.

Irreversible processes result in a non-zero FORC distribution, in contrast to reversible switching, which is characterized by a zero FORC distribution. To obtain the FORC diagram, the magnetic nanowires are initially saturated by applying H_s, then the field is decreased to reversal field H_r and FORC is acquired when sweeping H_r back to H_s (Fig. 6.15 a). The measurement is repeated in a series of regular steps for many values of H_r. At each step, the magnetization is measured to obtain $M(H_r,H)$ (Fig. 6.15 b), which can be shown in a two-dimensional grid in field space $M(H_r, H)$. The FORC distribution ρFORC(H_r,H) is defined as a second-order mixed partial derivative of $M(H_r,H)$ with respect to H and H_r:

$$\rho FORC(H_r, H) = (-\frac{1}{2})\frac{\delta 2M(H_r, H)}{\delta H_r \delta H}[165]. \tag{6.16}$$

To fit the $M(H_r,H)$ of the data points, the following polynomial is considered:

$$M(H_r, H) = a_1 + a_2H + a_3H^2 + a_4H_r + a_5H_r^2 + a_6HH_r[165] \tag{6.17}$$

where a_6 is ρFORC value at the center of the local grid.

The FORC diagram is shown on a color scale from blue (minimum) to red (maximum). The coordinates (H_r, H) are usually replaced by H_c = (H - H_r)/2 (corresponds to the distribution of switching field) and H_u = (H+H_r)/2 (corresponds to the distribution of interaction field), which rotates the FORC distribution by 45 deg.

The elongated narrow distribution of a FORC diagram along the Hu axis indicates magnetostatic interactions [105]. In the case of dipolar interactions, the distribution gives maximum spreading at positive Hu, while distribution at negative H_u indicates exchange interactions [166]. The half-width of the irreversible FORC distribution cross-section δH_u (taken from out-of-plane measurements) parallel to the Hu axis passing through the maximum coercivity describes quantitatively the magnetostatic interactions. The range of the spreading can be used to measure the extent of the domain wall pinning, domain nucleation, and annihilation [166].

On the other hand, the irreversible FORC distribution along the H_c axis at $H_u = 0$ allows the estimation of the individual coercivity of nanowires. As mentioned before, this coercivity distribution can result from different lengths of nanowires. These measurements provide a switching field of individual nanowires, which is an experimental challenge due to the very small magnetization of a single NW in the order of 10-11 emu [170]. The difference between the coercivity obtained from out-of-plane FORC measurements (H_c^{FORC}) and out-of-plane coercivity taken from the hysteresis loop shows the contribution of magnetostatic interactions $\Delta = H_c^{FORC} - H_c^{array}$.

The deviation from the coherent rotation is usually due to the magnetostatic interactions between nanowires, therefore the magnetic state of the system can be described based on the FORC diagram. The shape of a FORC diagram along the H_c axis informs about magnetization reversal. The increase in the distribution along the H_c axis can be attributed to a magnetization reversal by the propagation of TDW, while in the case of VDW, the coercivity distribution is not affected [105]. The elongated FORC distribution with closed contours extending along H_c indicates a single-domain structure. The transition to PSD causes oval-like contours with the peak moving along H_u, while the MD structure shows a broad, open contour extending along H, which diverges from the $H_u = 0$ axis and intersects the H_c axis [167, 202].

A more complicated continuous FORC diagram with small amplitudes may indicate a complex system of various weak magnetic nanostructures. A FORC diagram with distinct regions informs about different magnetic phases and complicated interactions.

Magnetic measurements presented in this work were measured for the nanowires embedded in the membrane, using a superconducting quantum interference device (SQUID) magnetometer (MPMS, Quantum Design, San Diego, California, USA), located in the IFJ PAN. Hysteresis loops were measured at room temperature, by applying an external field of up to 4 T in the plane and out of the plane of the membrane, and at angles ranging from 0 to 90^o in angle-dependent measurements. The diamagnetic signal of the sample holder and the polycarbonate membrane was subtracted from the hysteresis loops.

The FORC measurements were performed in out-of-plane measurements at room temperature using SQUID magnetometer. The samples were initially subjected to a maximum magnetic field of 40 000 Oe. Before each FORC measurement, the sample was saturated at 10000 Oe, and FORC was measured with the reversal field range from - 5000 to 5000 Oe and step of 100 Oe.

Chapter 7

Cyclic voltammetry of iron, cobalt, nickel and their alloys

The cyclic voltammetry (CV) method was used to optimize electrodeposition parameters and to understand the behavior of selected elements under the influence of cathodic potential. The measurements were performed using gold film electrodes immersed in various electrolytes containing $FeSO_4$, $CoSO_4$, $NiSO_4$, or their mixture (and boric acid as supporting electrolyte and ascorbic acid as anti-oxidant) with a pH adjusted at approximately 3.

First, the CV curves (*i.e.*, current vs. potential curves) were recorded separately for each cation (Fe^{2+}, Co^{2+}, Ni^{2+}) in electrolytes containing their sulfate salts (at a concentration of either 50 mM or 5 mM each) in view of gaining information on their electrodeposition potentials. The obtained CVs in the potential window between +0.2 V and -1.2 V for cobalt and nickel and between 0.0 V and -1.2 V for iron are shown in Figure 7.1 a. All CV experiments were performed at a scan rate of 10 mV/s.

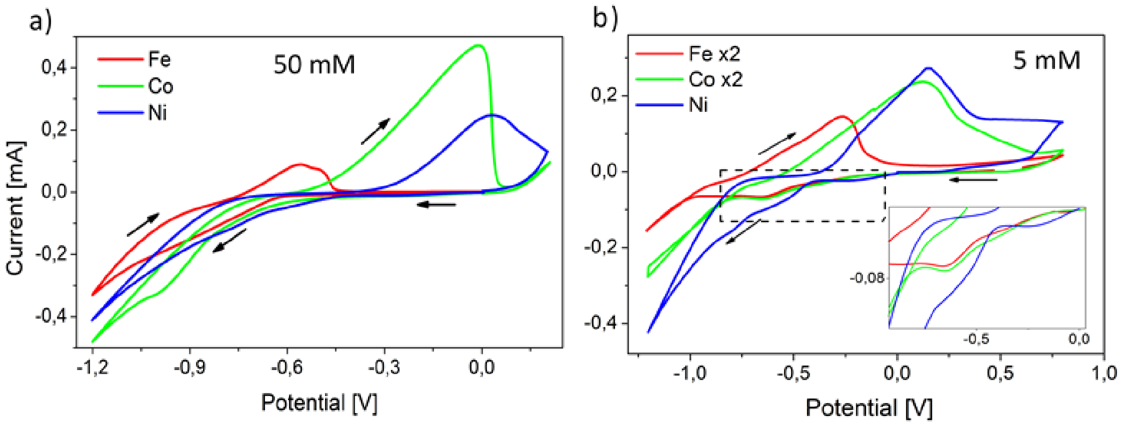

Figure 7.1: Cyclic voltammograms recorded in solutions containing separately $FeSO_4$, $CoSO_4$, or $NiSO_4$, at two different concentrations: (a) 50 mM and (b) 5 mM (+ 0.4 M HBO_3 and 5.7 mM ascorbic acid). All curves were recorded at a scan rate of 10 mV/s. Figure b represents the CV curves for Fe and Co magnified by a factor of two. The inset shows a magnified view of the area marked with a dashed line.

Measurements were made by applying a potential from 0 V and scanning first in the cathodic direction. The current response remained close to 0 over a wide voltage range down to approximately -0.4 V. Then, cathodic metal deposition occurred, starting with nickel followed by the reduction of cobalt and iron, which is consistent with values of standard potentials (Table 2.1). No clear cathodic peaks can be observed (only waves), and in the case of cobalt, two successive reduction waves are even visible. This is consistent with the literature data, notably that reporting two signals for cobalt reduction, which were attributed to two predominant complexes [175]. Behind the reduction waves, a further increase in cathodic voltage caused a quite sharp increase in current (to the point of reversal potential at -1.2 V), caused by hydrogen evolution. On scan reversal, metal dissolution is likely to occur, showing distinct anodic peaks that appear in the reverse order of cation reduction, in agreement with the redox properties of the considered species (Table 2.1). Moreover, one can observe a very slow increase in current at the stripping peaks, which suggests slow anodic dissolution processes.

The absence of well-defined cathodic peaks could be due to a too-high concentration of cations in the electrolyte solution, so the next measurements were performed with a lower cation content (*i.e.*, concentrations diluted 10 times). Cyclic voltammetry measurements performed in the potential window between +0.2 V and -1.2 V are shown in Figure 7.1 b. The magnification of CV curves (see inset) enables this time to observe cathodic peaks for Fe^{2+} and Co^{2+} reduction whereas the reduction of Ni^{2+} still remained in the form of two successive waves. Again, these cathodic signals appear in the order consistent with the standard potentials (first Ni, then Co and Fe). The approximate positions of the cathodic peaks are -0.63 V and -0.66 V for Co^{2+} and Fe^{2+}, respectively, and around -0.56 V for Ni^{2+}. In the latter case, one still observes the two sequential reductions for Ni^{2+} at close potential positions, as described in the literature [176]. They have been assigned to two steps of 1e- reduction [176]. On scan reversal, the slow anodic stripping is observed with peak currents appearing at lower anodic values compared to the more concentrated solutions (compare parts a and b of the figure) as a result of less deposited metals, confirming the successive dissolution of Fe, Co, and Ni.

Figure 7.2 depicts typical CV curves obtained for binary systems (*i.e.*, $FeSO_4/CoSO_4$ (denoted FeCo), see part (a), and $FeSO_4/NiSO_4$ (denoted FeNi), see part (b), which are compared to the responses of solutions containing each cation separately. In all measurements, the potential was scanned from positive to negative values with scan started from 0 V, at a scan rate of 10mV/s. The concentrations of separate cations were diluted like before (5 mM each), while the solution compositions for binary alloy depositions were adjusted to keep a molar ratio of 1:3 for FeCo and 1:5 for FeNi.

The CV curve obtained for the FeCo system seems to indicate a slightly easier reduction compared to the media with separate Fe^{2+} and Co^{2+} ions, with cathodic peaks observed at potentials of -0.61 V, -0.63 V, and -0.66 V for FeCo, Co^{2+}, and Fe^{2+}, respectively. This might suggest some stabilization of metal species in the alloy compared to separate Fe and Co elements. Again, hydrogen evolution occurred by further increasing potentials towards more cathodic values. As expected, on scan reversal, one can observe two peaks for the FeCo alloy, corresponding to the anodic dissolution of each element.

In the case of the FeNi system, the reduction of metal ions also starts at less cathodic values (-0.21 V) compared to the reduction of Ni^{2+} and Fe^{2+} in separate media, and currents observed at the main wave (-1.1 V) are significantly larger, suggesting more

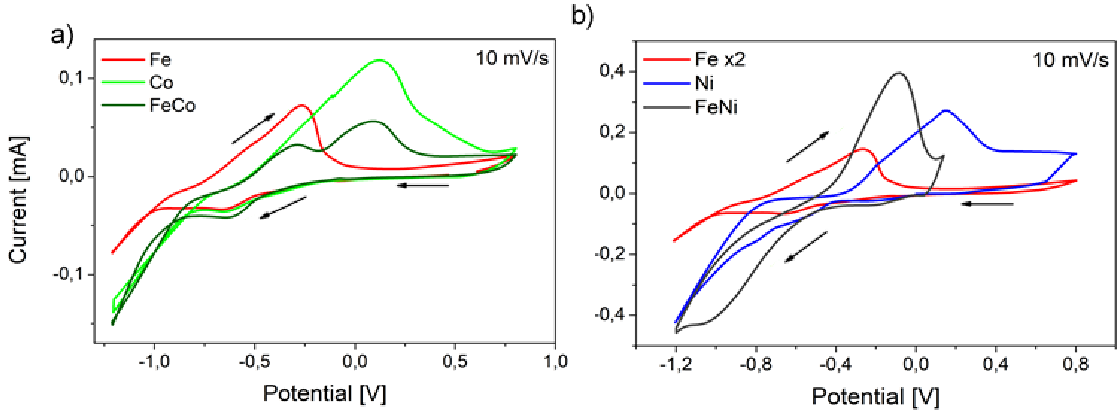

Figure 7.2: Cyclic voltammograms recorded in solutions containing $FeSO_4$, $CoSO_4$, and $NiSO_4$ or their mixture (in the binary systems), at concentrations equal to 5 mM for each element in separate electrolytes and 1 mM, 3 mM and 5 mM, respectively for Fe, Co and Ni, in binary systems ((a) FeCo and (b) FeNi). Figure b represents the CV curves for Fe magnified by a factor of two.

effective reduction when forming the alloy. Surprisingly, a single anodic stripping peak was visible on scan reversal for FeNi dissolution, which might be actually an overlap due to bigger deposits than for the FeCo system (compare y (current) scale in part (a) and (b) of Fig. 7.2).

Cyclic voltammetry was then performed using a solution containing all three elements ($FeSO_4$ + $CoSO_4$ + $NiSO_4$) at a concentration of 5 mM each at 10 mV/s. As shown in Figure 7.3, the CV curve obtained for this ternary system (FeCoNi) exhibits a reduction signal at a potential value of approximately -0.68 V (see top right inset in Fig. 7.3), which is a bit more cathodic than those observed for the separate metal ions (see bottom right inset in Fig. 7.3). Note that the high magnification view also shows the presence of an additional pre-wave appearing at a potential of approximately -0.41 V, which may suggest that the reduction from the ternary system started earlier. This may be related to anomalous deposition [56, 177]. On the other hand, the appearance of a peak at more cathodic potentials has been reported in the literature [177]. This shift (compared to separate cations) was explained by the fact that a larger overvoltage is needed during the alloy deposition process to overcome the higher kinetic barrier for chemical reactions caused by the species, which may inhibit electron transfer [177]. On scan reversal, one could observe only one anodic peak encompassing the stripping of all components of the alloy.

In the next experiment, I compared the behavior of the ternary system at two concentrations. As shown in Figure 7.4 a (inset), the CV curve obtained in a mixture of $FeSO_4$ + $CoSO_4$ + $NiSO_4$, at concentrations of 50 mM indicates the presence of small reduction pre-waves appearing at -0.58 V and -0.69 V while a single one (-0.68 V), a bit more intense, came from the system with lower concentration (5 mM) indicating possibly faster nucleation processes in this case. Then, the more intense reduction was observed for the more concentrated medium, as expected, with the corresponding more intense anodic stripping peak on scan

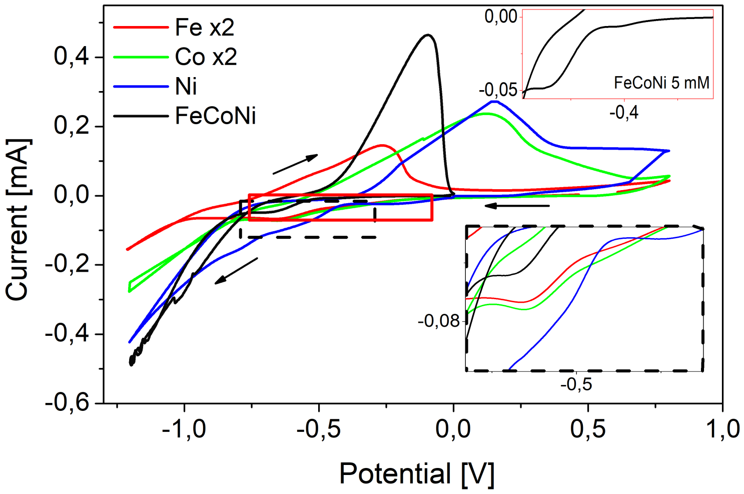

Figure 7.3: Cyclic voltammograms recorded in solutions containing $FeSO_4$, $CoSO_4$, and $NiSO_4$, alone or as a mixture of all of them (5 mM each). Right bottom inset: enlargement of the cathodic region marked black, right top inset: enlargement of the cathodic region only of FeCoNi system, marked red. The CV curves for Fe and Co are magnified by a factor of two.

reversal, consistent with a larger amount of electrodeposited material. Comparing the area under the peak indicates however only a two-times increase although the concentration of metal ion precursors was ten times larger, suggesting again kinetic limitations.

Finally, CV measurements in a solution containing all three elements ($FeSO_4$ + $CoSO_4$ + $NiSO_4$) in high concentrations (50 mM each) were carried out at various potential scan rates (from 10 to 160 mV/s) (Fig. 7.4 b). In this case, the reduction signals were not well-defined, similarly as was observed for individual metal ions, but small reduction waves can be noticed with the intensities increasing with the scan rate. An inverse relationship was observed for the anodic peaks, the intensities of which decreased with increasing scan rate, indicating less deposited amounts when applying cathodic potentials for shorter time (*i.e.*, faster scan rates). This confirms a lack of electrochemical reversibility and slow electron transfer and/or nucleation kinetics. Comparing this result to the deposition of single metals, it can also be seen that the alloy deposition starts at lower potential values, indicating anomalous co-deposition. This shows that the changes in the applied potential can significantly affect the individual metal reduction, leading to the modification in the chemical composition of their alloys.

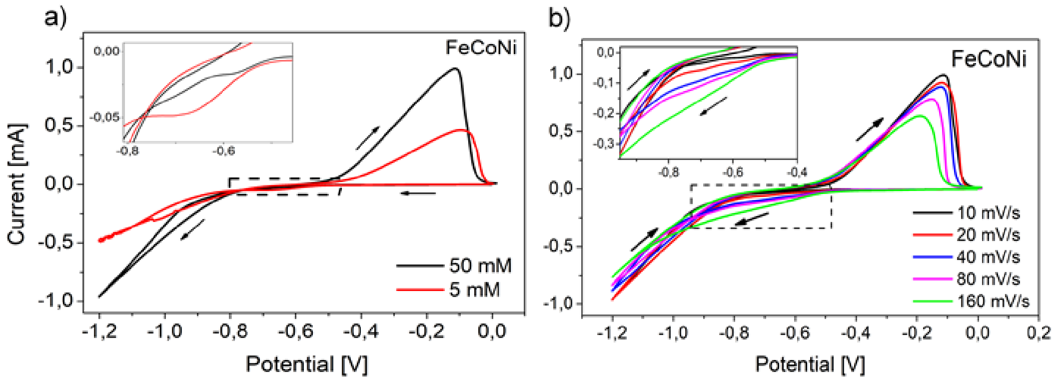

Figure 7.4: Cyclic voltammograms recorded in a solution containing a mixture of $FeSO_4$, $CoSO_4$, and $NiSO_4$: (a) comparison of two different concentrations (5 mM and 50 mM each) at 10 mV/s and (b) effect of potential scan rate (from 10 to 160 mV/s) for 50 mM of each compound.

Chapter 8

Single-component Fe, Co, Ni nanowires

In the beginning, single-component nanowires with two different diameters (100 nm and 120 nm) and a length of 6 µm were prepared. The electrodeposition parameters were selected to ensure the optimal condition for the growth of individual elements and the best possible filling of the pores, which is why they differ from each other, as shown in Table 6.1.

8.1. Electrochemical analysis

In electrodeposition processes, during the pore filling, the current and charge values were measured as a function of time (Fig. 8.1). In the current transient, the five different zones described in Chapter 2.3 can be distinguished. The region, where the current suddenly begins to increase was used to identify the complete filling of the pores and was a signal to stop the deposition process. Interruption of the electrodeposition process at this point allowed us to avoid the creation of the caps on the membrane surface (overdeposition).

The deposition time for smaller-diameter nanowires (100 nm) is shorter than for nanowires with larger diameters (120 nm) for all three elements. This is directly connected with the membrane porosity, larger in the case of 120 nm nanowires. The membrane porosity is also responsible for the lower current density measured for nanowires with larger diameters. The increasing current value with deposition time can be related to the shortening of the diffusion length as the pores are filled.

At the same time, the electrical charge, which was reduced into pores, was measured and is presented in insets in Fig. 8.1. The highest deposited charge is observed for iron (0.65 C for 100 nm), then for cobalt (0.55 C), and the lowest for nickel (0.45 C). The recorded charge results from the material reduced into the pores but may also be related to the evolution of hydrogen, which increases strongly at higher pH and more cathodic potential. In our case, the pH values were almost the same for Fe and Co (pH = 2.9 and 2.8) and much higher for Ni (pH = 3.2) (Table 6.1). A similar tendency can be noticed for nanowires with a diameter of 120 nm. The applied potential was slightly different for Fe and Co (U = 1.1 and -1.0 vs Ag/AgCl) and much higher for Ni (U = -2.0 V). This suggests stronger hydrogen evolution in the case of Ni and may result in a lower filling degree and a more porous nanowire structure, which is reflected in a lower charge reduced in the membranes. The charge reduced in the membranes for individual elements and different pore diameters varied equally over time, but was much larger for thicker nanowires, consistent with the increasing membrane porosity ($P_{100nm} = 3.1$ %, $P_{120nm} = 4.5\%$, see Table 2.2).

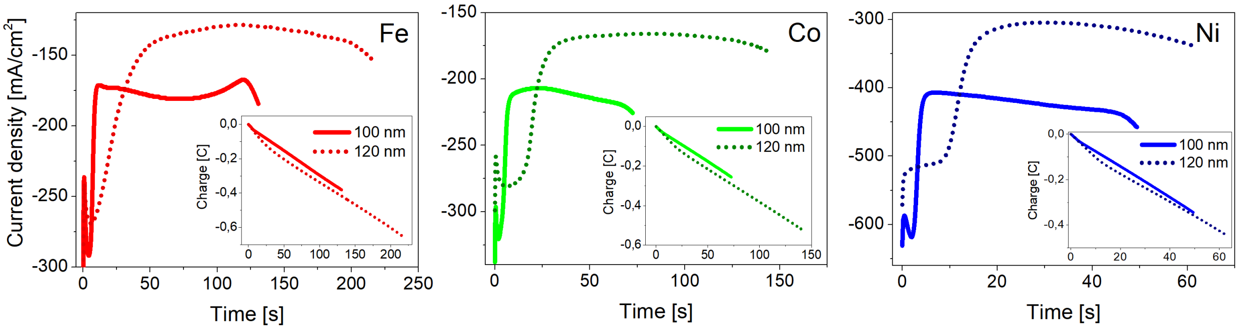

Figure 8.1: Cathodic current densities as a function of time, measured during the electrodeposition of Fe, Co, and Ni nanowires with two different diameters: 100 nm and 120 nm. The insets show the corresponding changes in electric charge over time.

Figure 8.2 shows the values of growth rate for two different diameters of Fe, Co, and Ni nanowires. Growth rate calculated as L/t, (where L is the nanowire length and t is the deposition time) varies between elements, which results from different overpotentials. As mentioned above, the growth rate for all elements is higher for smaller diameter nanowires and increases by 25%, 65%, and 100%, for Ni, Fe, and Co, respectively. This can be connected with the greater porosity of the membranes with a larger diameter, which may cause overlapping of spherical diffusion zones at the throat of nanopores (Fig. 2.7) resulting in a thicker outer diffusion zone and a slower growth rate [43].

The current as a function of time plots presented in the normalized form as $(i/i_{max})^2$ versus (t/t_{max}) allows determining the nucleation type using equations (2.21) and (2.22). Figure 8.3 shows the relationship between $(i/i_{max})^2$ and (t/t_{max}). Despite the small difference between the nanowire diameters, these dimensionless plots show significant differences. The curves obtained for smaller pore diameters from narrow peaks indicating progressive nucleation, while for larger pore diameters with broad peaks, instantaneous nucleation is predicted. These two types differ in the frequency of nucleation appearance

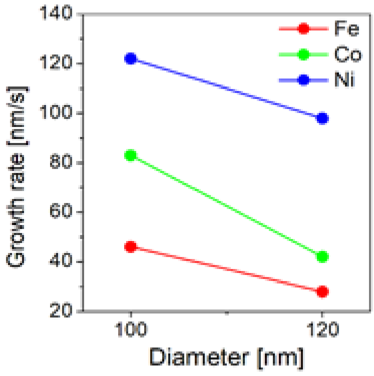

Figure 8.2: Growth rate for Fe, Co, and Ni nanowires as a function of their diameter.

and the rate of active site depletion. In the case of the progressive nucleation type, nuclei are formed continuously during the crystalline growth, whereas in the instantaneous type, nucleation occurs fast at a relatively small number of active sites, which are formed and exhausted at a very early stage of the deposition process. Therefore, an increase in the pore diameter causes a change in the nucleation mechanism from a progressive one, dominating in nanowires with a smaller diameter, to an instantaneous one, prevalent in larger nanowires. The instantaneous nucleation type favors crystal growth, leading to larger and more oriented crystallites. This suggests a fine crystalline structure for nanowires with a diameter of 100 nm and large columnar crystals for 120 nm nanowires. Such a difference in the nanowire morphology can also be expected based on the growth rate, which is higher in the case of nanowires with smaller diameters (Fig. 8.3).

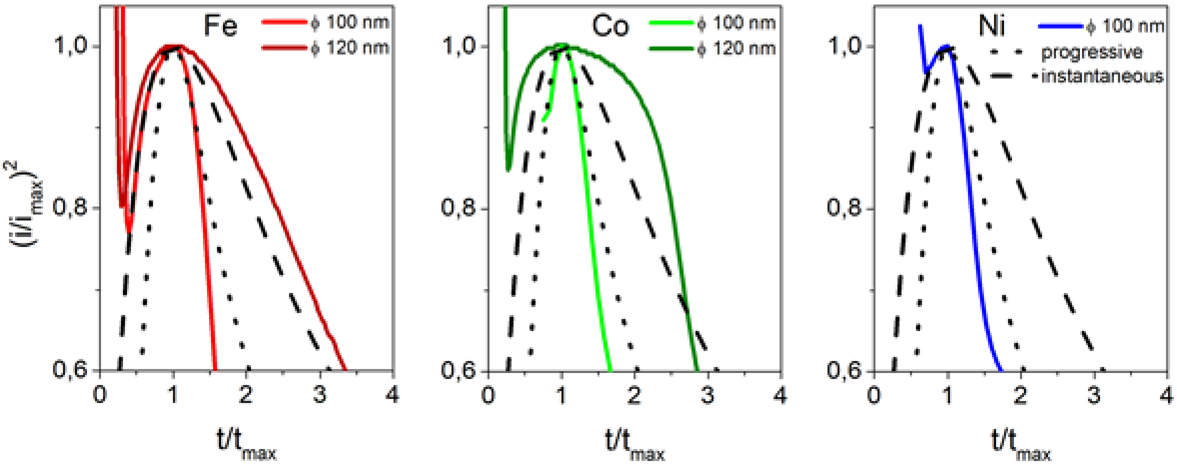

Figure 8.3: The dimensionless peaks (derived from the current transients) for Fe, Co, and Ni nanowires with different diameters presented with theoretical curves calculated for a progressive (dotted curve) and instantaneous nucleation (dashed curve).

8.2. Morphological and structural studies

After the deposition of the nanowires, the surfaces of the filled membranes were observed using an SEM microscope. Figure 8.5 shows images of the membrane surface after the electrodeposition process of (a) iron, (b) cobalt, and (c) nickel, with structures growing on nanowires visible in some places on the membrane surface. They appeared due to the extension of the electrodeposition process for several seconds. It can be observed that the created structures differ in shape. Iron caps resemble cauliflowers, showing a clear trace of oxidation in the form of an oxide coating covering metallic caps. The XPS studies performed on this surface revealed a high-spin spectrum of Fe2p with multiplet splitting (Fig. 8.4). The peaks at a binding energy of 710.9 and 724.6 correspond to the $Fe2p_{3/2}$ and $Fe2p_{1/2}$ photoelectron states, which together with the shake-up satellite of Fe2p3/2 confirmed the presence of iron in the oxidation state +3 (Fe_2O_3) [178, 179]. The structures growing on the Co nanowires take the form of regular crystals whose atomic planes show three-fold symmetry, while the nickel caps have the shape of spheres.

Insightful observation of the overdeposited cap allows prediction of the nanowire structure and preferred growth direction.

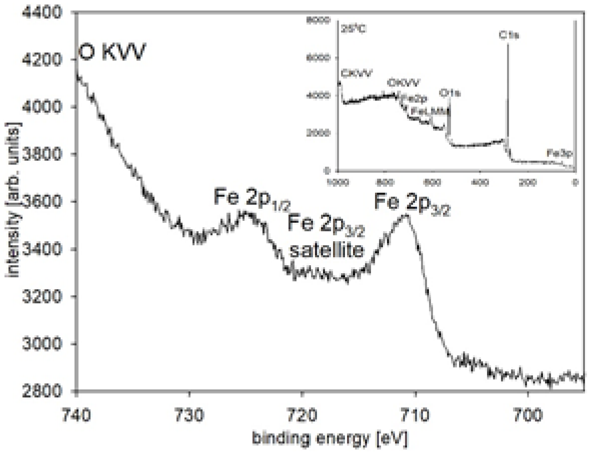

Figure 8.4: XPS spectra of Fe nanowires measured on the overdeposited caps formed on Fe nanowires with the survey scan presented in the inset [32].

The presence of overdeposited structures also may result from the deviation of the nanowire axis from the normal direction, caused by the imperfect orientation of nanochannels. The overdeposition can affect the results of the investigations, especially in the case of magnetic measurements, therefore stopping the process at the right moment is a crucial task in the nanowire preparation.

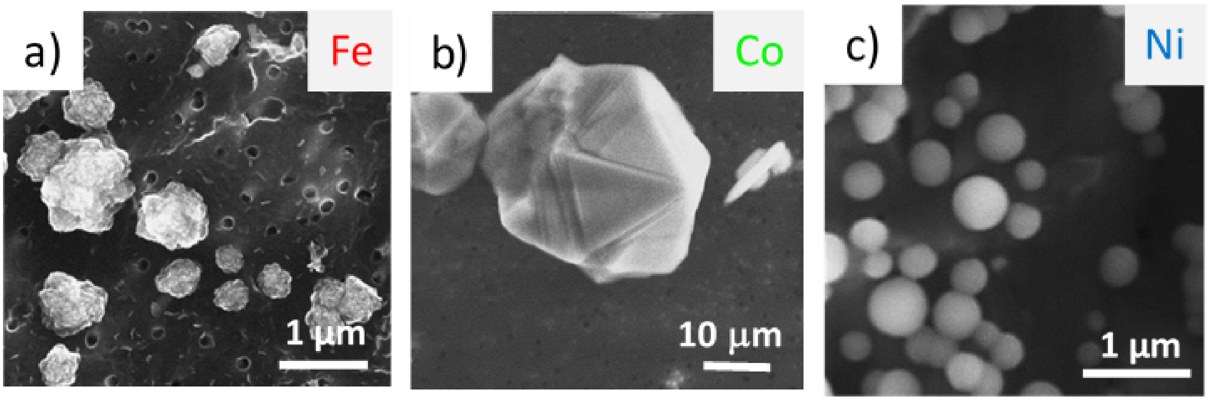

Figure 8.5: SEM images of the membrane surface after the electrodeposition process of (a) Fe, (b) Co, and (c) Ni nanowires, showing the overdeposited caps.

To observe the morphology of nanowires, polycarbonate membranes were dissolved in dichloromethane. SEM images show that there are no significant differences between the nanowires made of different elements (Fig. 8.6). All nanowires are smooth and continuous, without noticeable porosity, which means that the conditions of the deposition processes have been well selected.

The structure of the Fe, Co, and Ni nanowires with a diameter of 100 nm, was analyzed based on X-ray diffraction measurements. The diffractograms are presented in Fig. 8.7.

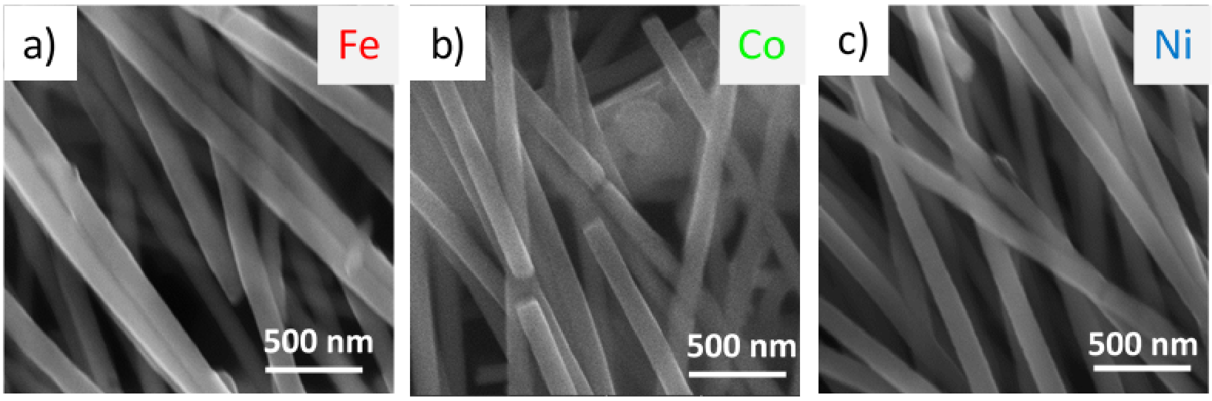

Figure 8.6: SEM images of the (a) Fe, (b) Co, and (c) Ni nanowires with a diameter of 100 nm observed after membrane dissolution.

In all samples, the most intense peaks, marked with an asterisk, originate from the copper contact layer sputtered on the membrane, before electrodeposition. Peaks characteristic of the studied elements described with Miller indices are listed in Table 8.1 in comparison with reference data with corresponding 2θ angles and relative intensities. They identify the polycrystalline nature for all samples with a bcc, hcp/fcc, and fcc structure for Fe, Co, and Ni, respectively. Among the peaks characteristic for particular phases, only the most intense peaks were recorded. The low intensity of the peaks results from the small amount of the studied material, constituting approximately 3% of the sample surface.

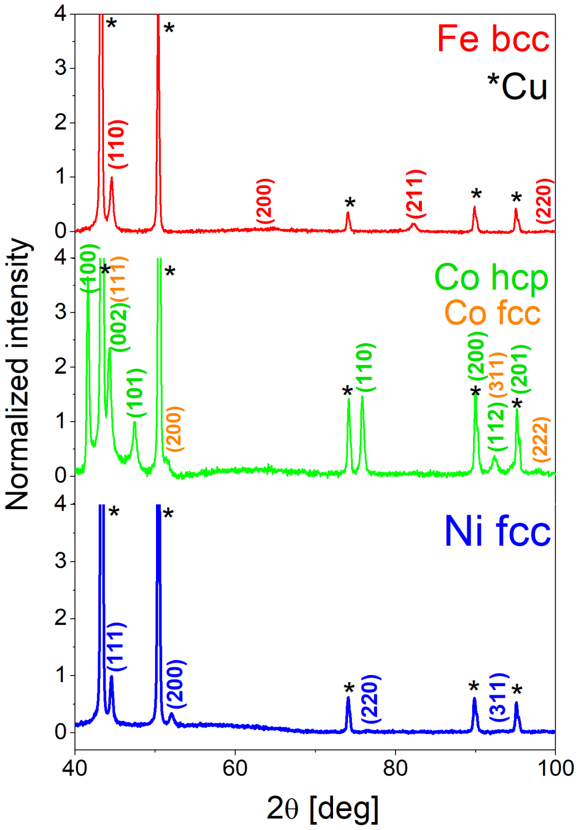

Figure 8.7: X-ray diffraction patterns measured for the Fe, Co, and Ni nanowires embedded in the polycarbonate membranes ($\phi = 100$ nm). The indexed peaks correspond to the Fe bcc, Co hcp, Co fcc, and Ni fcc phases (reference code: 03-065-4899, 00-005-0727, 00-001-1259, 03-065-0380 NIST Database), while the peaks marked with asterisks come from the copper layer (00-004-0836 NIST Database).

The positions of the peaks correspond well to the 2θ angles of the reference samples, showing no significant deviation from the lattice parameter of bulk materials. The relative intensities of the peaks taken from diffractograms for Fe and Ni are quite close to the reference samples (with larger deviation for Ni nanowires) suggesting rather isotropic polycrystalline growth of Fe and Ni. In both cases, the diffractograms show only the two most intensive peaks assigned to reflections from (110) and (211) planes for Fe nanowires and (111) and (200) for Ni nanowires. The situation changes for the Co sample, in which two phases with a clear dominance of the hcp structure were identified. In this structure, a distinct texture with a preferred direction along [100] can be distinguished. The (002) peak also shows a significant contribution, but it may be a superposition with the (111) peak of the fcc phase. The Co fcc structure is difficult to identify due to the overlap between the Co fcc peaks and those originating from the Co hcp phase and peaks coming from Cu. The appearance of these structures can be associated with the adjusted pH value (pH = 2.8, Table 6.1), which in this range favors the growth of both types of structures (Chapter 3).

In these samples, the crystallite size was estimated based on the Scherrer equation. The results of the calculations allowed us to estimate the crystallite size for iron and

Table 8.1: Results of XRD measurements of Fe, Co, and Ni nanowires with a diameter of 100 nm with the corresponding reference data. The values in the parentheses are the relative intensities.

hkl	**2θ**	
	Reference	Nanowires
	Fe bcc	
110	44.66 (100)	44.67 (100)
200	65.01 (12)	-
211	82.31 (17)	82.38 (15)
220	98.92 (5)	-
	Co hcp	
100	41.69 (20)	41.55 (365)
002	44.76 (60)	44.34 (235)
101	47.57 (100)	47.45 (100)
110	75.94 (80)	75.87 (150)
200	90.62 (20)	90.22 (155)
112	92.54 (80)	92.36 (40)
201	94.74 (60)	94.40 (125)
004	98.74 (20)	-
	Co fcc	
111	44.37 (100)	44.34 (100)
200	51.29 (8)	51.33 (15)
220	75.37 (83)	-
311	92.09 (100)	92.36 (16)
222	98.09 (8)	97.90 (6)
	Ni fcc	
111	44.35 (100)	44.51 (100)
200	51.67 (42)	51.89 (35)
220	76.10 (16)	76.24 (6)
311	92.56 (14)	-
222	98.02 (4)	-
	Cu fcc	
111	43.29 (100)	43.30 (100)
200	50.43 (46)	50.41 (33)
220	74.13 (20)	74.08 (3)
311	89.93 (17)	89.88 (3)
222	95.14 (5)	95.11 (2)

cobalt at 23-24 nm, and 27 nm (±1 nm) for Ni nanowires.

As shown, the Fe, Co, and Ni nanowires crystallize in different structures (excluding a small fraction of the Co fcc phase), which combined with various magnetic moments (Table 5.1) should result in different magnetic parameters of individual materials.

8.3. Magnetic measurements

Magnetic measurements of Fe, Co, and Ni nanowires were performed at room temperature with the magnetic field applied along the nanowire axis and perpendicular to it. The hysteresis loops of Fe, Co, and Ni nanowires embedded in the membranes are presented in Fig. 8.8. A clear magnetic anisotropy with an easy axis along the nanowires was observed for all nanowires. As shown in earlier chapters, the effective anisotropy of nanowires is affected by three factors: magnetocrystalline anisotropy, shape anisotropy, and dipolar interactions. In the case of polycrystalline samples without a preferred growth direction, magnetocrystalline anisotropy can be neglected. Therefore, shape anisotropy and dipolar interactions are the main parameters determining the magnetic behavior of Fe and Ni nanowires, while in Co nanowires, magnetocrystalline anisotropy can also play a significant role. The easy magnetic axis of the Co hcp structure aligns along the [002] direction, which may contribute to the ordering of the magnetization vector along the NWs axis, but the distinct texture along the [100] direction, which is the hard magnetic direction, implies the c-axis alignment perpendicular to the nanowire axis. This contributes to the ordering of the magnetization vector along an axis perpendicular to the nanowire axis, weakening an effective anisotropy with an easy axis along nanowires.

Additionally, as can be seen, the hysteresis loops measured along nanowires deviate slightly from the perfect square shape. Their slope can indicate the presence of dipolar interactions between nanowires, but the relatively low porosity should rather cause their reduction. Therefore, the parameter that finally determines the effective anisotropy turns out to be shape anisotropy, which favors the orientation of the magnetization direction along the nanowire axis.

The coercivity (H_c) and squareness (M_r/M_s) values for individual nanowires are presented in Table 8.2. The greatest coercive value measured with a magnetic field applied along the nanowires was obtained for Co nanowires, while squareness does not change much. The relatively high values of (M_r/M_s) confirm the marginal contribution of dipolar interactions to the effective anisotropy.

Table 8.2: Values of magnetic parameters: coercive field (H_c) and squareness (M_r/M_s) for Fe, Co, Ni nanowires, measured with a magnetic field applied in the membrane plane and out of it.

Nanowire	Easy axis	H_c in [Oe]	H_c out [Oe]	M_r/M_s in	M_r/M_s out
Iron	Along the NWs	773	435	0.20	0.73
Cobalt		590	645	0.11	0.79
Nickel		530	530	0.28	0.8

These values significantly differ from the parameters related to bulk materials (Table 5.1) and from maximal coercivities obtained in nanowires [180] cited in Chapter 5.1. The differences result from many parameters such as sample state (bulk/nanostructures) the nanowire geometry, their distribution, structure, and morphology, which determine the properties of the nanowires and can be relatively easily modified by electrodeposition parameters.

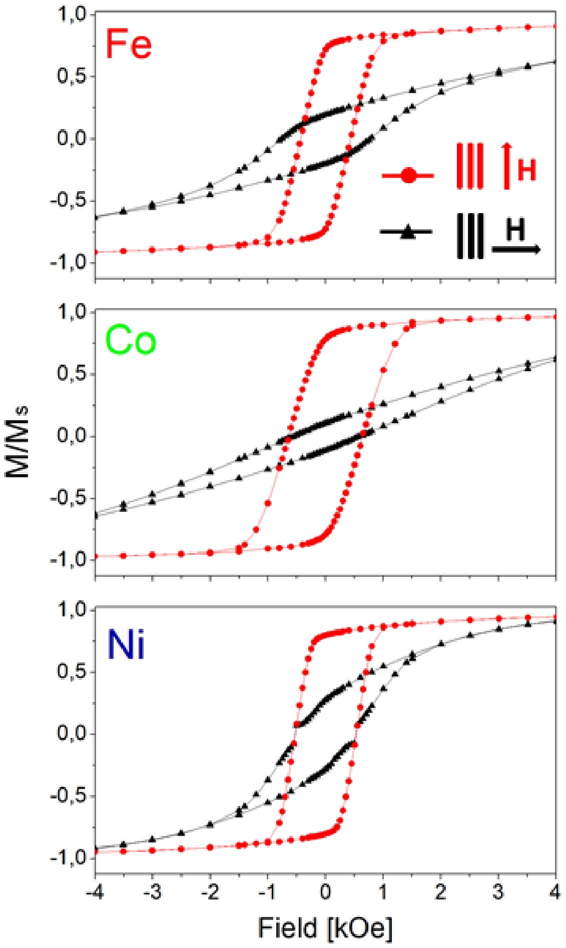

Figure 8.8: Hysteresis loops measured at room temperature with a magnetic field applied in the membrane plane (magnetic field applied perpendicular to the nanowire axis) and out of the membrane plane (magnetic field applied parallel to nanowire axis) for Fe, Co, and Ni nanowires with a diameter of 100 nm. The magnetization (M) value was normalized to the saturation magnetization (M_s).

8.4. Temperature dependance

As shown in Fig. 8.5, the overdeposited caps created on Fe nanowires are covered with an oxide layer. Oxidized materials change their magnetic properties. A positive example of the application of the Fe nanowire oxidation are the corrosion sensors, described in Appendix. However, this may be a problem in the case of the 3D race track memory units. To verify the stability of Fe nanowires especially their resistance to oxidation in terms of their future applications, temperature studies were performed. Nanowires with a pore diameter of 120 nm and a length of 6 µm were deposited in polycarbonate membranes from electrolyte (Table 6.1) whose temperature varied from 15^o to 40^o.

Electrochemical analysis

During electrodeposition, the cathodic current (Fig. 8.9 a) and electric charge transients

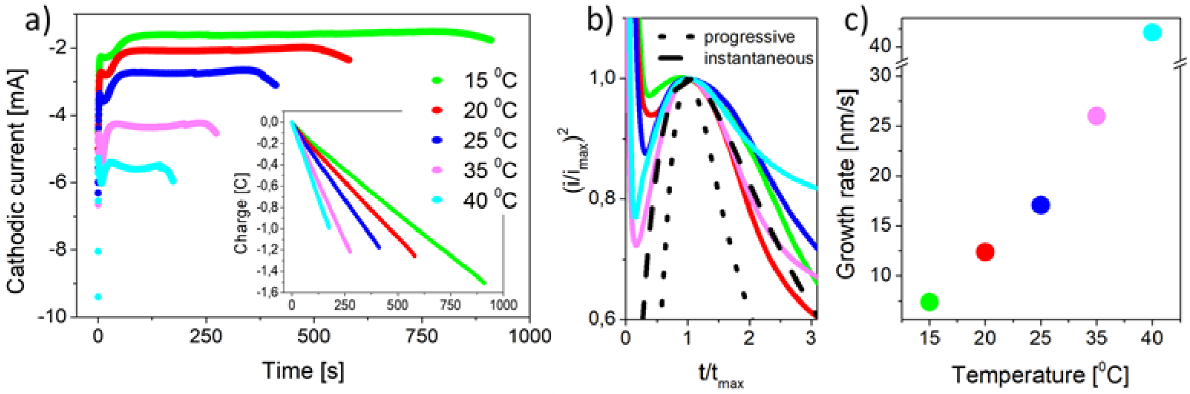

Figure 8.9: (a) Cathodic current and electrical charge (inset) reduced into porous membranes versus time measured during the deposition of Fe nanowires prepared at different electrolyte temperatures; (b) dimensionless peaks (derived from current transients) with theoretical curves for instantaneous (dashed curve) and progressive nucleation (dotted curve); (c) growth rate as a function of electrolyte temperature.

(Fig. 8.9 a - inset) were recorded at various temperatures as a function of time. Lowering the electrolyte temperature significantly extended the electrodeposition time and resulted in a lower cathodic current. At higher temperatures, the conductivity of the solution increases due to the increasing ion activity resulting in a higher cathodic current recorded at the same potential applied. At higher ion activity, the energy required to drive the reaction is lower and a lower overpotential is needed. Thus, the same potential applied at higher temperatures can result in the intensification of the hydrogen evolution [181, 182].

The charge measured during the process (shown in the inset of Fig. 8.9 a) at intermediate temperatures (20^{o}C - 35^{o}C) shows almost the same values, while at marginal temperatures it differs significantly. At low temperature, a high value of reduced charge is recorded, which may imply an increase in the degree of pore filling and a less porous material due to lower hydrogen evolution [75]. Lowering the deposition temperature elongates the diffusion layer, effectively reducing the ion concentration gradient and ion diffusion rate, which favor the uniform growth of the nanowires [73]. On the other hand, at high temperature, the reduced charge is small although, the process was stopped when a sudden increase in the current indicated a complete pore filling. This could mean the more porous structure and lower filling degree probably because of the high hydrogen evolution at elevated temperatures [181, 182], which block the pores and hinder the deposition process.

The electrolyte temperature can also affect the nucleation process [73]. In Fig. 8.9 b. the relationship between $(\mathrm{i}/\mathrm{i}_{max})^2$ and $(\mathrm{t}/\mathrm{t}_{max})$ was presented. In the studied temperature range, the experimental curves are close to the theoretical curve predicted for instantaneous nucleation, in which nucleation is rapid and on a relatively small number of active sites, which are exhausted early in the process [183]). Such a kind of nucleation process promotes the uniform growth of large columnar crystals. The changes in the electrolyte temperatures did not significantly influence the nucleation mechanism.

The increasing deposition temperature increases the growth rate of nanowires (Fig. 8.9 c). The temperature directly affects the diffusion of metal ions, causing their increase at higher temperatures. The ion diffusion together with the migration controlled by the overpotential, determines the rate of electrolytic deposition [38, 73].

Morphology

Figure 8.10 shows SEM images of nanowires after membrane dissolution, deposited at 15^{o}C (a, d), 25^{o}C (b, e), and 40^{o}C (c, f). The morphology of nanowires did not reveal any significant changes as a function of the electrolyte temperature. Densely packed nanostructures were observed in all cases, and the standing nanowires created uniform nanowire arrays (Fig. 8.10 a, b, c). At higher magnification, the nanowires exhibited a continuous structure with a smooth, lateral surface without any traces of porosity (Fig. 8.10 d, e, f).

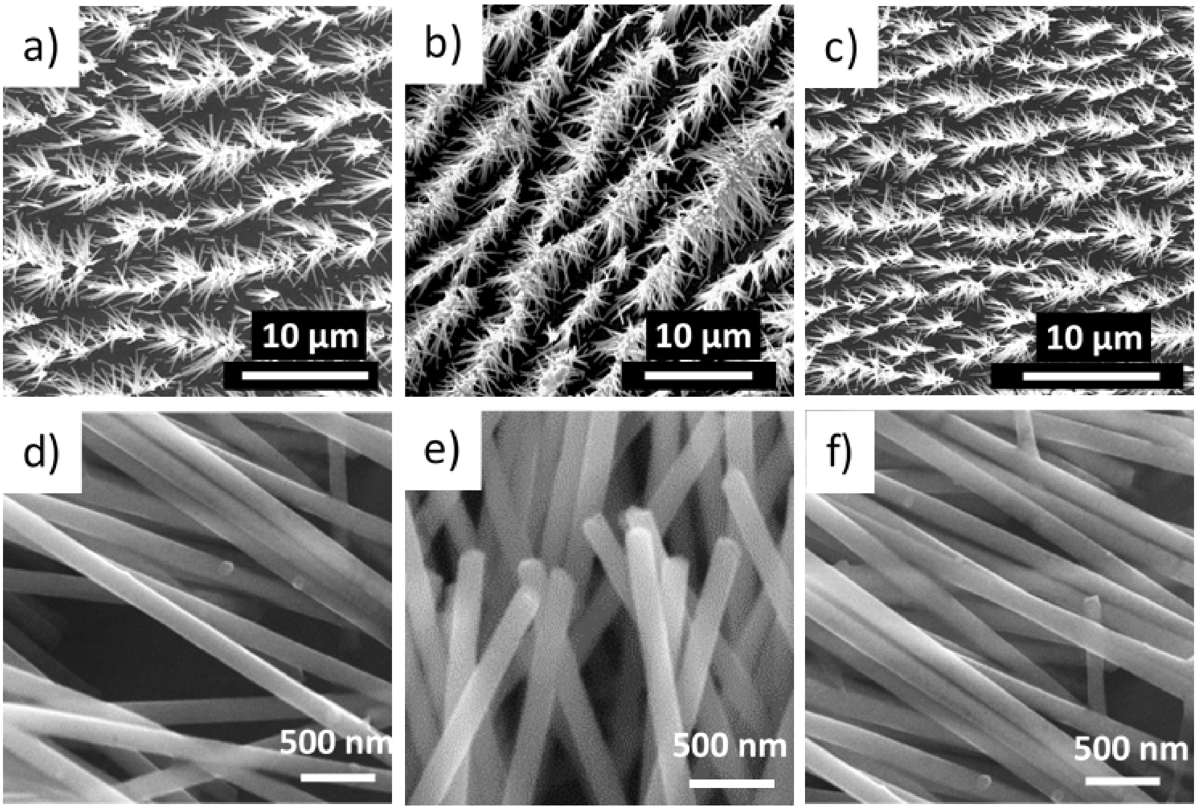

Figure 8.10: Scanning electron microscopy images of Fe nanowires observed after membrane dissolution measured for nanowires deposited at different electrolyte temperatures: (a, d) 15^{o}C, (b, e) 25^{o}C, and (c, f) 40^{o}C.

The nanowires observed at this scale did not show any morphological features (porous structure, low pore-filling degree) expected based on electrochemical analysis.

The morphology of nanowires visible in SEM images after membrane dissolution did not show any trace of oxide formation, although an oxide layer covered overdeposited caps growing on the Fe nanowires (Fig. 8.5 a). However, the nanowire diameter estimated from SEM images was larger, than the nominal one, suggesting the presence of a coating formed on the nanowire surface. To identify its chemical composition, X-ray photoelectron spectroscopy measurements were performed (Fig. 8.11).

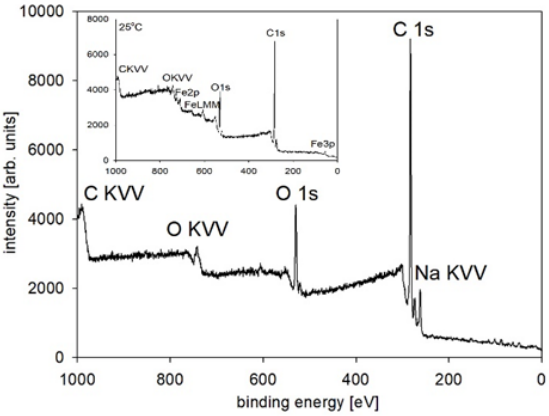

Figure 8.11: XPS spectra of Fe nanowires measured after membrane dissolution [32].

The XPS spectrum showed peaks that were neither characteristic of Fe oxide nor of metallic Fe, indicating the presence of a thin iron-free layer on the nanowire surface. The recorded peaks, especially the high-intensity peak from carbon, indicate a polycarbonate layer covering the surface of the nanowires and was probably formed during the process of membrane dissolving. The low-intensity sodium peak is characteristic of membrane contamination introduced during the etching of ion traces. This confirms the presence of a polycarbonate coating in the samples. The thickness of the polycarbonate coating estimated based on the SEM image and XPS sensitivity is in the range of 20-30 nm. This coating protects the Fe nanowires from oxidation, which is confirmed by the absence of peaks at 710.9 and 724.6 eV (inset Fig. 8.11) corresponding to the iron in the oxide state.

Figure 8.12 a and b present the TEM overview of the nanowires and prove their continuity. The diffraction patterns for all samples consisted of semicontinuous rings and elongated spots, which confirmed the polycrystalline Fe bcc structure of the nanowires (Fig. 8.12 c). Figures 8.12 e, f exhibit the high-magnification bright-field TEM images of nanowires deposited at extreme deposition temperatures. They are characterized by a fine-crystalline structure, with columnar crystallites growing along the nanowires. These crystallite sizes ranged from a few to 30 nm. No significant differences were noticed in the microstructure of Fe nanowires as a function of the electrolyte temperature. Additionally, on the lateral surface of a nanowire, a thin amorphous layer with approximately 15 nm thickness, identified as a polycarbonate, is visible (Figure 8.12 d).

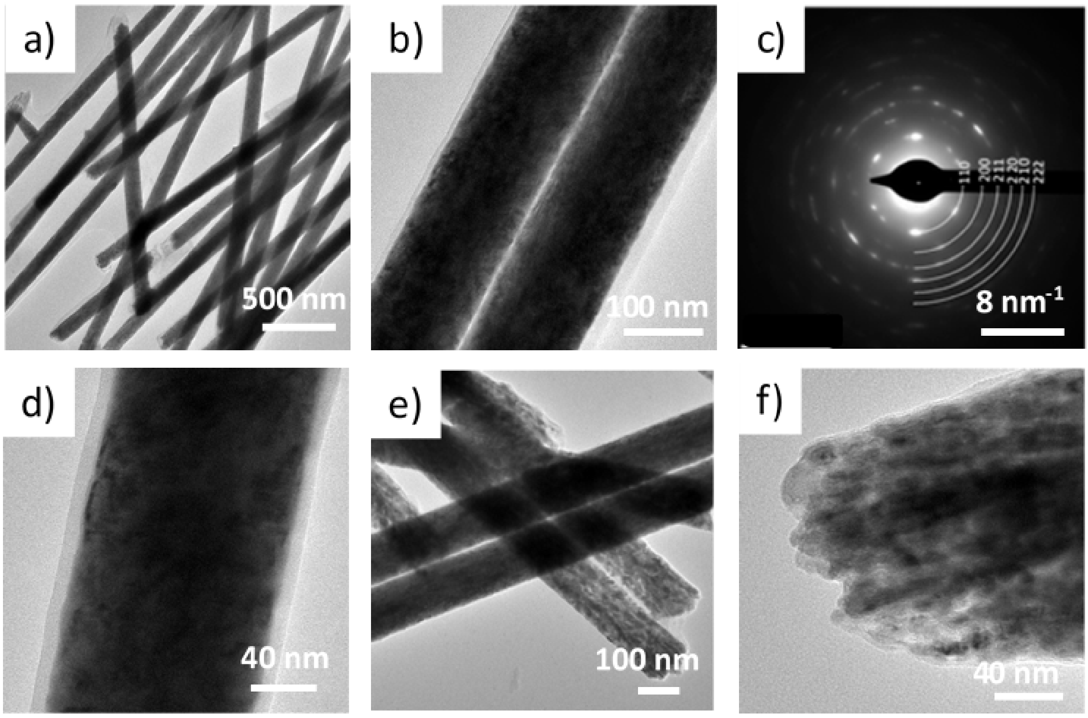

Figure 8.12: TEM images of Fe nanowires in the bright-field mode with the diffraction pattern (c) indexed with the lattice parameters of the Fe bcc structure (a, e) 25^{o}C, (b) 35^{o}C, (c) 20^{o}C, (d) 20^{o}C, (f) 15^{o}C.

Structure and phase analysis

The structure of the nanowires was also analyzed based on X-ray diffraction. Figure 8.13 shows the XRD spectra of the nanowires deposited at the lowest, medium, and highest electrolyte temperatures (15^{o}C, 25^{o}C, and 40^{o}C). The most intensive peaks, marked with asterisks as above, originate from the copper contact layer. The indexed peaks correspond to the polycrystalline Fe in the bcc structure and appear in all spectra with little difference in their intensity and width. Relative peak intensities correlated with a powder sample (reference code 03-065-4899 NIST Database) suggest a slight texture with a preferred growth along the [211] direction. Additionally, the texture coefficient was calculated using the Harris formula [184]. Calculations show that the growth in the preferred orientation weakens with increasing temperature, and becomes almost isotropic for the highest temperature.

For the most intensive peaks (110) and (211), shown in the insets of Fig. 8.14, a slight broadening was observed with increasing electrolyte temperature, suggesting a decrease in crystallite size. Figure 8.14 shows the mean values of the crystallite sizes calculated based on the Scherrer equation. The highest values, equal to approximately 25 nm, were obtained for nanowires prepared at lower electrodeposition temperatures (15^{o}C and 20^{o}C), and the lowest values, of about 20 nm, were calculated for samples deposited at higher temperatures (25^{o}C, 35^{o}C, 40^{o}C).

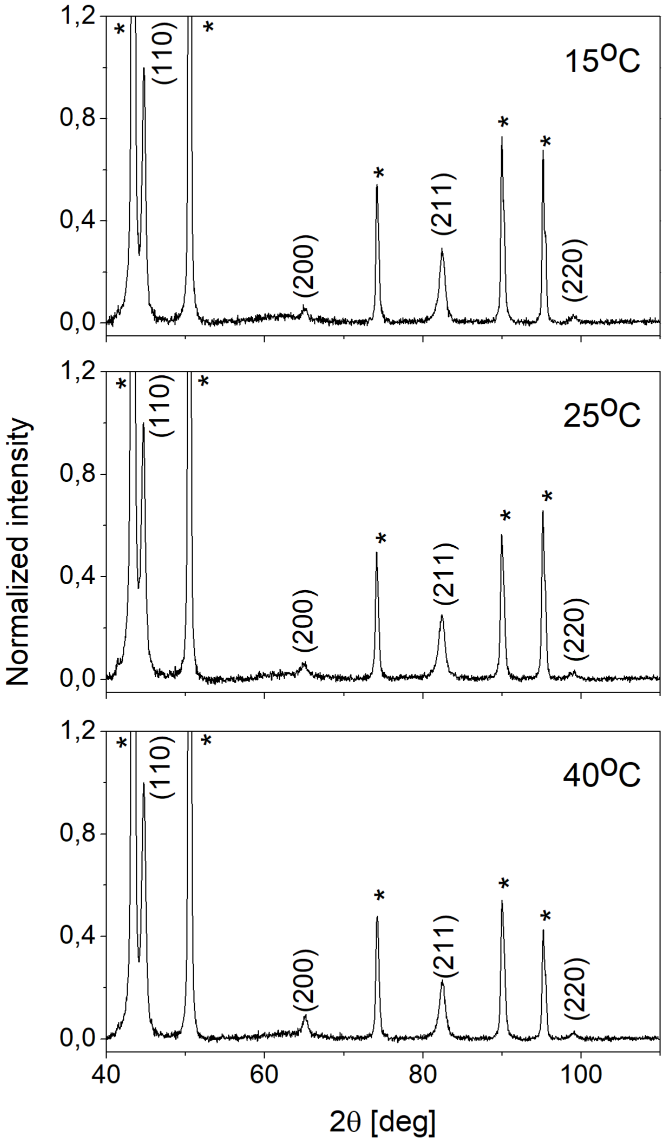

Figure 8.13: X-ray diffraction spectra measured for Fe nanowires embedded in polycarbonate membranes. The indexed peaks correspond to Fe-bcc (reference code: 03-065-4899 NIST Database) while the peaks marked with an asterisk come from the copper contact layer.

Our studies revealed a tendency for the crystallite size to decrease with increasing electrolyte temperature. Increasing electrodeposition temperature is associated with the increase in the electrodeposition rate, which may be the main reason for the observed crystalline reduction. Additionally, increasing hydrogen evolution can also block crystalline growth, resulting in a fine crystalline structure. Similar observations were reported by Azevedo et al. [75] in the studies of Fe nanowires deposited in alumina membranes.

Iron nanowires were also studied using Mössbauer spectroscopy. Figure 8.15 presents the Mössbauer spectra, measured at room temperature for nanowires embedded in PC membranes. The spectra were fitted with two components described by the hyperfine parameters (Table 8.3).

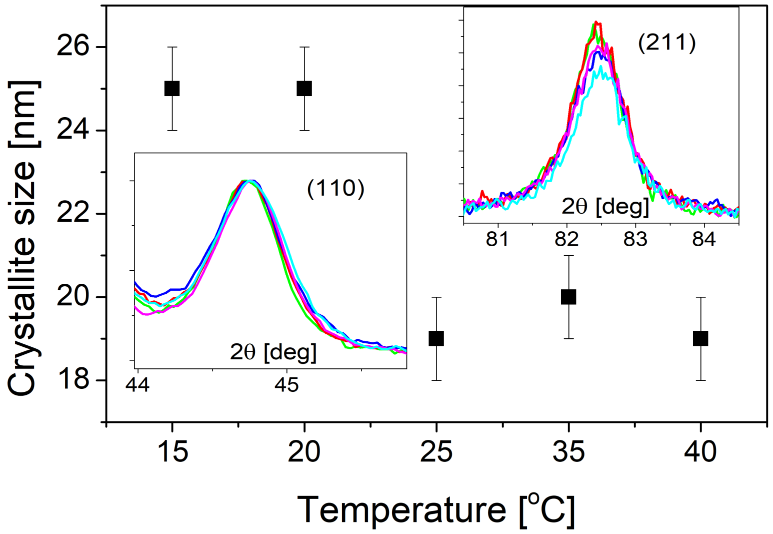

Figure 8.14: Average crystallite size calculated according to the Scherrer equation based on the (110) and (211) peaks [32].

The dominant component of the spectra is a sextet with a relative contribution of about 80%. This component is characterized by a hyperfine magnetic field that is equal to approximately 33 T, an isomer shift close to -0.10 mm/s, and nearly 0 vales of quadrupole splitting, which together are typical for bulk-like Fe atoms [185, 32]. This component is related to the Fe nucleus surrounded by Fe atoms that are arranged in a regular structure. The intensity ratio of second and third line (A2/A3), shown in Table 8.3, informs about the relationship between the γ-ray propagation and magnetization vector orientation (θ). The estimated value of θ changed from 30^o to 33^o, indicating the deviation of the magnetization vector from the normal direction.

The second component of the spectrum is a doublet characterized by an isomer shift and quadrupole splitting. The doublet indicates Fe atoms in a paramagnetic or superparamagnetic state. While sextets have been assigned to Fe atoms inside the nanowires, doublets could be associated with the Fe atoms at the edges or in voids that have a limited number of Fe atoms in a ferromagnetic state in close proximity to the nucleus.

The studies did not reveal the presence of iron oxide regardless of the electrolyte temperature. The low effect and noisy spectrum, caused by the small amount of ^{57}Fe (low porosity and abundance), make it impossible to study hyperfine parameters as a function of the electrolyte temperature.

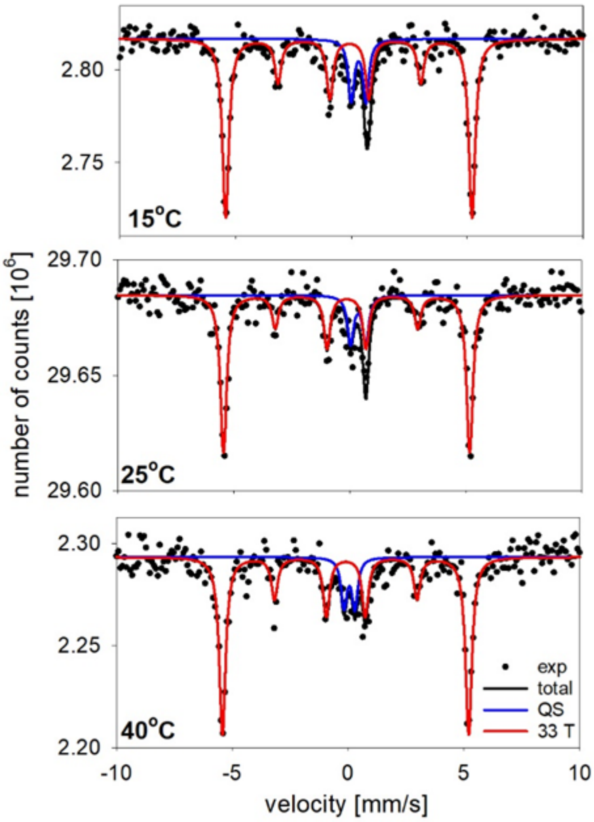

Figure 8.15: Mössbauer spectra measured at room temperature for nanowires embedded in polycarbonate membranes shown with their fit [32].

Table 8.3: The hyperfine parameters of the spectra measured for nanowires deposited at different temperatures.

Temperature	Subspectra	IS [mm/s]	QS [mm/s]	B_{hf} [T]	A_2/A_3	θ	Relative contribution
15^o	doublet	0.31	0.63	-	-	-	16
	sextet	-0.10	-0.01	32.97	0.7	33	84
20^o	doublet	0.26	0.65	-	-	-	23
	sextet	-0.10	0.00	32.98	0.6	30	77
25^o	doublet	0.37	0.65	-	-	-	16
	sextet	-0.13	0.00	32.94	0.6	30	84
35^o	doublet	0.06	0.46	-	-	-	13
	sextet	-0.11	-0.01	32.93	0.7	33	87
40^o	doublet	0.06	0.46	-	-	-	14
	sextet	-0.10	0.00	32.96	0.7	33	86

Magnetic measurements

Magnetic measurements of these samples were performed at room temperature with the magnetic field applied along the nanowire axis and perpendicular to it. Figure 8.16 exhibits the hysteresis loops of the Fe nanowires deposited at the lowest, medium, and highest temperatures. Magnetic anisotropy with an easy axis along nanowires was observed for all nanowires, regardless of the deposition temperature.

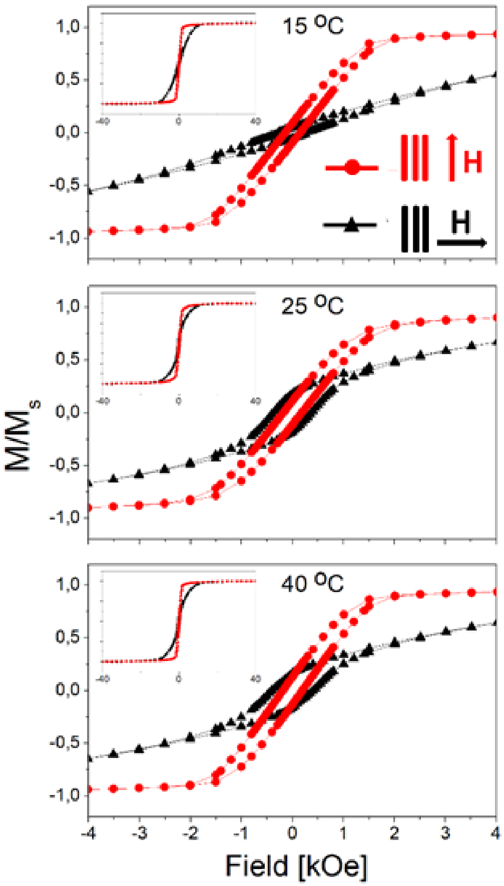

Figure 8.16: Hysteresis loops measured at room temperature in the membrane plane and out of it for nanowires with a diameter of 120 nm, deposited at different electrolyte temperatures.

The polycrystalline structure of the Fe nanowires with a slight texture along the [211] direction, which is not an easy direction, allows the magnetocrystalline anisotropy to be neglected. Therefore, effective anisotropy may result from dipolar interaction and shape anisotropy [186]. The hysteresis loops measured with a magnetic field applied along the normal to the membrane plane are saturated at a field of approximately 2 kOe. The narrow hysteresis loops cause the small coercivity values.

The inclination of the hysteresis loops, measured with the magnetic field applied along the normal to the membrane plane, suggests a deviation of the magnetization vector from the normal direction or a notable contribution of the dipolar interaction in the magnetic behavior of the Fe nanowire matrix. However, the low porosity of the membrane, and consequently, the large average distance between nanowires, indicates a relatively small influence of the dipolar interactions decreasing with the cube of distance. Considering the results of Mössbauer measurements, it can be concluded that the observed loop inclination was mainly related to the previously mentioned deviation of the nanowire axis from the normal direction, which could result in an inclination of the easy magnetic axis. This deviation may be the reason for the open hysteresis curves measured in both directions. The only exception for the curve measured in the membrane plane for nanowires deposited at 15^{o}C indicated a really hard magnetization direction, in which the magnetization rotated coherently towards the field.

The coercivity values are presented in Fig. 8.17 a as a function of electrolyte temperature. These low values can be explained by the deviation of the nanowire axis from the normal direction but they can also be related to the geometric parameters of the nanowires, in particular their aspect ratio (L/ϕ). If its value exceeds 28, the coercivity decreases significantly [98], and in the range of 30 - 120, it decreases twice [31]. Thus, the aspect ratio of these nanowires of 60 may be the main factor, apart from the nanowire tilt, responsible for the low value of the coercive field.

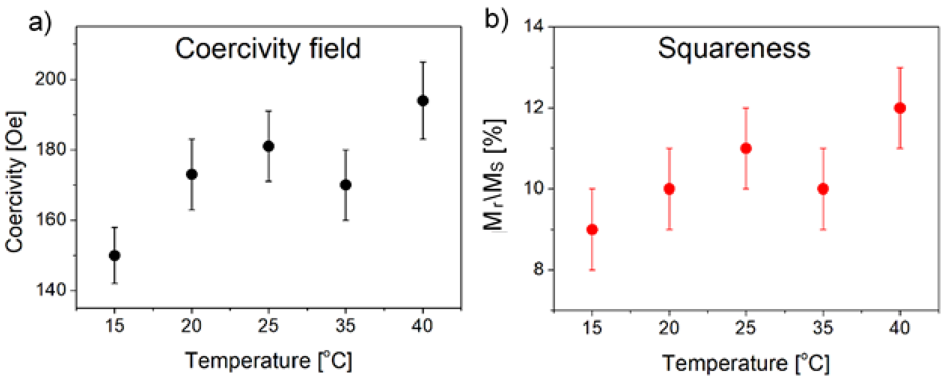

Figure 8.17: (a) Coercivity and (b) squareness values versus electrolyte temperature measured for Fe nanowires with a magnetic field applied out of the membrane plane.

In general, coercivity values measured with a magnetic field applied out of the membrane plane increase with the electrodeposition temperature (Fig. 8.17 a). This may be because nanowires deposited at higher temperatures may have a more porous structure with defects that can block the movement of the domain walls. Schlörb et al. observed higher coercivity values for irregularly shaped nanowires compared to low values for smooth ones [98]. Due to the large tilt of the loops, the squareness (M_r/M_s) parameter shows very small values with a slight increase with increasing temperature, consistent with the coercivity changes (Fig. 8.17 b).

The above studies show that the electrolyte temperature in the selected range does not significantly affect the structure and magnetic properties of nanowires, and importantly, it does not cause iron oxidation. Although the electrical charge indicated a low pore-filling degree and suggested a more defected structure at the highest electrodeposition temperature, no morphological or structural changes were revealed. A slight modification of the magnetic properties combined with morphological and structural stability confirms the stability of Fe nanowires at the studied temperature range.

Chapter 9

Binary systems FeCo, FeNi

9.1. Electrochemical study

After studying single-element nanowires, I investigated the FeCo and FeNi binary alloy nanowires with a diameter of 100 nm to find out how the applied potential influences the nanowire composition and how individual elements affect each other. For this purpose, the nanowires with a length of 6 µm were deposited at various voltages ranging from -1.0 to -2.0 V. Figure 9.1 presents example current vs time plots for FeCo (a) and FeNi (b) NWs. In both cases, an increase in the applied potential resulted in an increase in the recorded current, and consequently, shorter times were needed to fill the pore channels completely. The corresponding electrical charge variations (insets in Fig. 9.1) are linear, suggesting uniform growth of nanowires inside the pores. The final charge values *i.e.* the charge achieved after complete pore filling, decreased with increasing potential, which as in the case of single-element nanowires, may indicate a more porous nanowire morphology and lower degree of membrane filling due to the greater hydrogen evolution [61].

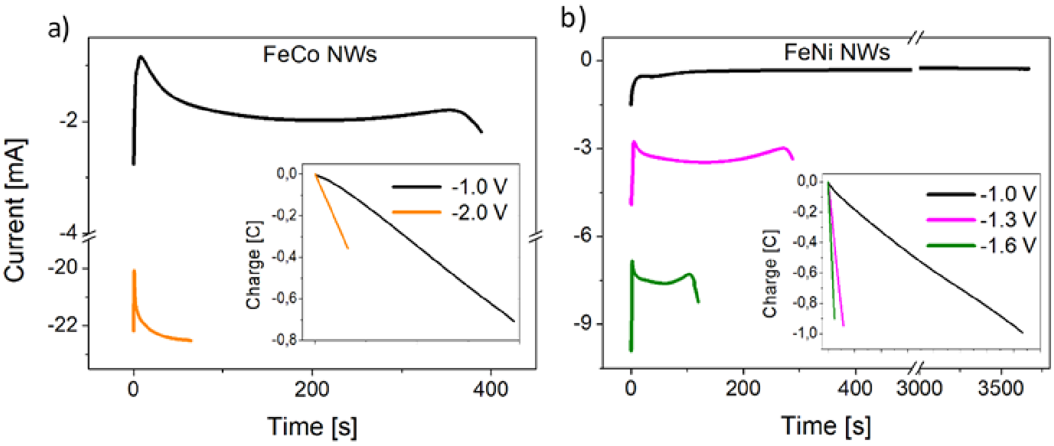

Figure 9.1: Variation of cathodic currents as a function of time measured during the electrodeposition of (a) FeCo and (b) FeNi nanowires with a diameter of 100 nm at different applied potentials. The insets show the corresponding electrical charge variations in time.

Different values of the standard potential of individual ions result in various overpotentials and current densities, which are responsible for different deposition rates as described in Chapter 2.5. A larger overpotential should cause the higher content of atoms with a less noble standard potential, but in the case of FeCo and FeNi alloys, the anomalous co-deposition occurs, thus the changes in the cathodic potential may lead to an unexpected chemical composition modification. Additionally, CV measurements performed for individual elements showed different behavior of Fe, Co, and Ni ions under the applied potential. Therefore, EDS measurements were performed to investigate the chemical composition of FeCo and FeNi nanowires deposited at various potentials or from different electrolytes.

9.2. Chemical composition

EDS studies were carried out on nanowires released from the membranes. Elemental fractions were given in the atomic concentrations. In the case of FeNi nanowires, changes in potential resulted in various compositions of nanowires, in contrast to FeCo nanowires, in which only extreme values of the applied potentials cause significant content changes. A weak sensitivity of the chemical composition of the FeCo nanowires on the applied potential has also been observed in the literature [19, 41, 153]. Thus, to obtain FeCo nanowires with different compositions and, consequently various structural and magnetic properties, different electrolyte compositions were used.

The concentrations of Fe and Ni in FeNi nanowires deposited at different cathodic potentials are plotted in Fig. 9.2. It can be observed that the Ni content increases with the cathodic potential, while the Fe concentration decreases, which is consistent with the literature studies [85, 148]. Changes in the Ni content from 46 to 90 at% suggest that, depending on the Ni concentration, different phases predicted based on the phase diagram (Fig. 5.3) can be stable. This will be discussed in the next section. The content of Fe and Ni in the electrolyte does not reflect the chemical composition of the FeNi nanowires deposited at -1.0 V, indicating the occurrence of anomalous co-deposition. The Fe concentrations in these samples are much higher than the Fe^{2+} ion concentrations in the electrolyte, clearly showing a preferential deposition of iron. At more negative potentials, the Fe content significantly decreases and at higher values, a constant low content is maintained. In this potential range, the atomic concentrations in nanowires reflect the ion concentration in the electrolyte.

The high Fe content can be explained by a larger partial current of Fe ions at low potential due to anomalous co-deposition [187]. At more cathodic potentials, the maximum partial current of Ni ions is achieved, which causes an increase and then saturation of the Ni content. The diffusion limit reached at higher potentials for both Fe and Ni ions results in a potential-independent composition of nanowires [148].

Based on the obtained iron and nickel concentrations, selectivity ratio (SR) values were calculated to indicate the type of electrodeposition. The molar ratio of Fe^{+2}/Ni^{+2} in the electrolyte used to obtain FeNi nanowires was 0.01/0.17. The determined SR coefficients for FeNi nanowires are presented in Fig. 9.2 b.

An SR value close to 1 suggested co-deposition predicted by standard potentials and electrolyte composition, while anomalous co-deposition occurred for a higher SR coefficient. The calculated SR parameters show a high value for low potential and close to 1 for higher potentials. Hence, the observable anomalous co-deposition appears only at the lowest potential, while at high cathodic voltages, the electrodeposition process loses

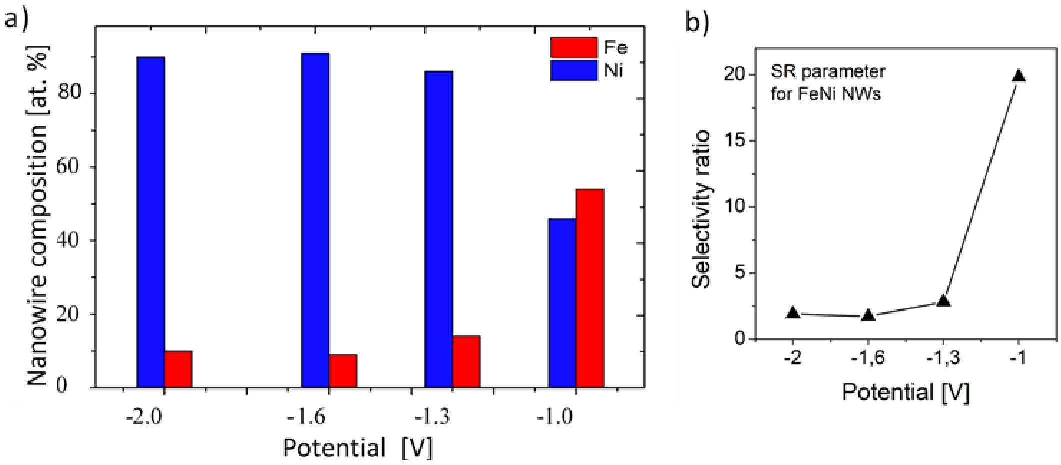

Figure 9.2: (a) Atomic composition of Fe and Ni in FeNi nanowires deposited at different potentials with the lines corresponding to the Fe (red) and Ni (blue) contents in the electrolyte (b) Selectivity ratio of Fe/Ni, calculated for FeNi nanowires. The particular elemental contents were given with an error of no more than ±1.

its anomalous character. These results confirm the influence of voltage on the anomalous co-deposition phenomenon. The FeNi alloy nanowires were found to be sensitive to the applied potential, which should affect the structural and magnetic properties of the FeNi nanowires. (Fig. 9.2 b).

Table 9.1: Chemical concentration of Fe and Co in electrolytes and nanowires.

Potential	Electrolyte composition $[\mathrm{mol/dm^3}]$		Molar ration in electrolyte Fe:Co	Nanowire composition [%]		Atomic ratio in NWs Fe:Co	SR parameter
	$FeSO_4$	$CoSO_4$		Fe	Co		
-1.0 V	0.06	0.12	0.5	47	53	0.9	1.3
-2.0 V	0.06	0.12	0.5	44	56	0.8	1.6
-1.0 V	0.01	0.02	0.5	40	60	0.7	1
-2.0 V	0.01	0.02	0.5	34	66	0.5	1

The chemical compositions of FeCo nanowires and the corresponding electrolyte compositions are shown in Table 9.1. While in the case of FeNi nanowires, the use of extreme potentials resulted in an almost 100% increase in the Ni concentration, the same potentials applied in FeCo systems caused an increase in the Co content (with increasing potential) by a few percent. The selectivity ratio parameters are equal to 1 or slightly higher, but neither of these values indicates anomalous co-deposition. According to the phase diagram (Fig. 5.2), for all Co concentrations ranging from 53 to 68 at%, only the FeCo bcc B2 phase is expected.

9.3. Morphology and structure

The membranes were then dissolved to check whether changing the composition of the nanowires had an impact on their morphology. SEM images show that there are no significant differences between the nanowires with various chemical compositions in both cases of FeCo and FeNi nanowires (Fig. 9.3). In all samples, the nanowires create densely packed nanostructures, forming matrices of nanowires with uniform diameters and lengths. No effect of the composition change on morphology was observed. All nanowires were smooth and continuous, with no noticeable porosity.

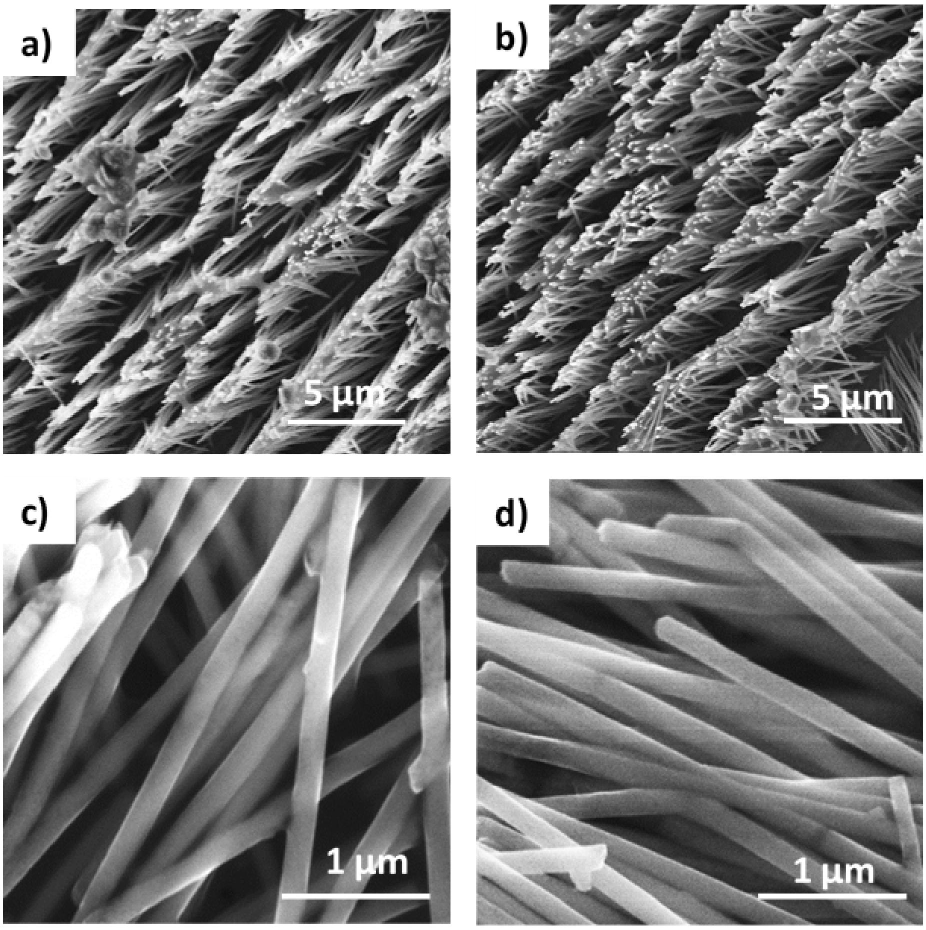

Figure 9.3: SEM images of (a, c) FeCo and (b, d) FeNi nanowires deposited at -1.0 V observed after membrane dissolution.

The structural properties and phase composition of the nanowires were examined by XRD measurements. The results are presented in Figure 9.4. As in the case of single nanowires, the very intense peaks marked with asterisks come from the Cu layer. The peaks described by Miller indices were assigned to the FeCo bcc and $FeNi_3$ fcc phases according to the reference data (03_065_6829 and 00-038-0419 NIST).

The peak positions and their intensities are listed in Table 9.2 with the reference data. All nanowires show a polycrystalline structure.

As shown above, the concentration range of the analyzed FeCo nanowires indicates the occurrence of the B2 phase. The most intense peaks for FeCo alloy come from the

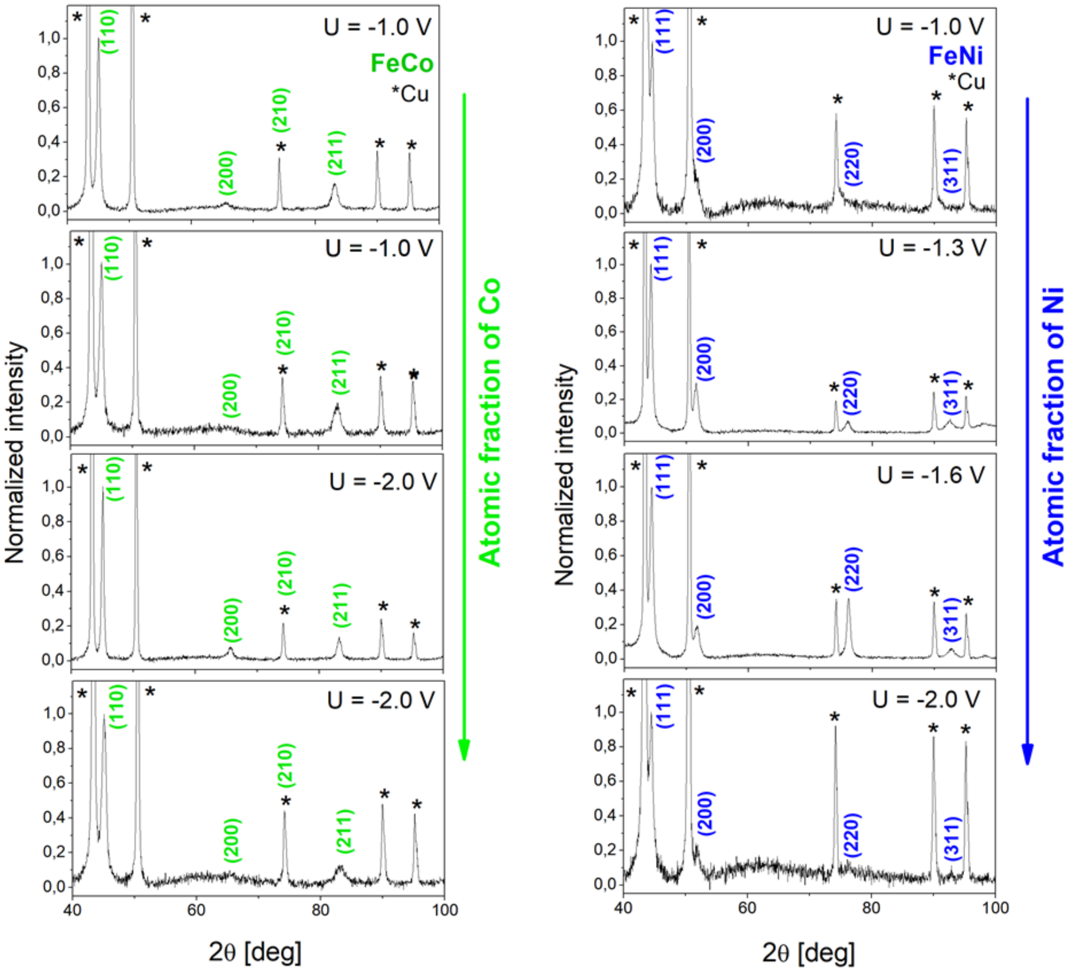

Figure 9.4: X-ray diffraction patterns measured for (a) FeCo and (b) FeNi nanowires embedded in PC membranes. The indexed peaks correspond to the FeCo bcc and $FeNi_3$ fcc phases (reference code: 03_065_6829 and 00-038-0419 NIST Database), while the peaks marked with an asterisk come from the copper layer.

(110) planes and appear at an angle of approximately $2\theta = 44.9^o$. Two other peaks with lower intensities are assigned to the reflections from the planes (200) and (211). Relatively small changes in Co concentration do not result in significant changes in peak positions and relative intensities, which correspond to the reference sample quite well. This suggests no changes in the lattice parameters and isotropic growth of FeCo nanowires.

In the case of FeNi nanowires, according to the phase diagram (Fig. 5.3) and the Ni content (46 - 90 at%), one can expect the appearance of FeNi $L1_0$ (at the lowest Ni concentration, U = -1.0 V) and $FeNi_3$ $L1_2$ phase (at higher Ni content U = -1.3 ÷ -2V). The peak positions were assigned to the reference data of the FeNi3 phase with the most intensive peak at an angle of approx. $2\theta = 44.4^o$ coming from (111) planes. The slight deviation from the peak position showed no correlation with changes in chemical compositions. The relative peak intensities indicate the preferred growth direction normal to the (111) planes, with one exception for the sample deposited at -1.6 V, which shows slight texture along [220] direction. The highest peak intensities found in the samples deposited at -1.3 V and -1.6 V may suggest that intermediate voltages create the most favorable conditions for the growth of crystalline FeNi nanowires. The analysis did not reveal the peaks typical of the FeNi phase.

The crystallite size, estimated based on the Scherrer equation, was approximately 17 nm and 20 nm for FeCo and FeNi, respectively.

Table 9.2: XRD measurement results of FeCo and FeNi nanowires compared to reference data* (03-065-6829 and 00-038-0419 NIST Database).

			FeCo		
hkl	Reference*	Fe47Co53 -1.0 V	Fe44Co56 -1.0 V	Fe40Co60 -2.0 V	Fe34Co66 -2.0 V
			2θ		
110	44.94	45.00	45.06	45.08	44.96
111	55.82	-	-	-	-
200	65.43	65.54	-	65.58	-
210	74.35	74.23	74.20	74.23	74.22
211	82.90	83.07	83.14	83.18	83.01
220	99.7	-	-	-	-
			Relative Intensity [%]		
110	100	100	100	100	100
111	0.1	-	-	-	-
200	11.3	6	-	8	-
210	0.1	31	35	22	44
211	17.0	16	20	14	13
220	4.4	-	-	-	-
			FeNi		
hkl	Reference*	Fe54Ni56 -1.0 V	Fe14Ni86 -1.3 V	Fe9Ni91 -1.6 V	Fe10Ni90 -2.0 V
			2θ		
111	44.28	44.42	44.31	44.43	44.44
200	51.53	51.52	51.59	51.72	51.67
220	75.87	-	75.90	76.14	-
311	92.21	-	92.53	92.68	92.85
			Relative Intensity [%]		
111	100	100	100	100	100
200	60	20	29	20	24
220	30	-	8	35	-
311	40	-	8	7	11

9.4. Magnetic studies

FeCo and FeNi nanowires were also studied magnetically, using SQUID measurements. Figure 9.5 presents the hysteresis loops of FeCo and FeNi nanowires with different chemical compositions. As before, the magnetic measurements were performed at room temperature with a magnetic field applied in the membrane plane and along normal to the membrane plane.

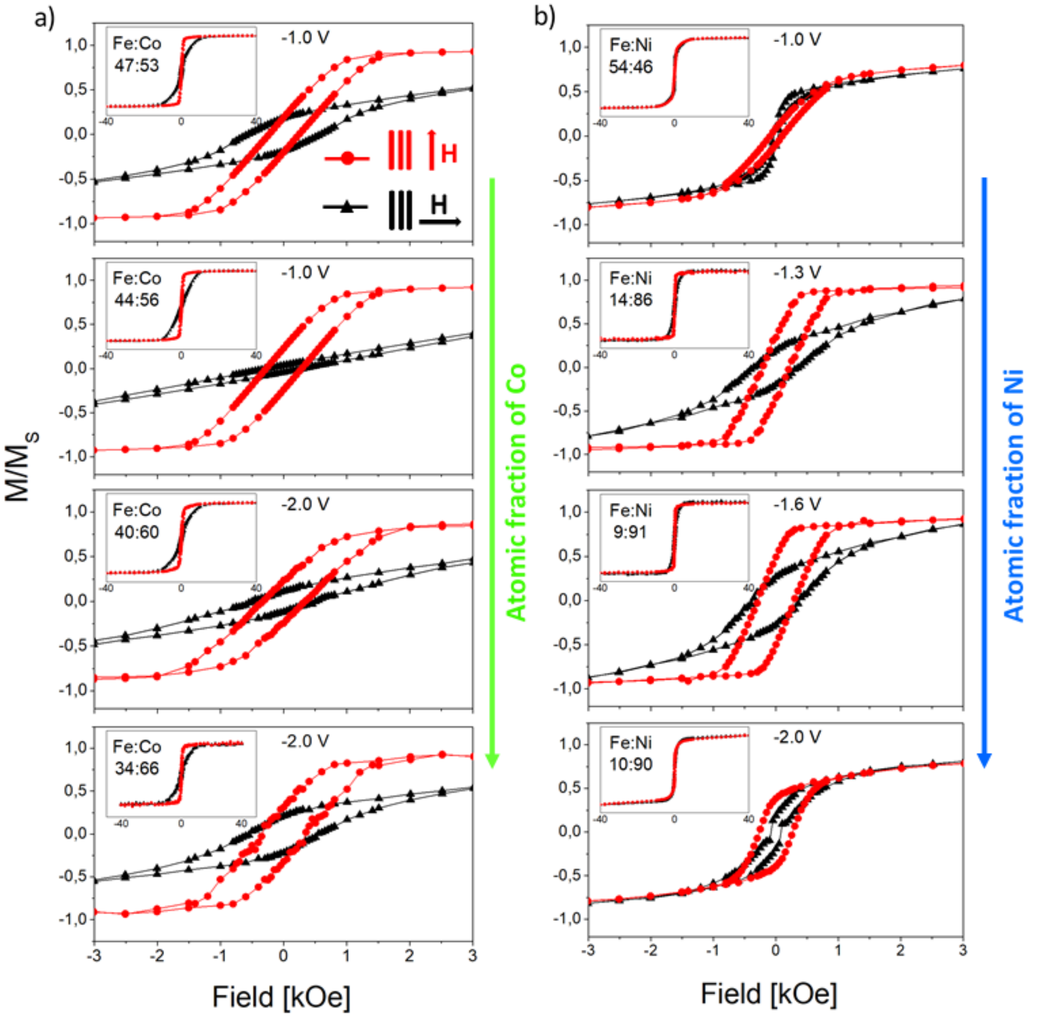

Figure 9.5: Hysteresis loops measured at room temperature with a magnetic field applied in the membrane plane and out of it for (a) FeCo and (b) FeNi nanowires ($\phi = 100$ nm) of different compositions. The magnetization (M) value was normalized to the saturation magnetization (M$_s$).

Figure 49 a shows the hysteresis loops for FeCo nanowires. It can be seen that all nanowires are characterized by magnetic anisotropy with the easy axis along or near the nanowire axis. The lack of a preferred growth direction excludes the magnetocrystalline anisotropy from the factors contributing to the magnetic behavior of FeCo nanowires. Thus, the magnetic anisotropy can result from shape anisotropy and dipole interactions.

Loops measured with a magnetic field applied out of the membrane plane deviate from a rectangular shape. As in the case of single-element nanowires, the deviation of the channels from the normal to the membrane surface or relatively strong dipolar interactions can be responsible for the observed shape. The in-plane curves, except for one sample, are open, which indicates the appearance of non-coherent rotation related to the domain wall motion. Increasing the Co content causes an increase in the out-of-plane coercivity and non-monotonic changes in the squareness (Fig. 9.6). It can be noticed that the samples deposited at higher voltages have greater coercivity compared to samples deposited from the same electrolyte at low potential. This can be associated with a higher deposition rate, a more porous structure, and a lower filling degree (lower charge Fig. 9.1 a). A more defected and more porous structure can create the pinning sites for the domain movements, while a lower filling degree reduces dipole interactions. These changes may cause an increase in the coercivity values.

Figure 9.5 b shows the hysteresis loops measured for FeNi nanowires. It is clearly visible that there is no direct correlation between the shape of the hysteresis loop and the Ni content in the nanowires. The main parameter determining the magnetic behavior of FeNi nanowires seems to be the applied voltage. Samples deposited at extreme voltages (with Ni contents of 90% and 46%) are magnetically isotropic, while samples deposited at intermediate voltages (containing 91% and 86% of Ni) exhibit magnetic anisotropy with an easy axis along the nanowire axis. As shown, the samples deposited at intermediate potentials had a better crystalline structure, in contrast to samples deposited at extreme potentials, which were characterized by low peak intensities in the diffractograms. Thus, the structural differences, especially poor crystalline structure, may be responsible for the isotropic behavior of nanowires. The preferred growth direction along the magnetic easy axis did not enhance magnetic anisotropy, suggesting its marginal contribution to the effective anisotropy. Although, the coercivity and squareness increase with increasing Ni content, only the sample showing magnetic anisotropy are interesting from the application point of view (Fig. 9.6 b).

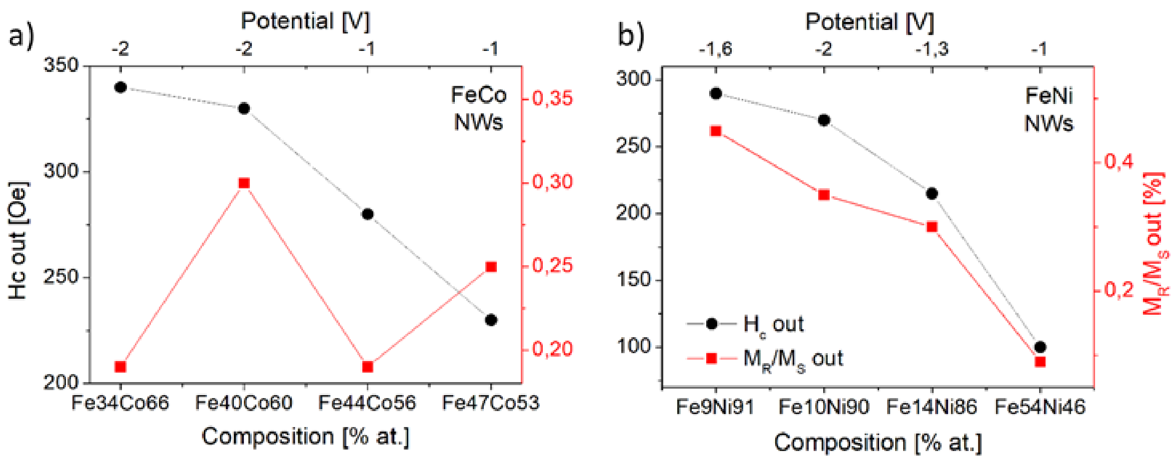

Figure 9.6: Out of plane coercivity and squareness shown as a function of sample composition (and cathodic voltage) for (a) FeCo and (b) FeNi nanowires.

The values of the coercivity and squareness of alloyed nanowires are much smaller than the parameters measured for single-element nanowires. The observed changes are directly related to the formation of new phases that crystalize in various structures with different properties.

Changes in the chemical composition of nanowires caused by modification of the electrolyte concentration turned out to be significant in the case of FeNi nanowires, but in this case, the extreme potential values applied led to a magnetic anisotropy loss. In the case of FeCo nanowires, the potential changes did not indicate a significant modification of the chemical composition, however, the increasing Co content, achieved by changing the concentration of Fe and Co in the electrolyte, caused an increase in the FeCo coercivity. Different coercivities create a boundary between soft and hard materials, which could become a desirable domain wall pinning center. An interesting observation revealing the different sensitivity of FeCo and FeNi alloys to the applied potential and appearance of the anomalous co-deposition in FeNi nanowires deposited at low potential demonstrates the different impacts of Co and Ni on the alloy behavior.

In the further part of the thesis, the three-element alloys with Fe, Co, and Ni are studied.

Chapter 10

Ternary system FeCoNi

After examining systems consisting of single and binary elements, I prepared ternary FeCoNi alloys. The influence of different voltages and geometries (length and diameter) on the nanowire properties was investigated in order to obtain the best possible materials for 3D memory units. All nanowires were deposited at room temperature from electrolytes carefully selected based on the literature studies so that the change in potential had an impact on the chemical composition of the nanowires (Table 6.1).

10.1. Electrochemical analysis

First, I examined the effect of the potential value on the nanowire deposition process. Figure 10.1 shows current vs. time plots recorded during the electrodeposition of nanowires with different diameters (a-b) and flat reference samples (c). All samples were deposited at four potentials ranging from -1.0 V to -1.8 V. As before, the processes were stopped when the currents suddenly started to grow, indicating complete membrane filling.

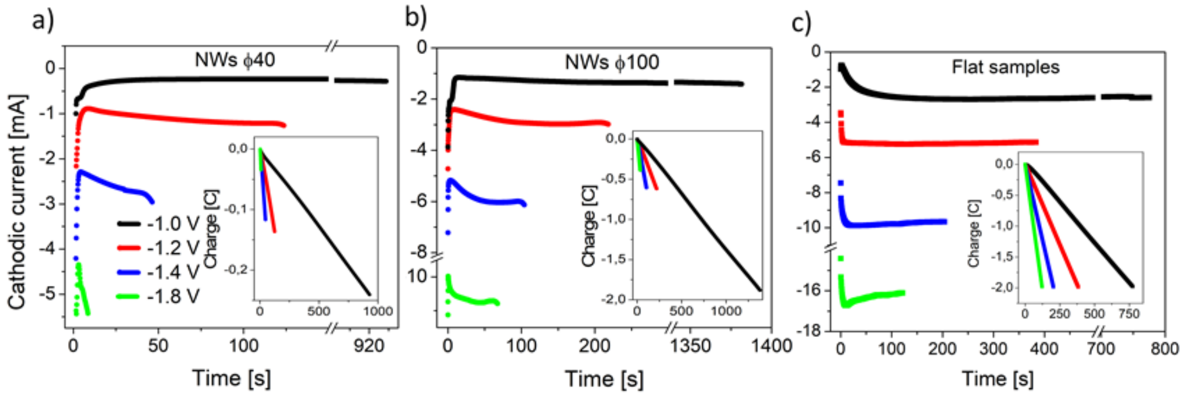

Figure 10.1: Cathodic currents as a function of time measured during the electrodeposition of FeCoNi nanowires at different applied potentials with pore diameters of (a) 40 nm (b) 100 nm, and (c) flat samples. The insets show the corresponding electrical charge variations in time.

As the applied potential increases, the cathodic current for all nanowires and flat samples increases and shorter times are needed to completely fill the membrane pores.

Additionally, one can observe, that the currents measured during the deposition of nanowires with larger diameters are higher than those recorded for smaller nanowires, which is connected with the greater porosity of membranes with larger pore diameters (Table 2.2). As the nanowires fill, the current increases slightly, which is related to the shortening of the diffusion length.

As in the case of single and double-element nanowires, the corresponding electrical charge variations are linear (insets), suggesting a constant growth of the alloy wires inside the pores. In all cases, the final charge achieves extreme values for the lowest (-1.0 V) and the highest (-1.8 V) potentials, while it is almost the same for the medium potentials (-1.2 V, -1.4 V). Such a dependency may suggest a different degree of membrane filling and is consistent with the results for Fe nanowires deposited at various temperatures, as well as for FeCo and FeNi nanowires deposited at different potentials (Chapter 9).

These changes in the applied potential affect the hydrogen evolution, which increases with overpotential, as written earlier. At high applied potential, hydrogen bubbles can block the pores and hinder the deposition process, leading to the creation of more defected structures with more porous or even discontinuous nanowire forms. This effect should be more pronounced in membranes with smaller diameters, which can easily be blocked by hydrogen bubbles. The different membrane porosity together with the difficulties in pore filling caused by hydrogen bubbles result in a lower charge (0.24 C to -0.035 C) reduced in nanowires with the smallest diameter compared to values ranging from -1.9 C to -0.4 C for nanowires with a diameter of 100 nm.

The value of the applied potential affects the rate of both charge transfer and migration of metal ions, inducing thereby different speeds of electrodeposition. The values of current density and growth rate for nanowires with diameters of 40 and 100 nm are presented as a function of applied potentials (Fig. 10.2). For both pore diameters, an increasing cathodic voltage results in larger values of cathodic current densities and deposition rate. The applied potential has a stronger effect on nanowires with a diameter of 40 nm, wherein this effect is more pronounced at higher overpotential probably due to the high hydrogen evolution. Obviously, an increase in the growth rate shortens the process duration. As a result, the time needed to fully fill the membrane changes from 1380 s to 70 s and from 930 s to 10 s, for nanowires with diameters of 100 nm and 40 nm, respectively.

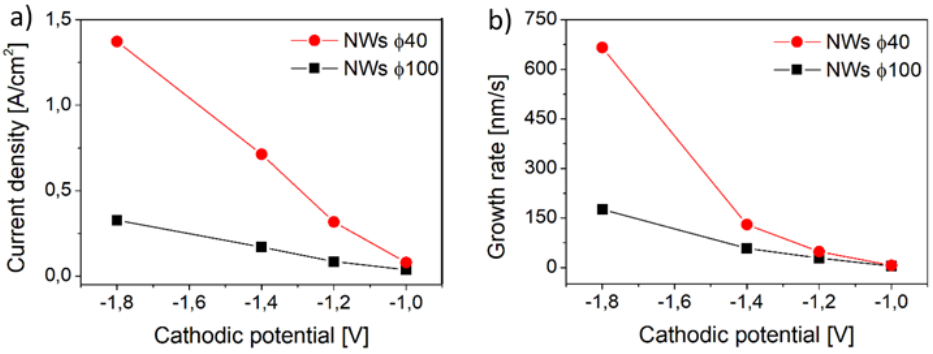

Figure 10.2: (a) Current density and (b) growth rate measured as a function of cathodic potential for nanowires with a diameter of 40 nm and 100 nm [188].

In addition to nanowires of various diameters, I made nanowires of different lengths, filling the membranes to $\frac{1}{2}$ and $\frac{1}{4}$ of the membrane thickness to obtain nanowires with a length of 3 µm and 1.5 µm, respectively. This was achieved by stopping the process when the appropriate amount of charge had been reduced. The selected nanowire lengths correspond to the length of the segments in segmented nanowires, which will be described in the last chapter. Figure 10.3 shows current and charge versus time graphs for different nanowire lengths and diameters. Besides intentional proportional changes in charge values, a similar dependence can be observed for current transient over time. The current curves measured for the same nanowire diameters have the same shape, which proves the repeatability of the process. A comparison of the currents measured during the deposition of nanowires with a length of 6 µm and different diameters confirmed the known relationship related to the various porosity of the membranes (Fig. 10.3 c).

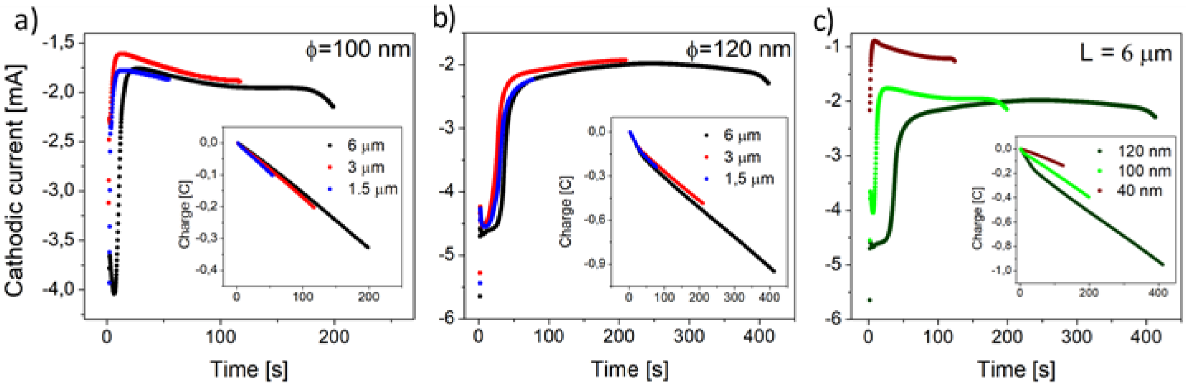

Figure 10.3: Cathodic currents as a function of time, measured during the electrodeposition of FeCoNi nanowires of different lengths and diameters, with charge variation in time shown in the insets.

Changes in the electrodeposition parameters as well as in the geometry of nanowires should modify their properties starting from the chemical composition through structure and ending with magnetic properties that are key from the application point of view. In the next part, the investigation of these properties will be performed.

10.2. Morphology

The deposition processes of nanowires with a length of 6 µm were stopped after the pores were completely filled (drop in the current curve). Figure 10.4 shows the SEM images of the membrane surface with visible nanowire ends without overdeposited caps. To observe the morphology of FeCoNi nanowires, PC membranes were dissolved using dichloromethane. In Figure 10.6 the nanowires with diameters of 40 nm and 100 nm deposited at the different potentials are presented. SEM images exhibit that there are no significant differences between these nanowires. In all samples, the nanowires create densely packed forest-like nanostructures. These vertically oriented objects form matrices of nanowires with uniform diameters and lengths. All nanowires are smooth and continuous, without noticeable porosity. Moreover, at higher magnification, we can see the coating covering nanowires. As in the previous samples, this is a polycarbonate layer (a side effect of the dissolution process) that protects nanowires against oxidation.

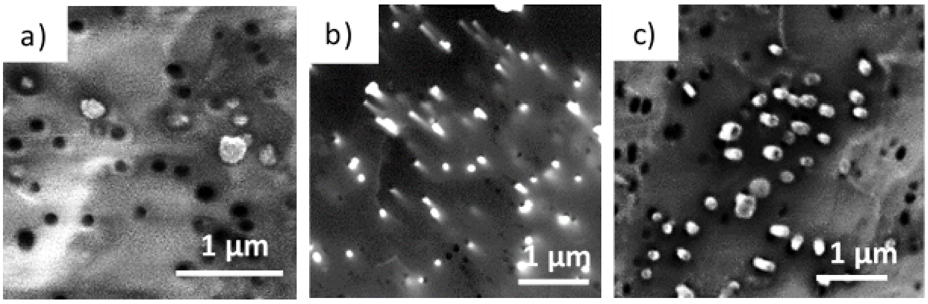

Figure 10.4: SEM images acquired on the membrane surface with a pore diameter of 100 nm, filled with FeCoNi NWs deposited at a cathodic potential of (a) -1.0 V, (b) -1.2 V, and (c) -1.4 V.

Furthermore, the FeCoNi nanowires with different lengths and diameters, prepared at -1.2 V are shown in Figure 10.5. One could observe that changes in nanowire geometry do not affect their morphology, the nanowires are continuous, without any porosity. Additionally, SEM measurements allowed us to confirm that the deposition processes were stopped appropriately and the desired nanowire lengths were obtained.

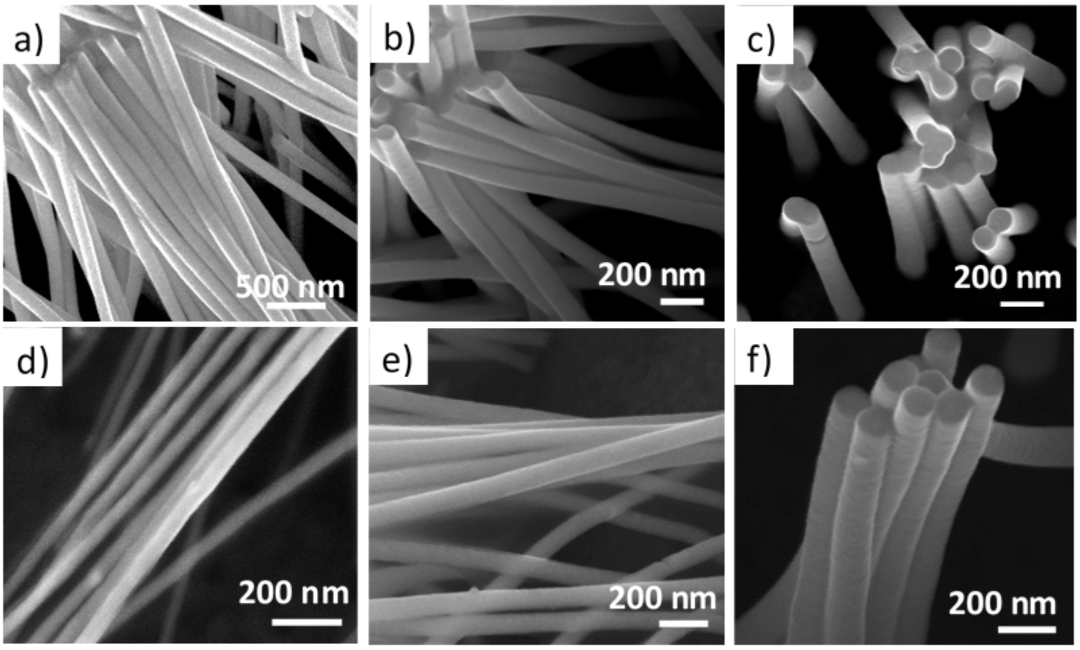

Figure 10.5: SEM images of the FeCoNi nanowires with a diameter of 100 nm and different lengths: (a) 6 µm, (b) 3 µm, (c) 1.5 µm and length of 6 µm and different diameters: (d) 40nm, (e) 100nm (f) 120nm.

The microstructure of the alloyed FeCoNi nanowires with a diameter of 40 nm (Fig. 10.7 a-c) and 100 nm (Fig. 10.7 d-f) was investigated using transmission electron microscopy (TEM) measurements. The overview TEM images show the uniform diameter nanowires in both cases. A thin polycarbonate layer covering the nanowire surface is visible in Fig. 10.7 a, d. The selected area electron diffraction pattern (SAED), taken along the

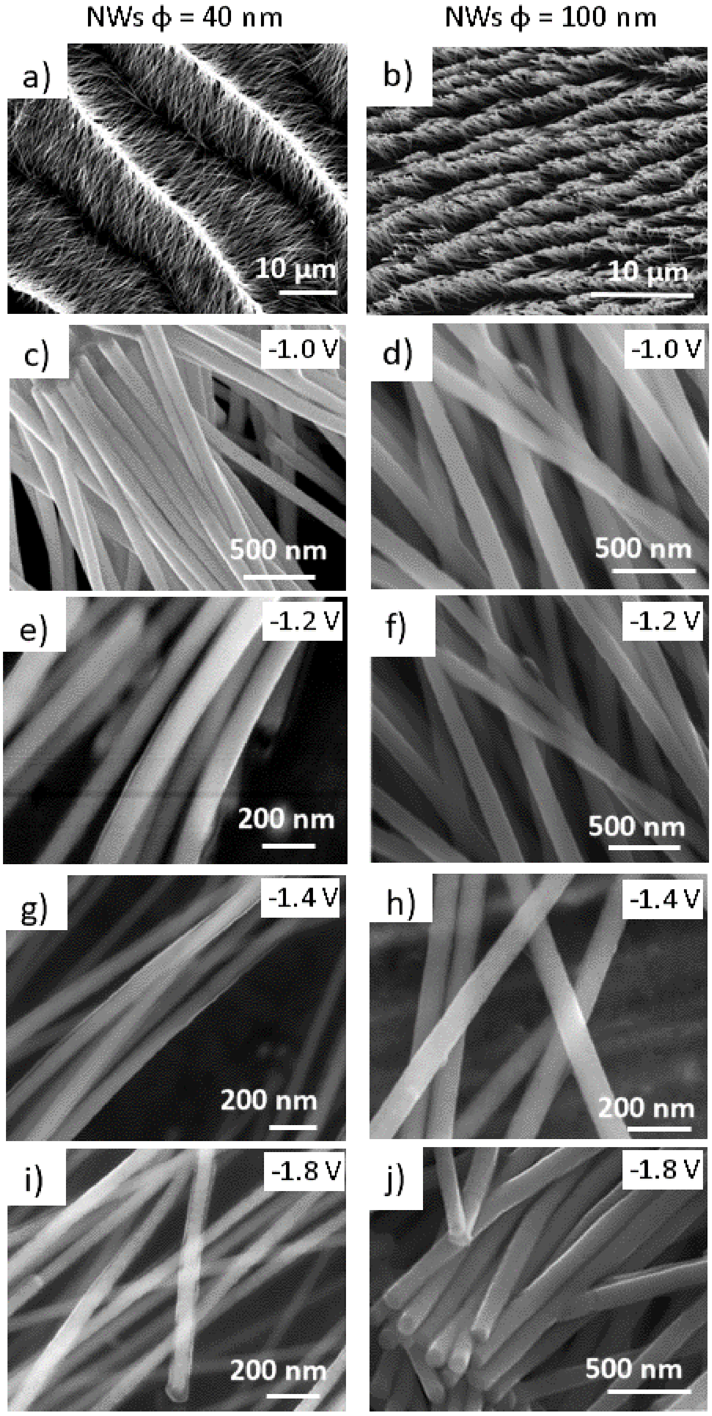

Figure 10.6: SEM images of the FeCoNi nanowires with two different diameters, deposited at the different potentials observed after membrane dissolution: (a, b) forest-like nanowire structure with 40 nm and 100 nm diameter and with higher magnification: 40 nm of diameter: -1.0 V (c), -1.2 V (d), -1.4 V (e), -1.8 V (f) and 100 nm of diameter: -1.0 V (h), -1.2 V (g), -1.4 V (i), -1.8 V (j).

[110] zone axis (ZA), indicates the [111] growth direction of nanowires with a diameter of 40 nm. However, the crystallite orientation along the [220] direction, confirmed by the SAED pattern with the zone axis along [111], was also found (not shown). The SAED pattern measured for 100 nm diameter nanowires exhibits a [112] zone axis indicating the growth direction along [111] with the (111) plane distance of 0.212 nm. Moreover, high-resolution TEM measurements of nanowires with a diameter of 40 nm revealed long straight lines along the growth direction of nanowires, shown in Figure 10.8. The SAED pattern indicates the doubled spots suggesting that the straight lines are twinning defects. Such twins oriented along the nanowire axis or slightly vertically tilted are common structural defects in our nanowires. Figure 10.8 c shows a high-resolution TEM picture with mirror-like boundaries between planes on the left and right sides confirming the nanotwin formation.

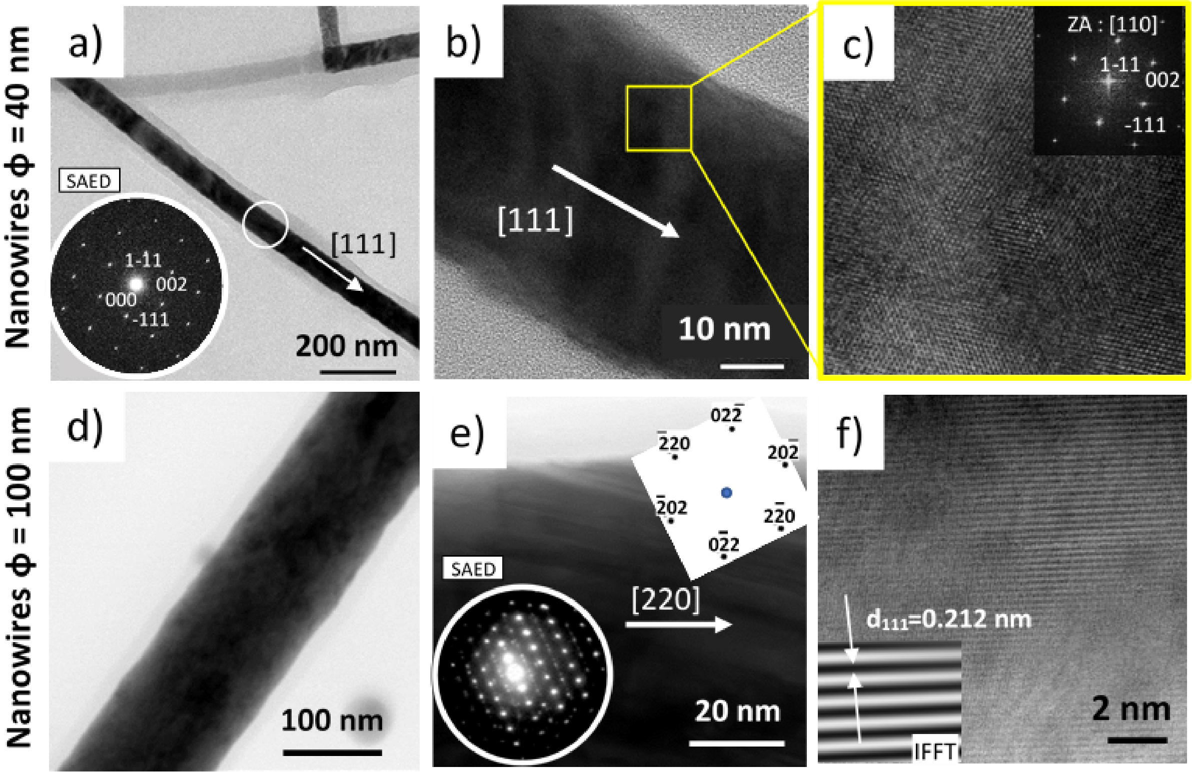

Figure 10.7: (a, d) Bright-filed TEM, (b, c) high-resolution TEM micrographs and (e, f) HAADF STEM images of FeCoNi nanowires with a diameter of 40 nm deposited at -1.2 V (a, b, c) and 100 nm deposited at -1.8 V (d, e, f) together with SAED patterns (a, e) and fast Fourier transform (FFT) (c) indexed with the lattice parameters of fcc FeCoNi or Ni structure. The (111) inter-plane distance was determined based on the inverse fast Fourier transform (IFFT).

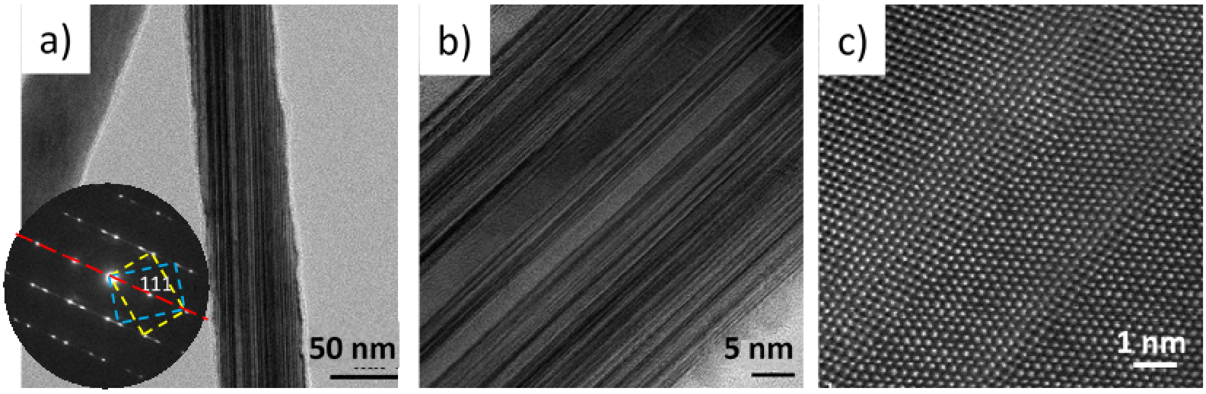

Figure 10.8: (a, b) Bright-field TEM with corresponding SAED pattern of FeCoNi nanowires with a diameter of 40 nm deposited at -1.2 V; (c) High-resolution TEM image confirming the formation of twin planes. reveals that the nanowire is composed of nanotwins on [111] planes.

10.3. Chemical composition

Based on cyclic voltammetry measurements in which different values of the cathodic current vs. potential were recorded for individual elements, different behavior of Fe, Co, and Ni ions deposition can be expected. Taking into account the literature, various standard potentials, and the possibility of anomalous co-deposition, I chose the ion concentrations in the electrolyte that should induce changes in the chemical composition of nanowires measured at various potentials.

The chemical composition of FeCoNi nanowires with 40 nm and 100 nm diameter (released from the membranes) and on the flat samples was analyzed using energy-dispersive spectroscopy measurements. The fractions are given in the atomic concentrations. The concentrations of Fe, Co, and Ni in the FeCoNi samples, deposited at different cathodic potentials are plotted in Figure 10.9. All samples show the same tendency with increasing cathodic potential, demonstrating an increase of Ni content with a simultaneous decrease in Co and Fe concentration, which is consistent with my previous results of FeNi nanowires and also literature data [19, 20, 21, 85]. For samples deposited at potentials ranging from -1.2 V to -1.8 V, the atomic concentration in the deposits reflects the ion concentration in the electrolyte. Hence, similar to double-element FeNi nanowires, the mass transfer is much greater for Ni^{2+} than for Fe^{2+} and Co^{2+} ions and in consequence, the anomalous co-deposition tendency is vanquished. Whereas, the chemical composition of the samples deposited at -1.0 V differs significantly from each other. The flat sample shows a concentration ratio relatively closer to the electrolyte composition, while in nanowires concentration of individual atoms clearly deviates from the electrolyte and order predicted by standard potential values. The main difference between porous templates and a flat sample is related to the diffusion length. As shown by Saedi et al. in their studies of FeCoNi nanowires deposited in membranes with different pore lengths and also different diameters, metals with lower concentrations in the electrolyte appear in higher concentrations in the nanowires when the pore lengths are shorter [50]. This behavior was explained with a shorter diffusion length, which creates more favorable conditions for the competition of low-concentration ions (Fe and Co) with high-concentration ions (Ni). Diffusion length can also explain the difference in the chemical composition of elements in the membrane pores and on the flat sample. By analogy, a lower deposition rate (at low cathodic potential) also creates more favorable conditions for very diluted ions, which may result in a higher concentration of them in the deposit. At a more cathodic potential mass transport limitation connected with low ion concertation dominates and metal with high concentration is preferentially deposited [26, 50]. Despite the large difference in the concentration of individual ions in the electrolyte (0.01 M Fe^{2+} / 0.02 M Co^{2+} / 0.17 M Ni^{2+}), the amount of the elements in nanowires at this potential is similar to each other and shows a relatively high concentration of Fe and a clear dominance of Co. This behavior of nanowires indicates anomalous co-deposition, which is not usually observed at more cathodic potentials, and suggests that the mechanism of anomalous co-deposition in nanowires can be more complicated than in flat samples.

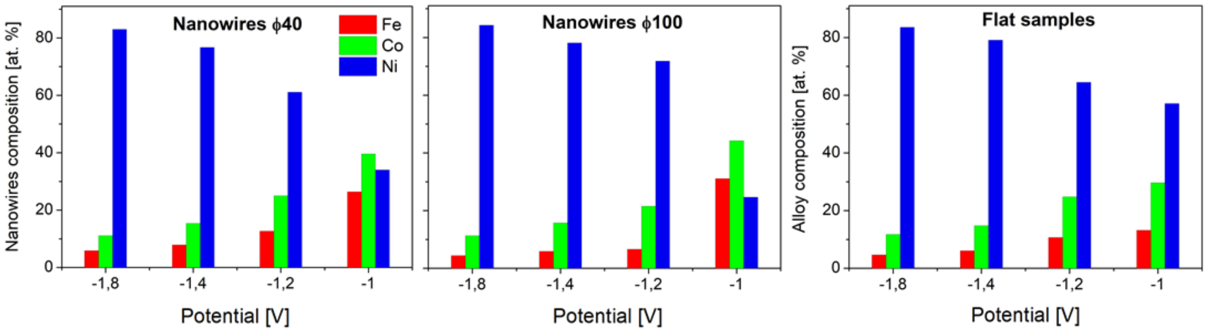

Figure 10.9: Atomic composition of Fe, Co, Ni in FeCoNi nanowires with diameters of 40 nm and 100 nm and also in FeCoNi films deposited at different potentials. The particular elemental contents were given with an error of no more than ±1 [188].

The chemical composition of FeCoNi nanowires deposited at different potentials was also analyzed by STEM-EDS measurements. Figure 10.10 presents the EDS maps measured for Fe, Co, and Ni. The images show a homogenous distribution of all elements. The results demonstrate the same tendency in the atomic concentration values as a function of the applied potential and correlate very well with the compositions obtained in SEM. To better describe the relationships between elements, as in the case of FeNi samples, I calculated the SR parameters for Co/Fe, Fe/Ni, and Co/Ni ratios as a function of applied potential (Fig. 10.11). As mentioned, an SR value close to 1 suggests co-deposition predicted by standard potentials, while anomalous co-deposition occurs for a higher SR coefficient.

The calculations demonstrated similar behavior of particular ratios versus voltages, as expected from chemical analysis and also based on the FeNi NWs results. But the details stand out. The first is the SR parameter calculated for the Co/Fe ratio, which maintains an almost constant value for all potentials and samples with a value close to 1. The second issue is the parameters calculated for Fe/Ni and Co/Ni ratios, which show the same values for higher potentials (close to 1) with a sharp increase in SR at lower voltages, which is consistent with the results for binary alloy nanowires. Additionally, these parameters reach the largest values for nanowires with a diameter of 100 nm and

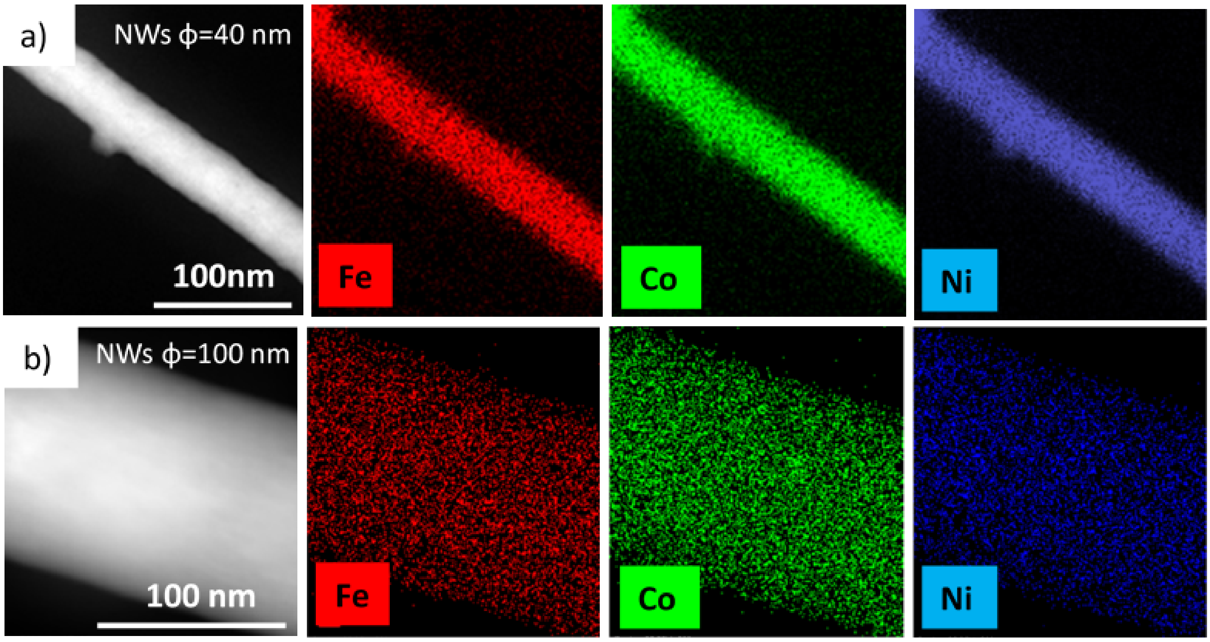

Figure 10.10: STEM-EDS maps of Fe, Co, and Ni measured in FeCoNi nanowires with diameters of (a) 40 nm and (b) 100 nm deposited at -1.2 and -1.0 V, respectively [188].

the smallest for flat samples. The above analysis reveals that the concentration of Fe and Co weakly depends on the applied potential, which is also confirmed by previously described studies of FeCo nanowires. Moreover, the results point out a strong potential dependence of the Fe/Ni ratio, which was also observed in FeNi nanowires. The behavior of the SR parameter calculated for Co/Ni is consistent with the changes in Fe/Ni, which suggests that the concentration of Ni is very sensitive to the applied potential and plays a dominant role in the anomalous co-deposition mechanism. Similar results were obtained for FeCoNi nanowires [19, 41] and for FeCo and FeNi nanowires [50, 153, 188].

As was pointed out earlier, anomalous co-deposition depends on the applied voltage, and at high cathodic overpotential, the electrodeposition process loses its anomalous character. A significant anomalous co-deposition only appears at the lowest potential, which is in accordance with direct observation of EDS measurements (Fig. 10.9). The difference between the SR parameters observed for nanowires and flat samples indicates less anomalous co-deposition for flat samples, which confirms a distinct mechanism for anomalous co-deposition in nanowires and coatings.

As shown by the presented results, anomalous co-deposition has a direct impact on the final composition of the iron group alloys. Consequently, this may affect the structural and magnetic properties of nanowires (such as coercivity or squareness). This impact was examined in the next chapters.

10.4. Structure

The structure of the nanowires was analyzed based on X-ray diffraction. Figure 10.12 shows the measurements of FeCoNi nanowires with a diameter of 100 nm and the flat

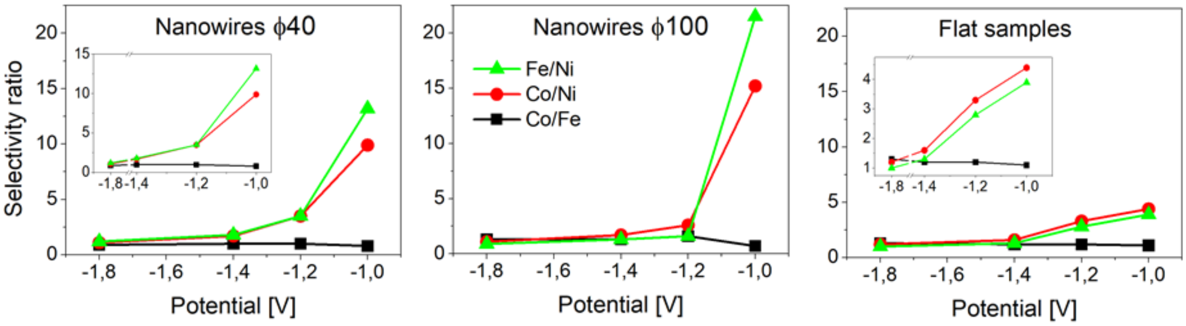

Figure 10.11: Selectivity ratios of Fe/Ni, Co/Ni, and Co/Fe calculated for FeCoNi nanowires with diameters of 40 nm and 100 nm and also for FeCoNi flat samples deposited at different cathodic potentials. The inset shows the same graph on a larger scale.

samples deposited at the different potentials. In all samples, the most intense, narrow peaks, marked with an asterisk originate from the copper contact layer for nanowires and the Cu substrate for flat samples. Small peaks at $2\theta = 45.34^o$ and 48.71^o observed in the diffractograms measured for flat samples come from the substrate contamination (marked with open circles). The peak intensities were normalized to the (111) peak, which is the most intense in the reference sample. The indexed peaks correspond to the FeCoNi phase crystallizing in the fcc structure. These peaks, described in Table 10.1, appear in all patterns with a slight difference in their position and significantly different intensities. Additionally, a trace of the hcp phase was found in the sample deposited at -1.2 V (marked with red) [188].

The diffractograms measured for samples deposited at more cathodic potentials show peaks with higher intensity than the samples prepared at lower potentials. In the case of nanowires, the intensity of the (220) peak increases the most, while in flat samples this observation refers especially to the (200) reflection, which increases even above the (111) peak. These deviations from the intensities observed for isotropic powder samples indicate a texture with a preferential orientation along [220] and [200] directions for nanowires and flat samples, respectively. Simultaneously, the small peak intensities observed for samples deposited at low potentials suggest a texture along the [111] direction in nanowires and quasi-isotropic growth in flat samples [188].

As shown above, the different values of cathodic potentials caused the changes in the chemical compositions. Such modification in the elemental content should result in a different phase composition. The phases that we can expect in conditions of thermodynamic equilibrium at 293 K are presented in the ternary phase diagram (Fig. 10.13). Points corresponding to the chemical composition of nanowires with a diameter of 100 nm are marked on the graph. The chemical composition of nanowires with a diameter of 40 nm and flat samples at particular voltages has nearly the same values, except for the -1.0 V potential, for which the points were also shown on the diagram. The samples deposited at potentials ranging from -1.2 V to -1.8 V, showing a Ni content above 70%, are localized in the area where, according to the phase diagram, only the γ-Ni phase should appear. The points showing the chemical concentration of the samples deposited at -1.0 V are localized at two different areas: the points corresponding to nanowires appear in the area where α-Fe, γ-Ni, and Ni_3Fe are thermodynamically stable, while the point related to the flat sample occupies the area where the γ-Ni and Ni_3Fe phases should be observed. The α-Fe, γ-Ni, and Ni_3Fe phases respectively correspond to the Fe-based solid solution with the bcc structure, Ni-based solid solution with the fcc structure, and the $L1_2$ intermetallic phase, which is the ordered counterpart of the fcc solid solution. Ni_3Fe phase, with Fe and Ni atoms located in the corners and on the faces of the unit cell, respectively, is indistinguishable from the disordered Ni phase in the XRD pattern [188].

In the XRD patterns measured for 100 nm diameter nanowires and flat samples, we only observed peaks that are attributed to the FeCoNi alloys [154], assigned to the γ-Ni phase with an fcc structure (with a slight trace of hcp in one sample). We have not observed any additional peaks that could come from Fe-based solid solution, which should appear in the samples deposited at -1.0 V exhibiting a relatively high Fe content of 31%. The discrepancy between the phase composition predicted by the trinary phase diagram and our nanowires, pronounced especially in the case of the lowest potential, may be explained by non-equilibrium conditions of the electrodeposition process. Similarly, only the fcc phase was observed in FeCoNi alloys with various concentrations by many researchers [147, 154, 186, 189, 190, 191]. Although, the mixture of fcc and bcc [105], or fcc and hcp has also been observed [151, 152]. These differences in the phase composition of the FeCoNi alloy indicate a strong dependence of the growth process on the electrodeposition parameters, which results in a different structure of the alloy despite a similar chemical composition or an identical structure observed for alloys with different chemical compositions [188].

Table 10.1: Results of XRD measurements of 100 nm diameter nanowires with lattice parameter (a), and average crystallite size (D) estimated with an error of 1 nm.

		$2\theta[deg]$			
hkl	Reference*	-1.0 V	-1.2 V	-1.4 V	-1.8 V
111	44.23	43.95	44.15	44.30	44.37
200	51.53	51.21	51.44	51.62	51.75
220	75.87	75.60	75.76	75.95	76.08
311	92.25	91.78	92.16	92.51	92.71
222	97.69	97.32	97.57	97.85	98.08
		Relative intensity [%]			
hkl	Reference*	-1.0 V	-1.2 V	-1.4 V	-1.8 V
111	100	100	100	100	100
200	41.8	17.5	12.0	21.6	20.8
220	16.4	8.2	6.4	30.4	25.8
311	14.6	4.2	4.6	9.8	6.9
222	4.0	2	2	2.9	2.4
		Lattice parameters			
a [Å]	3.544	3.565	3.555	3.538	3.530
D [nm]	-	12	18	19	22

* *the fcc* $Ni_{0.82}Fe_{0.18}$ *powder sample (JCPDS:04-003-2245)*

The increasing cathodic potential and the associated increase in the Ni content caused the changes in the peak positions. The shifts of the (111) and (220) peaks in nanowires

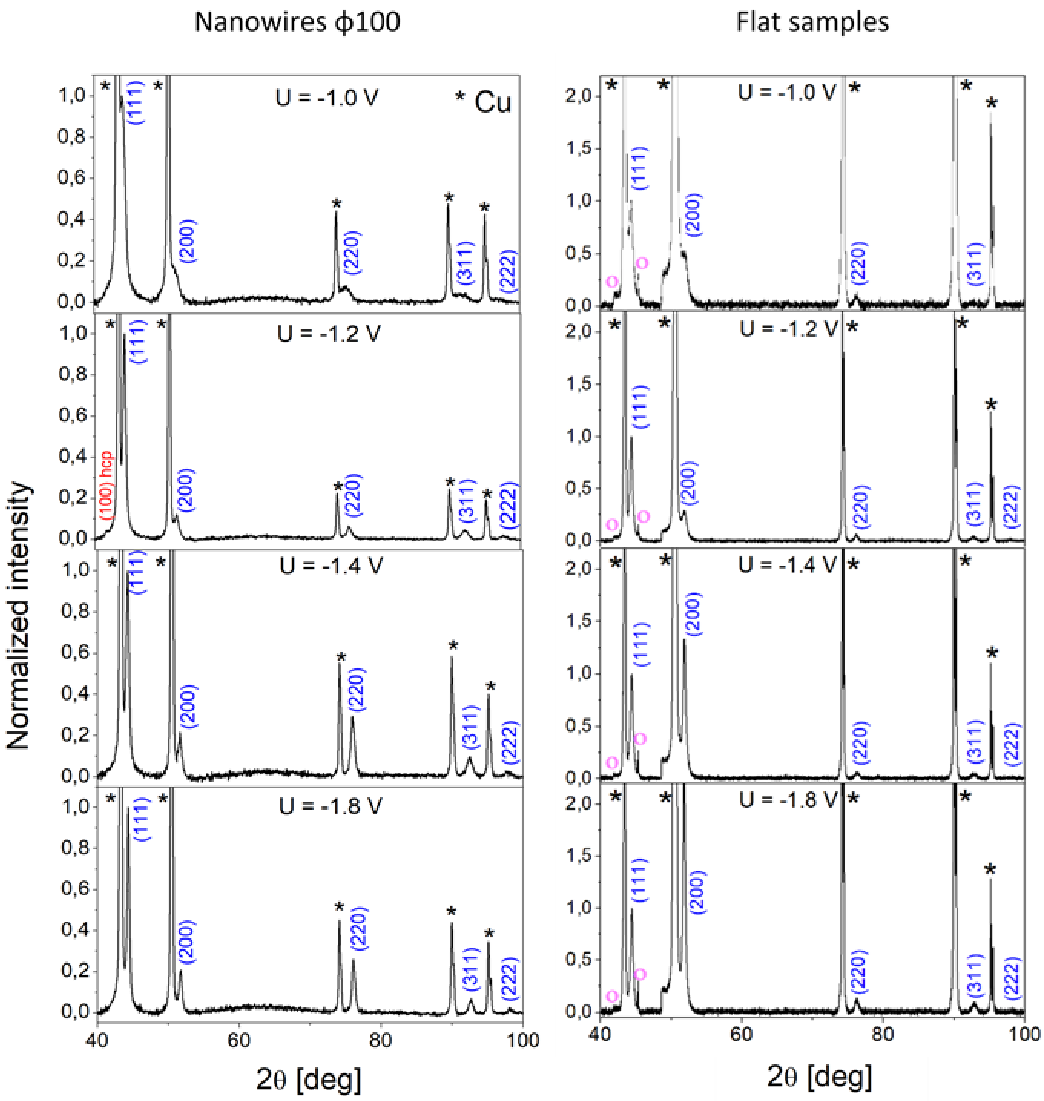

Figure 10.12: X-ray diffraction patterns measured for the FeCoNi nanowires with a diameter of 100 nm embedded in the (a) polycarbonate membranes and (b) flat samples. The indexed peaks correspond to the fcc Ni0.82Fe0.18 powder sample (JCPDS:04-003-2245), while the peaks marked with an asterisk and triangle-down come from the copper and its contamination, respectively [188].

with a diameter of 100 nm are shown in Figure 10.14. Peak maxima move towards higher angular values as the cathodic current increases. Such a shift is caused by the modification of the atomic distance due to the replacement of Fe and Co atoms with Ni atoms, which results from the changes in the chemical composition. As Ni content increases, the Fe and Co content decrease, which taking into account that the Fe (1.72 Å) and Co (1.67 Å) atomic radii are larger than the radius of the Ni (1.62 Å) may be responsible for shortening the lattice parameter. Moreover, as can be seen from the calculated lattice parameters (Table 10.1), with the increase in the nickel content this parameter approaches to the Ni lattice constant (a_{Ni} = 3.52 Å in the fcc structure). Similarly, Dalavi *et al.* observed expansion of the lattice with an increase in Fe content

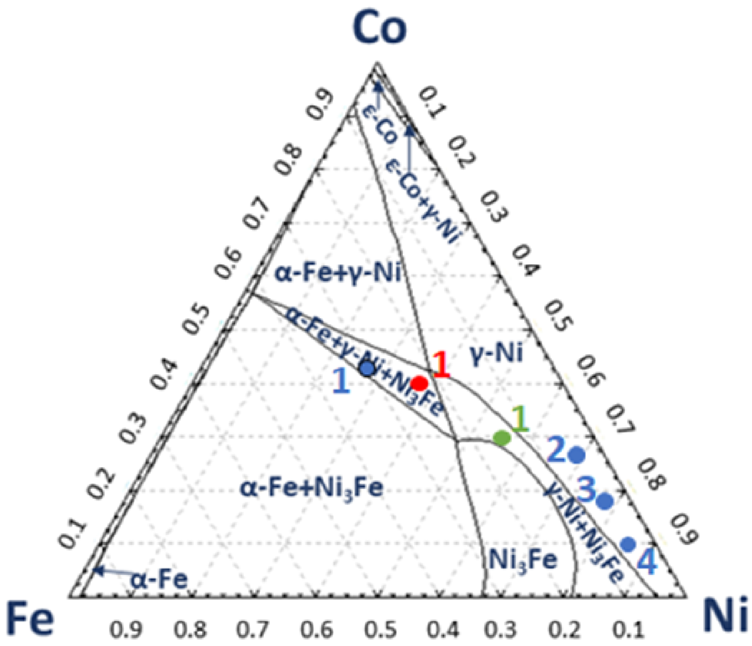

Figure 10.13: Ternary phase diagram of the FeCoNi system - isothermal cross-section at 293 K generated using the FactStage package and the SGTE database with points indicating the chemical composition of the samples (blue points - 100 nm diameter NWs, red point - 40 nm diameter NWs and green point - flat sample). The number from 1 to 4 correspond to the cathodic potentials from -1.0 V to -1.8 V [188].

in FeCoNi monocrystalline alloys [186]. The changes in the lattice parameter caused by modification of the chemical composition were also observed in FeCoNi films [21, 192].

Besides, the shift in the peak positions, a narrowing of the XRD reflection was observed. The normalized (220) peaks are shown in the inset of Figure 10.15. As can be seen, the width of the peaks decreases with increasing cathodic voltage (Ni content increases and the Co and Fe decrease), which suggests an increase in crystallite size for higher voltages. Calculations based on the Scherrer equation, shown in Figure 10.15, confirmed these observations. The average size of the crystallites, estimated with an error of 1 nm (larger only in the case of the smallest potential due to the inaccuracy of FWHM (full width at half maximum) determination), ranged from 12 to 22 nm for the lowest and highest voltage, respectively. The change in crystallite size with increasing voltage can be related to the change in current density. Higher current density at more cathodic potentials creates favorable conditions for crystal growth without ion deficiency, which promotes large crystallite sizes. Moreover, a greater amount of Ni, which crystallizes in its own structure with a low content of Fe and Co, which can be treated as impurities in the Ni lattice, may also explain the observed increase in crystal size. A decrease in the grain size with increasing Co content was also observed by Long *et al.* in FeCoNi coatings [151] and Yanai et al. in FeCoNi films [188, 191].

XRD measurements were also performed for nanowires with a diameter of 40 nm (Fig. 10.16 a). These nanowires were deposited in the membranes covered with a gold layer,

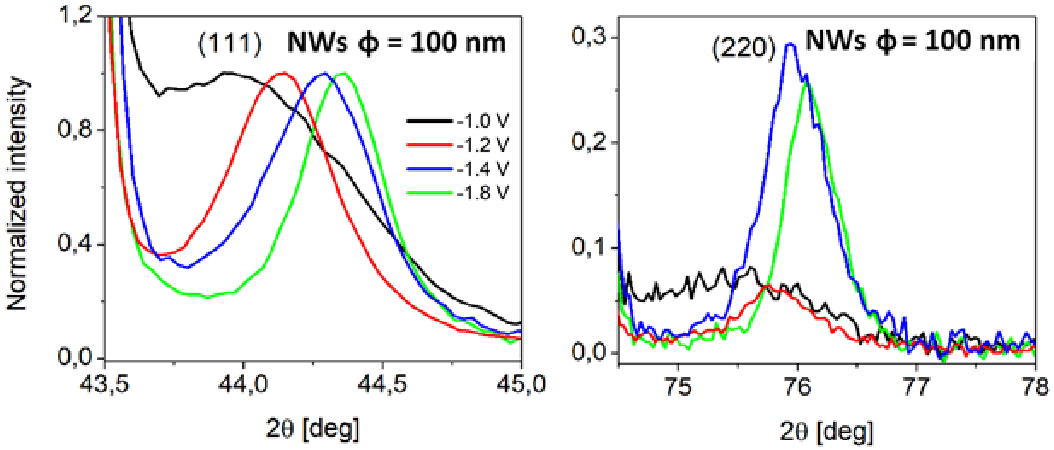

Figure 10.14: The (111) and (220) peaks with a visible shift towards higher 2θ values with increasing cathodic potential (measured for 100 nm diameter nanowires) [188].

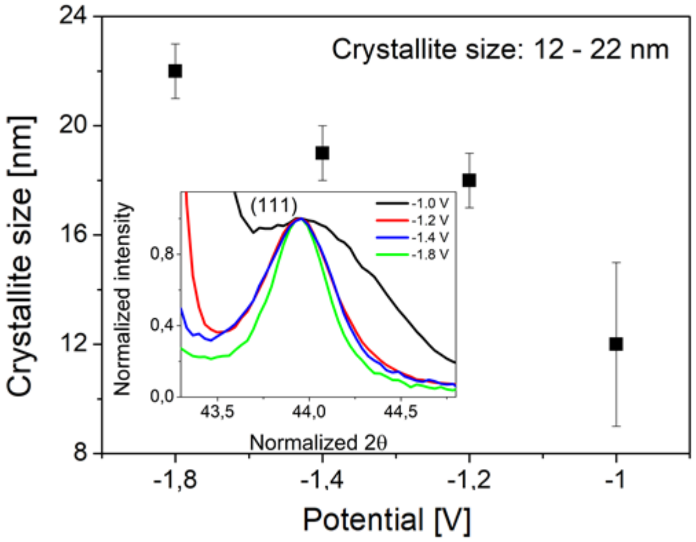

Figure 10.15: The mean value of crystallite size calculated according to the Scherrer formula based on the (220) peak broadening (measured for 100 nm diameter nanowires) [188].

which shows the most intense peak in the same position as the (111) FeCoNi reflex. The first pattern measured for a pure gold-coated membrane indicates the peaks characteristic of gold. Subsequent patterns, apart from gold reflections (unmarked), reveal low-intensity peaks described by Miller indices (blues), assigned to the fcc phase of FeCoNi. The most intense (111) peak coming from FeCoNi is observed at 44.4^o, which is also the position of the (200) reflex coming from gold. The increasing intensity of these peaks may suggest an increasing contribution of FeCoNi peaks (Fig. 10.16 b). This can be attributed to a better filling degree (increase in total charge, Fig. 10.1 insets) and more distinct texture along the (111) direction (Fig. 10.7 b). Moreover, the shift in peak positions towards higher angles with more cathodic potential shows the same changes as observed in 100 nm diameter nanowires, indicating a shortening of the lattice parameters. The shift also confirms that this peak is a superposition of the reflexes coming from the FeCoNi alloy and gold. Additionally, the patterns measured for the samples prepared at medium potentials show well-distinguished (220) peaks and low-intensity (200) and (311) peaks. Furthermore, in the case of the nanowires deposited at -1.2 V, two peaks arise, which can be assigned to the hcp Ni-based alloy. Such a mixture of hcp and fcc structure has also been observed in FeCoNi nanowires with a similar chemical composition [152] and in films with high Co content (61 at%) [151]. As was mentioned, a slight hcp fraction was also found in the nanowires with a diameter of 100 nm deposited at the same potential. The above results show a similar structural composition, which will not be analyzed in detail due to the mentioned superposition and low-intensity peaks. The very low peak intensities are due to the small amount of material which, in the case of membranes with a pore diameter of 40 nm, is embedded in pores constituting only 0.14% of the sample surface [188].

The preferred growth direction indicated by XRD measurements is consistent with the information taken from high-resolution TEM analysis. The performed studies reveal that for both nanowire diameters, the samples show a texture along the [111] direction or the [220] direction depending on the applied cathodic potential [188].

10.5. Magnetic measurements

The magnetic measurements of the FeCoNi nanowires were performed at room temperature with the magnetic field applied along the nanowire axis and perpendicular to it. The hysteresis loops of the FeCoNi with diameters of 40 nm and 100 nm deposited at the different potentials are presented in Fig. 10.17. Pronounced magnetic anisotropy with an easy axis along nanowires was observed for all nanowires, regardless of diameter and composition.

As was mentioned earlier, the magnetic behavior of nanowires is determined by completion between magnetocrystalline anisotropy, shape anisotropy, magnetoelastic anisotropy, and dipolar interactions, whereas, the first one may contribute to effective anisotropy only in single crystalline samples or in samples with clearly visible texture. According to the literature, the easy axis in fcc FeCoNi alloys lies along [111] direction [102], which is typical for a Ni-based fcc alloy. The shape anisotropy in high aspect ratio nanowires induces an easy axis along the nanowire axis and is larger than the magnetocrystalline anisotropy in Fe, Ni, and Co (fcc) [72, 193, 194]. The magnetoelastic anisotropy, arising due to stresses between the template and the nanowires, can be neglected at room temperature because its value is much smaller than the shape anisotropy [70, 195]. The last contribution connected with dipolar interaction, if appears, will cause an alignment of the easy axis perpendicular to the nanowire axis.

The nanowires with a diameter of 40 nm showed more rectangular hysteresis measured with a magnetic field applied along nanowires and significantly greater values of coercivity and squareness. Changes in the hysteresis loop shapes for nanowires with different diameters are known in the literature and result from smaller inter-wire interactions as the packing factor decreases (porosity) [112, 196]. Furthermore, the nanowires with diameters smaller than 55 nm are expected to be single-domain wires [112], which changes the magnetization reversal process. The presented structural studies (XRD/TEM) indicate

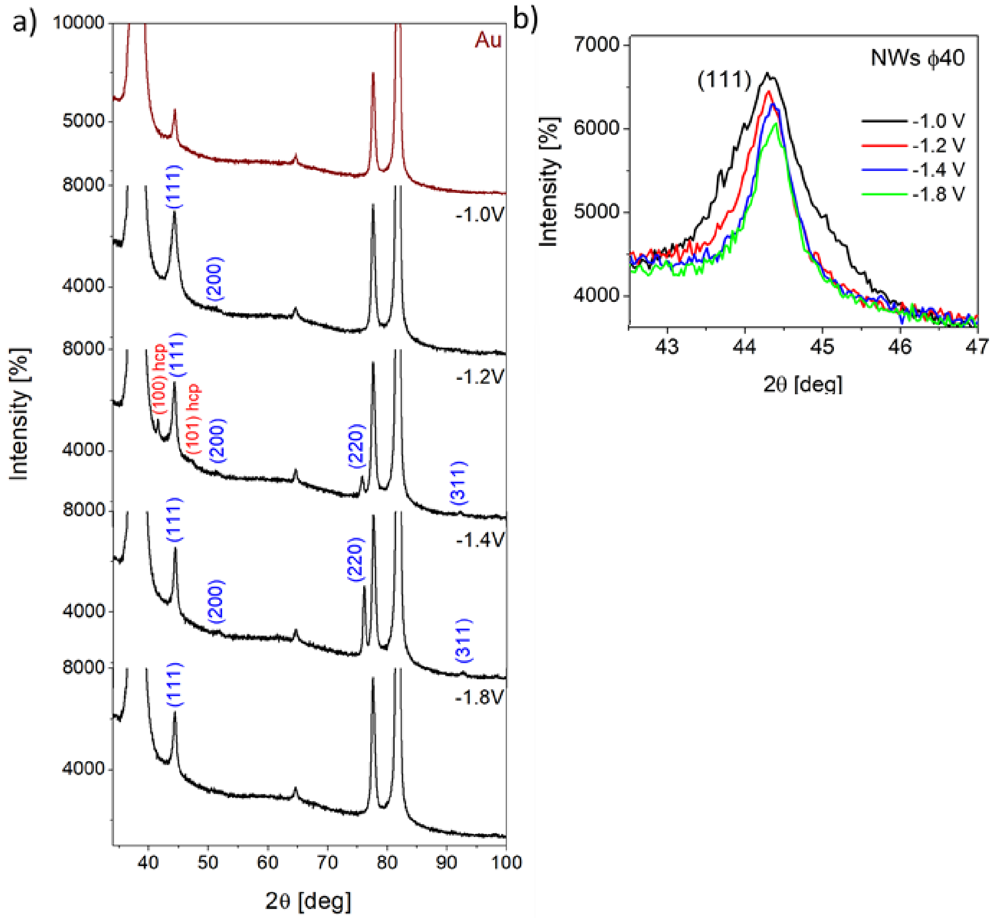

Figure 10.16: (a) X-ray diffraction patterns measured for the FeCoNi nanowires with a diameter of 40 nm embedded in the polycarbonate membranes and (b) superposition of (111) and (200) peaks coming from FeCoNi NWs and Au gold layer, respectively. The assigned peaks correspond to the fcc FeCoNi (blue description; JCPDS:04-003-2245) and hcp FeCoNi (red description; AtomWork calculator). Non-described peaks come from gold [188].

[111] growth direction or the [220] texture at lower and higher potentials, respectively. In nanowires with texture along the [111] direction, magnetocrystalline and shape anisotropies act in the same direction, increasing effective anisotropy along the nanowire axis. A slight fraction of the hcp structure with atomic planes growing along the [100] direction, *i.e.* along a hard magnetic axis, can be neglected. Moreover, for 40 nm diameter NWs, the low porosity templates suggest non-interacting nanowires with negligible dipolar interactions, which additionally increase coercivity and squareness. On the other hand, the texture along [220] deviates from the easy axis direction by about 35^o, thus it slightly contributes to the anisotropy along the nanowires axis. However, in the case of nanowires with a diameter of 100 nm, stronger dipole interactions, associated with the relatively small inter-wire distance, give the contribution to the magnetization alignment in the direction perpendicular to the nanowire axis and overshadow the effect of both anisotropy contributions.

The values of saturation magnetization (M_s), coercivity (H_c), and squareness (M_r/M_s) measured with a magnetic field applied along nanowires are presented in Fig. 10.18. The saturation magnetization normalized to the membrane surface (Fig. 10.18 a) decreases with increasing electrodeposition rate (cathodic potential increases). This behavior is consistent with the decrease in the charge reduced at the cathode, assigned to the decreasing filling degree. The smaller amount of magnetic material embedded into the membrane is one of the reasons for the observed magnetization saturation drop. The second reason may be changes in the chemical composition. Samples with higher M_s values contain a smaller amount of Ni (lower potential), which has three and four times lower saturation magnetization (M_s(Ni) = 57.5 emu/g) than cobalt (162.7 emu/g) and iron (217.9 emu/g) [153, 190, 197]. The described M_s variation as a function of applied potential was observed for both 40 nm and 100 nm diameter nanowires, but at the lowest potential, the amount of Ni was significantly smaller in the nanowires with a diameter of 100 nm, which may explain the large increase in saturation magnetization for this sample. There is also a significant difference in the M_s values measured for nanowires with diameters of 40 nm and 100 nm deposited at other potentials, which is related to the much higher porosity of membranes with a pore diameter of 100 nm equaled to 3.1% compared to 0.7% for membranes with a pore size of 40 nm (Table 2.2). Higher open area means a greater amount of magnetic material contributing to the saturation magnetization [188].

A surprising behavior was observed for coercivity and squareness dependence on the applied cathodic potential (Fig. 10.18 b-c). Both of these values demonstrate extremely different dependencies on the nanowire diameters. In the case of nanowires with a diameter of 100 nm, the expected increase in coercivity and squareness was observed with increasing cathodic voltage. This can be explained by the faster deposition rate, which resulted in a lower filling degree and therefore a more porous structure with a larger number of defects. These defects can block the domain wall movement and lead to a coercivity increase [32, 98]. Changes in the squareness, but also coercivity, can be attributed to smaller dipolar interactions caused by reduced saturation magnetization. Theoretically predicted and experimentally observed narrower, less squared and more oblique-shaped hysteresis has been reported for nanowires with decreasing distance thus increasing dipolar interactions [110, 111, 196, 198, 199, 200]. For nanowires with a diameter of 100 nm, the coercivity and squareness increased with increasing Ni content and decreasing Co and Fe content (higher potentials). These chemical changes resulted

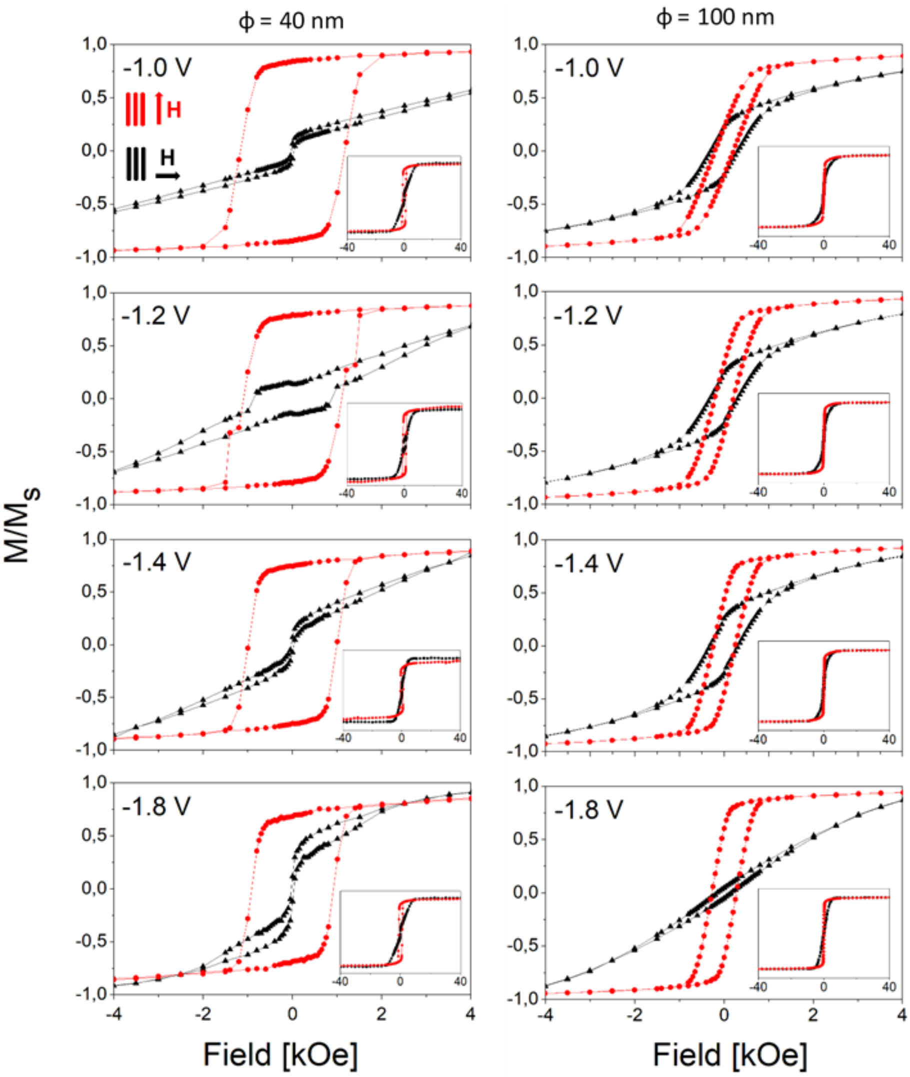

Figure 10.17: Hysteresis loops measured at room temperature with a magnetic field applied out of the membrane plane (red circles) and in the membrane plane (black triangles) for nanowires with a diameter of (a) 40 nm and (b) 100 nm deposited at different cathodic potentials. The magnetization (M) value was normalized to the saturation magnetization (M_s).

in a smaller saturation magnetization, which caused weaker magnetostatic interactions leading to higher coercivity and squareness. Together with the Ni content increase, an expansion of the grain size was observed (Fig. 10.18 c). In our case, the larger the grains, the higher values of the coercivity and squareness were noticed. It is usually assumed that the grain boundary can hinder the domain wall movement, thus the larger the crystallite size, the lower the grain boundary density occurs, which should cause the lowering of the coercivity [32, 96, 191]. The observed discrepancy can again be attributed to the dipolar interactions, which in FeCoNi nanowires with a diameter of 100 nm, turned out to be the dominant factor determining coercivity and squareness. Therefore, the higher the saturation magnetization, the higher the dipolar interactions and the smaller the coercivity and squareness. Unexpected changes in coercivity and squareness were noted

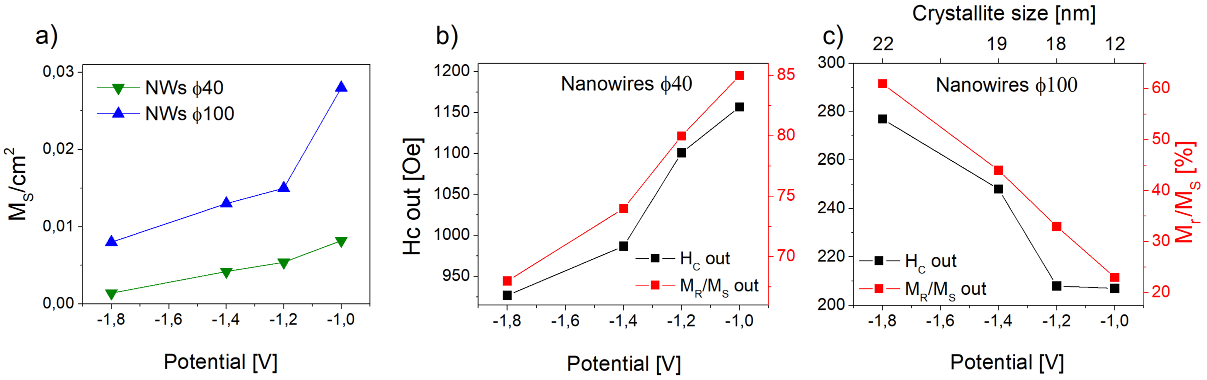

Figure 10.18: (a) Saturation magnetization, (b, c) out of plane coercivity and squareness shown as a function of cathodic potential (and crystallite size) for nanowires with 40 nm and 100 nm diameters.

for nanowires with a diameter of 40 nm (Fig. 10.18 b). In this case, both values decrease with increasing cathodic voltage. Nanowires with a diameter of 40 nm, like nanowires with a diameter of 100 nm, show the same changes in the chemical composition with an increase in Ni content and decreasing total charge reduced at the cathode as a function of cathodic potential. There are also the same trends in the growth rates. Despite these similarities, there is an important differentiating factor, which is porosity, as mentioned above. In nanowires with a diameter of 40 nm, which show low porosity, very weak dipolar interactions do not reduce coercivity and squareness, therefore these parameters are much higher than in nanowires with larger diameters.

Thus, in the case of non-interacting nanowires, the coercivity and squareness behave as saturation magnetization, *i.e.* they increase with increasing Fe and Co content. An increase in coercivity with increasing Co content has also been observed in the literature [20, 147, 180, 198]. According to Shama et al., for weak magnetostatic interactions between nanowires - as in the case of nanowires with a diameter of 40 nm - an increase in Ni content results in a decrease in the saturation magnetization and coercivity [153]. Changes in coercivity and squareness as a function of chemical composition can be analyzed based on the magnetic parameters of Fe, Co, and Ni nanowires. A larger amount of Fe and/or Co, showing higher values of saturation magnetization, coercivity, and squareness, directly results in an increase in these values in FeCoNi nanowires [151, 180]. At the same time, the opposite behavior observed in nanowires with a diameter of 100 nm results from dipolar interactions, which increased when the amount of elements with high saturation magnetization and coercivity increased.

According to the literature, dipolar interactions increase strongly with increasing nanowire length [31, 96, 105]. Although their influence dominated the magnetic behavior of nanowires with a diameter of 100 nm, a significant increase in coercivity and squareness as nanowire length drops down to 1.5 µm (predicted length of the magnetic segment in segmented nanowires) is expected. This suggests that dipolar interactions can also be neglected in nanowires with a diameter of 100 nm, which indicates that both 40 nm and 100 nm nanowires can be considered as potential candidates for racetrack memory applications.

Hysteresis loops were then measured for FeCoNi nanowires as a function of their length and diameter, with a magnetic field applied along the nanowire axis and perpendicular to it (Fig. 10.19 a and b). A clear magnetic anisotropy with an easy axis along the nanowires was observed for all nanowires, regardless of the nanowire geometry.

A decrease in the lengths of nanowires (6 µm, 3 µm, and 1.5 µm) with a diameter of 100 nm, causes slight changes in the hysteresis loops. It is known that if the aspect ratio is higher than 10 (as in our samples), the shape anisotropy contribution remains constant and does not depend on the nanowire length [26, 33, 110], so it will not affect the magnetic properties of considered nanowires. Fig. 10.19 c and d show how the out-of-plane coercivity and squareness change with length for two diameters of nanowires. These results exhibit small and non-monotonic changes for 120 nm diameter nanowires and slightly greater differences in the case of diameters of 100 nm, where the coercivity increases with decreasing length. Such behavior suggests that for larger nanowire diameters, dipolar interactions are strong even in the shortest nanowires, while for nanowires with a diameter of 100 nm they become smaller, which is reflected in the coercivity increase.

However, a change in the shape of the loop measured in the membrane plane can be observed. There are two interesting aspects: a narrowing of the loops with decreasing nanowire length and a small contribution from the rectangular loop. The shortest nanowires show a narrow, almost closed loop typical of measurements in hard directions. As nanowire length increases, the loops become more open with a visible jump associated with the appearance of an additional loop. This two-step magnetic switching suggests the appearance of a soft magnetic material. These may be small disc-shaped objects that exhibit an easy axis direction along the membrane plane. In the case of the longest nanowires, such structures may originate from overdeposited caps. Another explanation can be related to dipolar interactions that can result in the deviation of the magnetic moments from the nanowire axis at the ends of nanowires (vortex or other alignments along the direction perpendicular to nanowire axis), which allows the magnetic field lines to close and minimize magnetostatic energy.

The changes in diameter (Fig. 10.19 b) result in a modification of the hysteresis loops. First of all, as the diameter decreases, the out-of-plane loops become wider with a significant increase in the coercivity and squareness (Fig. 10.19 d). The observed behavior can be attributed to strongly reduced dipolar interactions in smaller-diameter nanowires due to larger inter-wire distance connected with lower porosities. The increase in coercivity and squareness with decreasing nanowire diameter is widely observed in the literature [26, 31, 82, 201]. The in-plane hysteresis loops are open and show a clear superposition of magnetic curves typical for materials magnetized along hard and easy directions, which can be explained as above.

Therefore, the nanowires with a diameter of 100 nm (or less) and a length corresponding to the length of the segment in multi-segmented nanowires can be considered as magnetically non-interacting objects and can meet the requirements for 3D magnetic memory media.

Changes in the nanowire geometry affect the magnetic anisotropy energy, which can be described by a parameter defined as the ratio of squarenesses measured out-of-plane and in-plane of membrane (M_r/M_s)out / (M_r/M_s)in. The larger this parameter, the greater the magnetic anisotropy. This parameter calculated for nanowires with diameters of 40, 100, and 120 nm equals 5.6, 3.6, and 2.5, respectively, and confirms a decrease in magnetic anisotropy energy with increasing nanowire diameter. Similarly, an increase in

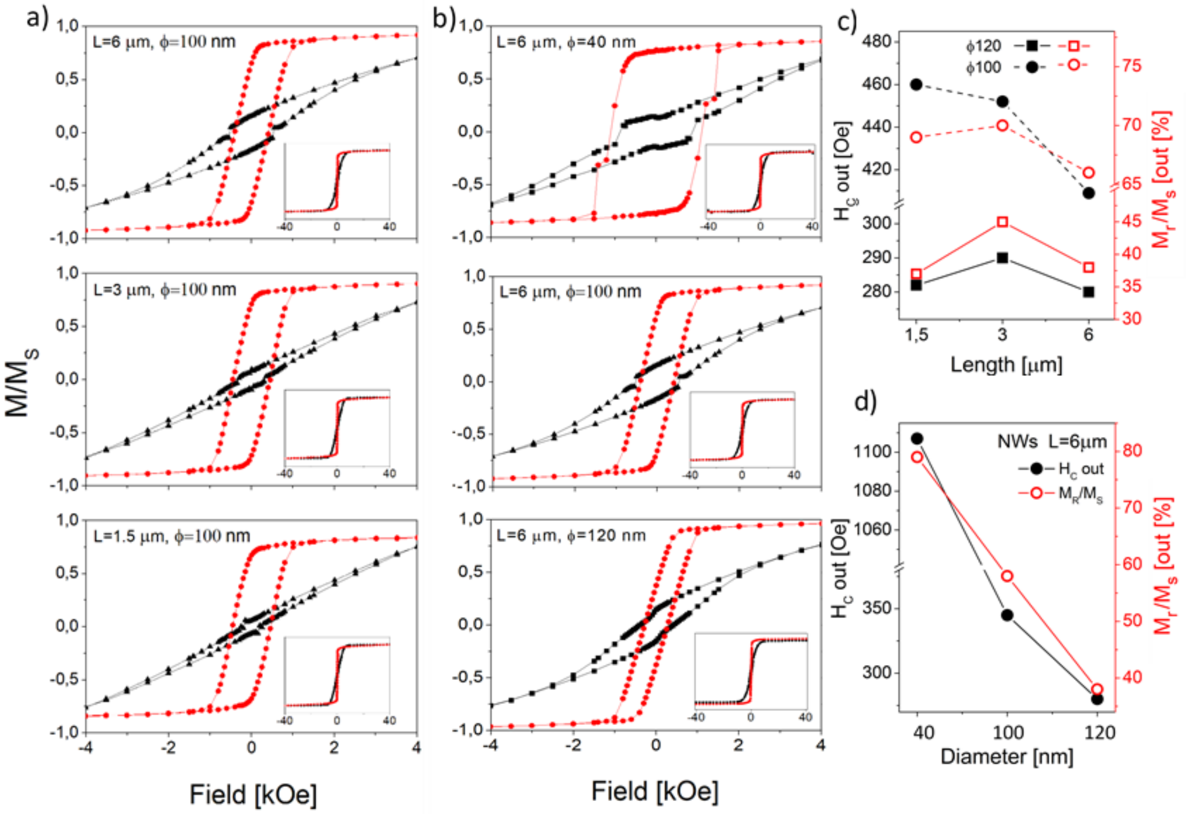

Figure 10.19: Hysteresis loops measured at room temperature with a magnetic field applied in the membrane plane and out of the membrane plane for nanowires (a) with a diameter of 100 nm and different lengths and also (b) for nanowires with a 6μm length and different diameters (U = -1.2 V). The magnetization (M) value was normalized to the saturation magnetization (M$_s$). Out of plane coercivity and squareness shown as a function of (a) length and (b) diameter.

the nanowire length results in a decrease in the magnetic anisotropy energy as shown by parameters 11.2, 8.9, and 4.1 calculated for nanowires with lengths of 1.5 μm, 3 μm, and 6 μm, respectively. The largest magnetic anisotropy is therefore achieved in nanowires with the smallest diameter and the shortest length. On the other hand, an increase in the diameter and length of the nanowire leads to an increase in the magnetostatic interaction, which causes a decrease in the magnetic anisotropy energy. These observations are consistent with the results reported in the literature [21, 202]. The described behavior is also connected with the magnetic structure of nanowires, which depending on nanowire geometry, changes from a single-domain structure to a pseudo-single-domain or multi-domain structure with a critical diameter of about 50 nm [112, 202] and a critical length of about 22 μm [105]. The magnetic structure of nanowires affects their reversal mechanism, which will be analyzed based on the angular dependence of coercivity.

To investigate the magnetization reversal mechanism in FeCoNi nanowires and the influence of nanowire length and diameter on this mechanism, the angular dependence of the hysteresis loops was studied. The angle changed from 0^o to 90^o, where 0^o and 90^o correspond to the magnetic field applied along the nanowire axis and perpendicular to

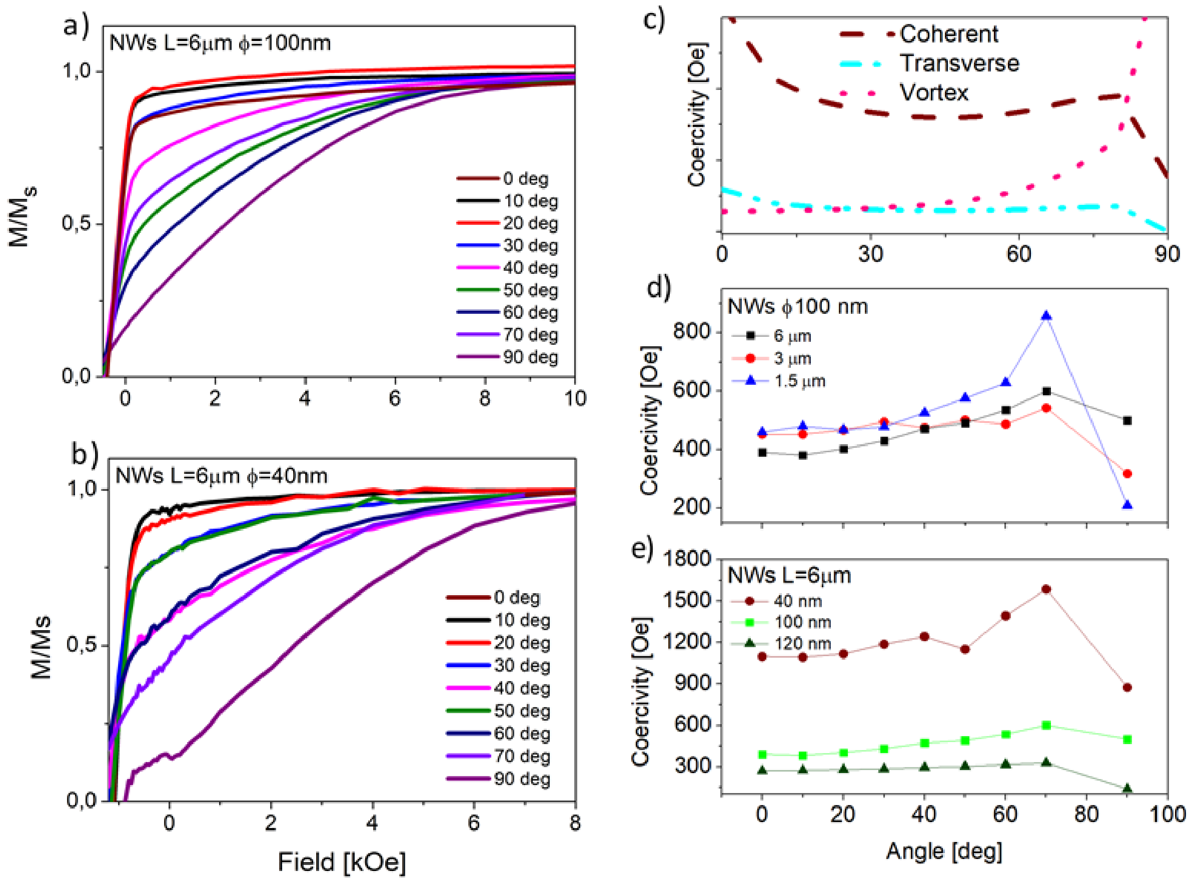

Figure 10.20: Angular dependence of: (a, b) hysteresis loops for FeCoNi nanowires of different diameters, (c) analytical calculations of H_c (θ) for FeCoNi nanowires and (d, e) experimental results of coercivity for different lengths and diameters.

it. The results obtained for nanowires of different lengths and diameters are presented in Figure 10.20. The increase in the angle caused a gradual tilting of the hysteresis loops, which changed from a shape close to rectangular, typical for the easy axis measurements, to almost closed loops observed for measurements along the hard direction (Fig. 10.20 a, c). The coercivity values taken from these measurements were plotted as a function of angle for different lengths (Fig. 10.20 b) and diameters (Fig. 10.20 d) of nanowires. Regardless of nanowire geometry, the changes of H_c versus θ showed similar transients. Initially, with increasing angle, the H_c increased slightly, then reached a maximum at 70 degrees, and decreased at $\theta = 90^o$. The most pronounced maxima were observed in the nanowires with the smallest length and diameter, while for longer nanowires with larger diameters, the changes of coercivity were much smaller. Similar $H_c(\theta)$ transients with maxima close to 70 degrees were observed by other groups [105, 165, 209] and were interpreted as a transition between different reversal modes. According to Figure 4.10, this non-monotonic coercivity variation can be explained by a combination of vortex domain wall propagation, dominating before the maximum was reached, and transverse or coherent rotation, which switches magnetic moments when the angles are close to the hard magnetic axis.

The magnetic structure of FeCoNi nanowires and the interactions between nanowires were analyzed using FORC methods. In Figure 10.21 the FORC diagrams measured for nanowires with a length of 6 µm and diameters of 40 nm and 100 nm are presented. The H_c axis presents the coercivity field distribution while the H_u axis shows the interaction field distribution. In the case of small diameter nanowires, a single elongated region can be observed along the H_c axis at $H_u = 0$ with a slight extension in the perpendicular direction. This indicates a small coercivity distribution (920 - 1420) probably related to the small difference in the nanowire length. The coercivity value determined from the hysteresis loop (1110 Oe) corresponds to the maximum of the FORC diagram. The distribution along the H_c axis suggests the magnetization reversal by the propagation of the transverse domain wall [105]. Such a contour closed around the central peak indicates a single-domain structure of nanowires. The relatively narrow distribution along the H_u axis demonstrates low magnetostatic interactions. The slight positive slope in this distribution can be interpreted as the appearance of another interaction field in addition to the almost constant interactions giving a small symmetrical broadening [167].

With the diameter increase, the shape of the FORC diagram undergoes a large change. In contrast to the previous case, the diagram is elongated in the direction parallel to the H_u axis. Such a distribution indicates the presence of magnetostatic interactions between nanowires. These interactions are responsible for the lower coercivity of nanowires with larger diameters as confirmed by the pattern shift towards lower H_c. The contours are symmetrically arranged with respect to H_u=0 (-400 Oe - 400 Oe) and slightly spread along H_c with a distribution between 280 - 570 ($\Delta = 290$ Oe). The closed contours with a steep slope suggest a single-domain structure of the nanowires [211]. However, the relatively long ridge with a tail extending along the H_c axis and the symmetrical pattern of the main part show some features of the multi-domain structure, which may appear as the magnetostatic energy increases [210]. Moreover, one can distinguish another small separated region with low coercivity, which can be assigned to the soft magnetic phase.

Thus, the increase in the nanowire diameter results in a significant broadening of the pattern distribution in the H_u direction due to the increasing interaction field. The larger diameter of nanowires and the associated larger inter-wire interactions may cause changes in the magnetic structure of nanowires. The studies in this direction will be continued.

Further investigations of the magnetic properties of the FeCoNi nanowires were carried out using Lorentz-TEM. Figure 10.22 shows the images obtained for nanowires with a length of 6 µm and a diameter of 40 nm and 100 nm (as in FORC). Under-focus and over-focus Lorentz-TEM images show bright and dark fringes along both sides of the nanowires and inside them, respectively. For smaller diameter nanowires, uniform Fresnel fringes along the whole nanowires indicate the single-domain structure without a domain wall in the analyzed area of nanowires [208]. Small perturbations along the nanowires reflect the sample morphology shown in the in-focus image. On this basis, it can be concluded that the presented nanowires behave like a material with an SD structure. The same observations were made for nanowires of a larger diameter. Analysis performed at different locations did not reveal the features expected in a multi-domain structure. Thus, studies carried out using a Lorentz microscope suggest a single-domain structure in nanowires of both diameters.

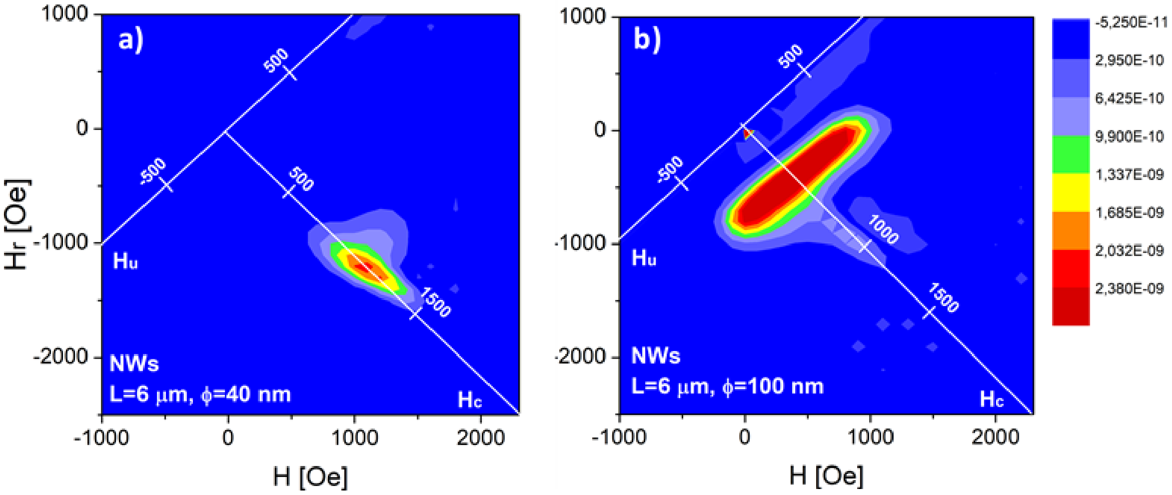

Figure 10.21: Out-of-plane FORC diagrams of FeCoNi nanowires with a length of 6 μm and different diameters: (a) 40 nm and (b) 100 nm.

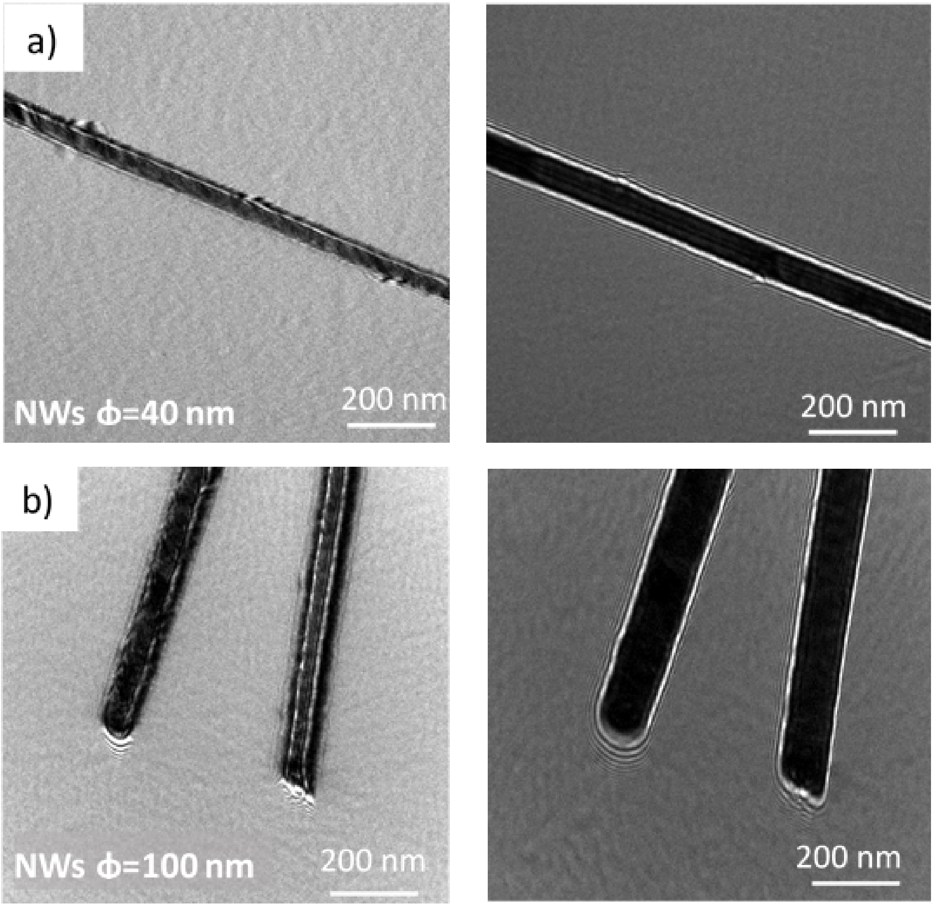

Figure 10.22: Lorentz-TEM in-focus and under-focus images of FeCoNi NWs for (a) 40 nm and (b) 100 nm diameter.

FeCoNi nanowires, depending on the applied voltage and their geometry, show differences in the filling degree, structure, and magnetic properties. Changes in the cathodic voltage resulted in modifications of the magnetic parameters of nanowires. Our preliminary studies using FORC measurements and Lorentz microscope give interesting results but require further systematical investigations to determine the difference in the magnetic behavior of nanowires with diameters of 40 nm and 100 nm, especially concerning their magnetic structure and mutual interactions. Such materials are promising candidates for 3D memory applications and have been investigated in the form of segmented nanowires. The results of these studies are presented in the next chapter.

Chapter 11

Segmented nanowires - FeCoNi

In Chapter 10, I analyzed the morphology, structure, and magnetic properties of ternary FeCoNi nanowires depending on the deposition potential and their geometry (diameter and length). As mentioned earlier, such nanowires can be a basis for building a 3D race-track memory. For this purpose, it is necessary to create nanowires containing domain walls distributed at desired locations along nanowires. These domain walls will serve as memory units. To obtain such a multi-domain structure, I prepared segmented nanowires. Particular segments will be composed of FeCoNi with different contents of these metals characterized by various magnetic parameters. I expect the boundaries between segments will be the places of domain wall formation with intentionally created domain wall pinning sites.

11.1. Single segment nanowires

Electrodeposition process

After preparing nanowires with a length equal to the membrane thickness (i.e. complete pore filling), I calculated the charge required to fill 1/3 of the pore channel length to obtain nanowires with a length of 2 µm. Based on previous studies, I produced FeCoNi nanowires of the desired length and diameter of 100 nm at three different cathodic potentials. Figure 11.1 shows the current vs. time dependence recorded during nanowire deposition. The processes occurring at different deposition rates were stopped at various electrodeposition times when the assumed charge (shown in the inset of Fig. 11.1) corresponding to the selected nanowire length was reached.

Nanowire morphology

Figure 11.2 shows FeCoNi nanowires with a length of 2 µm deposited at different potentials. As can be seen, the nanowires are continuous, without visible porosity, similar to their long counterparts (Fig. 10.6).

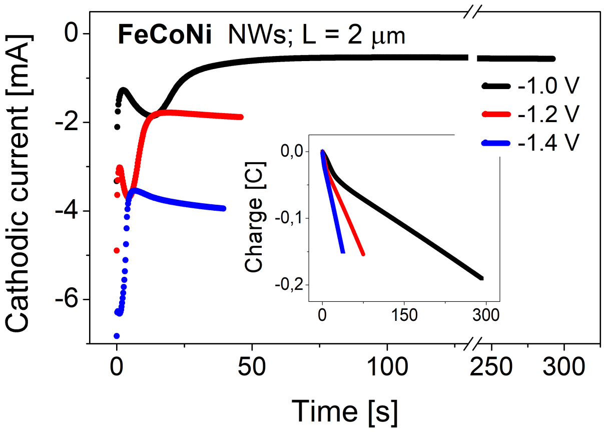

Figure 11.1: Cathodic current versus time measured during the electrodeposition FeCoNi nanowires at different potentials (L = 2 µm, $\phi = 100$ nm). The inset shows corresponding electrical charge variations in time.

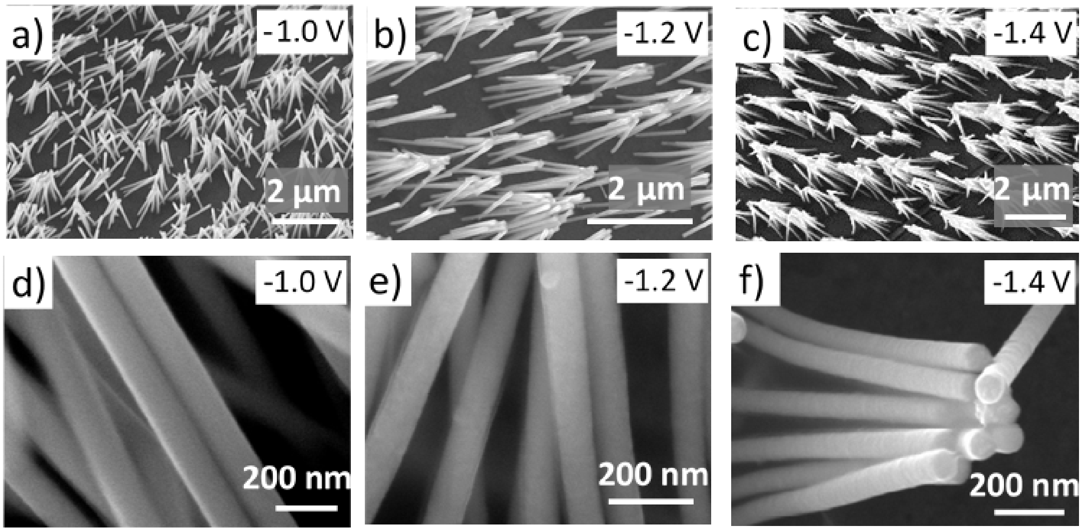

Figure 11.2: SEM images of FeCoNi nanowires (L = 2 µm, $\phi = 100$ nm) deposited at the various cathodic potentials observed after membrane dissolution: (a, b, c) lower magnification showing forest-like short nanowires, (d, e, f) higher magnification indicating smooth wires.

The chemical composition of the nanowires showed the same trend with the potential changes as in the case of 6 µm long nanowires with insignificant differences in the content of individual elements. Thus, with the potential increase, the nickel content in the samples increased, while the content of iron and cobalt decreased (Fig. 10.9).

Magnetic measurements

As it follows from the studies of FeCoNi nanowires of different lengths (Fig. 10.19), shorter nanowires with a diameter of 100 nm should exhibit higher coercivity and squareness due to lower saturation magnetization and smaller magnetostatic interactions.

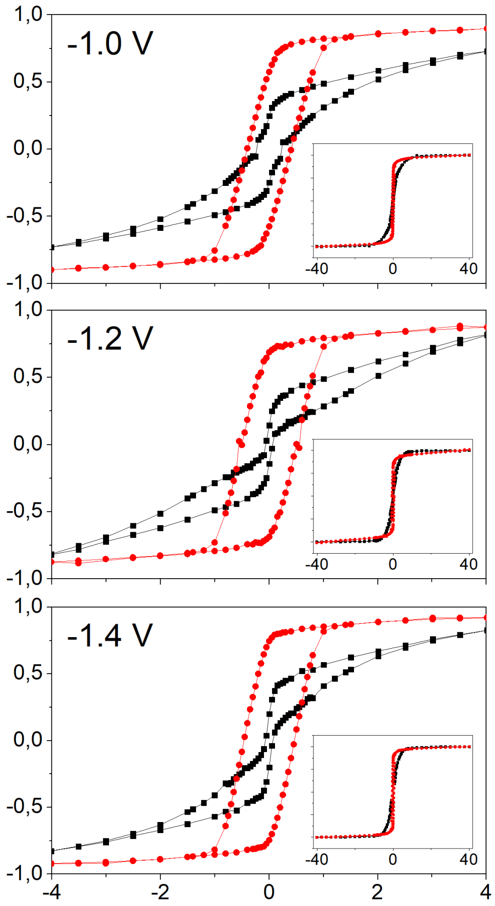

Figure 11.3: Hysteresis loops measured at room temperature with a magnetic field applied out of the membrane plane and in the membrane plane for FeCoNi nanowires with a length of 2 µm and diameter of 100 nm deposited at different cathodic potentials.

Magnetic measurements of 2 µm long and 100 nm in diameter FeCoNi nanowires were performed using a SQUID magnetometer under the same conditions as for the previous samples. Figure 11.3 presents the hysteresis loops of nanowires deposited at different potentials. Similar to long nanowires, the magnetic anisotropy with the easy axis along nanowires was observed in all cases, demonstrating that shape anisotropy still plays a dominant role in determining the easy axis parallel to the NWs. However, in-plane loops are not as narrow as in the case of 6 µm nanowires. In addition to the curve typical of the phase measured along the hard direction, a rectangular loop appears indicating the presence of the soft magnetic material. Furthermore, the 6 µm and 2 µm long nanowires differ significantly in the aspect ratio, which decreases from 60 to 20. This may suggest that in the shorter nanowires, the contribution of magnetostatic interactions may be smaller, which should result in higher coercivity and squareness of 2 µm long nanowires.

Figure 11.4 shows the coercivity (H_c) and squareness (M_r/M_s) for short nanowires compared to 6 µm long nanowires. Both parameters are significantly larger in the case of short nanowires. The coercivity measured for nanowires with a length of 2 µm exhibits non-monotonic behavior as a function of the applied voltage, with the highest value at a

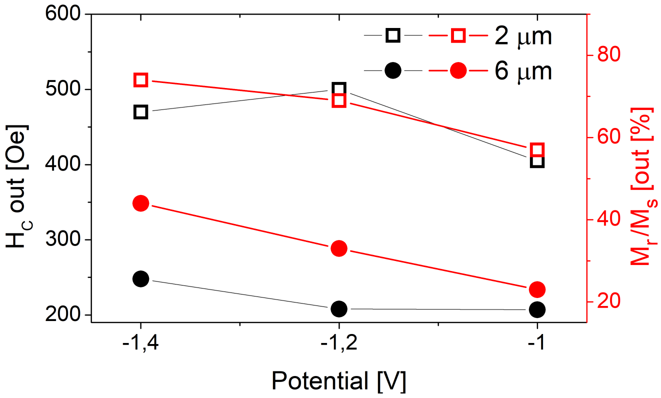

Figure 11.4: Out-of-plane coercivity and squareness shown as a function of cathodic potential for nanowires with a diameter of 100 nm and two different lengths: 2 µm and 6 µm.

potential of -1.2 V.

The magnetic properties of FeCoNi nanowires with a length of 2 µm were analyzed using FORC measurements. Figure 11.5 shows the FORC diagram with two regions. The largest one is extended along the H_u axis from -400 to 310 Oe (Δ=710) with weak distribution along the H_c direction (320-550 Oe, Δ=230), and asymmetric elongation (at H_u = -120 Oe) up to 580 Oe. Both the elongation in the H_u and H_c axes is smaller compared to the long nanowires. This may indicate smaller magnetostatic interactions, additionally its asymmetry with a larger part occupying negative H_u values may suggest a greater role of exchange interactions [166]. In contrast to the long nanowires, the diagram measured for short nanowires has a significantly lower FORC signal. The coercivity value taken from the hysteresis loop equal to 510 Oe is in the range of coercivity distribution taken from the FORC measurements. This broadening may result from nanowire length distribution. The relatively low spreading along H_u indicates a single-domain structure of the 2 µm nanowires.

In addition to the main pattern, a region with two objects can be distinguished at higher coercivities (700 and 900 Oe). These objects did not show any broadening either along the H_c or along the H_u axis indicating the presence of non-interacting harder (than the phase from the first region) magnetic phases.

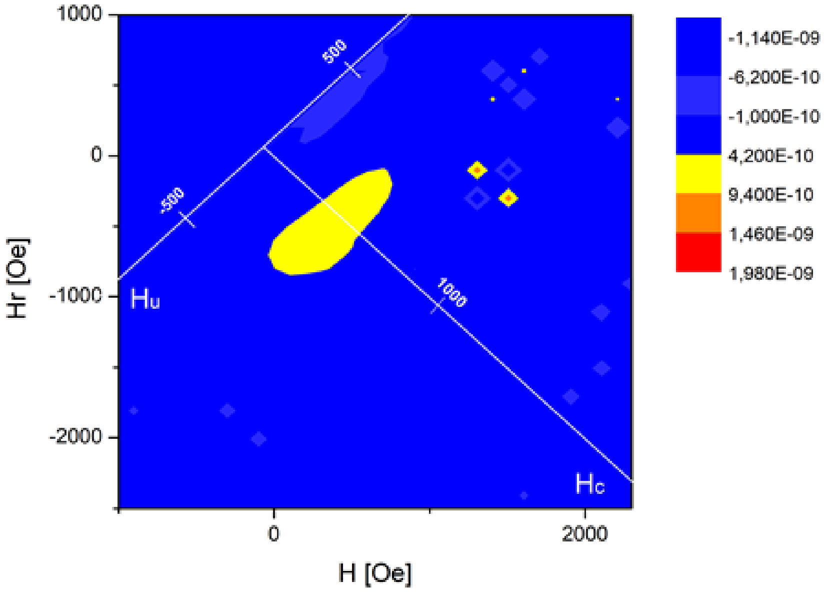

Figure 11.5: Out-of-plane FORC diagrams of FeCoNi nanowires with a length of 2 µm and a diameter of 100 nm (U = -1.2 V).

The magnetic structure of short nanowires was studied by Lorentz-TEM microscopy. Figure 11.6 shows the in-focus and under-focus images. The uniform Fresnel fringes visible along the whole nanowire (Fig. 11.6 b) indicate a homogenous magnetic object without magnetic domain walls. The observed deviation of the fringes at the nanowire ends suggests a slight perturbation in the magnetic moment ordering, typical for elongated objects.

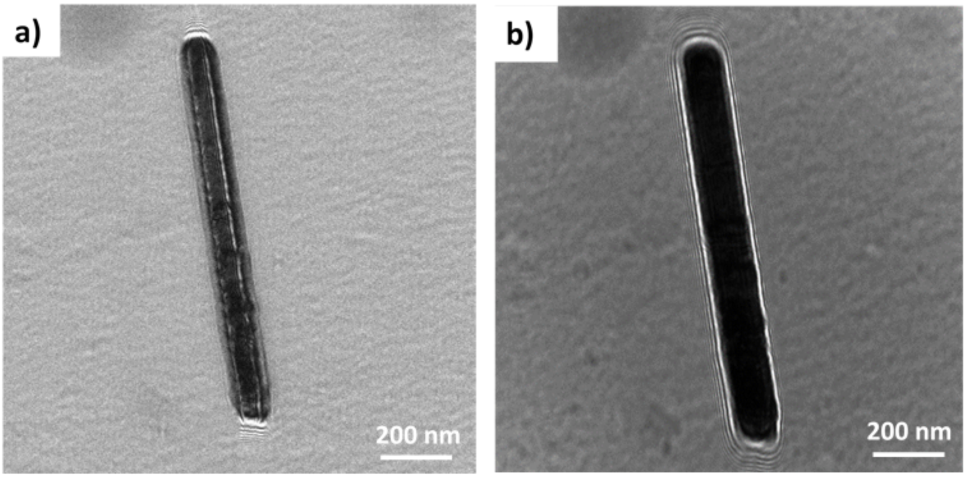

Figure 11.6: (a) In-focus and (b) under-focus Lorentz-TEM images of short FeCoNi nanowires with a diameter of 100 nm (U = -1.2 V).

The above studies demonstrated that the applied potentials enable the production of single-domain nanowires with different chemical compositions and various magnetic properties. This suggests that the nanowires composed of segments deposited at different potentials could be separated by domain walls pinned at the segment boundary. The studies of segmented nanowires are presented in the next subsection.

11.2. Segmented nanowires

The FeCoNi nanowires with a length of 2 µm prepared separately at different cathodic potentials allow me to learn about the chemical composition and magnetic properties of individual segments. Based on the information obtained, I deposited segmented FeCoNi nanowires with a total length of 6 µm and a diameter of 100 nm, consisting of three segments of 2 µm each. The electrodeposition process was performed in a single electrolytic bath applying a specific voltage sequence with an appropriate pulse duration.

Electrochemical analysis

Figure 5 shows the potential and current vs. time dependence recorded during the electrodeposition of segmented nanowires. The sequence of the applied potentials with different pulse durations (Fig. 11.7 a) starts from -1.0 V then switches to -1.2 V and ends at -1.4 V. In response to the applied voltage, different currents were recorded (Fig. 11.7 b) with values similar to those measured for single counterparts. Each step of the sequence was stopped when the previously estimated charge (Fig. 11.1) corresponding to a nanowire length of 2 µm was reached (Fig. 11.2 b). The charge measured at the lowest voltage shows a nonlinear transient associated with the current decrease (Fig. 11.7 b) caused by the mass transport limitation at the nucleation stage.

Morphology and chemical composition

Similar to the samples deposited at individual potentials, the SEM images (not shown) revealed that segmented FeCoNi nanowires were also continuous and smooth, without any visible porosity. These measurements did not show any features indicating a segmented structure of nanowires.

The chemical composition of the segmented nanowires was analyzed using the HAADF detector. Figure 11.8 presents the STEM-HAADF image with corresponding EDS maps showing the Fe, Co, and Ni content of the segmented nanowires. Following the content of the individual elements along the nanowires, one can distinguish clear changes in the chemical composition that correspond to the successive segments of nanowires.

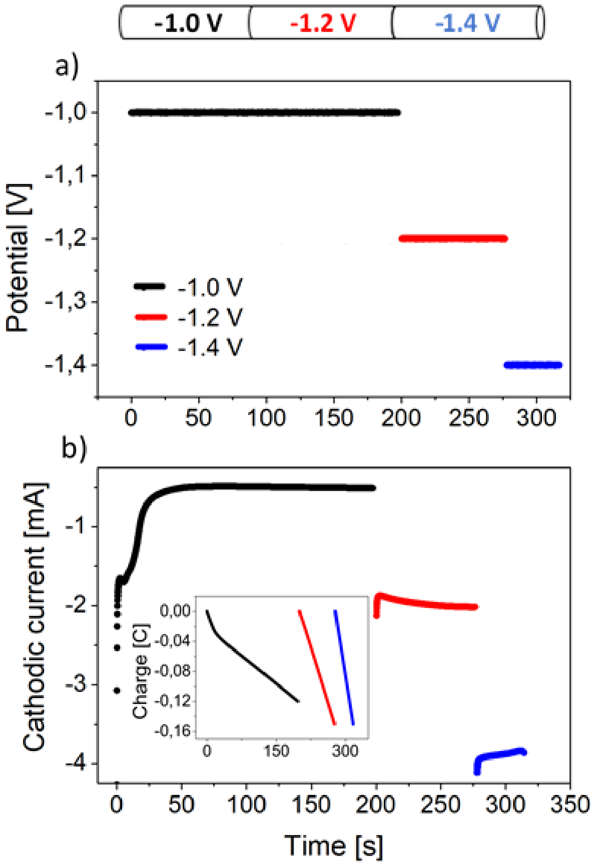

Figure 11.7: (a) Applied potential and (b) cathodic current versus time measured during the electrodeposition of 3-segmented FeCoNi nanowires with a diameter of 100 nm and a total length of 6 µm (each segment 2 µm). The inset in the current graph shows corresponding electrical charge variations in time. The drawing above the graphs shows the nanowire scheme.

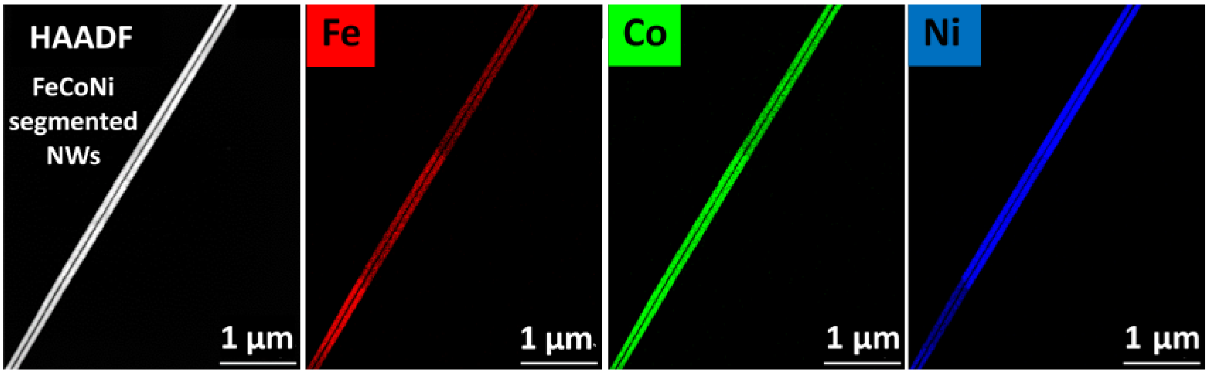

Figure 11.8: STEM-HAADF images and corresponding HAADF-EDS maps showing the content of Fe, Co, and Ni measured in segmented FeCoNi nanowires with a diameter of 100 nm and a length of 6 µm.

The segmented structure of nanowires is even more visible in the EDS map showing all elements together, presented in Fig. 11.9 a. The changes in the chemical composition along the nanowires are also confirmed by the linear EDS spectra depicted in Fig. 11.9 b. The spectra were measured from the nanowire end, thus the scan starts from U = -1.4 V. The atomic fraction shown on the left axis indicates slightly different values from those obtained during the deposition of nanowires prepared at individual potentials. However, general features such as increasing Ni content and decreasing Fe and Co content with increasing potential, similar content of elements at the lowest potential, highest Ni content at more cathodic potentials (-1.2 and -1.4 V), and larger Co content compared to Fe are kept.

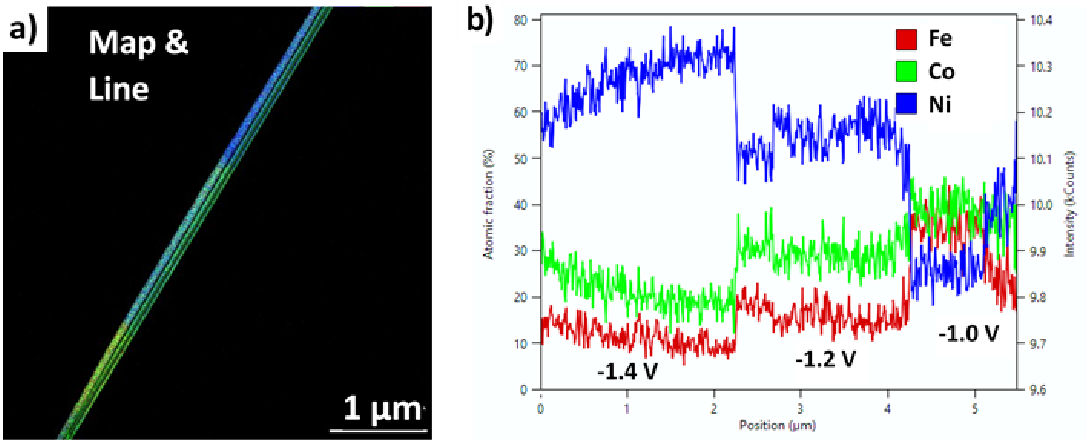

Figure 11.9: (a) EDS-map showing the Fe, Co, and Ni content together and (b) linear scan measured along the segmented FeCoNi nanowires.

The above studies show that it is possible to obtain segmented nanowires of a specific composition by applying different values of cathodic potential in a single electrolyte bath. Based on previous studies I expect that the difference in the chemical composition of individual segments will be sufficient to modify the magnetic properties of the nanowires and create domain walls at the boundaries of the segments.

Magnetic properties

Figure 11.10 a presents the hysteresis loops of segmented FeCoNi nanowires. Magnetic measurements confirm the alignment of the magnetic easy axis along nanowires. The coercivity and squareness taken from out of membrane plane measurements were 390 Oe and 64 %, respectively. Thus, the squareness value is within the range of parameters obtained for nanowires deposited at individual potentials, while the coercivity shows a lower value, which could result from stronger magnetostatic interaction or magnetically softer material. It was assumed that the magnetic parameters of individual segments are similar for 2 µm nanowires deposited at corresponding potentials (repeated in Fig. 11.10 b). The segmented nanowires were also studied using FORC measurements. The results are shown in Fig. 11.11. Three separated regions can be distinguished in the diagram. The main pattern has some similar features to the pattern obtained for homogeneous nanowires with lengths of 6µm and 2 µm (Fig. 10.21 b and Fig. 11.5). The contour

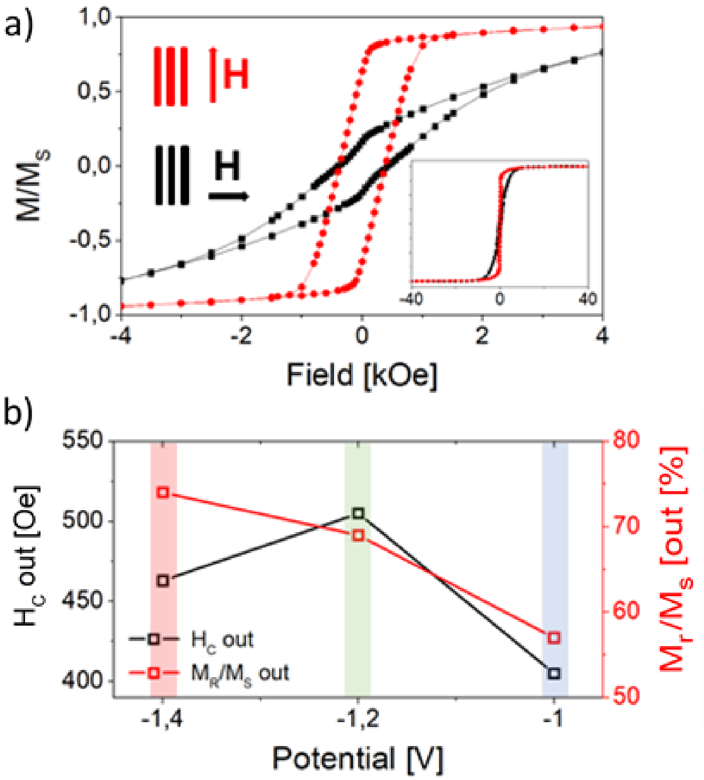

Figure 11.10: (a) Hysteresis loops of segmented FeCoNi nanowires measured with a magnetic field applied in the membrane plane and out of the membrane plane and (b) the dependence of the coercivity and squareness for 2 µm nanowires deposited at potentials corresponding to the voltages applied during the deposition of segmented nanowires.

is extended along the H_u axis between -500 and 550 Oe ($\Delta = 1050$ Oe) with a slight spreading along the H_c axis (at $H_u = 0$) between 250 and 540 Oe, with the distribution of $\Delta = 290$ Oe. The elongation in the H_u direction is larger compared to homogenous nanowires, while the spreading along the H_c axis is exactly the same as observed for long nanowires. The values of the coercivity expected for the individual segments based on the 2 µm nanowires are within the range of coercivity distribution determined from the FORC measurements. In contrast to the homogenous sample (Fig. 10.21 b), the slope of the main pattern is much gentle. The visible elongation in the H_c direction up to 580 Oe at $H_u \approx$ -250 Oe also appears in the short nanowires and reaches exactly the same coercivity but at a different H_u value.

The elongation in the H_u direction, which is larger than that of the homogeneous nanowires, and the less steep contour slope suggest multi-domain structures of the segmented nanowires [105].

Additionally, the diagram shows two double contours. One pair is in close proximity to the main pattern with coercivities of about 870 and 950 Oe (at H_u close to 0) and the other with coercivities of 1700 and 1900 Oe at high positive values of H_u (2610 and 2600 Oe). These regions indicate the presence of hard magnetic materials, with two different well-defined coercivities without the H_c distribution pointing out non-interacting objects. The coercivities determined from FORC measurements differ significantly from the values expected for the individual segments. An interesting feature requiring further studies is the appearance of the regions with double contours. We did not notice the soft magnetic phase observed in the homogeneous sample with a length of 6 µm.

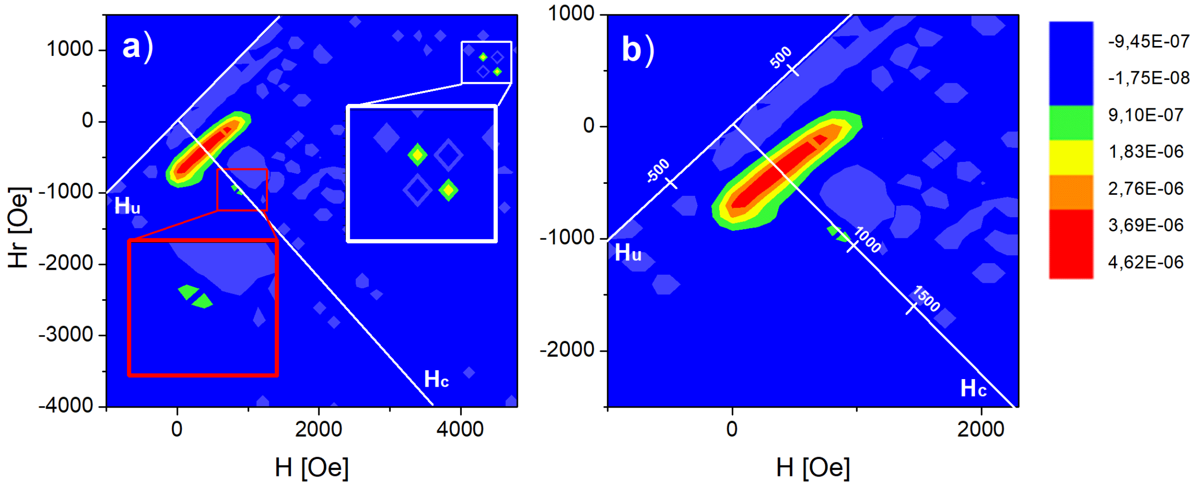

Figure 11.11: Out-of-plane FORC diagrams of segmented FeCoNi nanowires with a total length of 6 µm and a diameter of 100 nm. (a) diagram presenting all regions and (b) diagram shown at the same scale as the FORC diagram measured for homogeneous samples of different lengths (Fig. 10.21 b, Fig. 11.5) for comparison purposes. Insets show selected regions at a magnified scale.

These studies revealed a complex magnetic structure that induces complicated magnetic interaction expected in segmented nanowires. We hope that in time we will be able to satisfactorily explain all features observed in the diagram.

The segmented nanowires were also examined using Lorentz-TEM microscopy. Figure 11.12 shows in-focus and over-focus Lorentz-TEM images with insets presenting selected areas at higher magnifications. Fresnel fringes, difficult to see in the presented scale but clearly visible at higher magnifications (insets), appear on both sides of the nanowires. The fringes observed in the regions extending from the nanowire ends are uniform without any perturbation, which indicates a homogenous magnetic structure (blue inset). However, as can be seen in the yellow inset, two disturbances marked with arrows are observed in the central part of the nanowires. Their positions correspond very well to the sites of the chemical composition modification (Fig. 11.9 a). Such a perturbation observed by Venturi et al. in cobalt nanowires was interpreted as a domain wall [208]. They confirmed the above interpretation after applying the small magnetic field that caused its shift along nanowires. Thus, based on the literature reports and our studies we can attribute these deviations of Fresnel fringes to the domain walls, which, as can be concluded from their positions, are pinned at the segment boundaries.

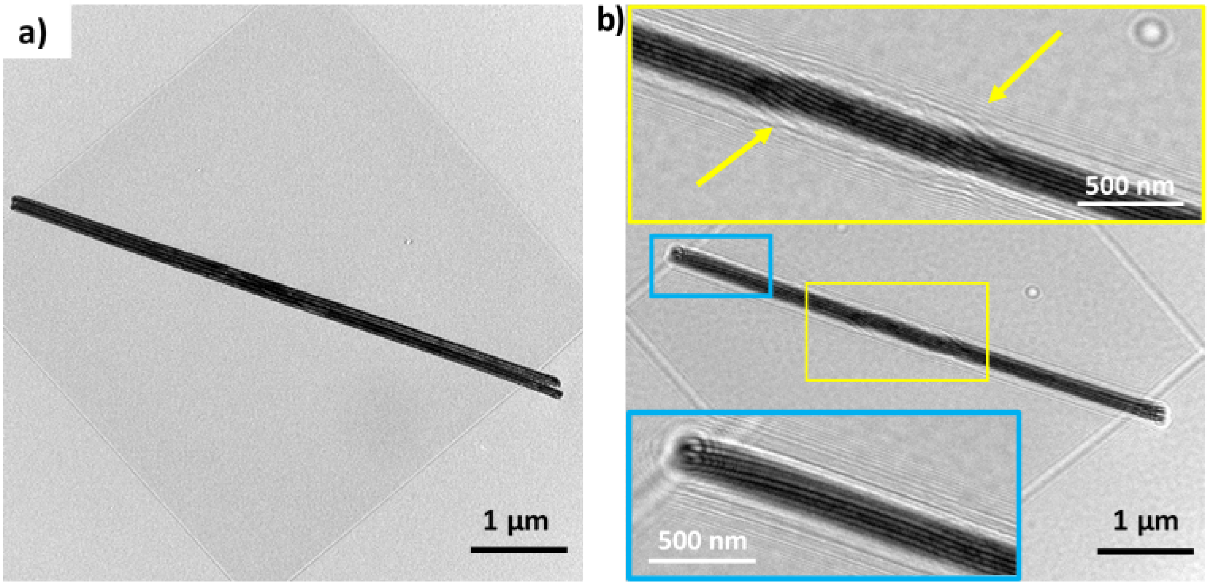

Figure 11.12: Lorentz-TEM (a) in-focus and (b) over-focus images of segmented FeCoNi nanowires with a diameter of 100 nm. Insets show selected regions at higher magnifications. Yellow arrows indicate the position of domain walls located at the segment boundaries.

The above results confirm that the boundaries between segments are the sites of domain wall formation. Thus, using an appropriately selected electrolyte and well-chosen cathodic potentials, I created nanowires with intentionally distributed magnetic domain walls. Nanowires prepared in this way meet the criteria required for 3D racetrack memory applications.

In my further scientific work, I will extend this study up to nanowires deposited in alumina membranes and doped with copper as will be shown in the last chapter. Moreover, the studies using the Lorentz microscope will be extended by the application of a small external magnetic field, which should induce the domain wall movement and finally confirm that observed perturbations are indeed domain walls. FORC studies also require more in-depth analysis, which will be expanded with further measurements.

Chapter 12

Conclusions

This interdisciplinary work entitled *Morphology, structure, and magnetic properties of metallic nanowires synthesized by electrodeposition* contains the results of studies on nanowires in the form of single-element (Fe, Co, Ni) binary systems (FeCo, FeNi) and ternary alloys (FeCoNi) with diameters of 40, 100 and 120 nm and length varying from 1.5 to 6 µm.

The main goal of this thesis was to modify the magnetic properties along nanowires to obtain segmented nanowires, the individual segments of which exhibit different chemical compositions and associated various magnetic properties. Such segmented nanowires with domain walls pinned at the sites of the segment boundaries can find application in 3D racetrack memory systems.

Single element nanowires of Fe, Co, and Ni prepared in polycarbonate membranes demonstrated bcc, hcp (with a small amount of fcc), and fcc polycrystalline structure, respectively, and various magnetic parameters such as coercivity and squareness.

Fe nanowires embedded in a polycarbonate template and released from membrane nanowires (covered with a thin polycarbonate layer) showed chemical stability without the formation of an oxide layer in the tested temperature range.

The use of different cathodic potentials and well-selected electrolyte allowed me to obtain alloy nanowires with different chemical compositions from a single electrolyte bath.

FeCo binary alloys showed poor sensitivity of the chemical composition to the applied potential, in contrast to Fe/Ni alloys, which demonstrate an increase in Ni content with increasing voltage and an associated increase in coercivity and squareness.

Increasing cathodic potential caused changes in the chemical composition of FeCoNi ternary alloys, the more cathodic potential, the higher the Ni content and the lower the content of Fe and Co. The increase in the Ni content resulted in changes in the preferred growth direction from [111] to [220], a shortening of the fcc lattice parameters, and an increase in crystallite size. Nanowires deposited at all applied potentials showed a magnetic easy axis along nanowires. Depending on nanowire geometry, the applied potential caused different dependence of saturation magnetization, coercivity, and squareness on the applied potential, explained based on magnetostatic interactions. The magnetic reversal mechanism was determined as the combination of the vertex domain wall propagation followed by transverse or coherent rotation. The nanowires demonstrated a single-domain structure, with magnetostatic interactions appearing in nanowires with larger diameter.

Segmented FeCoNi nanowires were successfully obtained by applying a specific voltage sequence with an appropriate pulse duration in a single electrolytic bath. The segment boundaries were identified as domain wall pinning sites, which makes such materials promising candidates for 3D racetrack memory applications.

Further studies will focus on nanowires prepared in alumina membranes and FeCoNi alloys doped with Cu. The results obtained by advanced magnetic techniques such as FORC and Lorentz-TEM microscopy will be extended with in-depth analysis and interpretation.

Chapter 13

Plans for the near future

In further scientific work, I plan to continue research on FeCoNi systems in two directions. The first is the studies of FeCoNi nanowires deposited in alumina membranes, the second is the investigations of this alloy doped with Cu. My preliminary studies, indicating the possibility of modifying magnetic properties, give promising results, which I will briefly describe in the next two subsections.

13.1. FeCoNi nanowires deposited in AAO

As was described in chapter 2.2 the alumina membrane shows a different pore distribution and porosity compared to polycarbonate membranes. The regular, hexagonal pore distribution is a favorable feature enabling the prediction of nanowire position (helpful in localization of magnetic units) and amount of studied material (for estimating M_s/cm^3 value). In turn, porosity, which can be even two orders of magnitude larger in comparison with polycarbonate, is a disadvantage due to the smaller inter-pore distance resulting in larger magnetostatic interactions, although on the other hand, it may increase magnetic unit density. Moreover, alumina membranes are usually much thicker than polycarbonate, which allows the production of long nanowires with a high aspect ratio.

Therefore, to study FeCoNi nanowires with higher length and porosity I deposited FeCoNi nanowires in AAO membranes with a pore diameter of 40 nm at four cathodic potentials. Increasing the cathodic potential caused a current increase and known from previous studies a significant decrease in the reduced charge, suggesting a lower filling degree in the sample deposited at more cathodic potential.

Figure 13.1 shows the cross-section of the AAO template with FeCoNi nanowires with completely filled membrane channels. I did not notice any differences in the morphology of nanowires deposited at selected potentials. As in the case of nanowires deposited in PC membranes, the nanowires obtained in AAO membranes showed similar composition at corresponding potentials with the same trend observed with varying voltage. The structure of nanowires deposited in alumina also did not differ significantly from samples deposited in PC and shows the same polycrystalline fcc structure with a texture along [220] direction.

The magnetic properties that are the most interesting in our studies, seem to be ideal for 3D racetrack memory applications. As shown in Fig. 13.2, the hysteresis loops measured along the nanowires are rectangular with high coercivity and squareness (much

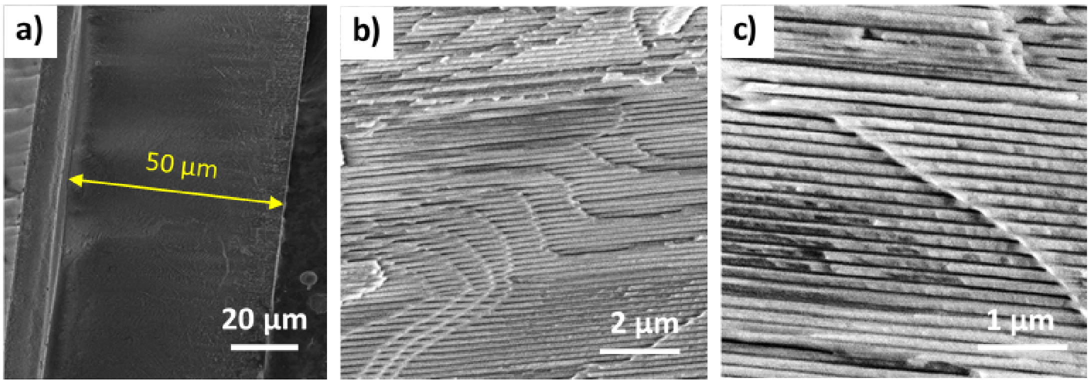

Figure 13.1: SEM images of the FeCoNi nanowires ($\phi = 40$ nm) inside the AAO template, deposited at -1.2 V.

higher than in PC membranes), while measurement with a magnetic field applied in the membrane planes shows curves typical of a hard magnetic axis with zero values of remanence and coercivity. This indicates a magnetic easy axis perfectly aligned along the nanowires. Similar to the case of nanowires produced in polycarbonate, the changes in magnetic parameters under the influence of applied potentials make this material a promising candidate for 3D magnetic memory applications. In the future, differences in interactions resulting from the distance between nanowires will be studied in more detail.

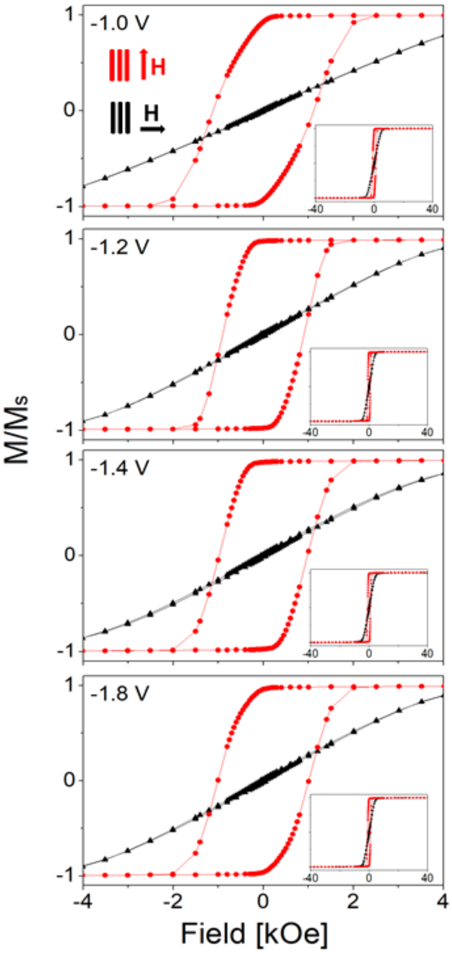

Figure 13.2: Hysteresis loops measured at RT with a magnetic field applied out of the membrane plane (red circles) and in the membrane plane (black triangles) for nanowires with a diameter of 40 nm deposited in AAO membranes at different cathodic potentials.

13.2. Copper addition to FeCoNi nanowires

The literature shows that even a small addition of non-magnetic copper to magnetic systems significantly changes their properties [26, 201, 203]. Copper can also be added to multilayered nanowires as a non-magnetic spacer [26, 204, 205, 206, 207]. To extend the scope of modifying the magnetic properties of nanowires, I prepared FeCoNi nanowires with Cu addition. I tested two Cu contents: (1.6 mM (0.26g/l) and 3.3 mM (0.53 g/l) $CuSO_4$ - Table 6.1) in nanowires with a length of 6 µm and a diameter of 100 nm, deposited at four different cathodic potentials, similarly to ternary systems.

Already at the preparation stage, I noticed significant and very interesting differences. The copper addition caused the lowering of the current compared to undoped FeCoNi nanowires, but simultaneously the complete filling was reached in a shorter time and with a smaller total charge (Fig. 13.3 a). This suggests a lower pore filling degree. The Cu addition increases the number of ions in the electrolyte, but doubling the Cu concentration (Fig. 13.3 b) did not affect the cathodic current, however, it shortens the deposition time and lowers the reduced charge.

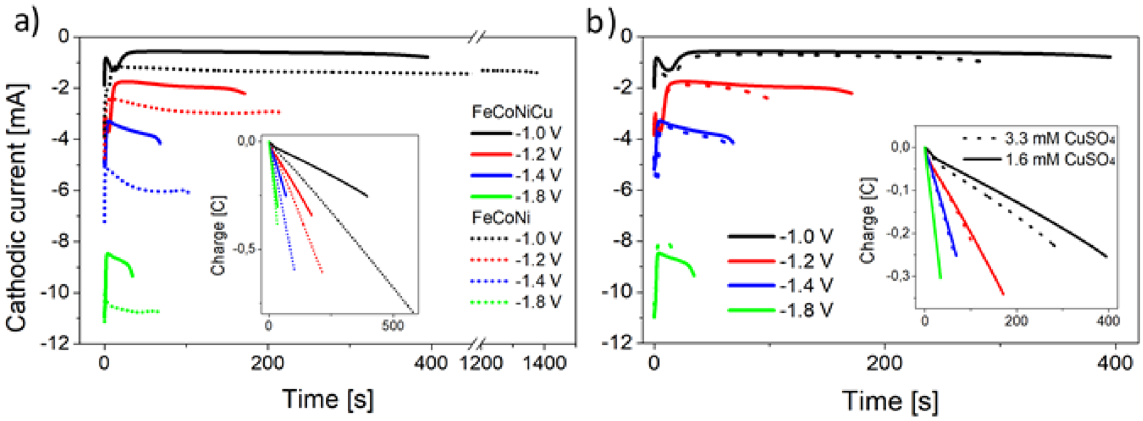

Figure 13.3: Cathodic current versus time measured at different potentials during the electrodeposition of (a) FeCoNi and FeCoNiCu nanowires (with lower Cu content) and (b) FeCoNiCu nanowires with two different copper concentrations (1.6 mM and 3.3 mM). The insets show corresponding electrical charge variations in time.

FeCoNiCu nanowires did not show any significant changes in morphology between the nanowires deposited at different potentials and compared to undoped samples.

The presence of Cu in the electrolyte did not influence the chemical composition of nanowires known from FeCoNi systems (Fig. 13.4), while the Cu content decreased with increasing potential for both tested Cu concentrations. The copper did not disturb the homogeneous distribution of elements shown in Fig. 13.5.

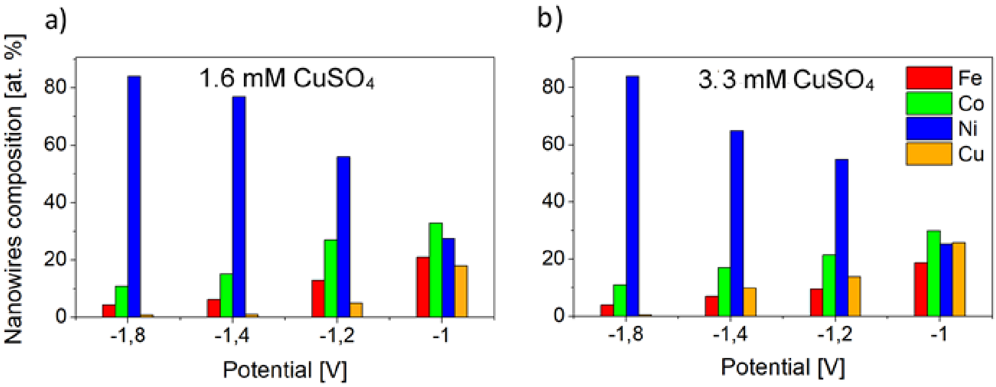

Figure 13.4: Atomic composition of Fe, Co, Ni, and Cu in FeCoNiCu nanowires deposited at different potentials with (a) lower and (b) higher Cu concentrations. Elemental contents are given with an error of no more than ±1.

FeCoNiCu nanowires deposited at different potentials show the same fcc structure with the same preferred growth direction changing from [111] to [220] with increasing potential. The Cu addition caused the refinement of the crystalline structure (Fig. 13.6 a) with a maintained trend of crystallite size as a function of applied potential. Similar to the case of undoped samples, the increase in cathodic voltage shifted the peak positions towards higher angles, but these changes were larger in FeCoNiCu systems (Fig. 13.6 b), which will be interesting to analyze considering the smaller Cu radius (1.5 Å) compared to the atomic radii of Fe, Co, and Ni (1.72, 1.67 and 1.62 Å, respectively).

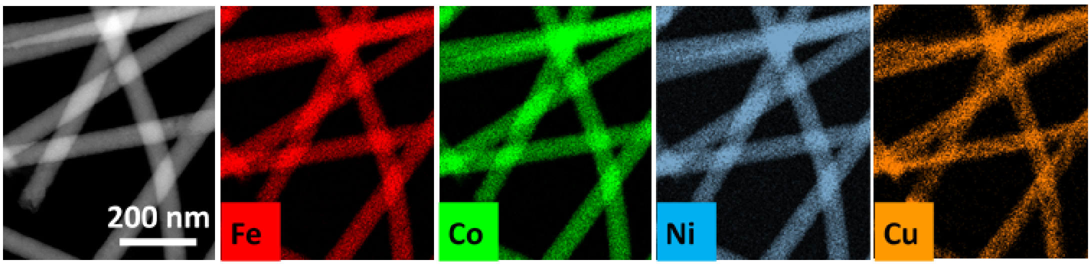

Figure 13.5: STEM-EDS maps of Fe, Co, Ni, and Cu of FeCoNiCu nanowires ($\phi = 100$ nm) deposited at a voltage of -1.0 V.

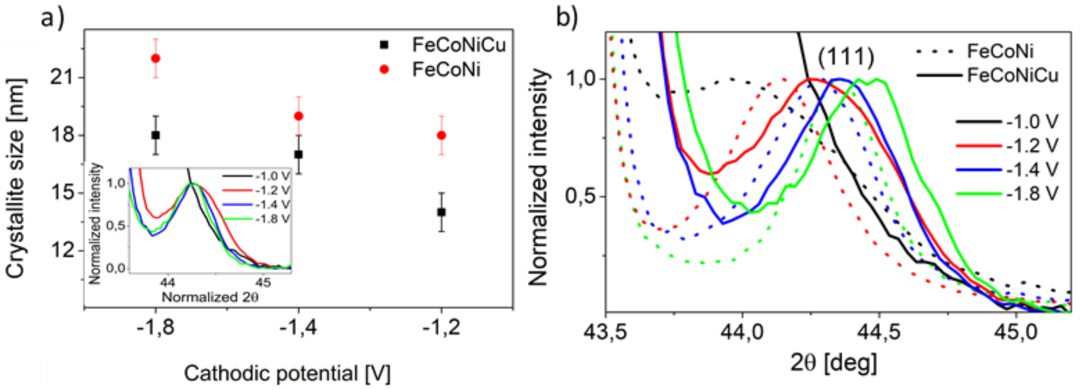

Figure 13.6: (a) Average value of crystallite size for FeCoNiCu nanowires calculated according to the Scherrer formula based on the broadening of the (111) peak (inset). (b) (111) peaks with a visible shift towards higher 2θ values with increasing cathodic potential for FeCoNiCu (solid line) and FeCoNi (dotted line) nanowires.

Magnetic measurements (Fig. 13.7) showed magnetic anisotropy with the easy axis along the nanowires (as observed in all cases), despite the large fraction of Cu, which is a non-magnetic element. Moreover, Cu addition caused a significant increase in coercivity and squareness (Fig. 13.8). Similar behavior induced by copper was observed in magnetic nanowires by other groups [201, 203].

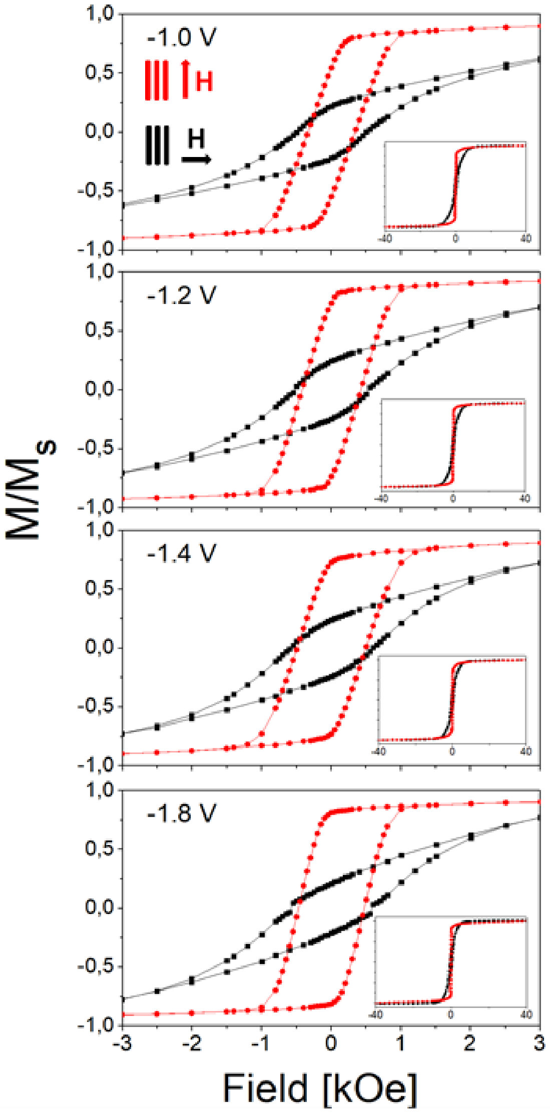

Figure 13.7: Hysteresis loops measured at room temperature with a magnetic field applied out of the membrane plane (red circles) and in the membrane plane (black triangles) for FeCoNiCu nanowires with a diameter of 100 nm (L = 6 µm) deposited at different cathodic potentials. The magnetization (M) value was normalized to the saturation magnetization (M_s).

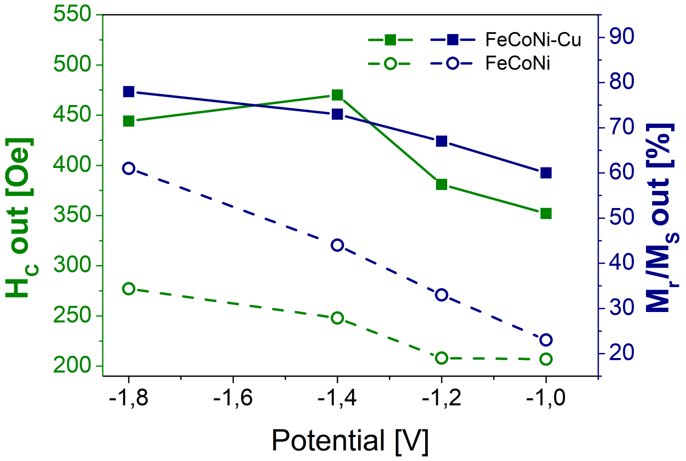

Figure 13.8: Out of plane coercivity and squareness shown as a function of cathodic potential for FeCoNiCu (full circles) and FeCoNi (empty circles) nanowires with a diameter of 100 nm.

The addition of Cu into FeCoNi nanowires results in unexpected electrochemical behavior manifesting by lower current but shorter deposition time and smaller charge. This may suggest a lower filling degree, which together with smaller grains may help explain the observed high values of coercivity and squareness. Such alloys also seem to be very promising materials for 3D memory applications and will be the subject of my studies, including the magnetic structure and reversal mechanism.

Appendix A

Nanowire applications

As mentioned above the size- and shape-dependent, magnetic, optical, and electrical properties of nanowires create conditions for their various applications, which are briefly described below.

Biomedical

The application of nanowires in biomedicine will be presented on two examples: 1) in the cancer treatment using hyperthermia and 2) in the drug delivery process.

In hyperthermia, also known as overheating, the temperature around cancer cells increases, leading to their death, without harming healthy cells that are more resistant to heat. Magnetic nanowires are the perfect candidates for this application. They are injected directly into the tumor area where a magnetic field is applied to cause them to rotate, which locally heats the cells. Nanowires have an advantage over nanoparticles due to their magnetic anisotropy, which facilitates heating at low-frequency fields [**?**] and requires only a small concentration of nanowires to achieve rapid heating [212].

Another application of nanowires in medicine is the drug delivery system. The nanowires can capture and then push, pull or rotate drug molecules and other cellular objects [34]. Drug-loaded nanowires are moved toward diseased cells where they release transported medicaments. There are several methods of attaching drugs to nanowires. This can be done using micro-gel that swells or shrinks depending on temperature, causing the drug to be absorbed or extracted; or chemically by functionalization due to native oxides formed on the surface of the metallic nanowires; or by a magnetic field with the drug-loaded magnetic microparticles or using porous nanowires that have the ability to carry a large amount of drug. Depending on the nanowires, transport through the microchannels into living cells occurs by the magnetic field or ultrasounds, while release can be controlled using thermal effect applying a magnetic field or irradiations with near-infrared light. In such applications, nanowires of Fe, Ni, Fe/Pd, or segmented Au/Ni/Au can be used [34, 213, 214]. Specially selected nanowires due to their biocompatibility and non-toxicity, are approved for in vivo use in humans and, thanks to their biodegradability, can be degraded to the small aggregates and distributed to the neighboring cells, leaving the treated area free from contamination.

Sensors

Thanks to their unique properties, nanowires can also be used as various types of sensors. One example is the application of magnetostrictive nanowires as acoustic sensors. Such nanowires change their magnetic properties under the influence of mechanical stress (compression or tension). These changes can be measured by a GMR sensor or pickup coil and converted into an electrical signal. The same effect is observed in the inner ear, where stress induced by sound waves causes electrical signals in response. In both cases, the acoustic signal is detected. This similarity makes arrays of magnetostrictive nanowires attractive materials for implants such as cilia in the inner ear. Promising candidates for this type of application are Co, Ni, and FeGa nanowires [215, 216].

Nanowires, due to their shape, are characterized by a high ratio of surface area to volume, while maintaining their nanosize. This feature and the unique catalytic properties of nanowires make them attractive as electrochemical biosensors with significantly higher efficiency compared to traditional electrodes. The nanowire-covered electrodes show at least an order of magnitude higher sensitivity than the bulk electrodes. For example, a Ni nanowire array electrode can be used as a glucose sensor with a stable and fast amperometric response and a significant increase in sensitivity. It is a nonenzymatic sensor that relies on the current response of glucose oxidation directly at the electrode surface [217]. Nanowire-based sensors are free from interference from other oxidable species in blood, which additionally increases their attractiveness. Ni nanowires can also be used as sucrose and methanol sensors [218, 219].

Another example of using nanowires as sensors is the detection of the degree of metal corrosion. As in the case of chemical sensors, the big advantage of these nanowire-based sensors is their large surface area to volume ratio, which causes the material to respond quickly to changes. Due to the oxidation in the environment, the magnetic properties of nanowires change, which allows for monitoring the corrosion process. For this purpose, the nanowires are correlated with a Magnetic Tunnel Junction (MTJ) and nanowire corrosion is observed as a change in its resistance [220](Masharei2018). An ideal candidate for this application are iron nanowires, which have a high magnetization value that decreases during oxidation of the nanowires.

Nanowires can also be used as magnetic field sensors. For this purpose, materials exhibiting the GMR (Giant Magnetoresistance) effect are needed, *i.e.* those that show large changes in electrical resistance in magnetic fields. This effect occurs in nanoscale multilayer materials consisting of alternating ferromagnetic and nonmagnetic layers. To observe GMR, the magnetization direction of ferromagnetic layers should show antiferromagnetic coupling (antiparallel arrangement of magnetic layers). Under the influence of the magnetic field, the magnetization vectors align along the external field and the system is ferromagnetically coupled, which causes a decrease in resistance. These changes allow for the detection of a magnetic field. In such applications, multilayered nanowires composed of Co/Cu, FeCoNi/Cu, Fe/Cu CoNi/Cu can be used [221, 222].

Environmental protection

In addition, nanowires can also be used in environmental protection. One example is Ni nanowires, which can be exploited in water purification and monitoring technologies [223](Pinherio2014). Functionalized Ni nanowires (covered with a hybrid coating composed of silica and dithiocarbamate groups) demonstrate efficient absorption of Hg(II) from water. Nanowires with uptaken mercury can be magnetically separated and removed from aqueous solutions. This indicates the ability of nanowires to absorb heavy metal ion contamination and improve water quality. Also, porous magnetic nanowires made of iron oxide doped with Mn have a high ability to absorb heavy metal ions and organic pollutants, which may be used in wastewater treatment [224](Cui 2013).

Another example is ZnO nanowires, which apart from a wide range of other applications are also interesting from an environmental protection point of view. In this case, the photocatalytic properties of ZnO nanowires allow for the inactivation of bacteria and viruses as well as the degradation of pesticides and volatile organic compounds [225]. In the photocatalysis process, as a result of oxidation performed under irradiation with appropriate light, the positive hole created in the valance band oxidizes organic contaminates (directly or in an indirect way by hydroxyl radical production), while an electron in the conduction band reduces the adsorbed oxygen. To observe such a reaction the pollutant molecules must be adsorbed onto the photocatalyst, thus the use of the nanowires supported on the steady substrate can increase photocatalytic efficiency (compared to a flat surface) thanks to their huge surface-to-volume ratio. Moreover, the nanowire application does not generate problems with separation, which is a serious drawback in the case of nanoparticles, which also have a large surface area.

Optical

Nanowires are also gaining increasing attention in optics showing potential applications such as UV photodetectors, waveguides, diodes, optical switches, and UV lasers [226]. ZnO nanowires also find numerous applications here. For example, their attractiveness in diode research was determined by the wide bandgap, high excitation binding energy, high refractive index (ensuring strong photonic confinement), low cost, and easy manufacturing processes. ZnO nanowires are also being investigated for applications as UV photodetectors or optical switches, which is due to the photo-induced changes in conductivity (with the resistivity that typically drops by several orders of magnitude, when ZnO nanowires are exposed to UV light). Taking into account the undisputed application potential of ZnO nanowires as well as the enormous interest in nanowire research, the optoelectronic future surely belongs to them.

Electronic elements and spintronic

The use of nanowires in electronics and spintronics is equally important. A variety of nanowire-based electronic devices play a key role, especially in the age of miniaturization, where it is required to reduce power consumption while increasing efficiency. In such applications, nanowires are nanoscale building blocks of field-effective transistors, GMR sensors, diodes, and other consumer electronics devices [227, 228].

Appendix B

Rozszerzone streszczenie

Prezentacja tematu pracy doktorskiej

Nanotechnologia to obecnie jedną z najdynamiczniej rozwijających się dziedzin nauki, głównie ze względu na jej potencjalne zastosowania w biomedycynie oraz różnych dziedzinach technologii, takich jak elektronika, optoelektronika, spintronika czy ochrona środowiska. Na szczególną uwagę zasługują nanodruty, jednowymiarowe nanostruktury, ze względu na ich rozmiar i zależne od kształtu właściwości magnetyczne, optyczne i elektryczne.

Istnieje wiele różnych metod wytwarzania nanodrutów metalicznych, w tym szeroki zakres technik litograficznych, bezpośrednie parowanie lub osadzanie elektrochemiczne. Ta ostatnia metoda, prosta i niedroga, staje się coraz częściej stosownym sposobem syntezy nanostruktur. Do jej głównych zalet należy wszechstronność i możliwość produkcji na dużą skalę, a także relatywnie duża łatwość w kontrolowaniu geometrii i struktury otrzymywanych obiektów. W przypadku nanodrutów technika elektrodepozycji jest stosowana w połączeniu z zastosowaniem membran, które wypełniane redukowanym metalem pozwalają na odwzorowanie średnicy i kształtu kanałów membrany oraz ich rozmieszczenie. Porowate membrany umożliwiają produkcję nanodrutów o monodyspersyjnej średnicy i łatwej do kontrolowania długości podczas jednokierunkowego wzrostu. Jednym z najczęściej stosowanych rodzajów membran są membrany poliwęglanowe (PC) otrzymywane w procesie trawienia śladów jonowych. Dzięki małej gęstości porów, membrany PC umożliwiają uzyskiwanie nanodrutów charakteryzujących się stosunkowo słabymi oddziaływaniami magnetostatycznymi, które w skrajnych przypadkach są zaniedbywalne. Ponadto membrany poliwęglanowe są dostępne w szerokim zakresie grubości, rozmiarów porów i ich gęstości, aż do jednego poru na membranę.

Próbki przygotowane w ramach tej pracy składają się z żelaza, kobaltu i niklu. Elektrochemiczne osadzanie stopów z grup żelaza, określa się jako anomalne, ponieważ zawartość bardziej aktywnych pierwiastków w uzyskanej próbce jest większa niż w elektrolicie. Choć istnieją modele opisujące zjawiska anomalne dla powłok, to złożony mechanizm procesów osadzania nanostruktur ze stopu FeCoNi w porowatej matrycy pozostaje kwestią otwartą i wymaga lepszego zrozumienia. Wiadomo, że elektrodepozycja Fe, Co i Ni odbywa się nie tylko na drodze redukcji jonów Fe^{2+}, Co^{2+} i Ni^{2+}, ale także z ich kompleksów hydroksylowych $FeOH^{+}$, $CoOH^{+}$ i $NiOH^{+}$, które wykazują wyższe stałe szybkości reakcji niż wolne jony. Tak więc, możliwe wyjaśnienie anomalnego współosadzania opiera się na hipotezie, że głównymi prekursorami konkurującymi ze sobą o miejsca na powierzchni elektrody są wodorotlenki metali MOH^{+} ($M = Fe, Co, Ni$). Przyjmuje się, że hamowanie elektrolizy najszlachetniejszych pierwiastków wynika z preferencyjnej redukcji jonów hydroksylowych w kolejności: $FeOH^+ > CoOH^+ > NiOH^+$, ze względu na różnice w kinetyce przenoszenia ładunku. Zatem współosadzanie anomalne jest zjawiskiem sprzyjającym osadzaniu metalu mniej szlachetnego w porównaniu z metalem szlachetniejszym. Jednocześnie efekt ten jest silnie zależny od potencjału katodowego, co sugeruje, że modyfikując przyłożone napięcie można kontrolować proces depozycji wzmacniając lub osłabiając anomalne osadzanie, a co za tym idzie, zmieniać skład chemiczny otrzymywanych materiałów.

Cylindryczne nanodruty magnetyczne wytwarzane techniką elektrodepozycji wspomaganej membranami są badane pod kątem ich zastosowania w urządzeniach do przechowywania danych nowej generacji, takich jak jednostki pamięci magnetycznej 3D. Wyjątkowa geometria nanodrutów jest źródłem anizotropii magnetycznej, którą można modyfikować i kontrolować na etapie procesu preparatyki, aby uzyskać materiały o pożądanych parametrach. Izolowane, jednodomenowe nanodruty magnetyczne powinny się charakteryzować kwadratową pętlą histerezy ze skokowym odwróceniem namagnesowania pomiędzy dwoma antyrównoległymi kierunkami. Jednakże jak wykazują pomiary magnetyczne, pętla histerezy matrycy nanodrutów jest wyraźnie odchylona, co może wynikać z zaburzeń, w normalnym do powierzchni, uporządkowaniu nanodrutów, a także z interakcji pomiędzy drutami. W zależności od geometrii nanodrutów, można wyróżnić trzy tryby przemagnesowania: koherentną rotację oraz przemieszczanie ścian domenowych poprzecznych i wirowych. Rotacja koherentna zachodzi zwykle w małych jednodomenowych obiektach, których średnica jest zbliżona do długości. W długich strukturach cylindrycznych, takich jak nanodruty, odwrócenie namagnesowania następuje poprzez zarodkowanie i propagację ścian domenowych z bardzo dużą prędkością. Tę cechę nanodrutów można wykorzystać do skonstruowania trójwymiarowych jednostek pamięci magnetycznej. W takich układach poszczególne bity są związane ze ścianami domenowymi, które do odczytu i zapisu informacji są przemieszczane wzdłuż nanodrutów o ściśle określoną odległość poprzez przyłożenie spolaryzowanych impulsów prądowych. Aby nie dochodziło do utraty informacji, poszczególne jednostki pamięci zlokalizowane w sąsiednich nanodrutach nie mogą ze sobą oddziaływać. Ponadto, aby wyeliminować niepożądane dryfty ścian domenowych konieczne jest ich zakotwiczenie, którym mogą być różne defekty, uskoki, zmiany średnicy nanodrutów lub zmiany ich składu na długości. Ten ostatni sposób zakotwiczenia ścian domenowych stał się motywacją dla moich badań.

Cel pracy doktorskiej

Celem tej pracy było uzyskanie nanodrutów FeCoNi o różnym składzie chemicznym, a co za tym idzie o różnych właściwościach magnetycznych, z jednej kąpieli elektrolitycznej o odpowiednio dobranym składzie, poprzez zastosowanie różnych potencjałów katodowych. Tak przygotowane nanodruty stały się punktem wyjścia do produkcji nanodrutów segmentowych, których poszczególne segmenty różniły się składem chemicznym i właściwościami magnetycznymi. Zakotwiczenie ścian domenowych na granicach pomiędzy segmentami jest głównym celem tej pracy i pozwoli na wykorzystanie segmentowych nanodrutów jako jednostki pamięci 3D.

Uzyskane wyniki

W celu optymalizacji parametrów osadzania elektrolitycznego i zrozumienia zachowania elektrochemicznego różnych pierwiastków w zależności od przyłożonego potencjału zastosowano

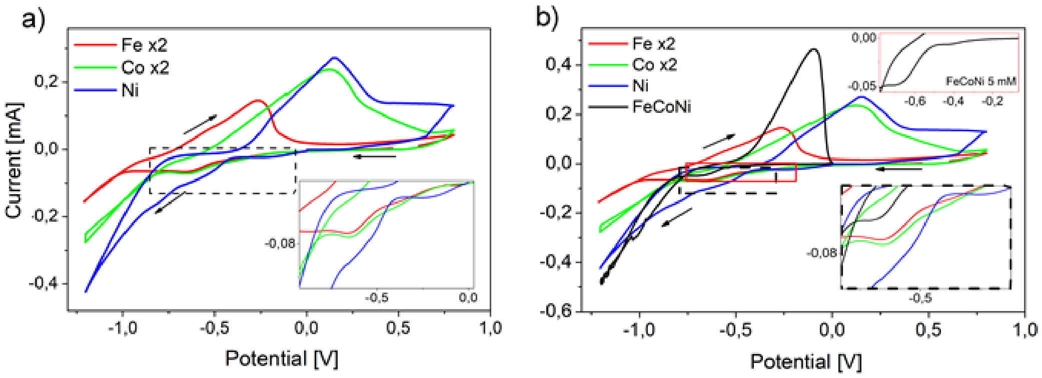

Figure B.1: Woltamperogramy cykliczne rejestrowane w roztworach zawierających $FeSO_4$, $CoSO_4$ i $NiSO_4$ w stężeniach równych 5 mM dla każdego pierwiastka w (a) oddzielnych elektrolitach oraz (b) mieszaninie wszystkich tych pierwiastków. Wstawki pokazują powiększenie oznaczonego obszaru katodowego. Krzywe CV dla Fe i Co powiększono dwukrotnie.

technikę woltamperometrii cyklicznej (CV). Pomiary wykonano za pomocą złotych elektrod zanurzonych w różnych roztworach elektrolitów zawierających $FeSO_4$, $CoSO_4$, $NiSO_4$ lub ich mieszaniny (oraz kwas borowy jako elektrolit pomocniczy i kwas askorbinowy jako przeciwutleniacz) o pH ustawionym na około 3. Pomiary woltamperometrii cyklicznej przeprowadzone w oddzielnych elektrolitach (ryc. B.1 a) ujawniły sygnały katodowe pochodzące od redukcji jonów żelaza, kobaltu i niklu, które pojawiają się w kolejności zgodnej z wartościami potencjałów standardowych (najpierw Ni , potem Co i Fe). W kolejnym etapie przeprowadzono pomiary, stosując roztwór zawierający wszystkie trzy pierwiastki ($FeSO_4 + CoSO_4 + NiSO_4$) w stężeniu 5 mM każdy, przy prędkości skanowania 10 mV/s. Uzyskana krzywa CV (ryc. B.1 b) dla tego układu trójskładnikowego pokazuje sygnał redukcji przy nieco większym potencjale katodowym niż obserwowany dla oddzielonych jonów metali. Przesunięcie to tłumaczy się faktem, że podczas procesu osadzania stopu wymagany jest większy impuls, aby pokonać wyższą barierę kinetyczną dla reakcji chemicznych, które mogą hamować przenoszenie elektronów. Po odwróceniu skanowania można było zaobserwować tylko pojedynczy pik anodowy, świadczący o rozpuszczaniu osadu.

Po przeprowadzeniu badań metodą woltamperometrii cyklicznej przygotowałam nanodruty złożone z pojedynczych pierwiastków Fe, Co, Ni o dwóch różnych średnicach (100 i 120 nm) i długościach 6 μm. W procesach elektrodepozycji, podczas wypełniania porów, mierzono wartości prądu i ładunku w funkcji czasu (rys. B.2). Obszar, w którym prąd nagle zaczyna się zwiększać, oznaczał całkowite wypełnienie porów i był sygnałem do zatrzymania procesu osadzania. Przerwanie procesu na tym etapie pozwoliło uniknąć struktur rozrastających się na powierzchni membrany.

Czas osadzania nanodrutów o mniejszej średnicy (100 nm) jest krótszy w porównaniu do nanodrutów o większej średnicy (120 nm) dla wszystkich trzech pierwiastków, co jest powiązane z porowatością membrany (P100 nm = 3,1%, P120 nm = 4,5%). Wzrost wartości prądu wraz z czasem osadzania może być związany ze skróceniem długości drogi dyfuzji w miarę wypełniania się porów.

W celu obserwacji morfologii nanodrutów, membrany poliwęglanowe rozpuszczono w dichlorometanie. Obrazy ze skaningowego mikroskopu elektronowego (SEM) nie wykazują

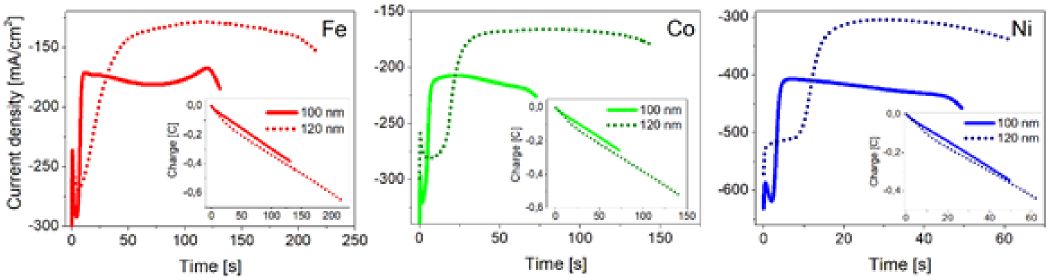

Figure B.2: Zmiana gęstości prądu katodowego w funkcji czasu, mierzona podczas osadzania elektrolitycznego nanodrutów Fe, Co i Ni o dwóch różnych średnicach: 100 nm i 120 nm. Wstawki pokazują odpowiednie zmiany ładunku elektrycznego w czasie.

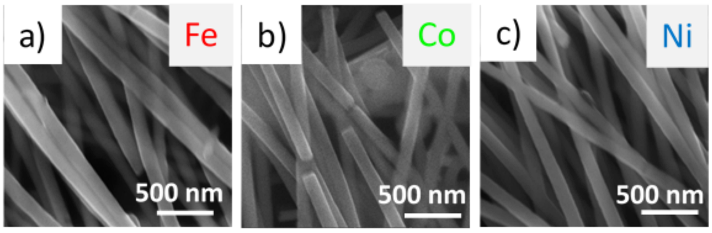

Figure B.3: Obrazy SEM (a) Fe, (b) Co i (c) nanodrutów Ni o średnicy 100 nm obserwowane po rozpuszczeniu membrany.

znaczących różnic pomiędzy nanodrutami wykonanymi z różnych pierwiastków (rys. B.3). Wszystkie nanodruty są gładkie i ciągłe, bez zauważalnej porowatości, co oznacza, że warunki procesów osadzania zostały dobrze dobrane.

Strukturę nanodrutów Fe, Co i Ni o średnicy 100 nm analizowano za pomocą pomiarów dyfrakcji rentgenowskiej (XRD). Wszystkie próbki wykazywały polikrystaliczną budowę, o strukturze bcc, hcp/fcc i fcc odpowiednio dla Fe, Co i Ni. Wielkość krystalitów oszacowana na podstawie równania Scherrera wynosiła 23-24 nm dla żelaza i kobaltu oraz 27 nm (±1 nm) dla nanodrutów Ni.

Pomiary magnetyczne nanodrutów Fe, Co i Ni przeprowadzono w temperaturze pokojowej poprzez przyłożenie pola magnetycznego wzdłuż osi nanodrutu i prostopadle do niego. Pętle histerezy nanodrutów Fe, Co i Ni osadzonych w membranach (rys. B.4) wykazują wyraźną anizotropię magnetyczną z łatwą osią wzdłuż nanodrutów dla wszystkich pierwiastków. Anizotropia kształtu i oddziaływania dipolowe to główne parametry określające zachowanie magnetyczne nanodrutów Fe i Ni, podczas gdy w nanodrutach Co anizotropia magnetokrystaliczna może również odgrywać ważną rolę. Z uwagi na fakt, że oś łatwa dla struktury hcp Co leży na kierunku [002], a kryształy wykazują wyraźną teksturę wzdłuż kierunku [100], który jest kierunkiem trudnym, anizotropia magnetokrystaliczna daje przyczynek do ułożenia wektora namagnesowania prostopadle do nanodrutu. Największą wartość koercji mierzoną przy polu magnetycznym przyłożonym wzdłuż nanodrutów uzyskano dla nanodrutów Co, ale prostokątny kształt pętli uzyskiwanych dla kierunku łatwego obserwowano dla we wszystkich próbkach. Stosunkowo wysokie wartości (M_r/M_s) potwierdzają marginalny udział oddziaływań dipolowych w efektywnej anizotropii.

Po przeanalizowaniu nanodrutów jednoelementowych, badałam nanodruty ze stopów

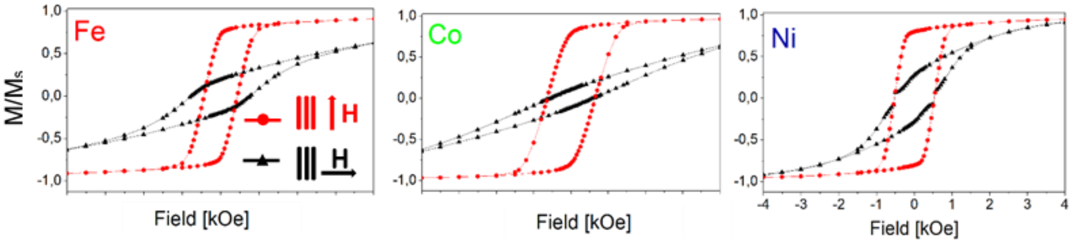

Figure B.4: Pętle histerezy mierzone z polem magnetycznym przyłożonym równolegle i prostopadle do płaszczyzny membrany dla nanodrutów Fe, Co i Ni o średnicy 100 nm. Wartość namagnesowania (M) jest znormalizowano do namagnesowania nasycenia (M_s).

podwójnych FeCo i FeNi o średnicy 100 nm, aby ocenić, jak przyłożony potencjał wpływa na skład nanodrutów i ich właściwości.

Różne wartości potencjału standardowego jonów żelaza, kobaltu i niklu skutkują różnymi wartościami nadnapięcia i gęstości prądu, co wpływa na szybkość osadzania poszczególnych pierwiastków. Większe nadnapięcie powinno powodować wzrost zawartości atomów o mniej szlachetnym potencjale standardowym, ale w przypadku tych stopów obserwujemy anomalne współosadzanie, dlatego zmiany potencjału katodowego mogą prowadzić do nieoczekiwanych zmian w składzie chemicznym. Analiza składu chemicznego nanodrutów FeCo i FeNi osadzonych przy różnych potencjałach katodowych pokazuje duże zmiany w przypadku układów FeNi (od 46 do 90% atomowych), w przeciwieństwie do nanodrutów FeCo, które dopiero dla skrajnych wartości przyłożonych potencjałów powodują istotne zmiany zawartości. W nanodrutach FeNi zawartość Ni wzrasta wraz z potencjałem katodowym, co sugeruje, że w zależności od stężenia Ni różne fazy mogą być stabilne. Względne stężenia Fe w próbkach osadzonych przy napięciu 1.0 V są znacznie wyższe niż względne stężenia jonów Fe^{2+} w roztworze wyjściowym, co wyraźnie wskazuje na preferencyjne osadzanie się żelaza. Ze wzrostem potencjału zawartość Fe znacznie maleje i utrzymuje się na niskim poziomie przy bardziej katodowych napięciach.

Właściwości strukturalne i skład fazowy nanodrutów zbadano za pomocą dyfrakcji rentgenowskiej. Piki opisane wskaźnikami Millera przypisano fazom FeCo bcc i $FeNi_3$ fcc zgodnie z danymi referencyjnymi (03-065-6829 i 00-038-0419 NIST). Najbardziej intensywne piki dla stopu FeCo pochodzą z płaszczyzn (110). Stosunkowo małe różnice w stężeniu Co nie powodują znaczących zmian w pozycjach pików i względnych intensywnościach, które całkiem dobrze odpowiadają próbce referencyjnej. Sugeruje to brak zmian w parametrach sieci i izotropowy wzrost nanodrutów FeCo. W próbkach FeNi niewielkie odchylenie od pozycji pików nie wykazało korelacji ze zmianami składu chemicznego. Względne intensywności pików wskazują preferowany kierunek wzrostu normalny do płaszczyzn (111) dla prawie wszystkich próbek niklowych. Najwyższe intensywności pików stwierdzone w próbkach zdeponowanych przy -1.3 V i -1.6 V mogą sugerować, że napięcia pośrednie stwarzają najkorzystniejsze warunki dla wzrostu krystalicznych nanodrutów FeNi.

Nanodruty FeCo i FeNi badano także magnetycznie za pomocą SQUID. Wszystkie nanodruty FeCo charakteryzują się anizotropią magnetyczną z osią łatwą wzdłuż lub w pobliżu osi nanodrutu. Wzrost zawartości Co w nanodrutach FeCo powoduje zwiększoną koercję mierzoną z polem magnetycznym przyłożonym wzdłuż nanodrutów i niemonotoniczne zmiany kwadratowości. Można również zauważyć, że próbki osadzone przy większym napięciu katodowym mają wyższą koercję w porównaniu z próbkami osadzonymi z tego samego elektrolitu przy niskim potencjale. Większe napięcie powoduje wzrost szybkości osadzania i bardziej porowatą strukturę z niższym stopniem wypełnienia, co bezpośrednio może wpływać na obserwowany wzrost koercji spowodowany kotwiczeniem ścian domenowych na defektach struktury.

W pętlach histerezy zmierzonych dla nanodrutów FeNi wyraźnie widać, że nie ma bezpośredniej korelacji pomiędzy kształtem pętli a zawartością Ni w nanodrutach. Głównym parametrem określającym zachowanie magnetyczne nanodrutów FeNi wydaje się być przyłożone napięcie. Próbki osadzone przy ekstremalnych napięciach (zawierające 90% i 46% Ni) są izotropowe magnetycznie, natomiast próbki osadzone przy napięciach pośrednich (zawierające 91% i 86% Ni) wykazują anizotropię magnetyczną z osią łatwą wzdłuż osi nanodrutu. Zmiany te korelują z wynikami uzyskanymi z pomiarów XRD, z których wynika, że próbki zdeponowane przy potencjałach pośrednich miały lepiej wykrystalizowaną strukturę, w przeciwieństwie do próbek wytworzonych przy potencjałach skrajnych, które charakteryzowały się liniami dyfrakcyjnymi o niskim natężeniu.

Po zbadaniu nanodrutów składających się z pojedynczych pierwiastków i stopów podwójnych przygotowałam trójskładnikowe stopy FeCoNi. W pracy przebadano wpływ przyłożonych napięć oraz zmian geometrii nanodrutów (długość i średnica) na właściwości uzyskanych nanostruktur w celu ich optymalizacji pod kątem zastosowania do produkcji jednostek pamięci 3D. Wszystkie nanodruty osadzano w temperaturze pokojowej z odpowiednio dobranych elektrolitów (na podstawie badań literaturowych), tak aby zmiana potencjału miała wpływ na ich skład chemiczny.

W pierwszej kolejności zbadałam wpływ przyłożonej wartości potencjału na proces elektrodepozycji nanodrutów FeCoNi (rys. B.5 a). Wraz ze wzrostem przyłożonego potencjału wzrasta prąd katodowy wszystkich nanodrutów, co skraca czas potrzebny do całkowitego wypełnienia porów membrany. Zgodnie z oczekiwaniami można zaobserwować, że prądy mierzone podczas osadzania nanodrutów o większych średnicach są wyższe niż te rejestrowane dla cieńszych nanodrutów, co jest związane z większą porowatością membran o większych średnicach porów. W miarę wypełniania porów, prąd nieznacznie wzrasta, co jest związane ze skróceniem długości drogi dyfuzji. ładunek końcowy osiąga wartości ekstremalne dla najmniejszych (-1.0 V) i najwyższych (-1.8 V) potencjałów katodowych, podczas gdy dla potencjałów pośrednich jest prawie taki sam (-1.2 V, -1.4 V). Te zmiany przyłożonego potencjału wpływają na wydzielanie się wodoru, którego ilość wzrasta wraz z napięciem. Pęcherzyki wodoru tworzące się przy wyższych potencjałach katodowych mogą blokować pory i utrudniać proces wzrostu nanodrutu, prowadząc do tworzenia struktur o większej liczbie defektów.

Dodatkowo wykonałam nanodruty o różnej długości, wypełniając membrany do $\frac{1}{2}$ i $\frac{1}{4}$ ich grubości, uzyskując nanodruty o długości odpowiednio 3 µm i 1,5 µm. Krzywe prądowe mierzone dla tych samych średnic nanodrutów mają ten sam kształt, co świadczy o powtarzalności procesu. Porównanie prądów zmierzonych podczas osadzania nanodrutów o długości 6 µm i różnych średnicach potwierdziło znaną zależność związaną z porowatością membran.

Podobnie jak poprzednio, morfologię nanodrutów FeCoNi obserwowano po rozpuszczeniu membrany. Obrazy SEM pokazują, że nie ma znaczących różnic pomiędzy nanodrutami osadzonymi przy różnych potencjałach. We wszystkich próbkach nanodruty tworzą gęste nanostruktury przypominające las. Wszystkie nanodruty są gładkie i ciągłe, bez zauważalnej

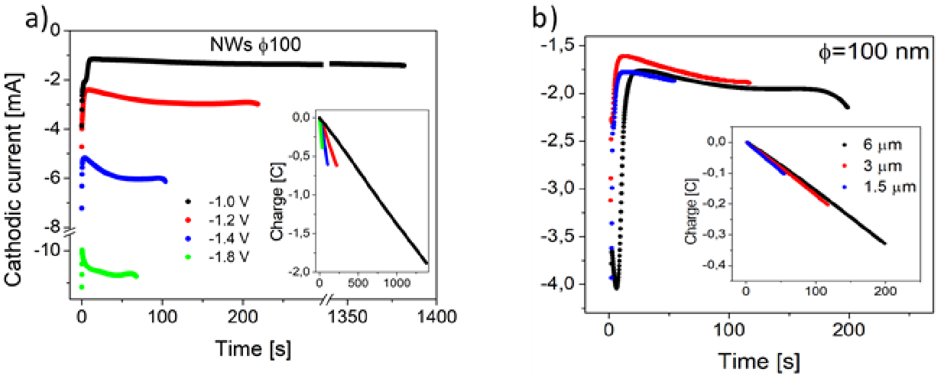

Figure B.5: Zmiany prądów katodowych mierzone w funkcji czasu podczas osadzania elektrolitycznego nanodrutów FeCoNi o średnicy porów 100 nm: (a) przy różnych potencjałach oraz (b) o różnych długościach. Wstawki pokazują odpowiednie zmiany ładunku elektrycznego w funkcji czasu.

porowatości. Zmiany długości i średnicy nanodrutów FeCoNi nie wpływają na ich morfologię.

Skład chemiczny nanodrutów analizowano za pomocą pomiarów EDS. Podobnie jak w przypadku nanodrutów ze stopów podwójnych, zwiększenie przyłożonego potencjału powodowało wzrost stężenia Ni przy jednoczesnym spadku zawartości Fe i Co. Proces depozycji przy potencjale -1.0 V wskazuje na anomalne współosadzanie, gdyż niezależnie od średnicy i pomimo dużej różnicy stężeń poszczególnych jonów w roztworze (0.01 M Fe^{2+}/0.02 M Co^{2+}/0.17 M Ni^{2+}) zawartość poszczególnych pierwiastków nie różni się znacząco i nie odzwierciedla składu kąpieli elektrolitycznej.

Badania dyfrakcyjne XRD wskazują na polikrystaliczną budowę nanodrutów o strukturze regularnej ściennie centrowanej stopu FeCoNi. średnia wielkość krystalitów obliczona na podstawie równania Scherrera wahała się od 12 do 22 nm odpowiednio dla najniższego i najwyższego napięcia i została oszacowana z błędem 1 nm. Zmiana wielkości krystalitów obserwowana wraz ze wzrostem przyłożonego napięcia może być powiązana ze wzrostem gęstości prądu, wpływającym na efektywne dostarczanie jonów, co stwarza korzystne warunki dla wzrostu nanodrutów. Analizując dyfraktogramy rentgenowskie, zaobserwowałam przesunięcie pików. Pik (220) obserwowany przy $2\theta = 43.95$ dla nanodrutów osadzanych przy najniższym potencjale przesuwa się w stronę wyższych wartości kątowych wraz ze wzrostem zawartości Ni. Sugeruje to zmniejszenie parametru sieciowego prawdopodobnie spowodowane zastąpieniem atomów Fe i Co atomami Ni, które mają mniejszy promień jonowy.

Pomiary magnetyczne nanodrutów osadzonych w membranie poliwęglanowej przeprowadzono przy użyciu pola magnetycznego przyłożonego wzdłuż osi nanodrutów i prostopadle do nich. Dla wszystkich próbek, niezależnie od ich składu, zaobserwowano anizotropię magne- tyczną z osią łatwą wzdłuż nanodrutów. Zmiana składu powodowała wyraźne różnice w wartościach koercji (H_c) i kwadratowości (M_r/M_s) pętli histerezy mierzonych w kierunku łatwym (ryc. B.6 a). Największe wartości H_c (277 Oe) i M_r/M_s (61%), uzyskano dla nanodrutów o największej zawartości Ni. Wzrost obu parametrów wraz ze wzrostem przyłożonego napięcia jest związany z zwiększeniem porowatości struktury, która sprzyja kotwiczeniu ścian domenowych, a także ze spadkiem wartości namagnesowania nasycenia i wynikającym z tego, osłabieniem oddziaływań dipolowych dla próbek osadzanych przy

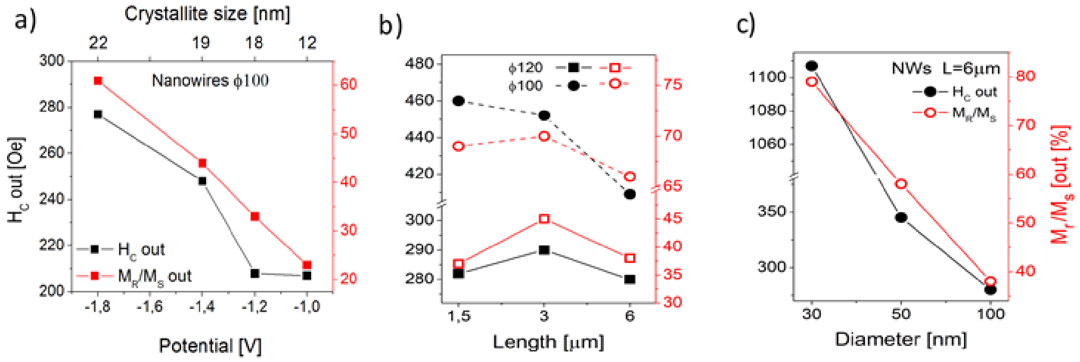

Figure B.6: Koercja i kwadratowość wykreślone jako funkcja (a) potencjału katodowego (i wielkości krystalitów), (b) długości i (c) średnicy nanodrutów ze stopu FeCoNi ((b) i (c) U =-1.2 V).

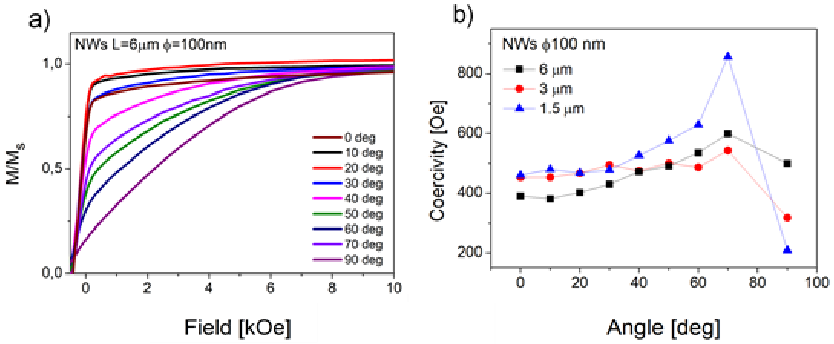

Figure B.7: (a) Zależność kątowa pętli histerezy dla nanodrutów FeCoNi oraz (b) wartości koercji dla różnych długości nanodrutów.

wyższych potencjałach. Ponadto zaobserwowano, że wzrost średnicy i długości nanodrutów prowadzi do wzrostu oddziaływań magnetostatycznych, które osłabiają anizotropię magnetyczną, powodując spadek energii anizotropii magnetycznej przejawiający się wzrostem koercji i kwadratowości ze zmniejszaniem średnicy nanodrutów (rys. B.6 b, c). Zmiany długości skutkowały niemonotonicznymi zależnościami.

Aby poznać mechanizm odwrócenia wektora namagnesowania w nanodrutach FeCoNi oraz wpływ długości i średnicy nanodrutów na ten mechanizm, zbadano zależność kątową koercji (rys. B.7). Wraz ze zmianą kierunku przyłożonego pola magnetycznego od $\theta = 0^o$ (kierunek łatwy) obserwowano wzrost koercji i po osiągnięciu maksimum przy $\theta = 70^o$ zanotowano spadek aż do kąta odpowiadającego kierunkowi trudnemu ($\theta = 90^o$). Zależność tę zinterpretowano jako zmianę trybu przemagnesowania, który dla kątów bliskich łatwemu kierunkowi był typowy dla przemieszczania się wirowej ściany domenowej, a dla kątów bliskich kierunku trudnego przechodził w tryb charakterystyczny dla ruchu poprzecznej ściany domenowej lub koherentnej rotacji.

Oddziaływania pomiędzy nanodrutami FeCoNi i struktura domenowa próbek była analizowana w oparciu o diagramy FORC. Analiza potwierdza wyraźny wzrost oddziaływań dla nanodrutów o większych średnicach i wskazuje na jednodomenową strukturę obu układów.

Dalsze badania właściwości magnetycznych nanodrutów FeCoNi przeprowadzono przy

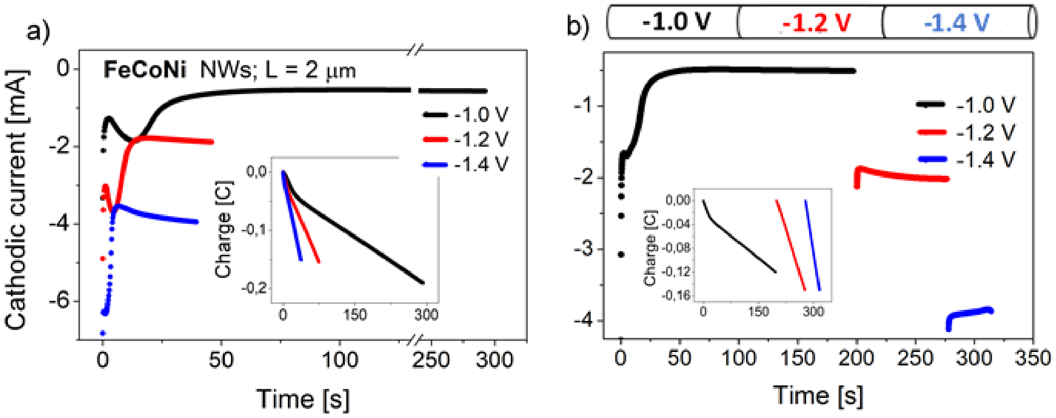

Figure B.8: Zmiana prądu katodowego w funkcji czasu mierzonego podczas osadzania elektrolitycznego nanodrutów FeCoNi: (a) pojedynczych segmentów o długości 2 µm i średnicy 100 nm przy różnych potencjałach oraz (b) wielosegmentowych nanodrutów FeCoNi o średnicy 100 nm i całkowitej długości 6 µm (każdy segment 2 µm). Wstawki pokazują odpowiednie zmiany ładunku elektrycznego w czasie. Nad wykresem dla próbki segmentowej znajduje się schemat przygotowanego nanodrutu.

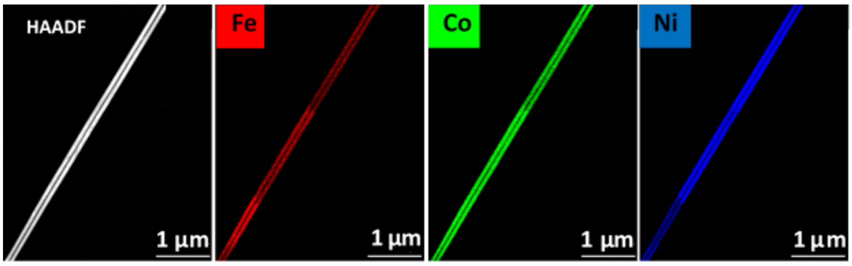

Figure B.9: Pomiar HAADF-EDS Fe, Co i Ni dla segmentowanych nanodrutów FeCoNi o średnicy 100 nm i całkowitej długości 6 µm.

użyciu transmisyjnej mikroskopii elektronowej Lorentza (L-TEM). Dla nanodrutów o średnicach 40 nm i 100 nm jednolite prążki Fresnela wzdłuż całych nanodrutów wskazują na strukturę jednodomenową bez ściany domenowej w analizowanym obszarze, co jest potwierdzeniem wyników otrzymanych w pomiarach FORC.

Po przygotowaniu nanodrutów o długości równej grubości membrany (czyli całkowitym wypełnieniu porów) obliczyłam, jaki ładunek jest potrzebny do wypełnienia 1/3 długości kanałów membrany. Bazując na wcześniejszych wynikach uzyskałam nanodruty FeCoNi o długości 2 µm i średnicy 100 nm przy trzech różnych potencjałach katodowych oraz nanodruty segmentowe z 3 segmentami magnetycznymi o długości 2 µm każdy. Wykres zależności prądu od czasu pokazuje przebiegi prądowe dla krótkich nanodrutów (rys. B.8 a) i nanodrutów segmentowych (rys. B.8 b).

Skład chemiczny segmentowanych nanodrutów analizowano za pomocą pomiarów HAADF (rys. B.9). Można zaobserwować wyraźną zmianę składu, odpowiadającą trzem segmentom. Wyniki wskazują na dobrą zgodność wartości stężeń atomowych z wynikami otrzymanymi dla nanodrutów osadzonych w postaci stopów przy ustalonym potencjale.

Badania wykonane przy użyciu mikroskopu Lorentza pokazują wyraźne zaburzenia liniowego przebiegu prążków Fresnela w środkowej części nanodrutów (rys. B.10). Zaburzenia

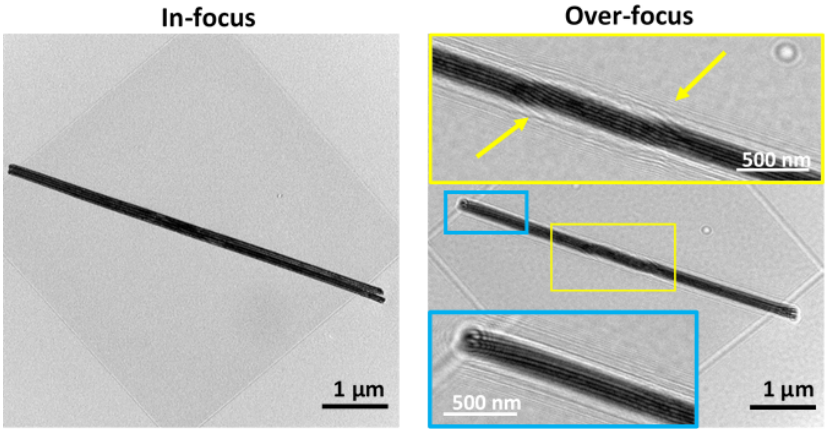

Figure B.10: Wyniki pomiarów nanodrutów segmentowych FeCoNi (ϕ = 100 nm) przeprowadzone z wykorzystaniem mikroskopu Lorentza. Wstawki przedstawiają wybrane obszary w powiększeniu. żółte strzałki wskazują pozycje ścian domenowych zlokalizowanych na granicach między segmentami.

te oznaczone żółtymi strzałkami wskazują pozycje ścian domenowych i odpowiadają pozycji granic pomiędzy segmentami.

Obecność wielodomenowej struktury sugerują także pomiary FORC. Przeprowadzone badania potwierdziły, że uzyskane segmentowane nanodruty są materiałami wielodomenowymi, co czyni je dobrymi kandydatami do konstruowania jednostek pamięci 3D.

Wnioski

Podsumowując, w niniejszej pracy wykazano wpływ parametrów elektrodepozycji na skład i właściwości magnetyczne otrzymanych nanodrutów, co może przynieść potencjalne korzyści w zastosowaniach takich materiałów do produkcji trójwymiarowych jednostek magnetycznych.

Appendix C

Résumé détaillé

Présentation du sujet de thèse

Les nanotechnologies font actuellement partie des domaines scientifiques les plus dynamiques en développement, principalement en raison de leurs applications potentielles en biomédecine et dans divers domaines technologiques tels que l'électronique, l'optoélectronique, la spintronique et la protection de l'environnement. En particulier, les nanostructures unidimensionnelles comme les nanofils ont recu une attention considérable tant du point de vue des études fondamentales que des applications potentielles, en raison de leur taille et de leurs propriétés magnétiques, optiques et électriques dépendantes de leur forme.

Il existe de nombreuses méthodes distinctes pour produire des nanofils métalliques, notamment un large éventail de techniques de lithographie, l'évaporation directe ou le dépôt électrochimique. Cette dernière approche, simple et peu coûteuse devient un moyen de plus en plus attrayant pour la synthèse de nanostructures. Sa polyvalence et son adéquation à la production à grande échelle de dépôts de forme et de caractéristiques cristallines bien définies sont sont bien adaptées pour des applications à base de nanofils. L'usage d'agents directeurs de structure (≪ templates ≫ en anglais) combiné à l'électrochimie constitue une approche générale pour préparer des matériaux à structure organisée, notamment sous la forme d'une matrice de pores cylindriques orientés. Les membranes poreuses permettent de produire des nanofils avec un diamètre monodisperse et une longueur facilement contrôlée pendant la croissance unidirectionnelle. L'un des types de membranes les plus utilisés sont les membranes en polycarbonate (PC) obtenues par gravure. Comme elles possèdent une faible densité de pores, elles permettent la création de nanofils quasi-séparés avec une interaction dipolaire faible ou négligeable. De plus, les membranes en polycarbonate sont disponibles dans une large gamme d'épaisseurs, de tailles de pores et de densités, jusqu'à un seul pore par membrane.

Les échantillons préparés dans le cadre de cette thèse seront constitués d'éléments comme le fer, le cobalt et le nickel. Le dépôt d'alliages du groupe du fer tels que Fe, Co et Ni par voie électrochimique est décrit comme un électrodépôt de type anormal, car la composition des dépôts en métaux les plus actifs est plus élevée que celle des solutions de départ. Bien qu'il existe des modèles décrivant les phénomènes anormaux pour les revêtements, le mécanisme complexe de dépôt de nanostructures d'alliages FeCoNi dans la matrice poreuse est une question qui reste ouverte et nécessite une meilleure compréhension des processus. L'électrodépôt de ces éléments peut se produire non seulement à partir des ions Fe^{2+}, $Co^{2+}+$ et Ni^{2+}, mais aussi à partir de leurs complexes hydroxylés $FeOH^{+}$,

$CoOH^+$ et $NiOH^+$, qui présentent des constantes de vitesse plus élevées que les ions libres. Une explication possible du co-dépôt anormal repose sur l'hypothèse que pour l'électrodépôt de métaux du groupe du fer, les hydroxyde métalliques MOH^+ (M = Co, Ni, Fe) sont les principaux précurseurs en compétition les uns avec les autres pour les sites de surface à l'électrode. On suppose que l'inhibition de l'électrolyse des éléments les plus nobles résulte d'un dépôt préférentiel dans l'ordre : $FeOH^+ > CoOH^+ > NiOH^+$, en raison des différences de cinétique de transfert de charge. Ainsi, le co-dépôt anormal est un phénomène montrant une préférence pour le dépôt d'un métal moins noble, par rapport à un métal plus noble, mais en même temps, elle dépend fortement du potentiel cathodique appliqué. Cela signifie qu'en modifiant le potentiel de réduction, il est possible de contrôler le type de dépôt et, par conséquent, la composition chimique des matériaux obtenus.

Les nanofils magnétiques cylindriques produits par la technique d'électrodépôt assisté par moule sont des matériaux intéressants pour les dispositifs de stockage de données de nouvelle génération comme les unités de mémoire magnétique 3D. La morphologie unique des nanofils est une raison de l'anisotropie magnétique, qui peut être modifiée et contrôlée au stade de la préparation pour obtenir des matériaux avec les paramètres souhaités. Les nanofils magnétiques isolés à domaine unique sont caractérisés par des boucles d'hystérèse carrées avec une inversion brusque de la magnétisation entre deux états résiduels possibles. Cependant, la boucle d'hystérèse du réseau de ces nanofils présente des formes non carrées résultant d'une déviation géométrique et d'interactions entre les fils. Dans les nanofils, en fonction de leur géométrie, trois modes d'inversion différents peuvent être observés : rotation cohérente, mouvement transversal et mouvement de paroi de domaine vortex. Le processus d'inversion cohérente se produit principalement dans des nanofils courts à domaine unique, lorsque leur diamètre est similaire à leur longueur. Dans les structures cylindriques longues telles que les nanofils, l'inversion de la magnétisation est provoquée par la nucléation et la propagation des parois de domaine. Selon la géométrie des structures magnétiques, l'inversion de l'aimantation se produit via le mouvement d'une paroi de domaine transversale ou vortex à très grande vitesse. Cette caractéristique des nanofils peut être exploitée pour construire des unités de mémoire magnétique tridimensionnelles. Dans de tels systèmes, des bits individuels sont associés à des parois de domaine, qui sont déplacées le long des nanofils sur une distance précisément définie pour lire et écrire des informations en appliquant des impulsions de courant polarisées. Pour éviter la perte d'informations, les unités de mémoire individuelles situées dans les nanofils adjacents ne peuvent pas interagir les unes avec les autres. De plus, pour éliminer les dérives indésirables des parois de domaines, il est nécessaire de les ancrer, ce qui peut être réalisé via les défauts, des modifications du diamètre des nanofils ou la modifications de leur composition sur la longueur. Cette dernière méthode d'ancrage des parois de domaine a été la motivation de mes recherches.

L'objectif de la thèse de doctorat

Le but de ce travail était d'obtenir des nanofils de FeCoNi de composition chimique différente et, par conséquent, de propriétés magnétiques différentes à partir d'un bain électrolytique de composition appropriée sélectionnée, en utilisant différents potentiels cathodiques. Les nanofils ainsi préparés sont devenus le point de départ pour la production de nanofils segmentés, dont les segments individuels différaient par leur composition chimique et leurs propriétés magnétiques. L'ancrage de parois de domaines aux frontières entre segments est l'objectif principal de ce travail et permettra d'utiliser des nanofils segmentés comme unité de mémoire 3D.

Résultats obtenus

La technique de voltampérométrie cyclique (VC) a d'abord été utilisée pour optimiser les paramètres de l'électrodépôt et pour comprendre le comportement électrochimique des différents éléments utilisés en fonction du potentiel imposé. Les mesures ont été effectuées en utilisant des électrodes à film d'or immergées dans diverses solutions électrolytes contenant $FeSO_4$, $CoSO_4$, $NiSO_4$ ou leurs mélanges (et de l'acide borique comme électrolyte de support et de l'acide ascorbique comme antioxydant) avec un pH ajusté à environ 3. Les mesures de voltampérométrie cyclique (Fig. C.1 a) ont permis d'observer des signaux cathodiques pour la réduction des ions fer, cobalt et nickel, qui apparaissent dans l'ordre cohérent avec les potentiels standards (d'abord Ni, puis Co et Fe). La voltampérométrie cyclique a ensuite été réalisée en utilisant une solution contenant les trois éléments ($FeSO_4$ + $CoSO_4$ + $NiSO_4$) à une concentration de 5 mM chacun à 10 mV/s. La courbe VC obtenue (Fig. C.1 b) pour ce système ternaire présente un signal de réduction à un potentiel un peu plus cathodique que ceux observés pour les ions métalliques séparés. Ce décalage s'explique par le fait qu'une surtension plus importante est nécessaire pendant le processus de dépôt de l'alliage pour surmonter la barrière cinétique plus élevée pour les réactions chimiques provoquées par l'espèce, ce qui peut inhiber le transfert d'électrons. Lors de l'inversion du balayage, on n'a pu observer qu'un seul pic anodique englobant le décapage de tous les composants de l'alliage.

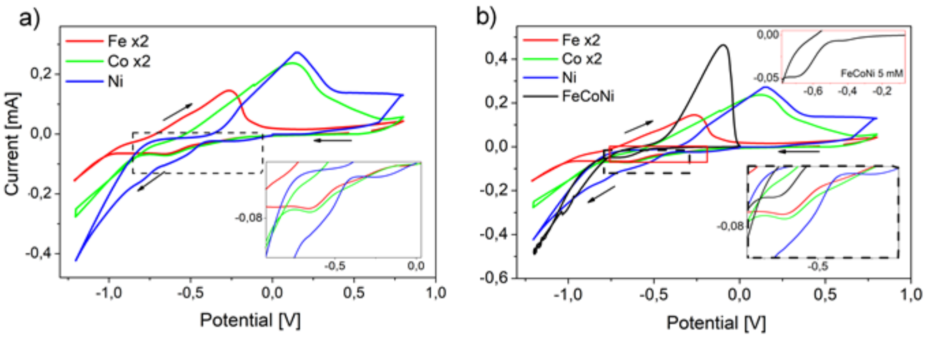

Figure C.1: Voltampérogrammes cycliques enregistrés dans des solutions contenant $FeSO_4$, $CoSO_4$ et $NiSO_4$ à des concentrations égales à 5 mM pour chaque élément dans (a) des électrolytes séparés et (b) un mélange de tous ces éléments. Les encarts présentent un agrandissement de la région cathodique marquée. Les courbes VC pour Fe et Co sont agrandies d'un facteur deux.

Après avoir effectué les études par voltampérométrie cyclique, j'ai préparé des nanofils constitués d'éléments singuliers Fe, Co, Ni avec deux diamètres différents (100 et 120 nm) et des longueurs de 6 µm. Dans les processus d'électrodépôt, pendant le remplissage des pores, les valeurs de courant et de charge ont été mesurées en fonction du temps (Fig. C.2). La région oĂą le courant commence soudainement à augmenter a été utilisée pour identifier le remplissage complet des pores et a constitué un signal pour arrêter le processus de dépôt. L'interruption du processus à ce stade nous a permis d'éviter la création dâ€™excroissance à la surface de la membrane.

Le temps de dépôt des nanofils de plus petit diamètre (100 nm) est plus court que

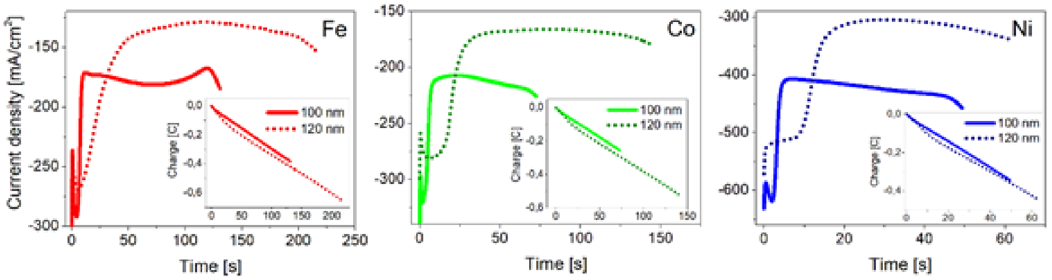

Figure C.2: Variation des densités de courant cathodique en fonction du temps, mesurées lors de l'électrodépôt de nanofils de Fe, Co et Ni de deux diamètres différents : 100 nm et 120 nm. Les encarts montrent les changements correspondants de charge électrique au fil du temps.

celui des nanofils de plus grand diamètre (120 nm) pour les trois éléments, ce qui est lié à la porosité de la membrane (P100 nm = 3,1 %, P120 nm = 4,5 %). L'augmentation de la valeur du courant avec le temps de dépôt peut être liée au raccourcissement de la longueur de diffusion à mesure que les pores se remplissent.

Pour observer la morphologie des nanofils, les membranes en polycarbonate ont été dissoutes dans du dichlorométhane. Les images de microscopie électronique à balayage (MEB) ne montrent aucune différence significative entre les nanofils constitués de différents éléments (Fig. C.3). Tous les nanofils sont lisses et continus, sans porosité notable, ce qui signifie que les conditions des processus de dépôt ont été bien sélectionnées.

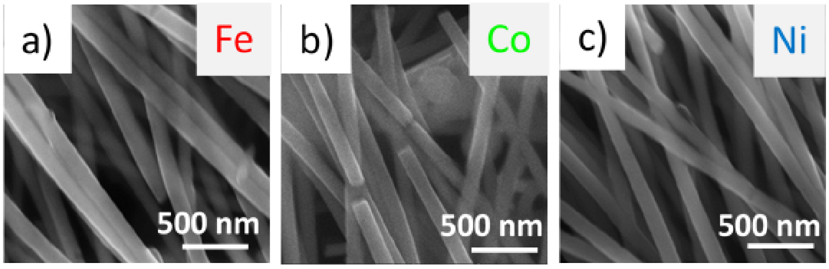

Figure C.3: Images MEB des nanofils (a) Fe, (b) Co et (c) Ni d'un diamètre de 100 nm observés après dissolution de la membrane.

La structure des nanofils de Fe, Co et Ni d'un diamètre de 100 nm a été analysée à partir de mesures de diffraction des rayons X (DRX). Elles identifient la nature polycristalline pour tous les échantillons avec une structure bcc, hcp/fcc et fcc pour Fe, Co et Ni, respectivement. La taille des cristallites a été estimée à partir de l'équation de Scherrer. Les résultats des calculs nous ont permis d'estimer la taille des cristallites pour le fer et le cobalt à 23-24 nm, et à 27 nm (±1 nm) pour les nanofils de Ni.

Les mesures magnétiques des nanofils de Fe, Co et Ni ont été effectuées à température ambiante en appliquabt le champ magnétique le long de l'axe du nanofil et perpendiculairement à celui-ci. Les boucles d'hystérèse des nanofils de Fe, Co et Ni intégrés dans les membranes (Fig. C.4) indiquent pour tous les nanofils une anisotropie magnétique claire avec un axe facile le long des nanofils. L'anisotropie de forme et les interactions dipolaires sont les principaux paramètres déterminant le comportement magnétique des nanofils de Fe et Ni, tandis que dans les nanofils de Co, l'anisotropie magnétocristalline peut également jouer un rôle important. On peut remarquer que l'axe magnétique facile de la structure hcp de Co s'aligne le long de la direction [002], ce qui peut contribuer à l'ordre du vecteur de magnétisation le long de l'axe NWs, mais la texture distincte le long de la direction [100], qui est la direction magnétique dure, implique l'alignement de l'axe c perpendiculaire à l'axe du nanofil. La plus grande valeur coercitive mesurée avec un champ magnétique appliqué le long des nanofils a été obtenue pour les nanofils de Co, alors que la forme carrée ne change pas beaucoup. Les valeurs relativement élevées de (M_r/M_s) confirment la contribution marginale des interactions dipolaires à l'anisotropie effective.

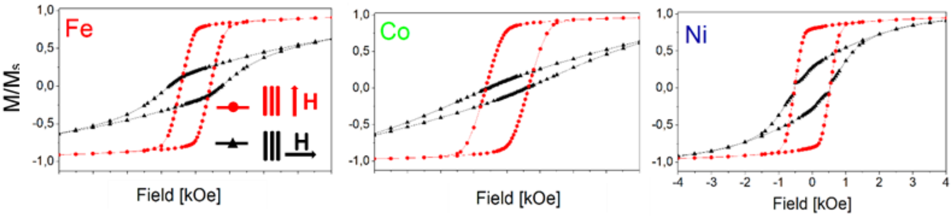

Figure C.4: Boucles d'hystérèse mesurées avec un champ magnétique appliqué dans et hors du plan de la membrane pour des nanofils de Fe, Co et Ni d'un diamètre de 100 nm. La valeur de magnétisation (M) a été normalisée par rapport à la magnétisation à saturation (M_s).

Après avoir étudié les nanofils mono-élémentaires, j'ai considéré les nanofils d'alliage binaire FeCo et FeNi d'un diamètre de 100 nm pour évaluer comment le potentiel appliqué influence la composition des nanofils et leurs propriétés.

Différentes valeurs du potentiel standard des ions fer, cobalt et nickel entraînent différentes surtensions et densités de courant, qui sont responsables du taux de dépôt des éléments individuels. Une surtension plus importante devrait entraîner une teneur plus élevée en atomes avec un potentiel standard moins noble, mais dans le cas de ces alliages, le co-dépôt anormal se produit, ainsi des modifications de potentiel cathodique peuvent conduire à une variation inattendue de la composition chimique. Par conséquent, j'ai effectué des mesures spectroscopiques de dispersion en énergie (EDS) pour étudier la composition chimique des nanofils FeCo et FeNi déposés à différents potentiels ou à partir de différentes solutions électrolytiques. Dans les nanofils FeCo, seules les valeurs extrêmes des potentiels appliqués provoquent des changements de teneur significatifs. à contrario, dans les nanofils FeNi la teneur en Ni augmente avec le potentiel cathodique (de 46 à 90 % atomique), ce qui suggère que, selon la concentration en Ni, différentes phases peuvent être stables. Les concentrations relatives en Fe dans les échantillons déposés à 1.0 V sont beaucoup plus élevées que les concentrations relatives des ions Fe^{2+} dans la solution de départ, montrant clairement un dépôt préférentiel du fer. à des potentiels plus négatifs, la teneur en Fe diminue considérablement et à des valeurs plus élevées, une faible teneur constante est maintenue.

Les propriétés structurales et la composition des phases au sein des nanofils ont été examinées par des mesures de DRX. Les pics décrits par les indices de Miller ont été attribués aux phases FeCo bcc et $FeNi_3$ fcc selon les données de référence (03-065-6829 et 00-038-0419 NIST). Les pics les plus intenses pour l'alliage FeCo proviennent des plans (110). Des variations relativement faibles de la concentration en Co n'entraînent pas de changements significatifs dans les positions des pics et les intensités relatives, qui correspondent assez bien à l'échantillon de référence. Cela suggère qu'il n'y a aucun changement dans les paramètres du réseau et la croissance isotrope des nanofils FeCo. Dans les échantillons FeNi, le léger écart par rapport aux positions des pics n'a montré aucune corrélation avec les changements de compositions chimiques. Les intensités relatives des pics indiquent une direction de croissance préférée normale aux plans (111) pour presque tous les échantillons. Les intensités de pointe les plus élevées trouvées dans les échantillons déposés à -1.3 V et -1.6 V peuvent suggérer que les tensions intermédiaires créent les conditions les plus favorables à la croissance de nanofils cristallins de FeNi.

Les nanofils FeCo et FeNi ont également été étudiés magnétiquement, à l'aide de mesures SQUID. Tous les nanofils FeCo sont caractérisés par une anisotropie magnétique avec l'axe facile le long ou à proximité de l'axe du nanofil. L'augmentation de la teneur en Co dans les nanofils FeCo entraîne un accroissement de la coercivité hors plan et des changements non monotones de la quadrature. On peut aussi remarquer que les échantillons déposés à des tensions plus cathodiques ont une coercivité plus élevée par rapport aux échantillons déposés à partir de la même solution électrolytique à faible potentiel. Cela peut être associé à une vitesse de dépôt plus élevée, à une structure plus poreuse et à un degré de remplissage plus faible.

Dans les boucles d'hystérèse mesurées pour les nanofils FeNi, il est clairement visible qu'il n'y a pas de corrélation directe entre la forme de la boucle et la teneur en Ni dans les nanofils. Le principal paramètre déterminant le comportement magnétique des nanofils FeNi semble être la tension appliquée. Les échantillons déposés à des tensions extrêmes (avec des teneurs en Ni de 90 % et 46 %) sont magnétiquement isotropes, tandis que les échantillons déposés à des tensions intermédiaires (contenant 91 % et 86 % de Ni) présentent une anisotropie magnétique avec un axe facile le long de l'axe du nanofil. Il a été observé que les échantillons déposés à des potentiels intermédiaires avaient une structure cristalline mieux définie, contrairement aux échantillons déposés à des potentiels extrêmes, qui étaient caractérisés par des raies de diffraction de faibles intensités.

Après avoir examiné des systèmes constitués d'éléments simples et binaires, j'ai préparé des alliages ternaires FeCoNi. L'influence de différentes tensions appliquées et géométries du moule (longueur et diamètre des canaux de la membrane) sur les propriétés des nanofils a été étudiée afin d'obtenir les meilleurs matériaux possibles pour les unités de mémoire 3D. Tous les nanofils ont été déposés à température ambiante à partir de solutions électrolytiques soigneusement sélectionnées sur la base des études de la littérature afin que le changement de potentiel ait un impact sur la composition chimique des nanofils.

Tout d'abord, j'ai examiné l'effet de la valeur du potentiel appliqué sur le processus de dépôt des nanofils (Fig. C.5 a). Lorsque le potentiel appliqué augmente, le courant cathodique de tous les nanofils augmente et des temps plus courts sont nécessaires pour remplir complètement les pores de la membrane. Comme attendu, on peut observer que les courants mesurés lors du dépôt de nanofils de plus gros diamètres sont plus élevés que ceux enregistrés pour des nanofils plus minces, ce qui est lié à la plus grande porosité des membranes avec des diamètres de pores plus importants. Au fur et à mesure que les pores se remplissent et que les nanofils croissent, le courant augmente légèrement, ce qui est lié au raccourcissement de la longueur de diffusion. La charge finale atteint des valeurs extrêmes pour les potentiels les moins cathodiques (-1.0 V) et les tensions les plus importantes (-1.8 V), alors qu'elle est presque la même pour les potentiels intermédiaires (-

1.2 V, -1.4 V). Ces changements de potentiel appliqué affectent l'évolution de l'hydrogène, qui augmente avec la surtension. Les bulles d'hydrogène qui se forment à des potentiels d'autant plus cathodiques peuvent bloquer les pores et entraver le processus de croissance des nanofils, conduisant à la création de structures présentant davantage de défauts.

De plus, j'ai réalisé des nanofils de différentes longueurs, en remplissant les membranes à $\frac{1}{2}$ et $\frac{1}{4}$ de leur épaisseur pour obtenir des nanofils d'une longueur de 3 µm et 1,5 µm, respectivement. Les longueurs de nanofils sélectionnées correspondent à la longueur des segments dans les nanofils multisegmentés (Fig. C.5 b). Les courbes de courant mesurées pour les mêmes diamètres de nanofils ont la même forme, ce qui prouve la répétabilité du procédé. Une comparaison des courants mesurés lors du dépôt de nanofils d'une longueur de 6 µm et de différents diamètres a confirmé la relation connue liée à la porosité variable des membranes.

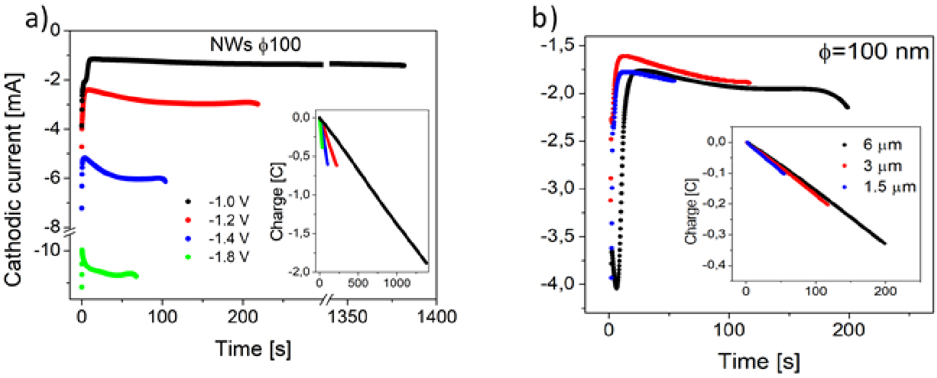

Figure C.5: Variations des courants cathodiques mesurés au cours du temps lors de l'électrodépôt de nanofils de FeCoNi avec des diamètres de pores de 100 nm : (a) à différents potentiels appliqués et (b) avec différentes longueurs. Les encarts montrent les variations de charge électrique correspondantes en fonction du temps.

Comme précédemment, la morphologie des nanofils de FeCoNi a été observée après dissolution de la membranes. Les images MEB montrent qu'il n'y a pas de différences significatives entre ces nanofils déposés à différents potentiels. Dans tous les échantillons, les nanofils créent des nanostructures denses en forme de ≪ forêt ≫. Tous les nanofils sont lisses et continus, sans porosité notable. De plus, on a pu observer que les changements de longueur et de diamètre des nanofils de FeCoNi n'affectent pas leur morphologie.

La composition chimique des nanofils a été analysée à l'aide de mesures EDS. Comme dans les nanofils d'alliage binaire, l'augmentation du potentiel appliqué a entraîné une augmentation de la concentration en Ni avec une diminution simultanée des teneurs en Fe et Co. On peut observer que pour les nanofils produits au potentiel de -1.0 V, quel que soit le diamètre et malgré la grande différence dans les concentrations des ions individuels dans la solution (0,01 M Fe^{2+}/0,02 M Co^{2+}/0,17 M Ni^{2+}), les teneurs de chaque élément ne diffèrent pas significativement et ne reflètent pas la composition du bain électrolytique initial, ce qui indique un co-dépôt anormal.

Des variabilités entre échantillons ont également été observées dans les études structurales réalisées par DRX. L'analyse a permis d'identifier des raies de diffraction correspondant à la structure fcc de FeCoNi. La taille moyenne des cristallites, calculée sur la base de l'équation de Scherrer, a été estimée avec une erreur de 1 nm et variait de 12 à 22 nm pour les tensions les plus basse et plus élevée, respectivement. Le changement de taille des cristallites observé avec l'augmentation de la tension appliquée peut être relié à une modification de la densité de courant, qui a un impact direct sur la vitesse de dépôt et donc de croissance des nanofils. En analysant les diffractogrammes RX, j'ai observé un décalage des signaux. Le maximum du pic (220) pour les nanofils préparés au potentiel le plus bas apparaît à $2\theta = 43{,}95$ et se déplace vers des valeurs plus élevées à mesure que la teneur en Ni augmente. Cela suggère une diminution du paramètre de réseau causée probablement par le remplacement des atomes de Fe et de Co par des atomes de Ni, qui ont un rayon ionique plus petit.

Les mesures magnétiques des nanofils intégrés dans la membrane de polycarbonate ont été réalisées avec un champ magnétique appliqué le long de l'axe du nanofil et perpendiculairement à celui-ci. Une anisotropie magnétique avec l'axe facile le long des nanofils a été observée pour tous les nanofils, quelle que soit leur composition. De plus, leurs propriétés magnétiques telles que la coercivité (H_c) et les caractéristiques de lla forme carrée (M_r/M_s) ont varié avec la composition chimique des nanofils (Fig. C.6 a). Les valeurs les plus élevées de Hc et Mr/Ms mesurées hors du plan de la membrane, égales à $H_c = 277$ Oe et $M_r/M_s = 61$ %, ont été obtenues pour les nanofils ayant la teneur en Ni la plus élevée. L'augmentation des deux paramètres avec l'augmentation de la tension appliquée est liée à l'augmentation de la porosité de la structure, qui favorise l'ancrage des parois du domaine, ainsi qu'à la diminution de la valeur de magnétisation à saturation et à l'affaiblissement des interactions dipolaires qui en résulte pour les échantillons déposés à des potentiels plus élevés. De plus, une augmentation du diamètre et de la longueur du nanofil entraîne un accroissement de l'interaction magnétostatique, ce qui provoque une diminution de l'énergie d'anisotropie magnétique se manifestant par une augmentation de la coercivité et de la squareité avec une diminution dans le diamètre des nanofils (Fig. C.6 b, c). Les changements de longueur ont entraîné des relations non monotones.

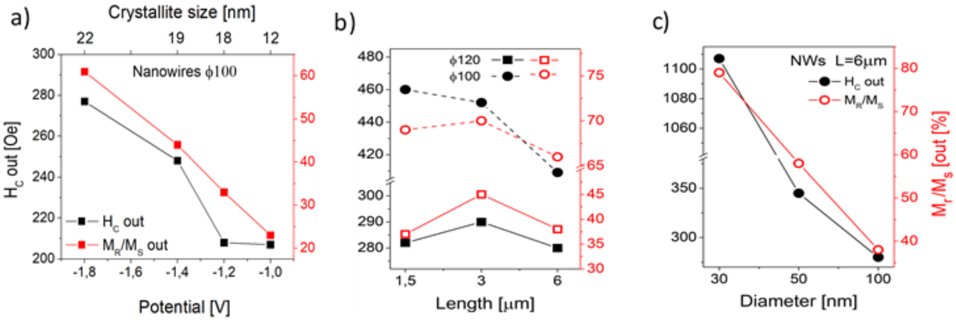

Figure C.6: Coercivité hors plan et circularité représentées en fonction (a) du potentiel cathodique (et de la taille des cristallites), (b) de la longueur et (c) du diamètre pour les nanofils en alliage FeCoNi ((b) et (c) U = -1.2 V).

Pour étudier le mécanisme d'inversion de l'aimantation dans les nanofils de FeCoNi et l'influence de la longueur et du diamètre des nanofils sur celui-ci, la dépendance angulaire de la coercivité a été étudiée (Fig. C.7). Lorsque l'orientation du champ a augmenté de $\theta = 0^o$, une augmentation de la coercivité avec un pic à $\theta = 70^o$ a été observée pour tous les échantillons. Pour $\theta \geq 70^o$, la coercivité a diminué pour atteindre un minimum le long de l'axe dur ($\theta = 90^o$). Cette dépendance peut s'expliquer par une combinaison de la rotation cohérente et du mode d'enroulement du processus d'inversion de l'aimantation.

Pour identifier la structure des domaines et des interactions dipolaires dans les nanofils FeCoNi, les diagrammes FORC ont été analysés. La structure à domaine unique est observée pour tous les nanofils, tandis qu'à mesure que le diamètre augmente, le rôle des interactions magnétostatiques devient plus prononcé.

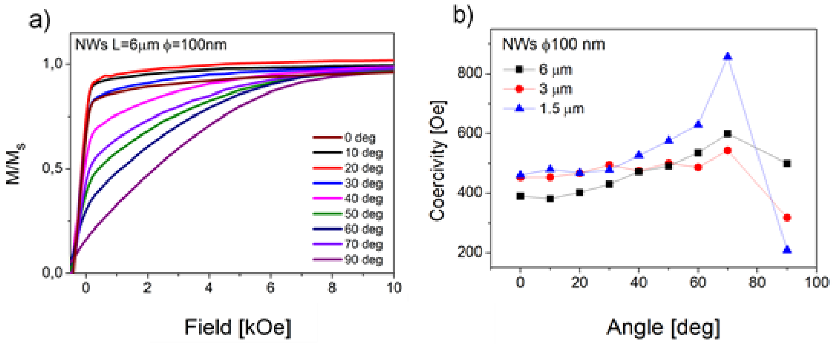

Figure C.7: (a) Dépendance angulaire des boucles d'hystérèse pour les nanofils FeCoNi et (b) valeurs de coercivité pour différentes longueurs de nanofils.

Des recherches plus poussées sur les propriétés magnétiques des nanofils FeCoNi ont été réalisées à l'aide de la microscopie électronique en transmission (MET) de Lorentz. Pour des nanofils de 40 nm et 100 nm de diamètre, des franges de Fresnel uniformes le long de l'ensemble des nanofils indiquent la structure à domaine unique sans paroi de domaine dans la zone analysée.

Après avoir préparé des nanofils d'une longueur égale à la largeur de la membrane (c'est-à-dire remplissant complètement les pores), j'ai calculé quelle charge est nécessaire pour remplir 1/3 de la largeur du gabarit. Sur la base des résultats précédents, j'ai produit des nanofils FeCoNi d'une longueur de 2 μm et d'un diamètre de 100 nm à trois potentiels cathodiques différents ainsi que des nanofils multisegmentés avec 3 segments magnétiques de 2 μm de longueur chacun. Le graphique courant/temps montre les formes d'onde de courant pour les nanofils courts (Fig. C.8 a) et les nanofils segmentés (Fig. C.8 b).

La composition chimique des nanofils segmentés a été analysée par des mesures HAADF (Fig. C.9). Un changement clair de composition peut être observé, correspondant à trois segments. Les résultats indiquent une bonne concordance des valeurs de concentration atomique avec les résultats des nanofils déposés sous forme d'alliages à un potentiel fixe.

Des études réalisées au microscope de Lorentz montrent de nettes perturbations du tracé linéaire des franges de Fresnel dans la partie centrale des nanofils (Fig. C.10). Ces perturbations marquées de flèches jaunes indiquent les positions des parois du domaine et correspondent aux positions des frontières entre segments.

La présence d'une structure multidomaine est également suggérée par les mesures FORC. Les recherches menées ont confirmé que les nanofils segmentés obtenus sont des matériaux multi-domaines, ce qui en fait de bons candidats pour la construction d'unités de mémoire 3D.

Conclusion

En résumé, ce travail de thèse a démontré l'importance des conditions d'électrodépôt de nanofils métalliques et d'alliage mono- et multi-segmentés sur la composition des matériaux obtenus et de l'influence de cette dernière sur leurs propriétés magnétiques, avec

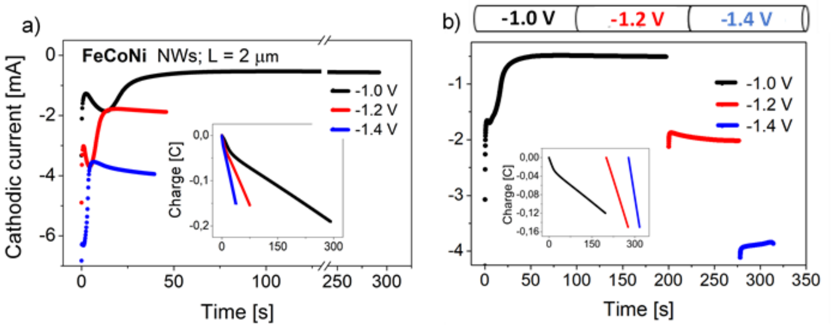

Figure C.8: Variation du courant cathodique en fonction du temps mesurée pendant l'électrodépôt de nanofils FeCoNi : (a) segments simples d'une longueur de 2 µm et d'un diamètre de 100 nm à différents potentiels et (b) nanofils FeCoNi multisegmentés d'un diamètre de 100 nm et d'une longueur totale de 6 µm (chaque segment de 2 µm). L'encart dans le graphique du courant montre les variations de charge électrique correspondantes dans le temps. Au-dessus du graphique de l'échantillon segmenté, il y a un schéma du nanofil préparé.

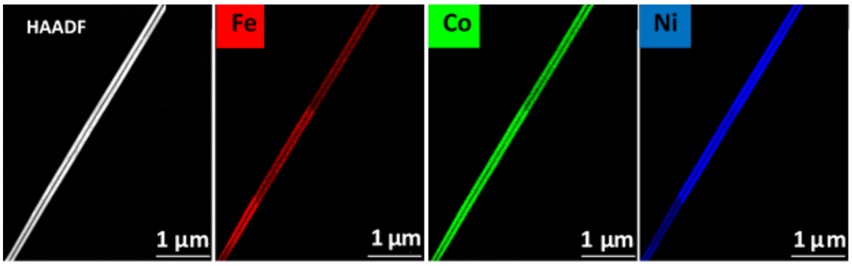

Figure C.9: HAADF-EDS de Fe, Co et Ni mesuré pour des nanofils FeCoNi segmentés de diamètre de 100 nm et d'une longueur totale de 6 µm.

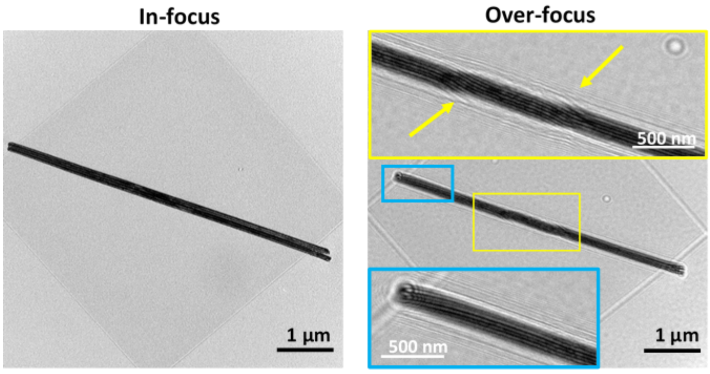

Figure C.10: Résultats de mesures de nanofils segmentés FeCoNi ($\phi = 100$ nm) réalisées à l'aide d'un microscope de Lorentz. Les encarts montrent les zones sélectionnées agrandies. Les flèches jaunes indiquent les positions des parois du domaine situés aux limites entre les segments.

des retombées potentielles pour des applications dans le domaine du stockage magnétique à base de structures tridimensionnelles.

Bibliography

[1] Um J., Zamani Kouhpanji M.R., Liu S., Porshokouh Z.N., Sung S., Kosel J., Stadler B. Fabrication of Long-Range Ordered Aluminum Oxide and Fe/Au Multilayered Nanowires for 3-D Magnetic Memory *IEEE Trans Magn.*, 2020, 56(2):2-7, doi:10.1109/TMAG.2019.2942946

[2] Ivanov Y.P., Chuvilin A., Lopatin S., Kosel J. Modulated Magnetic Nanowires for Controlling Domain Wall Motion: Toward 3D Magnetic Memories *ACS Nano.*, 2016, 10(5):5326-5332, doi:10.1021/acsnano.6b01337

[3] Bochmann S., Dohler D., Trapp B., Stano M., Fruchart O., Bachmann J. Preparation and physical properties of soft magnetic nickel−cobalt three-segmented nanowires *J Appl Phys.*, 2018, 124(16), doi:10.1063/1.5049892

[4] Bran C., Fernandez-Roldan J.A., Del Real R.P., Asenjo A., Chubykalo-Fesenko O., Vazquez M. Magnetic configurations in modulated cylindrical nanowires *Nanomaterials*, 2021, 11(3):1-27, doi:10.3390/nano11030600

[5] Parkin S.S.P., Hayashi M., Thomas L., Magnetic Domain-Wall Racetrack Memory *Science*, 2008, 320:190-194, doi:www.sciencemag.org

[6] Fernandez-Pacheco A., Streubel R., Fruchart O., Hertel R., Fischer P., Cowburn R.P. Three-dimensional nanomagnetism *Nature Communications*, 2017, 8(1), doi:10.1038/ncomms15756

[7] Hertel R., Kakay A. Analytic form of transverse head-to-head domain walls in thin cylindrical wires *Journal of Magnetism and Magnetic Materials*, 2015, 379, 45â€“49, doi.org/10.1016/j.jmmm.2014.11.073

[8] Parkin S., Yang S.H. Memory on the racetrack *Nature Nanotechnology*, 2015, 10(3):195-198, doi:10.1038/nnano.2015.41

[9] Jin T.L., Ranjbar M., He S.K., Law W.C., Zhou T.J., Lew W.S., Liu X. X. Piramanayagam S. N. Tuning magnetic properties for domain wall pinning via localized metal diffusion *Sci Rep.* 2017, 7(1):1-9, doi:10.1038/s41598-017-16335-z

[10] Yang S., Ryu K., Parkin S. Domain-wall velocities of up to 750 m s − 1 driven by exchange-coupling torque in synthetic antiferromagnets *Nature Nanotechnology*, 2015, doi:10.1038/nnano.2014.324

[11] Bhushan B. Springer Handbook of Nanotechnology, Springer, 2017, doi: 10.1007/978-3-662-54357-3

[12] Abid N., Khan A.M., Shujait S., Chaudhary K., Ikram M., Imran M., Haider J., Khan M., Khan Q., Maqbool M., Synthesis of nanomaterials using various top-down and bottom-up approaches, influencing factors, advantages, and disadvantages: A review *Advances in Colloid and Interface Science*, 2022, 300, 102597, 0001-8686, doi: 10.1016/j.cis.2021.102597

[13] Kong Y. C., Yu D. P., Zhang B., Fang W. SQF. Ultraviolet-emitting ZnO nanowires synthesized by a physical vapor deposition approach *Applied Physics Letters*, 2004, 407:1-4, doi:10.1063/1.1342050

[14] Manzhos R.A., Kochergin V.K., Krivenko A.G., Khodos I. Oxidation of Formaldehyde on PdNi Nanowires Synthetized in Superfluid Helium 1 *Russian Journal of Electrochemistry*, 2023, 59(10):714-718, doi:10.1134/S1023193523100105

[15] Nasirpouri F. Electrodeposition of Nanostructured Materials, Springer, 2017, DOI 10.1007/978-3-319-44920-3 Library

[16] Yalcin, O., Kartopu, G., Cetin, H. D. A. Y. E. T., Demiray, A. S., and Kazan, S., A comparison of the magnetic properties of Ni and Co nanowires deposited in different templates and on different substrates, *Journal of Magnetism and Magnetic Materials*, 2015, 373, 207-212, doi: 10.1016/j.jmmm.2014.04.004

[17] https://www.malecki.chemia.us.edu.pl/pojecia-chemii-nieorganicznej/elektrochemia/podwojna-warstwa-elektryczna/ - access 20.05.2024

[18] Chepuri K., Homem-De-Mello, T. Solving the Vehicle Routing Problem with Stochastic Demands using the Cross-Entropy Method *Annals of Operations Research*, 2005, 134, 153-181, https://doi.org/10.1007/s10479-005-5729-7

[19] Hanafi I., Daud A.R., Radiman S. Potentiostatic electrodeposition of Co-Ni-Fe alloy particles thin film in a sulfate medium *Port Electrochim Acta.* 2017, 35(1):1-12, doi:10.4152/pea.201701001

[20] Budi S., Muhab S., Purwanto A., Kurniawan B., Manaf A. Effect of the electrodeposition potential on the magnetic properties of FeCoNi films *Mater Sci Pol.* 2019, 389-394, doi:10.2478/msp-2019-0044

[21] Liu X., Zangari G., Shamsuzzoha M. Structural and Magnetic Characterization of Electrodeposited, High Moment FeCoNi Films *J Electrochem Soc.* 2003, 150(3):C159. doi:10.1149/1.1545462

[22] Tatiparti S.S.V, Ebrahimi F. Potentiostatic versus galvanostatic electrodeposition of nanocrystalline Al - Mg alloy powders *J Solid State Electrochem*, 2012, 16:1255-1262, doi:10.1007/s10008-011-1522-5

[23] Wu Z., Zhang Y., Du K. A simple and efficient combined AC-DC electrodeposition method for fabrication of highly ordered Au nanowires in AAO template *Appl Surf Sci.*, 2013, 265:149-156, doi:10.1016/j.apsusc.2012.10.154

[24] Gosh S., Capacitance effect on Co-layer dissolution during pulse potentiostatic deposition of Co-Cu/Cu multilayers *Electrochimica Acta*, 2008 53, 8070-8077, doi:10.1016/j.electacta.2008.06.019

[25] Kac M., Kopec M., Cieniek L., Zarzycki A., Kac S., Maximenko A. Dutkiewicz E.M., Marszalek M. Influence of Cu Layer Thickness on Morphology and Magnetic Properties of Co / Cu Nanowires *Acta Physica Polonica A*, 2018, 133(2):302-305, doi:10.12693/APhysPolA.133.302

[26] Kac M., Nykiel A., Pastukh O., Kopec M., Zarzycki A., Maximenko A., Parlinska-Wojtan M., Dutkiewicz E.M., Kopia A. The role of the addition of Cu in alloyed and multilayered Fe-based nanowires *Materials Science Engineering B*, 2022, 281(April):115732, doi:10.1016/j.mseb.2022.115732

[27] Ali G.A.M., Yusoff M.M., Hau Y., Ngee H., Feng K. Potentiostatic and galvanostatic electrodeposition of manganese oxide for supercapacitor application: A comparison study *Curr Appl Phys.*, 2015, 15(10):1143-1147, doi:10.1016/j.cap.2015.06.022

[28] Abdelfatah M., Ledig J., El-Shaer A., Sharafeev A., Lemmens P., Mosaad M.M., Waag A., Bakina A. Effect of Potentiostatic and Galvanostatic Electrodeposition Modes on the Basic Parameters of Solar Cells Based on Cu 2 O Thin Films *ECS Journal of Solid State Science and Technology*, 2016, 5(6) Q183-Q187, doi:10.1149/2.0191606jss

[29] Apel P.Y., Blonskaya I.V., Dmitriev S.N., Orelovitch O.L., Sartowska B. Structure of polycarbonate track-etch membranes: Origin of the 'paradoxic' pore shape. *Journal of Membrane Science*, 2006 393-400 doi:10.1016/j.memsci.2006.05.045

[30] Liu X., Hu S., Hong Y., Li Z., Luo J., Li K., Song K., Zhang Y., Younis U., Botcha V.D. Growth of necklace-like In2Se3 nanowires using MoS2 seed layer during PVD method *J Cryst Growth.*, 2019, 526:125215, doi:10.1016/j.jcrysgro.2019.125215

[31] Kac M., Zarzycki A., Kac S., Kopec M., Perzanowski M., Dutkiewicz E.M., Suchanek K., Maximenko A., Marszalek M. Effect of the template-assisted electrodeposition parameters on the structure and magnetic properties of Co nanowire arrays *Materials Science and Engineering B*, 2016, 211:75-84, doi:10.1016/j.mseb.2016.06.004

[32] Kac M., Mis A., Dubiel B., Kowalski K., Zarzycki A., Dobosz I. Template-assisted iron nanowire formation at different electro- lyte temperatures *Materials*, 2021, 14, 4080, https://doi.org/10.3390/ma14154080

[33] Maurer T, Zighem F, Fang W, Ott F., Chaboussant G., Soumare Y., Atmane K.A., Piquemal JY., Viau G. Dipolar interactions in magnetic nanowire aggregates. *J. Appl. Phys.*, 2011, 110 (12):123924, https://doi.org/10.1063/1.3671540

[34] Moreno J.A., Bran C., Vazquez M., Kosel J. Cylindrical Magnetic Nanowires Applications *IEEE Trans Magn.*, 2021, 57(4), doi:10.1109/TMAG.2021.3055338

[35] Montero-Rama M.P., Viterisi A., Eckstein C. MLF. In-situ removal of thick barrier layer in nanoporous anodic alumina by constant current Re-anodization *Surface and Coatings Technology*, 2019, 380(October):125039, doi:10.1016/j.surfcoat.2019.125039

[36] Patel Y, Janusas G, Palevicius A. Development of Nanoporous AAO Membrane for Nano Filtration Using the Acoustophoresis Method *Sensors*, 2020, 20, 3833, doi:10.3390/s20143833

[37] Alonso, J., Khurshid, H., Sankar, V., Nemati, Z., Phan, M. H., Garayo, E., and Srikanth, H. FeCo nanowires with enhanced heating powers and controllable dimensions for magnetic hyperthermia, *Journal of Applied Physics*, 2015, 117(17), doi:10.1063/1.4908300

[38] Saeki R., Ohgai T. Determination of activation overpotential during the nucleation of Hcp-cobalt nanowires synthesized by potentio-static electrochemical reduction. *Materials (Basel)*, 2018, 11(12):1-13, doi:10.3390/ma11122355

[39] Zhan Q., Gao J., Liang Y., Di N., Cheng Z. Dipolar interactions in arrays of iron nanowires studied by Mossbauer spectroscopy *Physical Review B*, 2005, 72, 024428, doi:10.1103/PhysRevB.72.024428

[40] Sorop, T. G., Nielsch, K., Goring, P., Kroll, M., Blau, W., Wehrspohn, R. B., and De Jongh, L. J., Study of the magnetic hysteresis in arrays of ferromagnetic Fe nanowires as a function of the template filling fraction. *Journal of Magnetism and Magnetic Materials*, 2004, 272, 1656-1657.

[41] Mansouri N., Benbrahim-Cherief N., Chainet E., Charlot F., Encinas T., Boudinar S., Benfedda B., Hamadou L., Kadri A. Electrodeposition of equiatomic FeNi and FeCo nanowires: Structural and magnetic properties *Journal of Magnetism and Magnetic Materials*, 2020, 493(August 2019):165746, doi:10.1016/j.jmmm.2019.165746

[42] Valizadeh S., George J.M., Leisner P., Hultman L. Electrochemical deposition of Co nanowire arrays; quantitative consideration of concentration profiles *Electrochimica Acta*, 2001, 865-874, doi.org/10.1016/S0013-4686(01)00797-6

[43] Kruglikov, S. S., Zagorskii, D. L., Kolesnikov, V. A., Doludenko, I. M., and Bedin, S. A. Analyzing the Conditions for the Electrolytic Formation of Ensembles from Metal Nanowires in the Pores of Track Membranes *Theoretical Foundations of Chemical Engineering*, 2021, 55, 942-951, doi 10.1134/S0040579521040266

[44] Whitney T.M., Jiang J.S., Searson P.C., Chien C.L. Fabrication and magnetic properties of arrays of metallic nanowires. *Science*, 1993, 261(5126):1316-1319, doi:10.1126/science.261.5126.1316

[45] Grujicic D., Pesic B. Electrochemical and AFM study of cobalt nucleation mechanisms on glassy carbon from ammonium sulfate solutions *Electrochimica Acta*, 2004, 49(26):4719-4732, doi:10.1016/j.electacta.2004.05.028

[46] Grujicic D., Pesic B. Iron nucleation mechanisms on vitreous carbon during electrodeposition from sulfate and chloride solutions. *Electrochimica Acta*, 2005, 50(22):4405-4418, doi:10.1016/j.electacta.2005.02.013

[47] Kaur D., Pandya D.K. Hydrogen Co-Deposition Induced Phase and Microstructure Evolution of Cobalt Nanowires Electrodeposited in Acidic Baths *Journal of The Electrochemical Society*, 2016, 163(6):D221-D229, doi:10.1149/2.0311606jes

[48] Gomez H., Riveros G., Ramirez D., Henriquez R., Schrebler R., Marotti R., Dalchiele E. Growth and characterization of ZnO nanowire arrays electrodeposited into anodic alumina templates in DMSO solution. *J Solid State Electrochem.*, 2012, 16(1):197-204, doi:10.1007/s10008-011-1309-8

[49] Hu H., Tan M., Liu L. Anomalous codeposition mechanism of Co-Ni alloy nanowires *Journal of Alloys and Compounds*, 2017, 715:384-389, doi:10.1016/j.jallcom.2017.05.002

[50] Saedi A., Ghorbani M. Electrodeposition of Ni-Fe-Co alloy nanowire in modified AAO template. *Materials Chemistry and Physics*, 2005, 91(2-3):417-423, doi:10.1016/j.matchemphys.2004.12.001

[51] Bai A., Hu C.C., Wen T.C. Composition control of ternary Fe-Co-Ni deposits using cyclic voltammetry *Electrochimica Acta*, 2003, 48(17):2425-2434, doi:10.1016/S0013-4686(03)00266-4

[52] Hanafi I., Daud A.R., Radiman S. Potentiostatic electrodeposition of Co-Ni-Fe alloy particles thin film in a sulfate medium *Portugaliae Electrochimica Acta*, 2017, 35(1), 1-12, DOI:10.4152/pea.201701001

[53] Dragos O, Chiriac H, Lupu N, Grigoras M, Tabakovic I. Anomalous Codeposition of fcc NiFe Nanowires with 5-55% Fe and Their Morphology, Crystal Structure and Magnetic Properties *Journal of The Electrochemical Society*, 2016, 163(3):D83-D94, doi:10.1149/2.0771603jes

[54] Phan N.H., Schwartz M., Nobe K. Electrodeposition of Fe-Ni-Co alloys part I: Direct current deposition *Journal Of Applied Electrochemistry*, 1991, 21(8):672-677, doi:10.1007/BF01034044

[55] Gong J., Riemer S., Morrone A., Venkatasamy V., Kautzky M., Tabakovic I. Composition Gradients and Magnetic Properties of 5ı100 nm Thin CoNiFe Films Obtained by Electrodeposition *Journal of The Electrochemical Society* 2012, 159(7):D447-D454, doi:10.1149/2.082207jes

[56] Hu C-C., Bai A. The Inhibition of Anomalous Codeposition of Iron-Group Alloys Using Cyclic Voltammetry *Journal of The Electrochemical Society*, 2002, 149(11):C615, doi:10.1149/1.1511753

[57] Dahms H., Croll I.M. The Anomalous Codeposition of Iron-Nickel Alloys *Journal of the Electrochemical Society*, 1965, 112.8 771, doi:10.1149/1.2423692

[58] Grande W., Talbot J. Electrodeposition of Thin Films of Nickel-Iron *J. Electrochem. Soc.*, 1993, 140, 3, DOI 10.1149/1.2056141

[59] Zhu J., Hu L., Zhao P., Lee L.Y.S., Wong K.Y. Recent Advances in Electrocatalytic Hydrogen Evolution Using Nanoparticles *Chemical Reviews*, 2020, 120(2):851-918, doi:10.1021/acs.chemrev.9b00248

[60] Gamburg, Y.D., Zangari, G. Theory and practice of metal electrodeposition *Springer Science and Business Media*, 2011

[61] Li D., Podlaha E.J. Template-Assisted Electrodeposition of Porous Fe-Ni-Co Nanowires with Vigorous Hydrogen Evolution. *Nano Letters*, 2019, 19(6):3569-3574, doi:10.1021/acs.nanolett.9b00532

[62] Dubouis N., Grimaud A. The hydrogen evolution reaction: From material to interfacial descriptors *Chemical Science*, 2019, 10(40):9165-9181, doi:10.1039/c9sc03831k

[63] Yang Y. Preparation of Fe-Co-Ni ternary alloys with electrodeposition, *International Journal of Electrochemical Science*, 2015, 10(6):5164-5175, doi:10.1016/s1452-3981(23)06694-4

[64] Hu H.N., Chen H.Y., Chen J.L., Wu G.H. Magnetic properties of (1 1 0)- and (2 0 0)-oriented Fe-nanowire arrays. *Phys B Condens Matter*, 2005, 368(1-4):100-104, doi:10.1016/j.physb.2005.07.002

[65] Agarwal S., Khatri M.S. Effect of pH and Boric Acid on Magnetic Properties of Electrodeposited Co Nanowires. *Proc Natl Acad Sci India Sect A - Phys Sci.*, 2022, 92(1):111-116, doi:10.1007/s40010-020-00708-7

[66] Kroll, M., Blau, W. J., Grandjean, D., Benfield, R. E., Luis, F., Paulus, P. M., and De Jongh, L. J., Magnetic properties of ferromagnetic nanowires embedded in nanoporous alumina membranes, *Journal of Magnetism and Magnetic Materials*, 2002, 249(1-2), 241-245, doi: 10.1016/S0304-8853(02)00537-1

[67] Li F., Wang T., Ren L., Sun J. Structure and magnetic properties of Co nanowires in self-assembled arrays. *J Phys Condens Matter.*, 2004, 16(45):8053-8060, doi:10.1088/0953-8984/16/45/027

[68] Nemtoi G., Chiriac H., Dragos O., Apostu M-O., Lutic D. The Voltammetric Characterization of the Electrodeposition of Cobalt, Nickel and Iron on Gold Disk Electrode. *Acta Chem Iasi.*, 2009, 17:151-168, https://api.semanticscholar.org/CorpusID:53330914

[69] Cortes A., Riveras G., Palma J.L, Denardin J.C., Marotti R.E., Dalchiele E.A., Gomez H. Single-Crystal growth of nickel nanowires: Influence of deposition conditions on structural and magnetic properties. *Journal of Nanoscience and Nanotechnology*, 2009, 9(3):1992-2000, doi:10.1166/jnn.2009.374

[70] Cortes A., Lavin R., Denardin J.C., Marotti R.E., Dalchiele E.A., Valdivia P., Gómez H. Template assisted electrochemical growth of cobalt nanowires: Influence of deposition conditions on structural, optical and magnetic properties *Journal of Nanoscience and Nanotechnology*, 2011, 11(5):3899-3910, doi:10.1166/jnn.2011.3826

[71] Nasirpouri F. Template Electrodeposition of Magnetic Nanowire Arrays, *International Journal of Electrochemical Science*, 2007, 10(6), 5164-5175, 10.1016/s1452-3981(23)06694-4

[72] Paulus P.M., Luis F., Kroll M., Schmid G., De Jongh L.J. Low-temperature study of the magnetization reversal and magnetic anisotropy of Fe, Ni, and Co

nanowires. *Journal of Magnetism and Magnetic Materials*, 2001, 224(2):180-196, doi:10.1016/S0304-8853(00)00711-3

[73] Shin S, Kong BH, Kim BS, Kim KM, Cho HK, Cho HH. Over 95% of large-scale length uniformity in template-assisted electrodeposited nanowires by subzero-temperature electrodeposition *Nanoscale Research Letters*, 2011, 6:467, doi.org/10.1186/1556-276X-6-467

[74] Xiang X.Z., Gong W.Y., Kuang M.S., Wang L. Progress in application and preparation of silver nanowires *Rare Metals*, 2016, 35(4):289-298, doi:10.1007/s12598-016-0695-6

[75] Azevedo J., Sousa C.T., Ventura J., Apolinario A., Mendes A., Araujo J.P. Ultra-long Fe nanowires by pulsed electrodeposition with full filling of alumina templates, *Materials Research Express*, 2014, 015028, doi:10.1088/2053-1591/1/1/015028

[76] Kaur D., Pandya D.K., Chaudhary S., Kashyap S.C. Structural and magnetic properties of electrochemically grown Ni-Fe and Co-Fe nanowire arrays Nanotechnol 2010 Electron Devices, NSTI-Nanotech, 2010, 118-121, https://www.researchgate.net/publication/236683581

[77] Wang F., Li L., Qiu S., Wang H. Ferronickel preparation using Ni-Fe co-deposition process *J Cent South Univ*, 2016, 23(12):3072-3078, doi:10.1007/s11771-016-3371-y

[78] Razeeb, K. M., Rhen, F. M., Roy, S., Magnetic properties of nickel nanowires: Effect of deposition temperature, *Journal of Applied Physics*, 2009, 105(8), doi: 10.1063/1.3109080

[79] Zach M.P., Ng K.H., Penner R.M. Molybdenum nanowires by electrodeposition *Science* 2000, 290(5499):2120-2123, doi:10.1126/science.290.5499.2120

[80] Jensen L.E., Bjork M.T., Jeppesen S., Persson A.I., Ohlsson B.J., Samuelson L. Role of surface diffusion in chemical beam epitaxy of InAs nanowires *Nano Letters* 2004, 4(10):1961-1964, doi:10.1021/nl048825k

[81] Xu J., Hong B., Peng X., Wang X., Ge H., Hu J. Preparation and magnetic properties of gradient diameter FeCoNi alloys nanowires arrays. *Chem Phys Letters*, 2021, 767, doi:10.1016/j.cplett.2021.138368

[82] Palmero E.M., Bran C., del Real R. P., Magen C., and Vazquez M. Magnetic behavior of NiCu nanowire arrays: Compositional, geometry and temperature dependence *Journal of Applied Physics*, 2015, 033908, doi:10.1063/1.4890358

[83] Alirezaei S., Samanifar B., Rashidi A. Magnetic Properties and Reversal Modes of Electrodeposited CoCr Nanowire Arrays with Different Diameters. *Journal of Superconductivity and Novel Magnetism*, 2021, 3199-3208, doi:10.1007/s10948-021-05982-z

[84] Ghazkoob N., Zargar S. M., Kazeminezhad I., Lari B.S.M. Structural, magnetic and optical investigation of AC pulse electrodeposited zinc ferrite nanowires with

different diameters and lengths *Journal of Magnetism and Magnetic Materials*, 2021, 537:168113, doi:10.1016/j.jmmm.2021.168113

[85] Zhang X., Zhang H., Wu T., Li Z., Zhang Z., Sun H., Comparative study in fabrication and magnetic properties of FeNi alloy nanowires and nanotubes, *Journal of Magnetism and Magnetic Materials*, 2013, 331, 162-167, 10.1016/j.jmmm.2012.11.033

[86] Xiao Y., Xu Q., Zhang J., Yin X., Duan S. Preparation and Magnetic Properties of Fe−Co−Ni Magnetic Nanowire Arrays with Three-Dimensional Periodic Structures *Journal of Superconductivity and Novel Magnetism*, 2023, 36(4):1161-1170, doi:10.1007/s10948-023-06555-y

[87] Szewczyk A., Wisniewski A., Puzniak R., Szymczak H. Magnetyzm i nadprzewodnictwo, Wydawnictwo Naukowe PWN, 2012

[88] Sun L., Hao Y., Chien C. L., Searson P. C., Searson P. C. Tuning the properties of magnetic nanowires *IBM J. Res. Dev.*, 2005, 49, 1, 79-102, doi: 10.1147/rd.491.0079

[89] Fernandez-Roldan J.A., De Riz A., Trapp B., Modeling magnetic-field-induced domain wall propagation in modulated-diameter cylindrical nanowires *Sci Rep.,* 2019, 9(1):1-12, doi:10.1038/s41598-019-40794-1

[90] Moreno, J. A., Mohammed, H., and Kosel, J. Effect of Segment length on domain wall pinning in multisegmented Co/Ni nanowires for 3D memory applications. *Journal of Magnetism and Magnetic Materials*, 2019, 484, 110-113, doi:10.1016/j.jmmm.2019.04.002

[91] Moreno R., Carvalho-Santos V.L., Altbir D., Chubykalo-Fesenko O. Detailed examination of domain wall types, their widths and critical diameters in cylindrical magnetic nanowires. *J Magn Magn Mater.* 2022, 542:168495, doi:10.1016/j.jmmm.2021.168495

[92] Jamet, S., Rougemaille, N., Toussaint, J. C., and Fruchart, O. Head-to-head domain walls in one-dimensional nanostructures: An extended phase diagram ranging from strips to cylindrical wires, *Magnetic Nano-and Microwires*, 2014, 783-811, doi:10.1016/B978-0-08-100164-6.00025-4

[93] Jamet S., Rougemaille N., Toussaint J.C., Fruchart O. Head-to-Head Domain Walls in One-Dimensional Nanostructures. *Elsevier Ltd.*, 2015, doi:10.1016/B978-0-08-100164-6.00025-4

[94] Russo U., Capolongo F. An Outline of the Prehistory of Magnetism Supermagnets, Hard Magnetic Materials, 1991, doi:10.1007/978-94-011-3324-1_2

[95] Getzlaff M. Fundamental of Magnetism, 2017, 6(11), 951-952, https://www.academia.edu/98297744/Fundamentals_of_Magnetism_Mathias_Getzlaff

[96] Wang J., Li J., Wang J. Bu, F. Kou H. Li C. Zhang P. Beaugnon E. Effect of solidification on microstructure and properties of FeCoNi(AlSi)0.2 high-entropy alloy under strong static magnetic field *Entropy*, 2018, 20(4), doi:10.3390/e20040275

[97] Srivastav A.K., Shekhar R. Crystal anisotropy induced temperature dependent magnetization in cobalt nanowires electrodeposited within alumina template *Journal of Magnetism and Magnetic Materials* 2014, 349:21-26, doi:10.1016/j.jmmm.2013.08.041

[98] Schlorb H., Haehnel V., Khatri M.S., Srivastav A. Kumar A. Schultz L., Fahler S. Magnetic nanowires by electrodeposition within templates *Phys Status Solidi Basic Res.* 2010, 247(10):2364-2379, doi:10.1002/pssb.201046189

[99] Kools F., Morel A. Ferrite Magnets: Improved Performance. *Encycl Mater Sci Technology*, 2004, 19:1-5, doi:10.1016/b0-08-043152-6/01908-2

[100] Cullity B.D., Graham C.D. Introduction to Magnetic Materials IEEE PRESS, John Wiley and Sons, 2009

[101] O'Handley. Magnetic materials *Springer Handbooks*, 2018, 753-807, doi:10.1007/978-3-319-69743-7_22

[102] Okamoto T., Yamada H., Sugawara S., Ishio S., Magnetocrystalline Anisotropy of Single Crystals and Magnetic Properties of Evaporated Films in Co-Ni-Fe Ternary Alloy, *J. Magn. Soc. Jpn*, 1995, 19, 445-448

[103] Grundy P.J., Magnetic Layers: Anisotropy *Encycl. Mater. Sci. Technol*, 2001, 6, 4788-4792, doi: 10.1016/b0-08-043152-6/00836-6

[104] Zighem F., Maurer T., Ott F., Chaboussant G., Dipolar interactions in arrays of ferromagnetic nanowires: A micromagnetic study *J. Appl. Phys.*, 2011, 109, 1, doi: 10.1063/1.3518498

[105] Samanifar S., Almasi Kashi M., Ramazani A., Alikhani M. Reversal modes in FeCoNi nanowire arrays: Correlation between magnetostatic interactions and nanowires length. *J Magn Magn Mater.*, 2015, 378:73-83, doi:10.1016/j.jmmm.2014.10.155

[106] Encinas-Oropesa A., Demand M., Piraux L., Huynen I., Ebels U. Dipolar interactions in arrays of nickel nanowires studied by ferromagnetic resonance. *Phys Rev B - Condens Matter Mater Phys.* 2001, 63(10):1044151-1044156, doi:10.1103/PhysRevB.63.104415

[107] Han G.C., Zong B.Y., Luo P., Wu Y.H. Angular dependence of the coercivity and remanence of ferromagnetic nanowire arrays. *J Appl Phys.* 2003, 93(11):9202-9207, doi:10.1063/1.1572197

[108] Bruno P. Geometrically Constrained Magnetic Wall Physical Review Letters, 1999, 2425-2428, doi.org/10.1103/PhysRevLett.83.2425

[109] Abo G.S., Hong Y.K., Park J., Lee J., Lee W., Choi B.C. Definition of magnetic exchange length *IEEE Trans Magn.*, 2013, 49(8):4937-4939, doi:10.1109/TMAG.2013.2258028

[110] Pastukh O., Kac M., Pastukh S., Kuzma D., Zelent M., Krawczyk M., Laskowski L. Magnetic Behavior of the Arrays of Iron Cylindrical Nanostructures: Atomistic Spin Model Simulations *Crystals*, 2023, 13(3):1-16, doi:10.3390/cryst13030537

[111] Velazquez J., Garcia C., Vazquez M., Hernando A. Interacting amorphous ferromagnetic wires: A complex system. *J Appl Phys.*, 1999, 85(5):2768-2774, doi:10.1063/1.369592

[112] Nielsch K., Wehrspohn R.B., Barthel J., Kirschner J., Gosele U., Fischer S. F., Kronmuller H. Hexagonally ordered 100 nm period nickel nanowire arrays. *Appl Phys Lett.* 2001, 79(9):1360-1362, doi:10.1063/1.1399006

[113] Henry Y., Ounadjela K., Piraux L., Dubois S., George J.M., Duvail J.L. Magnetic anisotropy and domain patterns in electrodeposited cobalt nanowires. *Eur Phys J B.*, 2001, 20(1):35-54, doi:10.1007/s100510170283

[114] Cornejo D.R., Padron-Hernandez E. Study of magnetization process in ordered Fe nanowire arrays. *J Magn Magn Mater*, 2007, 316:48-51, doi:10.1016/j.jmmm.2007.02.023

[115] Weissker U., Loffler M., Wolny F., Lutz M.U., Scheerbaum N., Klingeler R., Gemming T., MĂĽhl T., Leonhardt A., BĂĽchner B. Perpendicular magnetization of long iron carbide nanowires inside carbon nanotubes due to magnetocrystalline anisotropy. *J Appl Phys.* 2009, 106(5), doi:10.1063/1.3204495

[116] Roberts A.P., Almeida T.P., Church N.S., Harrison R.J., Heslop D., Li Y., Li J., Muxworthy A.R., Williams W. Zhao X. Resolving the Origin of Pseudo-Single Domain Magnetic Behavior. *J Geophys Res Solid Earth.* 2017, 122(12):9534-9558, doi:10.1002/2017JB014860

[117] Krimpalis S., Lupu N., Chiriac H. Mechanism of Magnetization Reversal in Arrays of Multilayered Nanowires *IEEE transactions on magnetics* 2011, 47(11):4534-4541, DOI: 10.1109/TMAG.2011.2151873

[118] Hertel R., Kakay A. Analytic form of transverse head-to-head domain walls in thin cylindrical wires. *Journal of Magnetism and Magnetic Materials*, 2015, 379:45-49, doi:10.1016/j.jmmm.2014.11.073

[119] Ferguson C.A., Maclaren D.A., Mcvitie S. Metastable magnetic domain walls in cylindrical nanowires. *Journal of Magnetism and Magnetic Materials*, 2015, 381:457-462, doi:10.1016/j.jmmm.2015.01.027

[120] Bran C., Prida V.M., Vazquez M. Tuning the magnetization reversal process of FeCoCu nanowire arrays by thermal annealing, *Journal of Applied Physics*, 2013, 043908, doi:10.1063/1.4816479

[121] Fernandez-Roldan J.A., Real R.P., Vazquez M., Chubykalo-Fesenko O. Micromagnetic evaluation of the dissipated heat in cylindrical magnetic nanowires *Appl. Phys. Lett. 112,*, 2018, 112, 212402, doi:10.1063/1.5025922

[122] Schobitz M., Novotny O., Trapp B., Bochmann S., Cagnon L., Thirion C., Mossang E., Fruchart O., Bachmann J. A Material View on Extrinsic Magnetic Domain Wall Pinning in Cylindrical CoNi Nanowires, *J. Phys. Chem. C*, 2023, 127, 2387â'2397, doi:10.1021/acs.jpcc.2c07687

[123] Ivanov A.A., Orlov V.A. A comparative analysis of the mechanisms of pinning of a domain wall in a nanowire *Phys Solid State*, 2011, 53(12):2441-2449, doi:10.1134/S1063783411120079

[124] Bogart L.K., Atkinson D., O'Shea K., McGrouther D., McVitie S. Dependence of domain wall pinning potential landscapes on domain wall chirality and pinning site geometry in planar nanowires. *Phys Rev B - Condens Matter Mater Phys.*, 2009, 79(5):1-8, doi:10.1103/PhysRevB.79.054414

[125] Nasirpouri F., Peighambari-Sattari S.M., Bran C., Palmero E.M., Berganza Eguiarte E., Vazquez M., Patsopoulos A., Kechrakos D. Geometrically designed domain wall trap in tri-segmented nickel magnetic nanowires for spintronics devices. *Scientific Reports*, 2019, 9(1):1-11, doi:10.1038/s41598-019-45553-w

[126] Atkinson D., Eastwood D.S., Bogart L.K. Controlling domain wall pinning in planar nanowires by selecting domain wall type and its application in a memory concept *Appl Phys Lett.* 2008, 92(2), doi:10.1063/1.2832771

[127] Schryer N.L., Walker L.R. The motion of 180^o domain walls in uniform dc magnetic fields *Journal of Applied Physics*, 1974, 45, 5406 (1974), https://doi.org/10.1063/1.1663252

[128] Lage E, Urs NO, Siddiqui S, Baldo M, Mccord J, Ross CA. Depinning of Domain Walls by Magnetic Fields and Current Pulses in Tapered Nanowires with Anti-Notches *IEEE Magnetic Letters*, 2016, doi:10.1109/LMAG.2016.2536668

[129] Li Z.D., Cui H., Li Q.Y., He P. B. Dzyaloshinskii-Moriya solitons in anisotropic ferromagnetic nanowires driven by magnetic field and spin-polarized current *Ann Phys (N Y).*, 2018, 388:390-397, doi:10.1016/j.aop.2017.11.019

[130] Han X.M., Ma J.H., Wang Z., Yao, Y. L. Zuo, Y. L. Xi, L. Xue, D. S. Tunable in-plane uniaxial anisotropy and the magnetization reversal mechanism of patterned high-frequency soft magnetic FeTa strips *J Phys D Appl Phys.*, 2013, 46(48), doi:10.1088/0022-3727/46/48/485004

[131] Mathews M., Houwman E.P., Boschker H., Rijnders G., Blank D.H.A. Magnetization reversal mechanism in La0.67Sr 0.33MnO3 thin films on NdGaO3 substrates. *J Appl Phys.*, 2010, 107(1):0-5, doi:10.1063/1.3273409

[132] Deng, H. Y., and Huang, H. L., Domain wall structure and the modified Kondorsky function. *Chinese Journal of Physics*, 2001, 39(5), 479-497, doi: 10.1109/20.280961

[133] Huang H.L., Lu J.J. On Switching Field and Coercivity of the Single Domain Particles *Journal of The Magnetics Society of Japan*, 1994, 18.S_1_PMRC_94_1: S1_241-244, https://doi.org/10.3379/jmsjmag.18.S1_241

[134] Urzhumtsev A.N., Mal V.E., Yarkov V.Y., Volegov A.S. A Modified Kondorsky Model for Describing the Magnetization Reversal Processes in Nd - Fe - B Permanent Magnets *Physics of Metals and Metallography,* 2022, 123(11):1124-1130, doi:10.1134/S0031918X22601238

[135] Cimpoesu D., Stoleriu L., Stancu A. Generalized Stoner-Wohlfarth model accurately describing the switching processes in pseudo-single ferromagnetic particles *J Appl Phys.* 2013, 114(22), doi:10.1063/1.4839895

[136] Schumacher, F., On the modification of the Kondorsky function. *Journal of applied physics*, 1991, 70(6), 3184-3187.doi: 10.1063/1.349301

[137] Han X.F., Shamaila S. and Sharif R. Ferromagnetic Nanowires and Nanotubes *Electrodeposited Nanowires and Their Applications*, 2010, 141-166, DOI: 10.5772/39474

[138] Zeng H., Skomski R., Menon L., Liu Y., Bandyopadhyay S., Sellmyer D.J. Structure and magnetic properties of ferromagnetic nanowires in self-assembled arrays *Physical Review B* 2002, 65:1-8, doi:10.1103/PhysRevB.65.134426

[139] Ohnuma I., Enoki H., Ikeda O., Kainuma R., Ohtani H., Sundman B., Ishida K., Phase equilibria in the Fe-Co binary system. *Acta Mater.*, 2002, 50(2):379-393, doi:10.1016/S1359-6454(01)00337-8

[140] Ramazani A., Almasi Kashi M., Ghanbari S., Eshaghi F. Dual behaviors of magnetic Co xFe 1-x (0≤x≤1) nanowires embedded in nanoporous with different diameters *J Magn Magn Mater.,* 2012, 324(19):3193-3198, doi:10.1016/j.jmmm.2012.05.036

[141] Alonso J., Khurshid H., Sankar V., Nemati Z., Phan M. H., Garayo E., GarcĂa J. A. Srikanth H. FeCo nanowires with enhanced heating powers and controllable dimensions for magnetic hyperthermia. *J Appl Phys*, 2015, 117(17), doi:10.1063/1.4908300

[142] Elbaile L., Crespo R.D., Vega V., Garcia J.A. Magnetostatic interaction in Fe-Co nanowires. *J Nanomater.* 2012, doi:10.1155/2012/198453

[143] Vernyhora I.V., Tatarenko V.A., Bokoch S.M. Thermodynamics of f.c.c.-Ni-Fe Alloys in a Static Applied Magnetic Field *ISRN Thermodyn.*, 2012, 2012:1-11, doi:10.5402/2012/917836

[144] Ramazani A., Asgari V., Montazer A.H., Kashi M.A. Tuning magnetic fingerprints of FeNi nanowire arrays by varying length and diameter *Current Applied Physics*, 2015, 15,7, 819-828, 10.1016/j.cap.2015.04.023

[145] Kunwar S., Chelvane J.A., Raja M.M. Structural , magnetic and Magnetic-Microstructural properties of sputtered FeCoNi thin films. *Journal of Magnetism and Magnetic Materials* 2023, 572(February):170597, doi:10.1016/j.jmmm.2023.170597

[146] Yang B., Fang J., Xu C., Cao H., Zhang R., Zhao B. One - Dimensional Magnetic FeCoNi Alloy Toward Low - Frequency Electromagnetic Wave Absorption *Nano-Micro Lett.* 2022, 14(1):1-13, doi:10.1007/s40820-022-00920-7

[147] Sarac U., Kaya M., Baykul M.C. A Comparative Study on Microstructures, Magnetic Features and Morphologies of Ternary Fe-Co-Ni Alloy Thin Films Electrochemically Fabricated at Different Deposition Potentials*J Supercond Nov Magn.* 2019, 32(4):917-923, doi:10.1007/s10948-018-4774-9

[148] Llavona A., Perez L., Sanchez M.C., Manuel V. Enhancement of anomalous codeposition in the synthesis of Fe-Ni alloys in nanopores *Electrochimica Acta,* 2013, 106 392â€“ 397, doi.org/10.1016/j.electacta.2013.05.116

[149] Song Y., Lu W., Xu Y., Shi J., Fang X. Growth of single-crystalline Co7Fe3 nanowires via electrochemical deposition and their magnetic properties *Journal of Alloys and Compounds*, 2015, 652, 179-184,10.1016/j.jallcom.2015.08.206

[150] Xu F., Yao B., Wang E., Fan Y., Lou B., Guo Y. Fabrication of FeCo and CoFe2O4 nanowire arrays and magnetic properties *Physica E*, 2021, 130 114695, 10.1016/j.physe.2021.114695

[151] Long V., Sarac U., Baykul M.C. Trong L.D.Talu S., Trong D.N. Electrochemical Deposition of Fe-Co-Ni Samples with Different Co Contents and characterization of Their Microstructural and Magnetic Properties *Coatings*, 2022, 12, 346, doi.org/10.3390/ coatings12030346

[152] Fu P., Chen G., Xu Y., Cai P., Wang X. H. Electrodeposition and magnetic properties of ternary Fe-Co-Ni alloy nanowire arrays with high squareness ratio *Materials Science-Poland*, 2012, 30(3), 259-263, 10.2478/s13536-012-0031-2

[153] Sharma G., Grimes C.A. Synthesis, characterization, and magnetic properties of FeCoNi ternary alloy nanowire arrays *Journal of Materials Research*, 2004, 19(12), 3695, 10.1557/JMR.2004.0476

[154] Ledwig, P., Kac, M., Kopia, A., Falkus, J., Dubiel, B. Microstructure and Properties of Electrodeposited Nanocrystalline Ni-Co-Fe Coatings *Materials* 2021, 14, 3886, https://doi.org/10.3390/ma 14143886

[155] Paganotti A., Bessa C.V.X., Silva C.C.S., Peixoto E.B., Duque J.G.S., Silva R.A.G. Effect of the Ni content on the thermal and magnetic properties of Fe-Ni-Co alloys, *Materials Chemistry and Physics*, 2021, 261, 124215, DOI:10.1016/j.matchemphys.2020.124215

[156] Geng X., Podlaha E. Coupled, Simultaneous Displacement and Dealloying Reactions into Fe-Ni-Co Nanowires for Thinning Nanowire Segments *Nano Lett.* 2016, 16, 7439-7445, 10.1021/acs.nanolett.6b03065

[157] Aslam S., Khanna M., Kuanr B.K., Celinski Z. One dimensional Fex Co1-x nanowires; ferromagnetic resonance and magnetization dynamics Shehreen *AIP Advances*, 2017, 7, 056027, 10.1063/1.4977724

[158] Ghemes A., Dragos-Pinzaru O., Chiriac H., Lupu N., Grigoras M. Controlled Electrodeposition and Magnetic Properties of Co35Fe65 Nanowires with High Saturation Magnetization *Journal of The Electrochemical Society*, 2017, 164 D13, 10.1149/2.0441702jes

[159] Doludenko I.M., Zagorskii D.L., Frolov K.V., Perunov I.V., Chuev M.A. Nanowires Made of FeNi and FeCo Alloys: Synthesis, Structure, and Mossbauer Measurements *Physics of the Solid State*, 2020, 62, 9, 1639-1646, 10.1134/S1063783420090061

[160] Zech N., Podlaha E. J. and Landolt D. Anomalous Codeposition of Iron Group Metals, *Journal of The Electrochemical Society*, 1999, 146, 8 2886-2891, doi 10.1149/1.1392024

[161] Elgrishi N., Rountree K. J., McCarthy B.D., Rountree E.S., Eisenhart T.T., and Dempsey J.L. A Practical Beginnerâ€™s Guide to Cyclic Voltammetry, *Journal of Chemical Education ACS*, 2017, 95.2: 197-206, doi 10.1021/acs.jchemed.7b00361

[162] Lindquist, A. K., Feinberg, J. M., Harrison, R. J., Loudon, J. C., and Newell, A. J. Domain wall pinning and dislocations: Investigating magnetite deformed under conditions analogous to nature using transmission electron microscopy, *Journal of Geophysical Research: Solid Earth*, 2015, 120(3), 1415-1430, doi 10.1002/2014JB011335

[163] Kashyap, I., Vetter, E. P., Floro, J. A., and De Graef, M. Lorentz TEM study of the magnetic microstructure in near-eutectoid Co-Pt alloys, *Journal of Magnetism and Magnetic Materials*, 2019, 479, 204-211, doi 10.1016/j.jmmm.2019.02.036

[164] Novikova I., The Mossbauer Effect, PHYS352 Experimental Modern Physics, William and Mary, March 2022, https://physics.wm.edu/ inovikova/phys352/PHYS352-Manuals-Instructions/Mossbauer%20Spectroscopy/

[165] Kashi, M. A., and Montazer, A. H. Template-based electrodeposited nonmagnetic and magnetic metal nanowire arrays as building blocks of future nanoscale applications, *Journal of Physics D: Applied Physics*, 2022, 55(23), 233002, doi 10.1088/1361-6463/ac4d48

[166] Roy, D., Sreenivasulu, K. V., and Anil Kumar, P. S., Investigation on non-exchange spring behaviour and exchange spring behaviour: A first order reversal curve analysis, *Applied Physics Letters*, 2013, 103(22), doi: 10.1063/1.4836015

[167] Roberts, A. P., Pike, C. R., and Verosub, K. L. First-order reversal curve diagrams: A new tool for characterizing the magnetic properties of natural samples, *Journal of Geophysical Research: Solid Earth*, 2000, 105(B12), 28461-28475, doi: 10.1029/2000JB900326

[168] Kotti, A. P., Sahu, R., Mishra, A. C. Magnetization reversal and coercivity mechanism in truncated conical nanowires of permalloy, *Journal of Materials Science*, 2023, 58(27), 11115-11138, doi 10.1007/s10853-023-08722-x

[169] Lavin, R., Denardin, J. C., Escrig, J., Altbir, D., Cortes, A., and Gomez, H. Angular dependence of magnetic properties in Ni nanowire arrays *Journal of Applied Physics*, 2009, 106(10), doi 10.1063/1.3257242

[170] Montazer, A. H., Ramazani, A., Kashi, M. A., and Zavasnik, J. Angular-dependent magnetism in Co (001) single-crystal nanowires: capturing the vortex nucleation fields. Journal of Materials Chemistry C, 2016, 4(45), 10664-10674, doi 10.1039/C6TC03697J

[171] de Campos, M. F., and de Castro, J. A. Predicting Recoil Curves in Stoner-Wohlfarth Anisotropic Magnets. *Acta Physica Polonica A*, 2019, 136(5), 737-739, doi http://doi.org/10.12693/APhysPolA.136.737

[172] Kouhpanji, M. R. Z., and Stadler, B. J. Projection method as a probe for multiplexing/demultiplexing of magnetically enriched biological tissues. *RSC advances*, 2020, 10(22), 13286-13292, doi 10.1039/D0RA01574A

[173] Emura, M., Cornejo, D. R., and Missell, F. P. Reversible and irreversible magnetization in hybrid magnets. *Journal of Applied Physics*, 2000, 87(3), 1387-1394, doi 10.1063/1.372025

[174] Crew, D. C., McCormick, P. G., and Street, R. An investigation of reversible magnetization in NdFeB. *Journal of applied physics*, 1999, 86(6), 3278-3284, doi 10.1063/1.371202

[175] Mendoza-Huizar, L., and Rios-Reyes, C. Cobalt electrodeposition onto polycrystalline gold from ammoniacal solutions. *Open Chemistry,* 2013, 11(8), 1381-1392, doi 10.2478/s11532-013-0269-5

[176] Barman, K., Edwards, M. A., Hickey, D. P., Sandford, C., Qiu, Y., Gao, R., and White, H. S., Electrochemical Reduction of [Ni (Mebpy) 3] 2+: Elucidation of the redox mechanism by cyclic voltammetry and steady-state voltammetry in low ionic strength solutions. ChemElectroChem, 2020, 7(6), 1473-1479, doi 10.1002/celc.202000171

[177] Budi, S., Afrizal, A., Handoko, E., and Fahdiran, R. The growth of FeCoNi nanoparticles electrodeposited from CTAB-assisted sulfate electrolyte. *IOP Conference Series: Materials Science and Engineering* 2018, 434, 1, 012099), doi 10.1088/1757-899X/434/1/012099

[178] Idczak, K.; Idczak, R.; Konieczny, R. An investigation of the corrosion of polycrystalline iron by XPS, TMS and CEMS. *Phys. B Condens. Matter*, 2016, 491, 37â€“45, doi 10.1016/j.physb.2016.03.018

[179] Abidov, A.; Allabergenov, B.; Lee, J.; Jeon, H.-W.; Jeong, S.-W.; Kim, S. X-Ray Photoelectron Spectroscopy Characterization of Fe Doped TiO2 *Photocatalyst. Int. J. Mater. Mech. Manuf.* 2013, 1, 294â€“296, doi 10.7763/IJMMM.2013.V1.63

[180] Sellmyer, D. J., Zheng, M., and Skomski, R., Magnetism of Fe, Co and Ni nanowires in self-assembled arrays. *Journal of Physics: Condensed Matter*, 2001, 13(25), R433, doi 10.1088/0953-8984/13/25/201

[181] Nikolic, N.; Pavlovic, L.; Pavlovic, M.; Popov, K. Effect of temperature on the electrodeposition of disperse copper deposits. *J. Serbian Chem. Soc.* 2007, 72, 1369â€“1381, doi http://dx.doi.org/10.2298/JSC0712369N

[182] Tang, Z.-Q.; Liao, L.-W.; Zheng, Y.-L.; Kang, J.; Chen, Y.-X. Temperature Effect on Hydrogen Evolution Reaction at Au Electrode *Chin. J. Chem. Phys.* 2012, 25, 469â€“474, doi 10.1088/1674-0068/25/04/469-474

[183] Scharifker, B.; Hills, G. Theoretical and experimental studies of multiple nucleation. *Electrochim. Acta* 1983, 28, 879â€“889, doi 10.1016/0013-4686(83)85163-9

[184] Velazquez-Galvan, Y.; Medina, J.D.L.T.; Piraux, L.; Encinas, A. Robustness of the enhanced magnetic anisotropy in Ni nanowires regardless of the deposition potential. *J. Magn. Magn. Mater.* 2020, 497, 165992, doi 10.1016/j.jmmm.2019.165992

[185] M. Kąc, J. Morgiel, A. Polit, Y. Zabila, M. Marszałek, Atomic scale structure investigations of epitaxial Fe/Cr multilayers, *Appl. Surf. Sci.* 2014, 305, 154-159, 10.1016/j.apsusc.2014.03.021

[186] Dalavi, S. B., Theerthagiri, J., Raja, M. M., Panda, R. N. Synthesis, characterization and magnetic properties of nanocrystalline FexNi80â' xCo20 ternary alloys *Journal of magnetism and magnetic materials*, 2013, 344, 30-34, doi 10.1016/j.jmmm.2013.05.026

[187] Matlosz, M. Competitive adsorption effects in the electrodeposition of iron-nickel alloys *Journal of the Electrochemical Society*, 1993, 140(8), 2272, doi 10.1149/1.2220807

[188] Nykiel, A., Ledwig, P., Pawlik, P., Ghanbaja, J., Cempura, G., Kruk, A., Walcarius A., and Kac, M. (2024). The influence of electrodeposition potential on the chemical composition, structure and magnetic properties of FeCoNi nanowires, *Journal of Alloys and Compounds*, 982, 173709, doi 10.1016/j.jallcom.2024.173709

[189] Zhang, Y., and Ivey, D. G. Characterization of Co-Fe and Co-Fe-Ni soft magnetic films electrodeposited from citrate-stabilized sulfate baths, *Materials Science and Engineering: B*, 2007, 140(1-2), 15-22, doi 10.1016/j.mseb.2007.03.004

[190] Toparli, C., Ebin, B., and Gurmen, S. Synthesis, structural and magnetic characterization of soft magnetic nanocrystalline ternary FeNiCo particles, *Journal of Magnetism and Magnetic Materials*, 2017, 423, 133-139, doi 10.1016/j.jmmm.2016.09.005

[191] Yanai, T., Koda, K., Kaji, J., Aramaki, H., Eguchi, K., Takashima, K., Nakano M. and Fukunaga, H. Electroplated Fe-Co-Ni films prepared in ammonium-chloride-based plating baths, *AIP Advances*, 2018, 8(5), doi 10.1063/1.5007782

[192] Iwasaki, Y., Kusne, A. G., and Takeuchi, I. Comparison of dissimilarity measures for cluster analysis of X-ray diffraction data from combinatorial libraries, *Computational Materials*, 2017, 3(1), 1-9, doi 10.1038/s41524-017-0006-2

[193] I. Dobosz, W. Gumowska, M. Czapkiewicz, Structure and magnetic properties of Co nanowires electrodeposited into the pores of anodic alumina membranes, *J. Solid State Electrochem.*, 2014, 18, 2963-2972, doi 10.1007/ s10008-014-2552-6.

[194] A. Kumar, S. Fahler, H. Schlorb, K. Leistner, L. Schultz, Competition between shape anisotropy and magnetoelastic anisotropy in Ni nanowires electrodeposited within alumina templates, *Phys. Rev. B - Condens. Matter Mater. Phys.*, 2006, 73, 1-5, doi 10.1103/PhysRevB.73.064421

[195] D. Navas, K.R. Pirota, P. Mendoza Zelis, D. Velazquez, C.A. Ross, M. Vazquez, Effects of the magnetoelastic anisotropy in Ni nanowire arrays, *J. Appl. Phys.*, 2008, 103, 103-106, doi 10.1063/1.2834719

[196] Dubitskiy I.S., Elmekawy A.H.A., Iashina E.G., Sotnichuk S.V., Napolskii K.S, Menzel D., Mistonov A.A., Effect of interactions and non-uniform magnetic states on the magnetization reversal of iron nanowire arrays, *J. Supercond. Nov. Magn.*, 2021, 34, 539-549, doi 10.1007/s10948-020-05711-y

[197] Schwerdt J. I., Goya G. F., Calatayud M.P., Herenu C.B., Reggiani P. C., Goya R. G., Magnetic field-assisted gene delivery: achievements and therapeutic potential, Curr. Gene Ther., 2012, 12, 116-126, 10.2174/156652312800099616

[198] Kartopu G., Yalin O., Es-Souni M., Basaran A.C., Magnetization behavior of ordered and high density Co nanowire arrays with varying aspect ratio, *J. Appl. Phys.*, 2008, 103, doi 10.1063/1.2917191

[199] Nielsch K., Muller F., Li A.P., Gosele U., Uniform nickel deposition into ordered alumina pores by pulsed electrodeposition, *Adv. Mater.*, 2000, 12, 582-586, doi 10.1002/(SICI)1521-4095(200004)12:8<582::AIDADMA582>3.0.CO;2-3

[200] Sampaio L., Sinnecker E.H.C.P., Cernicchiaro G., Knobel M., Magnetic microwires as macrospins in a long-range dipole-dipole interaction, *Phys. Rev. B - Condens. Matter Mater.*, 2000, 61, 8976-8983, doi: 10.1103/PhysRevB.61.8976

[201] Esmaeili, A., Kashi, M. A., Ramazani, A., and Montazer, A. H. Tailoring magnetic properties in arrays of pulse-electrodeposited Co nanowires: The role of Cu additive, *Journal of Magnetism and Magnetic Materials*, 2016, 397, 64-72, doi: 10.1016/j.jmmm.2015.08.085

[202] Xu, J., Zhang, J., Wang, J., Hong, B., Peng, X., Wang, X., and Hu, J. Effects of gradient diameter on magnetic properties of FeNi alloys nanowires arrays, *Journal of Magnetism and Magnetic Materials*, 2020, 499, 166207, doi: 10.1016/j.jmmm.2019.166207

[203] Garcia, J., Prida, V. M., Vivas, L. G., Hernando, B., Barriga-Castro, E. D., Mendoza-Resendez, R., and Vazquez, M., Magnetization reversal dependence on effective magnetic anisotropy in electroplated Co-Cu nanowire arrays. *Journal of Materials Chemistry C*, 2015, 3(18), 4688-4697, doi: 10.1039/C4TC02988G

[204] Piraux, L., Renard, K., Guillemet, R., Matefi-Tempfli, S., Matefi-Tempfli, M., Antohe, V. A., and Cros, V., Template-grown NiFe/Cu/NiFe nanowires for spin transfer devices, *Nano letters*, 2007, 7(9), 2563-2567, doi: 10.1021/nl070263s

[205] Abbas, M. H., Ramazani, A., Montazer, A. H., and Kashi, M. A., Capturing dual behavior of the parallel coercivity in FeNi/Cu nanowire arrays by fine-tuning of segment thicknesses, *Journal of Alloys and Compounds*, 2020, 825, 153992, doi: 10.1016/j.jallcom.2020.153992

[206] Abbas, M. H., Ramazani, A., Montazer, A. H., and Kashi, M. A. Fixed vortex domain wall propagation in FeNi/Cu multilayered nanowire arrays driven by reversible magnetization evolution, *Journal of Applied Physic*s, 2019, 125(17), doi: 10.1063/1.5092574

[207] Moraes, S., Navas, D., Beron, F., Proenca, M. P., Pirota, K. R., Sousa, C. T., and Araujo, J. P., The role of Cu length on the magnetic behaviour of Fe/Cu multi-segmented nanowires, *Nanomaterials*, 2018, 8(7), 490, doi: 10.3390/nano8070490

[208] Venturi, F., Gazzadi, G. C., Tavabi, A. H., Rota, A., Dunin-Borkowski, R. E., Frabboni, S., Magnetic characterization of cobalt nanowires and square nanorings fabricated by focused electron beam induced deposition, *Beilstein Journal of Nanotechnology*, 2018, 9(1), 1040-1049, doi: 10.3762/bjnano.9.97

[209] Goolaup, S., Singh, N., Adeyeye, A. O., Ng, V., and Jalil, M. B. A. Transition from coherent rotation to curling mode reversal process in ferromagnetic nanowires, *The European Physical Journal B-Condensed Matter and Complex Systems*, 2005, 44, 259-264, doi: 10.1140/epjb/e2005-00122-7

[210] Samanifar, S., Kashi, M. A., and Ramazani, A. Study of reversible magnetization in FeCoNi alloy nanowires with different diameters by first order reversal curve (FORC) diagrams, *Physica C: Superconductivity and its Applications*, 2018, 548, 72-74, doi: 10.1016/j.physc.2018.02.009

[211] Alikhanzadeh-Arani, S., Almasi-Kashi, M., and Ramazani, A., Magnetic characterization of FeCo nanowire arrays by first-order reversal curves, *Current Applied Physics*, 2013, 13(4), 664-669, doi: 10.1016/j.cap.2012.10.014

[212] Egolf P.W., Shamsudhin N., Pane S., Vuarnoz D., Pokki J., Pawlowski A., Tsague P., Marco B., Bovy W., Tucev S., Ansari M. H. D. and Nelson B.J. Hyperthermia with rotating magnetic nanowires inducing heat into tumor by fluid friction *Journal of Applied Physics*, 2016, 120, 064304, doi:10.1063/1.4960406

[213] Pondman K.M., Bunt N.D., Maijenburg A.W., Wezel R.J., Kishore U., Abelmann L., Elshof J., Haken B. Magnetic drug delivery with FePd nanowires *J Magn Magn Mater.*, 2015, 380:299-306, doi:10.1016/j.jmmm.2014.10.101

[214] Garcia-Gradilla V., Sattayasamitsathit S., Soto F., Kuralay F., Yardimci C., Wiitala D., Galarnyk M. and Wang J. Ultrasound-Propelled Nanoporous Gold Wire for Efficient Drug Loading and Release *Small*, 2014, 20, 4154−4159, doi:10.1002/smll.201401013

[215] McGary P., Tan L., Zou J., Stadler B., Downey P.R., Flatau A. B. Magnetic nanowires for acoustic sensors (invited) *Journal Of Applied Physics*, 2006, 08B310, doi:10.1063/1.2167332

[216] Atitoaie A., Stancu A., Ovari T., Lupu N. Magneto-mechanical modeling study of CO-based amorphous micro- and nanowires for acoustic sensing medical applications *Phys B Phys Condens Matter.*, 2016, 486:69-72, doi:10.1016/j.physb.2015.09.019

[217] Lu L., Zhang L., Qu F., Lu H., Zhang X., Wu Z., Huan S., Wang Q., Shen G., Yu R. A nano-Ni based ultrasensitive nonenzymatic electrochemical sensor for glucose: Enhancing sensitivity through a nanowire array strategy *Biosensors and Bioelectronics*, 2009, 25:218-223, doi:10.1016/j.bios.2009.06.041

[218] Garcia M., Escarpa A. Disposable electrochemical detectors based on nickel nanowires for carbohydrate sensing *Biosensors and Bioelectronics*, 2011, 26:2527-2533, doi:10.1016/j.bios.2010.10.049

[219] Wang J., Scampicchio M., Laocharoensuk R., Valentini F., Gonzalez-Garcia O., Burdick J. Magnetic tuning of the electrochemical reactivity through controlled surface orientation of catalytic nanowires *J Am Chem Soc.*, 2006, 128(14):4562-4563, doi:10.1021/ja061070u

[220] Mashraei Y., Amara S., Albu Z., Ivanov Y., Kosel J. Ultra-Low Power Corrosion Sensor Made of Iron Nanowires on Magnetic Tunnel Junctions *Adv Eng Mater.*, 2018, 20(10):1-6, doi:10.1002/adem.201800337

[221] Cox B., Davis D., Crews N. Creating magnetic field sensors from GMR nanowire networks *Sensors Actuators A Phys.*, 2013, 203:335-340, doi:10.1016/j.sna.2013.08.035

[222] Maqableh M., Huang X., Sung S., Reddy K., Norby G., Victora R. H., Stadler B. Low-Resistivity 10 nm Diameter Magnetic Sensors *Nano Letters*, 2012, 12, 4102-4109, dx.doi.org/10.1021/nl301610z

[223] Pinheiro P.C., Tavares D.S., Daniel-Da-Silva A.L., Lopes C.B., Pereira E., Araujo J.P., Sousa C.,Trindade T. Ferromagnetic sorbents based on nickel nanowires for efficient uptake of mercury from water *ACS Appl Mater Interfaces*, 2014, 6(11):8274-8280, doi:10.1021/am5010865

[224] Cui H., Shi J., Yuanb B. FM. Synthesis of porous magnetic ferrite nanowires containing Mn and their application in water treatment *J. Mater. Chem. A*, 2013, 1, 5902, doi:10.1039/c3ta01692g

[225] Zhang L., Petit T., Peyer K.E., Nelson B.J. Targeted cargo delivery using a rotating nickel nanowire *Nanomedicine Nanotechnology, Biol Med.* 2012, 8(7):1074-1080, doi:10.1016/j.nano.2012.03.002

[226] Dev A., Elshaer A., Voss T. Optical Applications of ZnO Nanowires *IEEE Journal Of Selected Topics In Quantum Electronics*, 2011, 17(4):896-906, doi:10.1109/JSTQE.2010.2082506

[227] Li Y., Qian F., Xiang J., Lieber C.M. Nanowire electronic and optoelectronic devices Electronic and optoelectronic devices *Materials Today*, 2006, 9(10):18-27, doi:10.1016/S1369-7021(06)71650-9

[228] Lieber C.M., Wang Z.L. Functional Nanowires *MRS Bulletin*, 2007, 32, 99-108, doi.org/10.1557/mrs2007